Experimental multi-photon entanglement and quantum enhanced metrology

Roland Patrik Krischek

München 2011

Experimental multi-photon entanglement and quantum enhanced metrology

Roland Patrik Krischek

Dissertation
an der Fakultät für Physik
der Ludwig–Maximilians–Universität
München

vorgelegt von
Roland Patrik Krischek
aus Sarnen (Schweiz)

München, den 24. Mai 2011

Erstgutachter: Prof. Dr. Harald Weinfurter

Zweitgutachter: Prof. Dr. Stefan Kehrein

Tag der mündlichen Prüfung: 06.07.2011

Contents

Abstract

Quantum theory developed at the beginning of the last century has made enormous progress in the last few decades. The experimental achievements to generate and control different quantum systems in the laboratory not only led to partial answers to fundamental questions of quantum theory, but also to numerous proof-of-principles demonstrations pushing the technological progress of quantum information science. This includes, for example, the developments towards a quantum computer, promising faster computation for several tasks or the implementation of quantum enhanced metrology improving the precision of measurements beyond the limits imposed by classical physics. Entanglement is a key ingredient to all this developments and it is therefore essential to characterize and generate entangled quantum states suited for different applications.

In this thesis, we will use photons to generate entangled quantum states and contribute to photonic quantum information with mainly two aspects: First, we develop a new source to generate multi-photon entangled states with high count rates, which enables us to observe and characterize different quantum states up to six photons. And second, we experimentally demonstrate the applicability of these states for quantum enhanced metrology and are able to identify useful multi-particle entanglement for the estimation of an unknown phase shift.

The new source of multi-photon entangled states is based on the well known process of spontaneous parametric down conversion (SPDC). Previous sources have increased the yield of multi-photon generation using ultra-short laser pulses directly pumping a non-linear crystal for SPDC, but these sources still suffer from low six-photon count rates. Here, we additionally enhance these laser pulses in a cavity for ultraviolet (UV) femtosecond pulse trains. With this cavity, we improve the count rates for six-photon entangled states by two orders of magnitude, compared to previous sources, and demonstrate the applicability of our source with the observation of a six-photon symmetric Dicke state. In addition, we are interested to fully characterize our quantum states in an efficient way. But performing full quantum state tomography is demanding, because the measurement effort scales exponentially with the number of qubits. We therefore demonstrate the applicability of permutationally invariant quantum state tomography, which applies to all permutationally invariant quantum states, like for example, all Dicke states or the Greenberger-Horne-Zeilinger state. This enables us to reduce the measurement effort to only quadratic scaling and paves the way for future characterisations of quantum states of higher qubit numbers.

For the second part of this thesis we experimentally prove the applicability of entangled quantum states for quantum enhanced metrology. In the experiment, the improved performance of an entangled state is clearly revealed by the direct comparison to a separable state. In addition, we demonstrate a general criterion to characterize the entanglement useful for the estimation of an unknown phase shift. This provides a guideline for the future technological exploitation of multi-particle entanglement to outperform current metrological limits.

Zusammenfassung

Seit der Entdeckung der Quanten-Mechanik zu Beginn des letzten Jahrhunderts, wurden vor allem in den letzten zehn bis zwanzig Jahren enorme Fortschritte erzielht. Aus experimenteller Sicht führte diese Entwicklung zur besseren Kontrolle verschiedener Quantensysteme im Labor, zur teilweisen Beantwortung von verschiedenen offenen Fragestellungen in der Quanten-Mechanik, sowie zu Beweisen der experimentellen Machbarkeit neuer Prinzipien. Der damit mit einhergehende technologische Fortschritt kann grundsätzlich bis zur Entwicklung eines Quantencomputers führen, von dem man sich - für verschiedene Anwendungen - eine höhere Rechenleistung verspricht. Aber zum Beispiel auch in der Quantenmetrologie konnte man bereits zeigen, dass man mit nichtklassischen Teilchen genauer messen kann, als dies mit normalen Teilchen überhaupt möglich ist. Dies ist im Wesentlichen durch die Eigenschaft der Verschränkung von mehreren Teilchen zu begründen, was gegenüber klassischen Teilchen der entscheidende Vorteil ausmacht. Die Erzeugung und Charakterisierung von verschränkten Zustanden für verschiedene Anwendungen ist deshalb von grosser Bedeutung.

In dieser Arbeit befassen wir uns mit der Verschränkung von Photonen und tragen zur weiteren Entwicklung dieses Gebiets bezüglich zwei Punkten bei: Dies beinhaltet einerseits die Entwicklung einer neuen Quelle zur Erzeugung und Charakterisierung von Sechs-Photonen-Zuständen mit hohen Zählraten. Andererseits nutzen wir diese Zustände für Phasenmessungen und sind in der Lage, diejenige Verschränkung des Zustands, die zu einer nutzbar genaueren Phasenmessung beiträgt, zu identifizieren.

Die Quelle zur Erzeugung von mehrfach verschränkten Photonen basiert auf dem Prozess der spontanen parametrischen Fluoreszenz (SPF). Bisherige Quellen konnten durch den Einsatz von gepulsten Lasern die Zählraten für Vier-Photonen-Zustände erhöhen, was aber für Sechs-Photonen-Zustände immer noch sehr niedrig ist. Deshalb zeigen wir experimentell, wie man die für den Pumpprozess der SPF benötigten ultravioletten Laserpulse in einem Resonator weiter erhöht. Mit diesem Resonator sind wir in der Lage die Zähraten für Sechs-Photonen-Zustände, im Vergleich zu bisherigen Quellen, um zwei Grössenordnungen zu erhöhen. Dies wird mit der Erzeugung eines symmetrischen Sechs-Photonen-Dicke-Zustands gezeigt. Darüber hinaus möchten wir möglichst effizient Quantenzustände vollkommen charakterisieren können. Dies ist anspruchsvoll, denn für Quantenzustandstomographie skaliert die Anzahl der Messbasen exponentiell mit der Anzahl der Qubits. Eine Alternative bietet die hier gezeigte permuationsinvariante Quantenzustandstomographie. Da zum Beispiel alle Dicke-Zustände und der "Greenberger-Horne-Zeilinger"-Zustand permutationsinvariant sind, wird diese Symmetrie genutzt, so dass die Anzahl der Messbasen nur noch quadratisch mit der Anzahl der Qubits skaliert.

Im zweiten Teil dieser Arbeit zeigen wir experimentell, dass man mit verschänkten Zuständen eine Phase genauer bestimmen kann, als mit separablen Zuständen. Allgemein können wir mit Hilfe eines Kriterums diejenige Verschränkung eines Zustands identifizieren, die nutzbar zur genaueren Phasenmessung beiträgt. Damit schaffen wir neue Richtlinien zur optimalen Nutzung verschränkter Zustände für Phasenmessungen.

1

Introduction

One of the foundation of quantum mechanics was laid at the beginning of the twentieth century by Max Planck. He concluded in his quantum hypothesis, that energy is not emitted or absorbed in continuous amounts, but only in discrete quantities. Few years later, this development motivated Albert Einstein to the explanation of the photoelectric effect, where a light quantum or photon absorbed by a photoelectric material leads to the emission of an electron [1]. On the one hand, Albert Einstein contributed decisively to the development of quantum mechanics, but on the other hand he was also one of the biggest critics concerning the interpretation of quantum mechanics. This was mainly due to the feature of entanglement, which describes a quantum system of two or multiple particles being in a superposition of, for example, two states – the ground and excited state. The system as a whole is fully described by this superposition, but the state of a single particle is completely unknown. If one performs now a measurement on such a system of, for example, two entangled particles then there is no prior information available about the result of the first particle to be measured, but once the experimental outcome is revealed, the state of the other particle is determined immediately. This behaviour was confusing to Albert Einstein and together with Boris Podolsky and Nathan Rosen he questioned in the famous EPR[1] paper of 1935 [2] the complete description of physical reality by quantum mechanics. A theory can only be considered complete if for each element of this theory a corresponding element of reality exists, which is according to EPR in contradiction to quantum mechanics. It took then 30 years until John Bell formulated in 1964 the ideas of the EPR paper in an inequality based on the joint assumptions of locality and realism [3]. Locality implies that a space-like separated, for example, two body system, which has interacted in the past, cannot communicate faster than the speed of light. Realism is attributed to the assumption, that independent of observation an external reality exists, which can be described by a hidden variable model. Later on, more revised versions of Bell inequalities have been developed [4, 5] which all allowed to experimentally test whether a physical system follows quantum mechanics or obeys local realism. To date, all experiments are in complete accordance with quantum theory [6, 7, 8, 9, 10] and exclude locality and realism to hold at the same time. However, for the sake of completeness one has to

---

[1]Einstein, Podolsky and Rosen

mention that despite the apparent violation of local realism, mostly technical loopholes exist that could allow to explain the observed correlations by local realism. These are mainly the locality loophole, which can be closed if space-like separated measurements are performed not allowing the particles to communicate within the speed of light [9] and the detection loophole, which requires an overall detection efficiency of more then $66.\bar{6}\%$ [11] to close it [10]. Although the violation of local realism is well established a conclusive experiment closing those two loopholes at the same time is still missing. Today also other interpretations of quantum mechanics exist assuming, for example, a class of non-local realistic theories developed by Anthony James Leggett [12], which have recently been violated experimentally [13, 14, 15] pointing towards alternative directions of the demanding[2] goal to reveal the essence of quantum mechanics by empirical means.

Entanglement reveals not only fundamental aspects of quantum theory but also emerged to be the key ingredient of new research fields improving multiple tasks with respect to classical physics, such as, for example, quantum information and computation [16]. One possible future technology resulting from this field is the so called quantum computer, which promises exponential faster computation for several tasks [17, 18] or more efficient factorisation of large numbers [19]. Another benefit of quantum information is quantum key distribution, which allows in principle perfectly secure communication, because every measurement on a quantum state perturbs the system and immediately allows to notice the presence of an eavesdropper [20]. Further technological improvements on the basis of entanglement are demonstrated with quantum lithography, which enables to write features smaller than the classical diffraction limit [21, 22] or quantum metrology which pushes the ultimate limit of measurement precision beyond the classical shot noise limit, which can be implemented, for example, in an interferometer to measure the path length difference between two propagating non-classical light beams [23].

To physically implement all the aforementioned tasks different two-level systems exist, which are also called qubits, to produce the desired superposition. For the quantum computer the requirements for such a physical implementation are summarized by the Di Vincenzo criteria [24]. These criteria are very similar to the general conditions to further exploit entanglement. These are the implementation of a scalable two level system for large qubit numbers, a general set of gates to manipulate and create entanglement, long coherence times of the qubits much longer than the gate operation time, which enables them to interact without suffering from decoherence by disturbances of the environment and finally, the ability to read out the quantum states with high fidelity to generate the desired output. In the laboratory several numbers of qubits have been achieved based on different physical realization like photons [25, 26, 27], atoms in optical cavities [28, 29] or ultra cold atoms in optical lattices [30], trapped ions [31, 32, 33], nuclear spin of molecules [34, 35], solid state based quantum dots [36, 37], superconducting qubits [38, 39] or nitrogen vacancy centres in bulk diamond [40, 41].

---

[2]or maybe even unachievable

The maximal number of prepared qubits so far is 14 [42], but today it is still very difficult to absolutely favour one of these attempts with respect to another, which is also represented by the fact that so many distinct physical implementations exist.

Here we will focus on the implementation with photons for quantum information using their polarization as a physical qubit. This has several advantages [26]. For example, the decoherence of photons is negligible due to their weak coupling to the environment and they are the fastest carrier of information, which can simply be transmitted by optical glass fibres over large distances. The downside of marginal decoherence is the small probability of interaction with other photons, which is essential to generate qubit gates for quantum computing. A solution to this problem is proposed by the scheme of optical one-way quantum computing [25], which has also been demonstrated experimentally [43] allowing to manipulate the photons by projective measurements, phase shifters and interference at beam splitters [26]. Another benefit of photons is the fact that different states of entangled photons can be produced in a "straightforward" manner using the process of spontaneous parametric down conversion (SPDC) in combination with linear optical elements. Proceeding in this way, photons have been intensively used for several proof-of-principle demonstrations in the last decades [20, 44, 26].

In this work, we proceed with the development of photonic entanglement and implemented to this aim a new SPDC source allowing a high yield of multi-photon generation to characterize and observe entangled states up to six photons. This is achieved by considerably increasing the laser pump power for the SPDC process within an enhancement cavity for ultraviolet (UV) femtosecond (fs) pulse trains. Only recently, fs pulses in the infrared wavelength region have been successfully enhanced in a cavity [45, 46, 47], but the extension to the UV is not obvious and is demonstrated in this work for the first time (see publication 3.1.1 [48] and Nature Photonics News & Views [49]). To further characterize the enhancement cavity we determine the duration of the circulating laser pulses inside the cavity. For this purpose, we profit from the non linearity of the SPDC process, which emits in its nth order $2n$ photons with half the wavelength of the pump photons (see section 2.2). The desired pulse length is then determined by counting the four photon events in dependence on two delayed pump pulses, implemented by a Mach-Zehnder interferometer in front of the enhancement cavity (see preprint 3.2.1).

After this short excursus to ultra short laser pulses, we will further concentrate on the characterization and utilization of entangled quantum states based on the aforementioned SPDC source for different tasks in quantum information science. For this reason, we built a specific linear optics setup to observe the six photon entangled symmetric Dicke state with three excitations (see publication 3.3.1 [50]). This state has remarkable properties: on the one hand it has a high entanglement persistence against qubit loss [51] and on the other hand, it severs as a resource to generate other states of lower qubit number by projective measurements [52]. Proceeding in this way we are thus able to observe a 4 photon W state, which has the first time been observed, or a 4 photon Greenberger-Horne-Zeilinger (GHZ) state, which has already intensively been studied for different number of qubits [53, 54, 55, 56]. In addition we violate a

Bell inequality and apply tailored entanglement witnesses to prove genuine 6-partite entanglement for our symmetric Dicke state (see publication 3.3.2 [57]). In the next step, we are further interested in a full characterisation of our state. To this aim, full quantum state tomography is the method of choice [58], but the price we pay for the complete characterisation is the exponential scaling measurement effort with the number of qubits. Especially for higher qubit numbers this is a general problem. Because the most prominent quantum states , like the GHZ and all Dicke states, are all permutationally invariant[3], we propose to measure only the permutationally invariant part of our probe state. This enables us to reduce the measurement effort to only quadratic scaling with the number of qubits. In a proof-of-principle experiment with a 4 photon symmetric Dicke state we demonstrate the applicability of permutationally invariant quantum tomography for future characterisations of quantum states (see publication 3.4.1 [59]).

At the beginning we have mentioned that entangled states can in principle improve several tasks with respect to classical states. Although the benefit of entanglement is demonstrated in numerous experiments it is not obvious to find the best suited entangled state for the desired application. In the last chapter of this thesis we therefore study the usefulness of quantum states, on the example of symmetric Dicke states, for entanglement enhanced metrology. For this purpose we identify useful multi-particle entanglement, intrinsic to our probe state, for the estimation of an unknown phase shift beyond the classical shot noise limit (see preprint 4.1.3 [60]). Our criterion is used for an experiment with a symmetric four photon Dicke state proving sub shot noise sensitivity and we also compare two complete phase estimation protocols. With this criterion at hand, useful multi-particle entanglement to directly improve a specific technological task can be successfully characterized (see preprint 4.1.5). In addition, we achieve in an experiment with a six photon symmetric Dicke state sub shot noise sensitivity, which has not yet been observed for this photon number (see preprint 4.2.1).

This thesis is organized as follows: Before presenting the appropriate publications in each chapter, every topic is introduced and parts, which are only shortly described in the publication, will be explained in more detail. In chapter 2 the very basics for the understanding of all the further explained experiments are given. Chapter 3 describes the new SPDC source and the observation of the six photon symmetric Dicke state, followed by the explanation and demonstration of permutationally invariant quantum tomography. In the last chapter, the applicability of symmetric Dicke states with respect to quantum phase estimation is studied and demonstrated with different experiments.

---

[3]which means that the state after exchange of two qubits stays the same

<div align="right">

2

</div>

Multi-partite entanglement with photons

In this chapter we will discuss the very basics, which will be used throughout this work. It starts with the description of qubits compared to classical bits and the formal definition of entanglement. Further characterizations of entangled states by entanglement witnesses or Bell inequalities are explained in section 3.3 on the example of the experimental observation of a symmetric Dicke states. The same holds also for full quantum state tomography, which will be described on the example of permutationally invariant quantum state tomography in section 3.4. As motivated in the introduction, all experiments described in this thesis use photons as qubits and we therefore introduce their polarization encoded notation. In the last part of this chapter the theoretical background to spontaneous parametric down conversion (SPDC) is given, which is here the relevant process to generate multiple entangled photons, followed by an introduction to the general experimental framework to observe a desired entangled state by linear optical elements.

2.1 Qubit notation and entanglement

In the classical world of ordinary computers a bit of information is either in the well defined state 0 or 1. The difference from classical to quantum bits, or qubits, is, that the latter can also be in a superposition of 0 and 1. This is described in quantum mechanics by the normalized state $|\psi\rangle$, as

$$|\psi\rangle = \alpha |0\rangle + \beta |1\rangle \tag{2.1}$$

with $|\alpha|^2 + |\beta|^2 = 1$. For photons the polarization encoded qubit notation is used and they can therefore be described as a vector on the Bloch sphere (see Fig. 2.1) as [16]

$$|\psi(\theta, \phi)\rangle = \cos\frac{\theta}{2} |H\rangle + e^{i\phi} \sin\frac{\theta}{2} |V\rangle \equiv \begin{pmatrix} \cos\frac{\theta}{2} \\ e^{i\phi} \sin\frac{\theta}{2} \end{pmatrix}; \tag{2.2}$$

with $\theta \in [0, \pi]$, $\phi \in [0.2\pi)$. Here, H denotes a horizontally and V a vertically polarized photon. A measurement on such a quantum state is represented by an observable and the outcome of the measurement is expectation value of this observable. A general
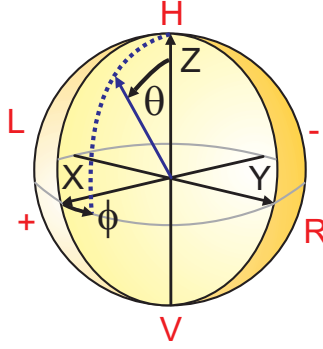
Figure 2.1: **Bloch sphere representation of a polarization encoded qubit**. The state $|\psi(\theta,\phi)\rangle$ is represented by a point on the surface of the Bloch sphere. The angle ϕ corresponds to a rotation around the Z-axis and the angle θ to a rotation around the Y-axis. The horizontal polarization H is represented by the point $(0,0)$. V: vertical polarisation $(\pi,0)$; +: positive diagonal polarisation $(\frac{\pi}{2},0)$; −: negative diagonal polarization $(\frac{\pi}{2},\pi)$; R: right circular polarization $(\frac{\pi}{2},\frac{\pi}{2})$; L: left circular polarization $(\frac{\pi}{2},\frac{3\pi}{2})$.

observable can, for example, be described as the linear combination of the Pauli spin operators as

$$\hat{\sigma}(\theta,\phi) = \cos(\phi)\sin(\theta)\hat{\sigma}_x + \sin(\phi)\sin(\theta)\hat{\sigma}_y + \cos(\theta)\hat{\sigma}_z \tag{2.3}$$

where the Pauli spin operators are given by

$$\hat{\sigma}_0 = \mathbb{1} = \begin{pmatrix} 1 & 0 \\ 0 & 1 \end{pmatrix}; \hat{\sigma}_x = \begin{pmatrix} 0 & 1 \\ 1 & 0 \end{pmatrix}; \hat{\sigma}_y = \begin{pmatrix} 0 & -i \\ i & 0 \end{pmatrix}; \hat{\sigma}_z = \begin{pmatrix} 1 & 0 \\ 0 & -1 \end{pmatrix} \tag{2.4}$$

Further, the eigenstates of the Pauli spin operators are lying directly on the X-, Y- and Z-axis of the Bloch sphere shown in Fig. 2.1 and are denoted by H/V, +/− (positive/negative diagonal polarization) and L/R (left/right circular polarization) with

$$\hat{\sigma}_z\,|\,H/V\,\rangle = \qquad\qquad\qquad\qquad \pm\,|\,H/V\,\rangle \tag{2.5}$$

$$\hat{\sigma}_x\,|\,+/-\,\rangle = \hat{\sigma}_x\big(|\,H\,\rangle \pm |\,V\,\rangle\big) = \pm\,|\,+/-\,\rangle \tag{2.6}$$

$$\hat{\sigma}_y\,|\,R/L\,\rangle = \hat{\sigma}_y\big(|\,H\,\rangle \pm i\,|\,V\,\rangle\big) = \pm\,|\,R/L\,\rangle \tag{2.7}$$

In the following, we explain the concept of entanglement, which only makes sense if we talk about multiple particles and we therefore define states of more than one qubit. A two qubit state is, for example, given by the tensor product of $|\,H\,\rangle_1 \otimes |\,H\,\rangle_2 = |\,HH\,\rangle$, which corresponds to a $2^2 = 4$ dimensional system. The generalization to N qubits is very natural and a 2^N dimensional quantum state is, for example, given by $|\,H\,\rangle_1 \otimes ... \otimes |\,H\,\rangle_N = |\,H...H\,\rangle$. Entanglement can now be specified either for pure or mixed states. A pure state is given, in the language of quantum mechanics, by a single ket-vector $|\,\phi\,\rangle$ and is given as its projector

$$\rho_{pure} = |\,\phi\,\rangle\langle\,\phi\,|. \tag{2.8}$$

A mixed state is then a mixture of several pure states and can be written in its matrix form as

$$\rho_{mixed} = p_i \sum_i |\phi_i\rangle\langle\phi_i| \tag{2.9}$$

with $p_i \geq 0$ and $\sum_i p_i = 1$ [4]. A possibility to check whether a state is pure or mixed is to calculate the trace of the states density matrix squared, which is $\text{Tr}(\rho^2) = 1$ for pure states and for mixed states $\text{Tr}(\rho^2) < 1$ [16]. An example of a well known mixed state is, for example, the state

$$\rho_{wn} = \frac{1}{2}\begin{pmatrix} 1 & 0 \\ 0 & 1 \end{pmatrix}, \tag{2.10}$$

which is also called totally mixed state. This is the origin of equally probable measurement results described as white noise. A pure quantum state is now called entangled if it can not be written as a tensor product of two other states, as [61]

$$|\psi_{ab}\rangle \neq |\varphi_a\rangle \otimes |\phi_b\rangle \tag{2.11}$$

or for mixed states

$$\rho \neq \sum_i p_i \rho_a \otimes \rho_b \tag{2.12}$$

with $p_i \geq 0$ and $\sum_i p_i = 1$. If a quantum state is not entangled it is called separable. Eq. 2.11 and 2.12 are the formal mathematical definitions of entanglement. Proving entanglement of a quantum state in the experiment is not a obvious task and can be realized by using witness operators or Bell inequalities, which will be explained later on the example of a symmetric Dicke state (see section 3.3). Other methods to detect entanglement are further described in [62, 63, 64] or in the review articles [65, 66]. In the next section we describe how to generate entangled photons in the experiment by using the process of spontaneous parametric down conversion.

2.2 Spontaneous parametric down conversion and photon processing

The process of SPDC originates from the interaction of an intense laser beam with a non-linear medium, like for example, a non-linear crystal. An applied electric field $\vec{E}$ (with its components E_k) induces the polarization $\vec{P}$ (with its components P_k) in an anisotropic medium. The polarization P_k can be expanded into a Taylor series of the form [67]

$$P_k = \epsilon_0\left(\chi_{k,l}^{(1)}E_l + \chi_{k,l,m}^{(2)}E_l E_m + \chi_{k,l,m,n}^{(3)}E_l E_m E_n + ...\right) \tag{2.13}$$

with ϵ_0 the permittivity of the vacuum and $\chi^{(1)}$ is the linear contribution of the dielectric susceptibility. For the case of SPDC we are basically interested in the non-linear second

---

[4]Note that the decomposition of a mixed state into pure states is not unique.

order term $\chi^{(2)}$, which is also used for the well known second harmonic generation. The success probability of the SPDC process is rather low and on the order of 10^{-10}. This means that only for high electric fields, this process yields a non negligible contribution[5]. However, during the process of SPDC a photon incident to the non-linear medium converts into two photons with lower frequency. In terms of angular frequencies and because of the conservation of energy we obtain

$$\hbar\omega_p = \hbar\omega_s + \hbar\omega_i \tag{2.14}$$

where p stands for pump and s, i for signal and idler. This is not the only condition which has to be fulfilled for SPDC. Because optical materials are dispersive, they cause relative shifts between the propagating light fields inside the medium resulting in a phase mismatch over a specific region in space. Phase-matching is therefore needed for conservation of momentum and we observe

$$\vec{k}_p = \vec{k}_s + \vec{k}_i \tag{2.15}$$

where k_m $(m = p, s, i)$ are the components of the wave vector with angular frequencies ω_m with

$$k_m = \frac{\omega_m n(\omega_m)}{c}. \tag{2.16}$$

where $n(\omega_m)$ are the refractive indices of the three interacting waves and c the speed of light. Phase-matching $\Delta\vec{k} = 0 = \vec{k}_p - \vec{k}_s - \vec{k}_i$ is naturally achieved in uniaxial crystals, where two refractive indices are equal $n_o = n_1 = n_2$ and the third different $n_e = n_3 \neq n_o$. If the light is polarized in the plane with the wave vector $\vec{k}$ it is described by the extraordinary refractive index n_e and perpendicular to it with the ordinary refractive index n_o. In general, the difference in the refractive indices n_e and n_o is called birefringence. Crystals are said to be positive if $n_e > n_o$ and negative if $n_e < n_o$. In practice, the refractive indices n_e and n_o are obtained by using the Sellmeier formula. Characteristic coefficients for different material are, for example, given in Ref. [68]. Further, two choices in the polarizations of the down-converted photons exist, also known as type I or type II phase matching. In the first case, the idler and signal photons have identical polarizations and in the second case they are orthogonal. If the momentum vectors are all aligned in parallel ($\vec{k}_p \,||\, \vec{k}_{s,i}$), collinear, and otherwise non collinear phase matching occurs.

In the experiment throughout this work we use a negative uniaxial crystal of $\beta-$barium-borate (BBO) for type II phase matching in a collinear configuration illustrated in Fig. 2.2. The birefringence of the crystal leads to polarization dependent splitting of the SPDC emission cones. This birefringence causes an additional temporal walk-off between horizontally and vertically polarized photons and reduces therefore the temporal indistinguishability affecting the entanglement of our probe state. In the experiment,

---

[5]Because SPDC is a second order process we neglect in the following the impact from cubic and higher order susceptibilities
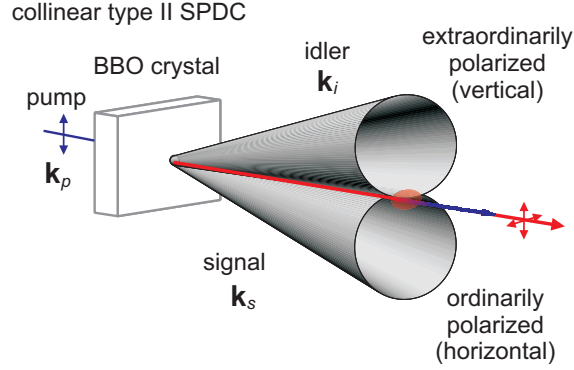
Figure 2.2: **Collinear SPDC emission from a type II cut BBO crystal.** The photons are emitted in two degenerate cones of horizontal and vertical polarization. The photon emission cones intersect in a line (collinear) and will be collected by a single mode fiber defining one spatial mode [69].

the temporal walk-off is compensated with a half wave plate and another BBO crystal with half of the length of the initial BBO [70]. The half wave plate turns the polarization from horizontally to vertically and vice versa. After passing through the second BBO crystal[6] with switched polarizations the temporal walk-off is compensated.

To describe the full quantum mechanical state emitted from the crystal we will use the notation of second quantization with creation and annihilation operators of photon number n. The creation $\hat{a}^\dagger$ and annihilation $\hat{a}$ operators have the following properties:

$$\hat{a}^\dagger \ket{n} = \sqrt{n+1} \ket{n+1} \ \text{and} \ \hat{a} \ket{n} = \sqrt{n} \ket{n-1}. \tag{2.17}$$

The relevant Hamiltonian for the single mode a, collinear[7] type II SPDC is given by [72]

$$\hat{\mathcal{H}} = i\hbar\kappa(\hat{a}_H^\dagger \hat{a}_V^\dagger + h.c.) \tag{2.18}$$

where κ is proportional to $\chi^{(2)}$ of the crystal and the amplitude of the electric pump field $|E_p|$. The state vector $\ket{\psi}$ is then given as

$$\ket{\psi} = e^{\frac{i}{\hbar}\hat{\mathcal{H}}t} \ket{0} \tag{2.19}$$

where t is the time of pump field propagating through the crystal and $\ket{0}$ the state of the vacuum. A detailed derivation of the state vector for collinear type II SPDC is, for example, given in [64] and we obtain

$$\ket{\psi} = \sqrt{1 - \tanh^2 |\tau|} \sum_{n=0}^\infty \frac{\tanh^n |\tau|}{n!} (\hat{a}_H^\dagger \hat{a}_V^\dagger)^n \ket{0} \tag{2.20}$$

---

[6]which is also called compensation crystal

[7]the non-collinear case is, for example, treated in [71]

with $\tau \propto \kappa t$ ($\propto |E_p|$). An often used approximation for low pump powers ($\tau \ll 1$) is $\tanh \tau \approx \tau$ and therefore $(1 - \tanh^2 |\tau|)^{\frac{1}{2}} \approx 1$. Assuming a pulsed laser source[8] the probability q_n to create n photon pairs per pump pulse is $q_n = (1 - \tanh^2 |\tau|)^{\frac{1}{2}} \tanh^{2n} \tau \approx \tau^{2n}$. With the previous approximations for low pump powers P we observe that the photon count rate $c_n = q_n f_r$ (with f_r the repetition rate of the pulses) depends on the pump power as

$$c_n \ \propto \ \tau^{2n} \ \propto \ |E_p|^{2n} \ \propto \ (P)^n. \tag{2.21}$$

For the observation of multiple photon pairs, the pump energy for the non linear crystal is thus concentrated in short pulses, increasing the emission probability considerably [73]. In our experiments we use therefore a mode-locked Ti:sapphire oscillator at central wavelength of 780nm and pump our BBO crystal at a wavelength of 390nm obtained after second harmonic generation. The repetition rate of the laser is ~ 80MHz and the pulse duration lies typically between 100-200fs.

To observe entanglement of multiple emission pairs, we have in addition to guarantee indistinguishability between the emission time of the multiple photon pairs within the coherence time of the pump pulse [73, 74, 75]. This can be achieved with a narrow bandwidth interference filters, which broadens the coherence time of the SPDC photons and therefore makes it impossible to determine the creation time of the photon pairs. The coherence time for Sech shaped pulses is given as [76]

$$t_c = \frac{4\lambda_0^2 \mathrm{arcsech}(1/\sqrt{2})}{c\pi^2 \Delta\lambda_{FWHM}}, \tag{2.22}$$

with $\Delta\lambda_{FWHM}$ the full with half maximum spectral bandwidth of the SPDC photons and λ_0 the central wavelength. For a typical interference filter of a bandwidth of 3nm the coherence time calculates to approximately 241fs, which is clearly above the typical pulse duration of the pump photons. In addition, the interference filter also washes-out the indistinguishability of the (slightly) distinct spectra of signal and idler photons emitted by a pulsed SPDC source. Finding the optimal bandwidth for the interference filter is thus an important task, because narrow filtering leads to high quality entangled states but also lowers the count rates significantly.

In the next step we would like to observe a specific entangled state emitted from the previously described SPDC process. Because the desired state is often not directly observed from the SPDC itself, the photons have to be processed with linear optical elements, like for example mirrors, beam splitters or phase shifters (wave plates), which are the key ingredients to construct any unitary operator building arbitrary complex networks using optical devices [26]. If we now would like to create a state of photon number $2n$ we have to split the photons into $2n$ different spatial modes and after detection of one photon in each mode we have observed the state of the desired photon number $2n$. To rotate and analyse our probe state in every desired polarization basis introduced in Eq. 2.5 we perform a polarization analysis with half- and quarter wave

---

[8]which will be explained right away

plates followed by a polarizing beam splitter in each arm. The state is finally observed if in each arm a photon is detected by silicon avalanche photo diodes, which destroys the state after observation. A possible alternative to generate a desired state without destroying it is the heralded generation by conditioned detection of auxiliary photons, where a coincidence detection of four auxiliary photons leads to the generation of a two photon entangled state [77, 78]. Unfortunately, the generation of more than two entangled photons is still very challenging with this approach, because of the need of auxiliary photons.

3

Experimental observation and characterization of multi-photon Dicke states

Multi-photon entangled states are commonly observed using pulsed SPDC sources and dedicated linear optical setups. So far, this approach resulted in a wealth of observed states, but with rather low multi-photon count rates. In section 3.1 we introduce a new SPDC source and utilize it throughout all experiments in this thesis. The difference to previous sources is, that here the SPDC is performed inside an enhancement cavity of UV femtosecond pulse trains increasing the available pump power for SPDC drastically. For the successful enhancement of ultra short UV laser pulses several more conditions, in comparison to a continuous-wave (cw) laser, have to be fulfilled, which will be outlined in the following and the experimental results are described in publication 3.1.1 [48]. In the next section 3.2 and also in the preprint 3.2.1, we demonstrate additionally how to measure the length of these pulses inside an UV enhancement cavity. To determine the pulse length in the UV alternatives to the commonly used second harmonic generation (SHG) are necessary to produce the desired autocorrelation signal. Therefore, we propose to use the nonlinearty of our SPDC process instead (see Eq. 2.20).

Based on the aforementioned new SPDC source, we are able to observe entangled states of up to six photons with high count rates. This enables the observation and characterization of a symmetric six photon Dicke state, which is described in section 3.3 and in publication 3.3.1 [50]. Symmetric Dicke states serve as a resource to generate other entangled states, which will also be described. Furthermore, the entanglement of the state is proven by entanglement witnesses described in publication 3.3.2 [57]. Finally, in section 3.4 and in publication 3.4.1 [59] we describe and verify in a proof of principle experiment with a symmetric four photon Dicke state the applicability of permutationally invariant quantum tomography. In comparison to full tomography, which scales exponentially with the number of qubits, permutationally invariant quantum state tomography scales only quadratically. This is a considerable advantage in the characterization of permutationally invariant quantum states, which includes, for example, the GHZ or all Dicke states.

3.1 High power spontaneous parametric down conversion source with a ultraviolet enhancement cavity

In the end of the 1980s, the first experiments to generate correlated photons with spontaneous parametric down conversion (SPDC) were performed. At this time, argon-ion lasers were typically used to pump a nonlinear crystal of $LiIO_3$ [79] or potassium dihydrogen phosphate [80]. This led to the first successful attempts to violate a Bell inequality with a SPDC source [81, 82]. Later, in the 1990s SPDC sources were developed still using argon-ion lasers, but with a non-linear crystal of β-barium borate (BBO) in a type-II configuration. The advantage of this configuration was the possibility to produce two photon entangled states without additional interference at a beam splitter [83, 84, 70]. In the end of the 1990s, the development of frequency doubled femtosecond Ti:sapphire lasers[9] pumping a nonlinear crystal for SPDC led to generation and observation of higher photon numbers than two. The reason for this improvement comes from the fact that the energy of laser pulses is concentrated in short pulse trains, which considerably increases the emission probability of SPDC photon pairs with respect to continuous-wave (cw) lasers [73]. Hence, pulsed femtosecond lasers pumping a nonlinear crystal for SPDC have become the workhorse observing multi-particle states with three [53, 85], four [54, 55, 86, 87, 88], five [89] or even six photons [56, 50, 90, 91, 92]. But nowadays, the frontiers of commercially available laser systems are clearly visible, resulting in low count rates already for six photons (on the order of 10 to 80 per hour, depending on the linear optics setup [90, 56]) due to limited ultraviolet (UV) pumping powers on the order of $\sim 1.4W$ [56, 90, 91]. Another attempt achieved to increase the pulse energy with a frequency-doubled, amplified Ti:sapphire laser with a repetition rate of 20kHz, but did not succeed to observe a specific multi-photon entangled state of large photon numbers [93], because of limited detection efficiency of single photon detectors and noise originating from higher order SPDC emissions, due to too high pulse energies compared to other SPDC experiments.

In general, higher order emissions are SPDC' Achilles heel, which can be explained by having a closer look at the process itself. The state emitted by a type-II, collinear SPDC process is (see Eq. 2.20)

$$| \Psi \rangle \;\; = \;\; \sqrt{1 - \tanh^2 \tau} \sum_{n=0}^{\infty} \tanh^n \tau \, | H^{\otimes n} V^{\otimes n} \rangle \tag{3.1}$$

$$= \;\; \sqrt{1 - \tanh^2 \tau} \Big(\underbrace{\tanh \tau \, | HV \rangle}_{1\text{st order}} + \underbrace{\tanh^2 \tau \, | H^{\otimes 2} V^{\otimes 2} \rangle}_{2\text{nd order}} + ... \tag{3.2}$$

$$... + \underbrace{\tanh^n \tau \, | H^{\otimes n} V^{\otimes n} \rangle}_{n\text{th order}} \Big) \tag{3.3}$$

---

[9]with a repetition rate on the order of about 100MHz

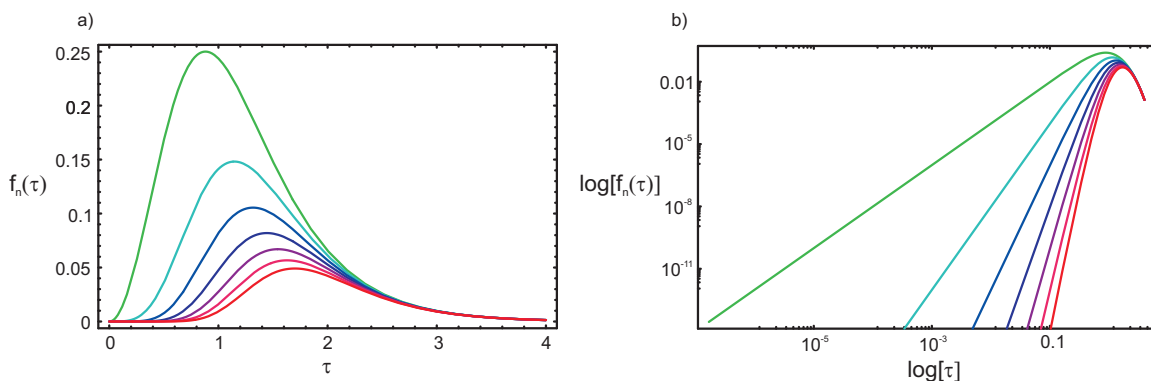## 3.1. HIGH POWER SPONTANEOUS PARAMETRIC DOWN CONVERSION SOURCE WITH A ULTRAVIOLET ENHANCEMENT CAVITY

Figure 3.1: **SPDC emission**. In a) and b) the emission probability amplitude $f_n(\tau) = (1 - \tanh^2 \tau) \tanh^{2n} \tau$ as a function of τ is exemplary shown for n=1 (green) up to n=7 (red), once in a linear plot a) and once in a logarithmic plot b). The integer n corresponds to the nth order SPDC emission.

with horizontally (H) and vertically (V) polarized photons and τ is proportional to the pump field amplitude and the coupling between the electromagnetic field and the crystal. In Fig. 3.1 a) the down conversion emission probability amplitude is exemplary shown for the first up to the seventh order. It is clearly visible that with increasing τ, the observation of higher order emissions becomes more and more probable. In addition, the contribution from the desired to the next higher order emission increases for big τ (which is visible in the logarithmic plot of Fig. 3.1 b)). This means that for big τ the ratio of the emission of the desired, for example, third SPDC order to the undesired forth order decreases. If one would like, for example, to observe a desired state of six photons from the third order SPDC emission, we will end up with noise originating from the forth order SPDC emission (of eight photons) reducing the visibility of the desired six photon state. This is a general problem inherent to SPDC and reduces the fidelity to observe multi-qubit states of larger photon number [10].

In the following publication 3.1.1 [48] we will increase the yield of multi photon generation by enhancing the UV pump power for SPDC in an enhancement cavity for ultra short laser pulses. This enables us to address a regime of τ, which allows for high count rates compared to other state of the art SPDC sources, an in-depth state characterization [50] and, despite the contribution of higher order SPDC emissions, the observation of genuine six photon entanglement. The initial laser pulses are generated by a commercially available laser system[11] with a 10W Nd:YVO$_4$ laser pumping a mode-

---

[10]A solution to the problem of higher order emissions in the future is the development of photon number resolving detectors with high detection efficiency (see for example [94, 95] and references therein). Another promising attempt is the development of triggered single photon sources, which would allow, by coupling of several single photon sources, the generation of a desired multi-photon state (for a review see, for example, [96]).

[11]The cw-diode pumped solid state Nd:YVO$_4$ laser is a 10W Millenia®XS by Spectra Physics®,
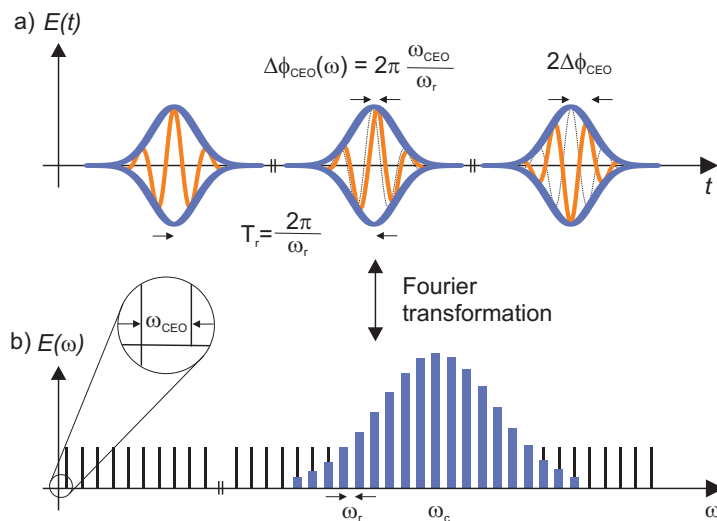
Figure 3.2: **Time and angular frequency domain picture of ultra short laser pulses**. In the time domain a) the carrier wave (orange) of the pulses emitted from the laser is shifted with $\Delta\phi$ after each round trip with respect to the pulse envelope (blue). In the angular frequency domain b) this phase shift corresponds to a carrier envelope offset $\omega_{CEO} = \frac{\Delta\phi_{CEO}}{T_r}$ and T_r is the periodicity. The angular frequency ω_c denotes the center of the frequency comb and ω_r the angular repetition frequency (figure is adapted from [97]).

locked Ti:sapphire oscillator delivering 130fs short pulses with a repetition rate f_r of 80.8MHz at a wave length of 780nm with an output power of 2.05W. These pulses are then frequency doubled with a lithium-borate (LBO) crystal delivering ~ 0.54W at 390nm. Now, instead of directly pumping our BBO crystal for SPDC we additionally enhance these femtosecond UV pulses in a cavity and place our BBO crystal inside. Due to the cavity enhancement of the UV pulses the pump power is thus considerably increased.

For the infrared regime, ultra short laser pulses[12] have been successfully enhanced in cavities to generate, for example, high order harmonics [45, 46, 47] and we adopt this technique to the UV, a wavelength region which has not yet been applied to femtosecond enhancement cavities. In general, the enhancement of ultra short laser pulses is more challenging than in the cw case, because the spectrum of a mode-locked laser contains not only a single cw mode but a comb of such modes (see Fig. 3.2) containing the frequencies

$$\omega_n = n\omega_r + \omega_{CEO} \tag{3.4}$$

with $\omega_r = 2\pi f_r$ the angular repetition frequency and ω_{CEO} the angular carrier envelope

---

the Ti:sapphire oscillator is a Tsunami®by Spectra Physics®

[12]on the order of 200fs

offset frequency [98]. Therefore, to achieve coherent pulse addition in a cavity basically three conditions have to be fulfilled:

(I) The round trip time of a laser pulse inside the cavity has to be set in such a way that a cavity pulse perfectly overlaps with an external laser pulse entering the cavity. Or in frequency language: the laser frequency f_r and the cavity frequency $\frac{c}{L_{cav}}$ have to match (c is the velocity of light and L_{cav} the length of the cavity).

(II) The difference between the carrier envelope offset frequency of a cavity and laser pulse has to be zero.

(III) Dispersion inside the cavity has to be minimized, in order to avoid a shift of the frequency comb modes inside the cavity, with respect to the frequency comb of the laser.

Dispersion inside the cavity mentioned in point (III) can be compensated by chirped mirrors [99] inserting negative dispersion to the pulses. Point (I) can be fulfilled by controlling the cavity length L_{cav} according to an error signal, which is typically generated either by the Hänsch-Couillaud technique [100] or the Pound-Drever-Hall technique [101] and for point (II) the carrier envelope offset can be stabilized - if necessary - using a f-to-$2f$ interferometer, which is explained, for example, in Ref.[102] [13].

To calculate the power enhancement inside the cavity with respect to the input power, we assume an incident electric light field of $E_0(t) = \frac{1}{2}(E_0 e^{i\omega t} + E_0 e^{-i\omega t})$ in front of the input coupler (IC). This is incident to a four mirror bow-tie cavity shown in Fig. 3.3. The electric field after transmission through the input coupler $t_{IC}(\omega)$, reflectivity on the mirrors $r_M(\omega)$ and transmission through additional components $t_{loss}(\omega)$ after one round trip calculates to $E_1 = t_{IC}(\omega)t_{loss}(\omega)r_M(\omega)^3 r_{IC}(\omega)E_0 e^{i\phi(\omega)}$ with $\phi(\omega)$ the round trip phase. In the following we denote the quantity $G(\omega)$ as the round trip gain with $G(\omega) = t_{loss}(\omega)r_M(\omega)^3 r_{IC}(\omega)e^{i\phi(\omega)}$. If the electric field amplitude is now superimposed after every round trip and the circulating field amplitude calculates to

$$E_{cav} = t_{IC}(\omega)E_0 + t_{IC}(\omega)E_0 G(\omega) + t_{IC}(\omega)E_0 G(\omega)^2 + ... \qquad (3.5)$$

Eq. 3.5 corresponds to a geometric progression and we obtain

$$E_{cav} = t_{IC}(\omega)E_0 \sum_{n=0}^{\infty} \left(G(\omega)\right)^n = \frac{t_{IC}(\omega)E_0}{1 - G(\omega)}. \qquad (3.6)$$

---

[13]In our case, we did not use chirped mirrors, because the enhancement was sufficient even without dispersion compensation. Adjusting the length of the cavity was performed according to the Hänsch-Couillaud technique and we did not have to actively stabilize the carrier envelope offset, because the drift was small and allowed for a stable cavity operation on the order of some days (for details see publication 3.1.1 [48])
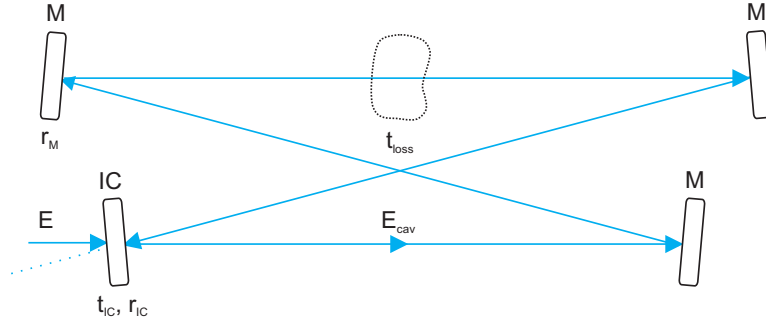
Figure 3.3: **Schematic four mirror bow-tie cavity**. The input laser beam has an electric field of E_0 and is transmitted through the input coupler (IC) with transmittivity $t_{IC}(\omega)$. The circulating electric field inside the cavity E_{cav} is reflected by the mirrors (M) with reflectivity $r_M(\omega)$ and by the input coupler with reflectivity $r_{IC}(\omega)$. Additional losses introduced by, for example, a nonlinear crystal, air or additional components is denoted by the transmittivity $t_{loss}(\omega)$.

The power enhancement PE can now be calculated as the ratio between the absolute value squared of the circulating field inside and in front of the cavity [103]

$$PE(\omega) = \frac{|E_{cav}|^2}{|E_0|^2} = \frac{|t_{IC}(\omega)|^2}{1 + |t_{loss}(\omega)r_M(\omega)^3 r_{IC}(\omega)|^2 - 2|t_{loss}(\omega)r_M(\omega)^3 r_{IC}(\omega)|\cos\phi(\omega)}.$$
(3.7)

In the experiment further described in the following publication 3.1.1 [48] and shown in Fig. 3.4, we achieve with our 4 mirror bow-tie cavity and a 1mm BBO crystal inside an overall power enhancement of $PE_{cavity} = 13.3 \pm 0.5$ resulting in a circulating UV power of $P_{UV,cav} = 7.2 \pm 0.2$W. In comparison with a UV power of ~ 1.4W, which is typically available for commercial laser systems used in other experiments [56, 90, 91], we improved the pumping power for SPDC by a factor of 5. To quantify the performance of our enhancement cavity with respect to SPDC, we count the number of six fold events observed by the linear optics setup shown in Fig. 3.4. To this aim, we calculate the effective six photon count rate at the output of the fibre.

Every linear optics setup has a well defined probability to observe a desired state. Here, we count all six fold events with 3H and 3V polarized photons of all combinations between the 12 detectors (6 detectors for H and 6 for V polarized photons). In our linear optics setup we observe such a six fold event with probability $p_{exp} = 0.284$, which is close to the theoretical probability of $p_{th} = 25/81 = 0.309^{14}$. The observed count rates are then divided by p_{exp} and the effective six photon count rate is 527 ± 6 coincidences

---

[14]The probability p_{1H} to observe one H photon in any out of six H detectors is 1. The probability p_{2H} to observe one H photon in five out of six H detectors is $\frac{5}{6}$. The probability p_{3H} to observe one H photon in four out of six H detectors is $\frac{4}{6}$. Proceeding the same way with V we get also $p_{1V} = 1$, $p_{2V} = \frac{5}{6}$ and $p_{3V} = \frac{4}{6}$. The probability to observe 3H and 3V events in 6H and 6V detectors is therefore $p_{th} = \prod_{i=1H,2H,3H,1V,2V,3V}^{6} p_i = \frac{25}{81}$
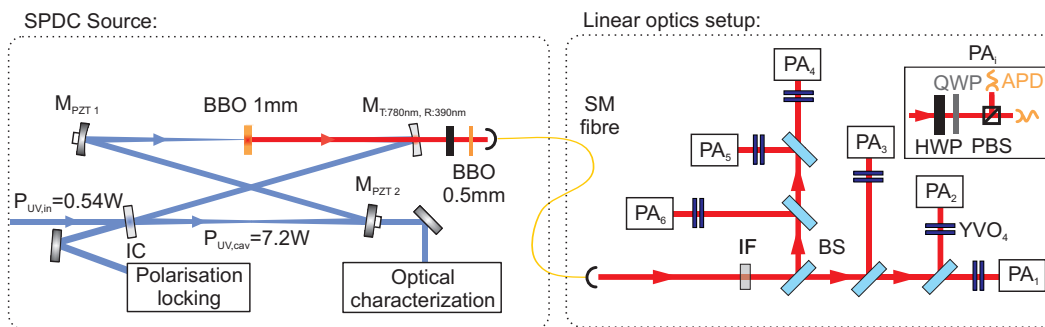
Figure 3.4: **Enhancement cavity and linear optics setup**. The spontaneous parametric down-conversion (SPDC) source consists of a 4 mirror (M) bow-tie cavity with a β-barium borate (BBO) crystal of 1mm length inside. The cavity is pumped with a pulsed laser of 130fs at 390nm and 0.54W input power. The error signal of the polarization lock drives two piezo electric transducers (PZT) mounted on mirrors M. The down converted photons, generated in the BBO crystal, leave the cavity through a mirror reflective (R) at 390nm and transmissive (T) at 780nm and are then guided with a single mode (SM) fibre to the liner optics setup. The photons coupled out of the fibre are spectrally filtered with a interference filter (IF) of $\Delta\lambda = 3$nm. After dividing the photons with beam splitters (BS) on six spatial modes, birefringence of the BS is compensated with a pair of YVO_4 crystals. In each arm a polarization analysis (PA) is performed with half- and quarter wave plates (HWP & QWP) followed by a polarizing beam splitter (PBS). The photons are detected by twelve avalanche photo diodes (APD).

per minute. This is more than one magnitude higher than in any other state-of-the-art experiment [56, 90].

In the following publication 3.1.1 [48] we characterize the cavity and measure the spectra of the external and circulating UV pulses to observe the spectral power enhancement. We further demonstrate the performance by using our enhancement cavity as SPDC source. We measure the multi-photon count rates in dependence of the UV pump power and show the influence of higher order SPDC emissions according to the model of Eq. 2.21. Additionally, we apply entanglement witness to our observed states and are able to proof genuine six-partite entanglement even for high pump powers.

3.1.1 Publication: Ultraviolet enhancement cavity for ultrafast nonlinear optics and high-rate multiphoton entanglement experiments

Ultraviolet enhancement cavity for ultrafast nonlinear optics and high-rate multiphoton entanglement experiments

Roland Krischek[1,2]*, Witlef Wieczorek[1,2], Akira Ozawa[1], Nikolai Kiesel[1,2]†, Patrick Michelberger[1,2], Thomas Udem[1] and Harald Weinfurter[1,2]

Ultrafast, ultraviolet light pulses are a key tool for spectroscopic studies (for example, molecular formation[1,2] and carrier dynamics in semiconductors[3]) as well as a source for non-classical states of light[4–13]. The power required for many nonlinear processes makes amplifier systems mandatory, which significantly reduces the available repetition rate and thus often lengthens the experimental acquisition time. Here we adopt techniques recently developed for the infrared regime[14–16] to design the first enhancement cavity for femtosecond ultraviolet pulses. An average ultraviolet power of more than 7 W at a repetition rate of 81 MHz is now available to pump a nonlinear crystal inside the cavity, applied here to implement a powerful source for high-rate experiments with entangled multiphoton states. The field enhancement enables a new scale of experiments in photonic quantum logic and in nonlinear optics research, for example, to operate optical parametric amplifiers at high repetition rates or to create high-harmonic-frequency combs[14–16].

Recent developments in generating infrared (IR) frequency combs show that spectrally broad, ultrashort pulses can be enhanced in narrowband resonators, provided that they are phase-coherent with one another[14–17]. In the time-domain picture, a laser pulse can then add to the circulating field inside the resonator. In the frequency domain, this corresponds to the condition in which the frequency comb characterizing a series of mode-locked pulses[18] has sufficient overlap with the mode spectrum of the cavity. The transfer of these methods to the ultraviolet regime (UV), a frequency regime not yet tested for femtosecond pulse enhancement, needs special care due to the significantly higher dispersion of nonlinear crystals and air, and the higher demands on the quality of the optical components and the stability of the set-up.

An example of a nonlinear optics process in constant need of higher pump powers is spontaneous parametric down-conversion (SPDC), where n photon pairs are available in its nth-order emission; this process is widely applied in multiphoton entanglement experiments. With typical systems using a frequency-doubled Ti:sapphire mode-locked laser with an average pump power of 0.6 W at a repetition rate of ~80 MHz, a wavelength of ~400 nm and a pulse duration between 100 and 150 fs, a series of experiments on four-photon entangled states have been performed[5,7,10,12]. More recently, high-power oscillators providing UV pump power of ~1 W have enabled six-photon experiments, but count rates are rather low and limit state analysis due to the long measurement times[6,8,13]. In contrast, increasing the pulse energy by several orders of magnitude, as realized in amplified femtosecond laser sources working in the kilohertz regime[19], leads, at the expense of

the repetition rate, to a very high number of generated photon pairs per pulse. However, owing to the limited detection efficiency of the single-photon detectors, noise originating from higher-order emissions fully dominates and renders this approach unsuitable for studies of multipartite entangled states. Developments in alternative sources are promising but not yet mature enough for multiphoton entanglement generation[20–23] (see Supplementary Information). Here, we use, for the first time, a femtosecond UV enhancement cavity with a nonlinear crystal inside to address a regime in which high multiphoton count rates allow an in-depth state characterization[9] and the observation of genuine six-partite entanglement.

In the experiment, the output of a Ti:sapphire laser, delivering 130-fs pulses centred at 780 nm with an average power of 2 W and a repetition rate of $f_r = 81$ MHz, is frequency doubled by a 3-mm lithium triborate (LBO) crystal, yielding an average power of 0.54 W at 390 nm. It is crucial for multiphoton experiments to achieve stability in the system over days because of the long measurement times necessary, even with increased pump power. A beam pointing stabilization is therefore implemented to correct for position and direction fluctuations originating in the laser and frequency doubling unit. The femtosecond UV enhancement cavity is designed as a bow-tie resonator with an input coupler of 97.5% reflectivity and a dichroic mirror to couple the SPDC photons out of the cavity (Fig. 1).

The cavity has to be stabilized to continuously match the modes of the free running, Ti:sapphire laser. The characteristic frequency-comb spectrum $f_m = mf_r + f_{CE}$ depends on two parameters: the repetition frequency of the pulses f_r and the carrier-envelope offset frequency f_{CE}. First, we equalize f_r between the laser oscillator and the enhancement cavity by actively adjusting the cavity length. To this end, an error signal is generated using the Hänsch–Couillaud method[24]. This signal, resulting from interference between the cavity field leaking through the input coupler and a component reflected directly therefrom, is spectrally selected to reduce the impact of the spectral envelope instabilities of the laser. The error signal controls two piezoelectric transducer (PZT)-driven mirror mounts, where the mirror on PZT 1 compensates for short-term (maximum 2 μm travel range, ~10 kHz) and the mirror on PZT 2 for long-term drifts (12 μm, ~3 Hz). Second, additional servo motors steer the Ti:sapphire laser wavelength and prism insertion to keep its central wavelength at 780 nm and to optimize the offset frequency f_{CE} to maximize the intracavity power over a long timescale (typical locking time of 24 h). Hence, no feedback signal, for example, as generated by an $f/2f$ interferometer[18], is required to control f_{CE} of the Ti:sapphire laser. With this

[1]Max-Planck-Institut für Quantenoptik, D-85748 Garching, Germany, [2]Fakultät für Physik, Ludwig-Maximilians-Universität München, D-80799 München, Germany; †Present address: Institute for Quantum Optics and Quantum Information, A-1090 Vienna, Austria. *e-mail: roland.krischek@mpq.mpg.de

20

## 3.1. HIGH POWER SPONTANEOUS PARAMETRIC DOWN CONVERSION SOURCE WITH A ULTRAVIOLET ENHANCEMENT CAVITY
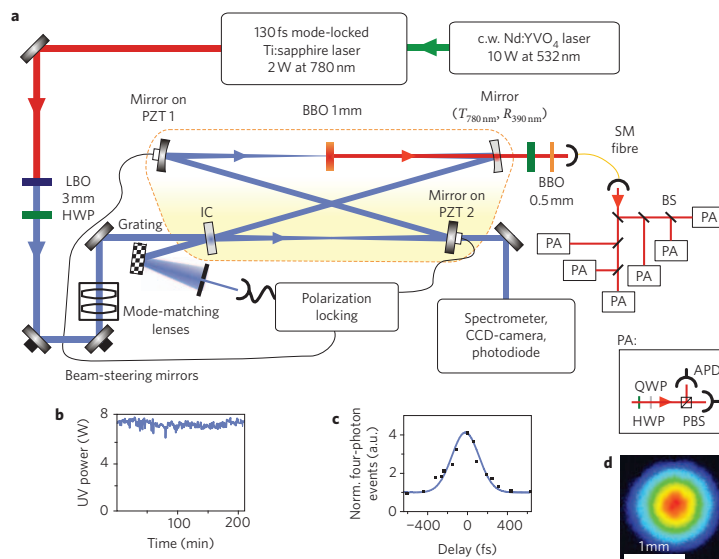
Figure 1 | Schematic experimental set-up. a, The output beam of a frequency-doubled femtosecond Ti:sapphire laser is spatially stabilized and subsequently guided to a UV enhancement cavity. Inside the bow-tie shaped cavity (orange dashed line) with an optical length of ~3.7 m, two focusing mirrors with a radius of curvature of −800 mm generate two beam waists of 100 μm and 330 μm. A β barium borate (BBO) crystal is placed at the smaller waist. Except for the input coupler, all mirrors are highly reflective ($R_{390nm} > 99.9\%$) at 390 nm, and one is additionally highly transmittive ($T_{780nm} > 99.5\%$) at 780 nm for the SPDC photons, which are analysed in a linear optics set-up. **b**, Long-term stability of the cavity over several hours. **c**, Envelope of an interferometric autocorrelation obtained by measuring four-photon coincidences in dependence on the delay between split UV pulses. **d**, Transversal mode profile of the cavity (beam quality of $M^2 = 1.15 \pm 0.03$). HWP, half-wave plate; QWP, quarter-wave plate; PZT, piezoelectric transducer; IC, input coupler; SM, single-mode fibre; BS, non-polarizing beamsplitter; PBS, polarizing beamsplitter; PA, polarization analysis; APD, avalanche photodiode.

configuration, we achieve, for operation over a long time, a UV power of $P_{UV} = 7.2 \pm 0.2$ W inside the cavity (Fig. 1b), which corresponds to an overall power enhancement of 13.3 ± 0.5. We estimate the intracavity pulse length to be ~175 fs from an interferometric autocorrelation measurement (Fig. 1c; see also Methods).

Air and the nonlinear crystal, here β-barium borate (BBO), cause dispersion inside the cavity, which shifts the resonant cavity modes away from being equidistant in frequency and consequently changes the cavity spectrum relative to the laser spectrum. For our set-up (Fig. 1a), the relevant group delay dispersion (GDD) calculated at 390 nm is essentially due to air ($\sim$190 fs^2) and the BBO crystal ($\sim$190 fs^2), with a negligible contribution from the mirrors. The influence of dispersion is estimated from the spectrally resolved power enhancement (Fig. 2a, blue line), which results from dividing the measured intracavity spectrum (orange) by the measured one in front of the resonator (black). The two spectra are similar, indicated by the flat dependence of the power enhancement around the centre wavelength, even without dispersion compensation. Removing the crystal and consequently choosing an input coupler of 99% reflectivity decreases loss, yielding a UV power of 21 ± 1 W, that is, a power enhancement of almost a factor of 40, again with flat spectral dependence (Fig. 2a, inset) due to the lower dispersion inside the cavity. The similarity of the two power enhancement curves can be attributed to an increase in acceptance bandwidth of the resonator for the case with a BBO crystal inside, because the finesse decreases with higher loss. These measurements are in good agreement with calculations[16] (Fig. 2b, orange and black line). Additionally, Fig. 2b shows the expected cavity spectra for an evacuated cavity and for a reduced crystal thickness with a broadband spectrum as cavity input. Remarkably, our calculations show that, in an evacuated cavity

with a 0.5-mm-thick crystal (overall GDD $\approx$ 95 fs^2), pulses with durations as low as 40 fs (corresponding to $\Delta\lambda = 3.9$ nm) can be enhanced without the need for dispersion compensation.

To illustrate the potential of this enhancement cavity we have used it as a new source for experiments on linear optics quantum logic. To evaluate its performance, we analysed the statistics of multiphoton events and the achieved entanglement of two-, four- and six-photon Dicke[25] states (see Supplementary Information) in dependence on the intracavity UV pump power. For this purpose, IR photons created inside the cavity were coupled into a single-mode fibre, and a linear optics set-up was used to distribute them to six polarization analysers (see Methods). To evaluate the photon detection statistics and contributions from higher-order emissions, we used this set-up merely as a polarization-sensitive photon number detector[26]. In the type-II collinear SPDC process that was used, which generates an equal number of horizontally (H) and vertically (V) polarized photons, the emission rate of n photon pairs for typical pump powers is proportional to $(P_{UV})^n$ (see Methods). The experimentally measured count rates are shown in Fig. 3 and are divided into two groups: the first comprises coincidences with an equal number of H and V polarized photons (square symbols, Fig. 3) and thus, to a good approximation, is proportional to $(P_{UV})^n$ (solid lines in Fig. 3). All other possible coincidences with an unequal number of H and V polarized photons (diamond symbols, Fig. 3) form the second group and can only be due to an emission of $(n + 1)$ photon pairs followed by photon loss (dashed lines in Fig. 3). Consequently, this rate is proportional to $(P_{UV})^{n+1}$. The decreasing distance between solid and dashed lines in Fig. 3 for higher n shows clearly the increasing influence of higher-order emissions. To compare our count rates with other
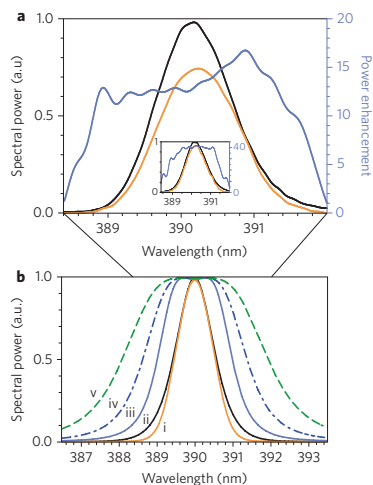
Figure 2 | UV spectra and power enhancement. a, Measured intracavity and external UV spectra with corresponding spectral power enhancement for the case of a 1-mm BBO crystal inside the cavity and an input coupler of 97.5% reflectivity. The inset shows the data for the empty cavity without a BBO crystal and an input coupler of 99% reflectivity. **b**, Calculated cavity UV spectra for different dispersion scenarios. The first curves correspond to our experiment: (i) orange, 1-mm BBO crystal and air inside the cavity compared to (ii) black, the external UV spectrum. The others are calculated for a broadband input spectrum and thus show the dependence of the achievable power enhancement: (iii) azure, 1-mm BBO crystal and air inside the cavity, (iv) dash-dotted blue, evacuated cavity with a 1-mm BBO crystal, (v) dashed green, evacuated cavity with a 0.5-mm BBO crystal. For these calculations a total loss of 2.66% inside the cavity and an input coupler of 2.5% transmittivity were assumed. The full-width at half-maximum of the cavity spectrum increases for these cases from 1.1 nm to 3.9 nm, corresponding to sech-shaped pulse widths of 140 fs down to 40 fs.
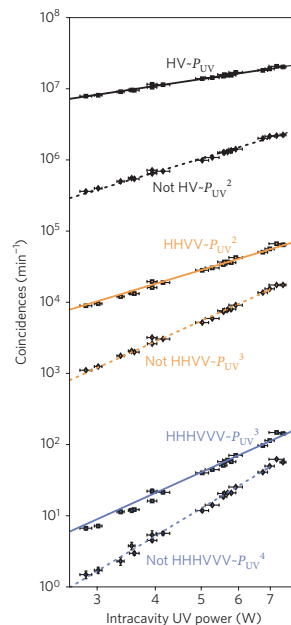
Figure 3 | Count rate statistics in dependence on the average UV pump power circulating in the cavity. The data show the role of $2n$ detection events either with n horizontally (H) and n vertically (V) detected photons (square symbols) originating predominantly from a $2n$-photon emission, or with an unequal number of H and V detections (diamond symbols), essentially due to a $2n + 2$-photon emission with two photons lost. The solid and dashed curves for $n = 1$ (black), $n = 2$ (orange) and $n = 3$ (blue) are fits, and are proportional to $(P_{UV})^n$ or $(P_{UV})^{n+1}$ (according to the approximation of equation (1) for the rates with equal or unequal numbers of H and V detections, respectively).

state-of-the-art experiments we evaluate the yield of the cavity source by estimating the number of six- and eight-photon events at the output of the fibre (see Methods). For a pump power of $P_{UV} = 7.2$ W, effective six- and eight-photon count rates of 527 ± 6 and 3.9 ± 1.0 coincidences per minute are obtained, respectively. The six-photon count rate is almost two orders of magnitude higher than achieved in any other state-of-the-art experiment[6,8]. Despite the high pump power, which results on the one hand in an increased photon count rate, but, on the other hand, in a higher contribution from SPDC noise, all observed states still show genuine multiphoton entanglement[9]. The overall entanglement and state fidelity are even increased thanks to an improved collection efficiency caused by the mode filtering of the cavity (see Supplementary Information and Fig. 1d).

In this Letter, we have introduced a femtosecond UV enhancement cavity as a novel device in ultrafast nonlinear optics. For the particular case of a 1-mm BBO crystal inside the cavity, we have demonstrated its benefits by significantly increasing the yield in multiphoton experiments. UV pulses with an approximate duration of 175 fs have been enhanced by an overall factor of 13 (or even 40 for the case without a crystal), which has resulted in an improvement of the six-photon count rate by almost two orders of magnitude without sacrificing genuine multiphoton entanglement. With an average circulating UV power of more than 7 W and a pulse energy of about 100 nJ at a repetition frequency of 81 MHz, this long-term stable

enhancement cavity is well suited for a series of different applications in nonlinear optics such as an efficient source generating squeezed light inside the cavity[27,28], a pump source for optical parametric amplifiers used, for example, to study molecular dynamics[1,2], or as a possible extension of recent developments for generating high-harmonic far-UV light in a gas jet[14–16].

Methods

SPDC photon preparation and analysis. Photons collinearly emitted by the cavity-pumped SPDC were transmitted through a dichroic mirror with $R_{390nm} > 99.9\%$ and $T_{780nm} > 99.5\%$. To compensate for walk-off effects between the H and V polarized photons emitted from the SPDC BBO crystal, a half-wave plate together with another 0.5-mm-thick BBO crystal were positioned outside the cavity. The SPDC photons were subsequently focused into a single-mode fibre to define their spatial mode. To achieve spectral selection, a narrowband interference filter ($\Delta\lambda = 3$ nm) was placed at the output of the fibre. After distributing the photons into six modes by polarization-independent beamsplitters, the birefringence of these beamsplitters was compensated by pairs of perpendicularly orientated 200-μm-thick birefringent yttrium-vanadate crystals (YVO_4) (not shown in Fig. 1). For each mode, we chose the direction of the polarization analysis with half- and quarter-wave plates and detected photons in the outputs of polarizing beamsplitters using single-photon avalanche photodiodes. The detection signals were evaluated by an FPGA-controlled coincidence logic, which allows the simultaneous registration of any possible coincidences. To detect the $2n$-fold coincidences, we considered all possible combinations of the 12 detectors. To compare our count rates with other experiments we evaluated the effective number of six- or eight-photon coincidences (with an equal number of H and V polarized photons) at the output of the fibre, taking all possible combinations of the 12 detectors into account. For this purpose,

LETTERS

we divided the experimental count rates by the probability of observing such events, which was calculated to be 0.284 for six-photon events and 0.065 for eight-photon events, deviating slightly from the theoretical probabilities for optimal beamsplitters of 25/81 and 25/324, respectively, due to small asymmetries in the beamsplitting ratios. The coincidences for the calculation of the entanglement witness were corrected for the different relative detector efficiencies. The total uncertainty was determined from errors on the independently measured relative detector efficiencies and Poissonian counting statistics.

SPDC photon statistics. For a type-II collinear SPDC process we obtained the state[19]

$$|\Psi_{\mathrm{SPDC}}\rangle = \sqrt{1 - \tanh^2 \tau} \sum_{n=0}^{\infty} (\tanh \tau)^n |V^{\otimes n} H^{\otimes n}\rangle \qquad (1)$$

where $|V^{\otimes n} H^{\otimes n}\rangle$ represents n horizontally (H) and n vertically (V) polarized photons emitted by the source, and τ is the coupling between input and output fields, which depends linearly on the pump field amplitude, the nonlinearity of the crystal and its length. From this state it is possible to obtain the probability of creating n photon pairs per pulse with $p_n = (1 - \tanh^2 \tau)(\tanh \tau)^{2n}$ and thus the rate of emission of n pairs, c_n, as $c_n = p_n f_r$. For $\tau \ll 1$, that is, for low pump powers, we can approximate $\tanh \tau \approx \tau$, $(1 - \tanh^2 \tau) \approx 1$ and thus $p_n \approx \tau^{2n}$. Hence, increasing the pump power P_{UV} increases the rate of n photon pairs according to $c_n \propto (P_{\mathrm{UV}})^n$. For high pump powers, the observed rate of the nth-order emission is contaminated by photons originating from higher-order emissions due to the limited detection efficiency, predominantly from the $(n+1)$th-order emission and the loss of two photons. In our case, we obtained $\tau \in [0.26, 0.46]$ and an overall detection efficiency of about 14%. We applied the simple model $c_n \propto (P_{\mathrm{UV}})^n$ to illustrate the trend for growing pump powers. A more elaborate analysis is described in ref. 29.

Pulse length measurement of the intracavity UV pulses. Estimating the length of ultrashort pulses can be achieved by interferometric autocorrelation. The general idea is to overlap two pulses with different time delays and subsequently measure the intensity of a signal derived from a nonlinear process, such as second harmonic generation (SHG). Applying SHG is quite problematic for UV pulses, so we instead make use of the nonlinear intensity dependence of the second-order SPDC emission. A Michelson interferometer was therefore used in front of the cavity to create two delayed pulses. We measured the count rates of four photon events as a function of the pulse delay. The interferometric autocorrelation envelope provided an approximate pulse duration of 175 fs, when assuming a sech-shaped pulse. This value is slightly above that deduced from the spectrum (Fig. 2) because the set-up was optimized for high entanglement visibility in the latter case. The contrast of the signal, being approximately 4:1 (compared to an ideal of 8:1), can be attributed to a reduced interference visibility. We would also like to note that there is no background noise on the offset outside the interference region as random fourfold coincidences have not been registered.

References

1. Schrader, T. E. *et al.* Light-triggered β-hairpin folding and unfolding. *Proc. Natl. Acad. Sci. USA* **104**, 15729–15734 (2007).
2. Schriever, C., Lochbrunner, S., Riedle, E. & Nesbitt, D. J. Ultrasensitive ultraviolet-visible 20 fs absorption spectroscopy of low vapor pressure molecules in the gas phase. *Rev. Sci. Instrum.* **79**, 013107 (2008).
3. Choi, C. K., Kwon, Y. H., Krasinski, J. S., Setlur, G. & Song, J. J. Ultrafast carrier dynamics in a highly excited GaN epilayer. *Phys. Rev. B* **63**, 115315 (2001).
4. Bouwmeester, D., Pan, J.-W., Daniell, M., Weinfurter, H. & Zeilinger, A. Observation of three-photon Greenberger–Horne–Zeilinger entanglement. *Phys. Rev. Lett.* **82**, 1345–1349 (1999).
5. Kiesel, N., Schmid, C., Tóth, G., Solano, E. & Weinfurter, H. Experimental observation of four-photon entangled Dicke state with high fidelity. *Phys. Rev. Lett.* **98**, 063604 (2007).
6. Lu, C.-Y. *et al.* Experimental entanglement of six photons in graph states. *Nature Phys.* **3**, 91–95 (2007).
7. Wieczorek, W., Schmid, C., Kiesel, N., Pohlner, R., Gühne, O. & Weinfurter, H. Experimental observation of an entire family of four-photon entangled states. *Phys. Rev. Lett.* **101**, 010503 (2008).
8. Prevedel, R. *et al.* Experimental realization of Dicke states of up to six qubits for multiparty quantum networking. *Phys. Rev. Lett.* **103**, 020503 (2009).
9. Wieczorek, W., Krischek, R., Kiesel, N., Michelberger, P., Tóth, G. & Weinfurter, H. Experimental entanglement of a six-photon symmetric Dicke state. *Phys. Rev. Lett.* **103**, 020504 (2009).
10. Walther, P. *et al.* Experimental one-way quantum computing. *Nature* **434**, 169–176 (2005).
11. Zhao, Z., Chen, Y.-A., Zhang, A.-N., Yang, T., Briegel, H. J. & Pan, J.-W. Experimental demonstration of five-photon entanglement and open-destination teleportation. *Nature* **430**, 54–58 (2004).
12. Lanyon, B. P. *et al.* Experimental demonstration of Shor's algorithm with quantum entanglement. *Phys. Rev. Lett.* **99**, 250505 (2007).
13. Rådmark, M., Zukowski, M. & Bourennane, M. Experimental test of fidelity limits in six-photon interferometry and of rotational invariance properties of the photonic six-qubit entanglement singlet state. *Phys. Rev. Lett.* **103**, 150501 (2009).
14. Jones, J. R., Moll, K. D., Thorpe, M. J. & Ye, J. Phase-coherent frequency combs in the vacuum ultraviolet via high-harmonic generation inside a femtosecond enhancement cavity. *Phys. Rev. Lett.* **94**, 193201 (2005).
15. Gohle, C. *et al.* A frequency comb in the extreme ultraviolet. *Nature* **436**, 234–237 (2005).
16. Ozawa, A. *et al.* High harmonic frequency combs for high resolution spectroscopy. *Phys. Rev. Lett.* **100**, 253901 (2008).
17. Yanovsky, V. P. & Wise, F. W. Frequency doubling of 100-fs pulses with 50% efficiency by use of a resonant enhancement cavity. *Opt. Lett.* **19**, 1952–1954 (1994).
18. Udem, T., Holzwarth, R. & Hänsch, T. W. Optical frequency metrology. *Nature* **416**, 233–237 (2002).
19. Eisenberg, H. S., Khoury, G., Durkin, G. A., Simon, C. & Bouwmeester, D. Quantum entanglement of a large number of photons. *Phys. Rev. Lett.* **93**, 193901 (2004).
20. U'Ren, A. B., Silberhorn, C., Banaszek, K. & Walmsley, I. A. Efficient conditional preparation of high-fidelity single photon states for fiber-optic quantum networks. *Phys. Rev. Lett.* **93**, 093601 (2004).
21. Fulconis, J., Alibart, O., OBrien, J. L., Wadsworth, W. J. & Rarity, J. G. Nonclassical interference and entanglement generation using a photonic crystal fiber pair photon source. *Phys. Rev. Lett.* **99**, 120501 (2007).
22. Li, X., Voss, P. L., Sharping, J. E. & Kumar, P. Optical-fiber source of polarization-entangled photons in the 1550 nm telecom band. *Phys. Rev. Lett.* **94**, 053601 (2005).
23. Fan, J., Migdall, A. & Wang, L. J. Efficient generation of correlated photon pairs in a microstructure fiber. *Opt. Lett.* **30**, 3368–3370 (2005).
24. Hänsch, T. W. & Couillaud, B. Laser frequency stabilization by polarization spectroscopy of a reflecting reference cavity. *Opt. Commun.* **35**, 441–444 (1980).
25. Dicke, R. H. Coherence in spontaneous radiation processes. *Phys. Rev.* **93**, 99–110 (1954).
26. Achilles, D., Silberhorn, C., Śliwa, C., Banaszek, K. & Walmsley, I. A. Fiber-assisted detection with photon number resolution. *Opt. Lett.* **28**, 2387–2389 (2003).
27. Ou, Z. Y., Pereira, S. F., Kimble, H. J. & Peng, K. C. Realization of the Einstein–Podolsky–Rosen paradox for continuous variables. *Phys. Rev. Lett.* **68**, 3663–3666 (1992).
28. Zavatta, A., Parigi, V. & Bellini, M. Toward quantum frequency combs: Boosting the generation of highly nonclassical light states by cavity-enhanced parametric down-conversion at high repetition rates. *Phys. Rev. A* **78**, 033809 (2008).
29. Wieczorek, W., Kiesel, N., Schmid, C. & Weinfurter, H. Multiqubit entanglement engineering via projective measurements. *Phys. Rev. A* **79**, 022311 (2009).

Author contributions

All authors contributed significantly to the work presented in this paper.

Additional information

The authors declare no competing financial interests. Supplementary information accompanies this paper at www.nature.com/naturephotonics. Reprints and permission information is available online at http://npg.nature.com/reprintsandpermissions/. Correspondence and requests for materials should be addressed to R.K.

173

Supplementary information: Ultraviolet enhancement cavity for ultrafast nonlinear optics and high rate multi-photon entanglement experiments

Roland Krischek[1,2], Witlef Wieczorek[1,2], Akira Ozawa[1], Nikolai Kiesel[1,2,3], Patrick Michelberger[1,2],

Thomas Udem[1] & Harald Weinfurter[1,2]

[1]*Max-Planck-Institut für Quantenoptik, D-85748 Garching, Germany*

[2]*Fakultät für Physik, Ludwig-Maximilians-Universität München, D-80799 München, Germany*

[3]*Present address: Institute for Quantum Optics and Quantum Information, A-1090 Vienna, Austria*

Alternative multi-photon sources:

Recently, promising methods have been developed to generate multi-photon states. These methods are well suited regarding the number of generated photons as a function of the pump power, but the observation of multi-photon polarisation entangled states imposes further requirements, namely spectral, spatial and temporal indistinguishability[1,2]. So far, the highest number of photon pairs for pulsed sources was obtained using spontaneous processes in waveguide structures[3] and photonic crystal fibres (PCF)[4-6]. Though these sources are promising, their application for multi-photon entanglement studies has still to be proven. For example, the PCF sources are usually operating in the non-degenerate mode, resulting in different wavelengths for the signal and idler photons. This prevents the use of signal and idler photons for the same linear optics logic gates. Alternatively, working at telecom wavelengths for down converted photons might simplify their generation due to high available pump powers. However, in this case the detection efficiency

of about 10% for InGaAs-avalanche diodes is still too low for multi-photon experiments. In the future, these systems might profit from the development of high-efficient cryogenic single photon detectors or more elaborate waveguide and PCF structures. To date, sources based on our approach are still the workhorses for multi-photon entanglement studies.

Multipartite entanglement depending on the intra-cavity UV pump power:

In general, distributing $2n$ photons from the nth order emission of a type II collinear SPDC process symmetrically into $2n$ spatial modes allows to observe polarisation-entangled multi-photon Dicke[7] states. Formally, these states are described by

$$D_{2n}^{(n)} = \begin{pmatrix} 2n \\ n \end{pmatrix}^{-\frac{1}{2}} \sum_i \mathcal{P}_i(\, | \, V^{\otimes n} H^{\otimes n} \, \rangle_{\,1,...,2n} \,),$$

(1)

where $\sum_i \mathcal{P}_i(...)$ represents the sum over all distinct symmetric permutations of distributing $2n$ photons one in each of $2n$ different output modes $(1, ..., 2n)$. Here, we are able to observe the states $D_2^{(1)}$, $D_4^{(2)}$ and $D_6^{(3)}$, whose genuine $2n$-partite entanglement has been shown recently experimentally[8–11]. The high symmetry of the Dicke states enables one to formulate entanglement witnesses, which use the collective spin-component in the x- and y-direction[12], $\mathcal{W}_{2n} = J_{x,2n}^2 + J_{y,2n}^2$, where $J_{x/y,2n} = \frac{1}{2} \sum_k \sigma_{x/y}^k$ with $\sigma_{x,y}$ being the Pauli matrices $\sigma_x^3 = \mathbb{1}^{\otimes 2} \otimes \sigma_x \otimes \mathbb{1}^{\otimes(2n-3)}$. The expectation value $\langle \mathcal{W}_{2n} \rangle$ is determined from a measurement of all photons in the σ_x and all in the σ_y basis, which corresponds to polarisation analysis along $\pm 45°$ linear and left/right circular polarisation, respectively.

We evaluate the multipartite entanglement, which is achieved with the cavity enhanced SPDC

SUPPLEMENTARY INFORMATION

source using $\mathcal{W}_{2n}$[12]. Two-, four- and six-photon polarisation-entangled Dicke states can be observed with the same linear optics setup used to determine the photon statistics. Extending previous measurements on the six-photon Dicke state[10,11], here we focus on the change of the observed entanglement depending on the pump power (Fig. 1). All observed values are within the required bound (shaded region) proving genuine multipartite entanglement. However, for increasing pump power $\langle \mathcal{W}_{2n} \rangle$ decreases as the state is contaminated by coloured noise from higher order contributions. This is also reflected by the fidelity $\langle F_{D_{2n}^{(n)}}(\rho) \rangle = Tr(\rho\,|D_{2n}^{(n)}\rangle\langle D_{2n}^{(n)}|)$, which measures the quality of the observed states ρ to the expected Dicke state $D_{2n}^{(n)}$. For the data shown it is remarkable that the fidelity obtained at high pump powers, where the noise contribution is highest, does not fall below $\langle F_{D_2^{(1)}}(\rho) \rangle > 0.860 \pm 0.002$, $\langle F_{D_4^{(2)}}(\rho) \rangle > 0.694 \pm 0.002$ and $\langle F_{D_6^{(3)}}(\rho) \rangle > 0.57 \pm 0.02$ for two-, four- and six-photon entangled Dicke states, respectively. The fidelities have been estimated using a three-setting witness described in ref.[11]. To increase the fidelity the pump power has to be decreased, which results in a reduced noise contribution, but also in a lower $2n$-photon count rate. The effect of this noise can also be recognised by comparing the rates for analysis along H/V-direction for low and high pump powers (insets in Fig. 1).

1. Żukowski, M., Zeilinger, A. & Weifurter, H. Entangling photons radiated by independent pulsed sources. *Ann. N. Y.* **755**, 91 (2006).

2. Rarity, J. G. Interference of Single Photons from Separate Sources. *Ann. N. Y.* **755**, 624 (1995).

3. U'Ren, A. B., Silberhorn, C., Banaszek, K. & Walmsley, I. A. Efficient conditional preparation of high-fidelity single photon states for fiber-optic quantum networks. *Phys. Rev. Lett.* **93**,

093601 (2004).

4. Fulconis, J., Alibart, O., OBrien, J. L.,Wadsworth, W. J. & Rarity, J. G. Nonclassical Interference and Entanglement Generation Using a Photonic Crystal Fiber Pair Photon Source. *Phys. Rev. Lett.* **99**, 120501 (2007).

5. Li, X.,Voss, P. L., Sharping, J. E. & Kumar, P. Optical-Fiber Source of Polarization-Entangled Photons in the 1550 nm Telecom Band. *Phys. Rev. Lett.* **94**, 053601 (2005).

6. Fan, J.,Migdall, A. & Wang, L. J. Efficient generation of correlated photon pairs in a microstructure fiber. *Opt. Lett.* **30**, 3368 (2005).

7. Dicke, R. H. Coherence in spontaneous radiation processes. *Phys. Rev.* **93**, 99–110 (1954).

8. Kiess, T. E., Shih, Y. H., Sergienko, A. V. & Alley, C. O. Einstein-Podolsky-Rosen-Bohm experiment using pairs of light quanta produced by type-II parametric down-conversion. *Phys. Rev. Lett.* **71**, 3893–3897 (1993).

9. Kiesel, N., Schmid, C., Tóth, G., Solano, E. & Weinfurter, H. Experimental observation of four-photon entangled Dicke state with high fidelity. *Phys. Rev. Lett.* **98**, 063604 (2007).

10. Prevedel, R., Cronenberg, G., Tame, M. S.,Paternostro, M.,Walther, P., Kim, M. S. & Zeilinger, A. Experimental Realization of Dicke States of up to Six Qubits for Multiparty Quantum Networking. *Phys. Rev. Lett.* **103**, 020503 (2009).

3.2 Intra cavity ultraviolet pulse length measurement using spontaneous parametric down conversion

The development of ultra short laser pulses goes along with techniques to actually measure their duration. In general, different methods have been developed to characterize femtosecond pulse trains in the near infrared and in the visible wavelength region to reconstruct the actual pulse duration and temporal structure. Commonly used methods are the so called FROG [104] or SPIDER [105] techniques. Other methods are based on interferometric autocorrelation if only information about the pulse length is desired [106]. To this aim, non-linearities have to be involved, but the widely applied second harmonic generation is not possible with crystals in the UV wavelength region. Therefore, other methods have been developed, for example, two photon absorption in diamond [107] or recently in diamond pin photo diodes [108], two photon ionization [109], two photon fluorescence [110, 111], degenerate four wave mixing in fused silica [112] or by using the optical Kerr effect [113].

In the preprint 3.2.1 and introduced in the following[15], we present a method to determine the pulse length of femtosecond UV pulses at 390nm inside the previously described UV enhancement cavity (see section 3.1 and [48]). This constitutes the first direct measurement of a pulse length inside an enhancement cavity. To this end, we profit from the process of spontaneous parametric down-conversion (SPDC), which emits in its nth order $2n$ photons with twice the wavelength of the UV pump photons (see section 2.2). To observe the desired autocorrelation signal to retrieve the pulse length, we split the pump pulses for the SPDC process in front of the cavity by implementing a Mach-Zehnder interferometer[16]. These pulses recombine again on a beam splitter and we count the number of photons emitted by the nth order process of the SPDC in dependence of the delay between the split pulses. These count rates are in general described by the nth order autocorrelation function by superposition of two electric fields with delay τ and width parameter Δt as

$$g_n(\tau) = \frac{\int |(E(t) + E(t - \tau))^n|^2 dt}{\int |(E(t)^n|^2 dt + \int |E(t - \tau)^n|^2 dt}. \tag{3.8}$$

Assuming a sech-shape for the delayed UV pulses [114] with unbalanced amplitudes a and b as

$$E_{sech}(t) = a E_0 \operatorname{sech}\left(\frac{t}{\Delta t}\right) \cos(\omega_0 t) \tag{3.9}$$

and

$$E_{Sech}(t - \tau) = b E_0 \operatorname{sech}\left(\frac{t - \tau}{\Delta t}\right) \cos(\omega_0(t - \tau)), \tag{3.10}$$

---

[15]Please consider also the Diploma thesis of Patrick Michelberger [76], where all the calculations and results are described in detail

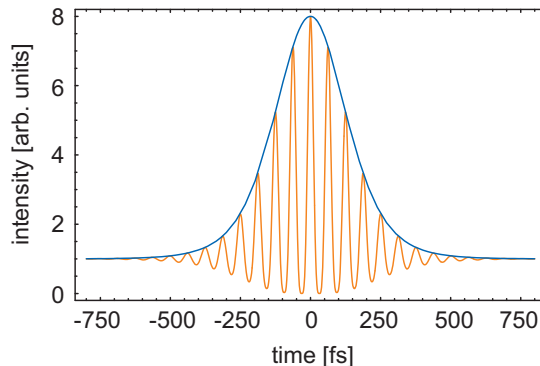[16]Experimental details are described in the preprint 3.2.1

Figure 3.5: **Autocorrelation function**. In blue the theoretical autocorrelation envelope of second order $g_2(\tau)$ is given for the case of $\Delta t = 100$fs. The oscillating light field (orange) is shown for an arbitrary wavelength for illustration.

the envelope of the autocorrelation of first and second order calculates then to [76]

$$g_1(\tau) = 1 + \frac{2ab}{a^2 + b^2} \frac{\frac{\tau}{\Delta t}}{\sinh(\frac{\tau}{\Delta t})} \tag{3.11}$$

$$g_2(\tau) = 1 + \frac{18a^2b^2}{a^4 + b^4} \frac{\frac{\tau}{\Delta t}\cosh\frac{\tau}{\Delta t} - \sinh\frac{\tau}{\Delta t}}{\sinh^3(\frac{\tau}{\Delta t})} + \frac{3(ab^3 + a^3b)}{a^4 + b^4} \frac{\sinh\frac{2\tau}{\Delta t} - \frac{2\tau}{\Delta t}}{\sinh^3(\frac{\tau}{\Delta t})}. \tag{3.12}$$

For our purpose it is sufficient to monitor the envelope of the autocorrelation functions (see Fig. 3.5), because a fit to the measured envelope already delivers Δt, out of which the pulse length can be calculated. The connection between the full width half maximum (FWHM) pulse duration τ_{FWHM} and Δt for equal amplitudes[17] ($a = b = 1$) is given by the bandwidth product for first and second order autocorrelation function as [76]

$$\tau_{FWHM}^{g_{1,2}} = 2\operatorname{arcsech}\left(\frac{1}{\sqrt{2}}\right)\Delta t = 1.7628\,\Delta t \tag{3.13}$$

From the measurement of the first order SPDC emission, further described in the preprint 3.2.1, we observe $g_1(\tau)$ and can determine the Fourier transform limited pulse duration to $\tau_{FWHM}^{g_1} = 140.1 \pm 11.7$fs. This pulse length is determined from the first order autocorrelation function originating from a linear process. Therefore it reveals the minimal pulse length without taking into account additional broadening coming from higher order effects like, for example, dispersion. The broadening of the pulse is revealed by measuring the second order autocorrelation function by counting the number of second order SPDC emissions and finally the pulse length inside our enhancement cavity can be determined to $\tau_{FWHM}^{g_2} = 176.1 \pm 13.7$fs.

To interpret this result for SPDC experiments the pulse duration has to be related to the coherence time of the SPDC photons. A coherence time of the SPDC photons of

---

[17]For unbalanced amplitudes see [76]

approximately 241fs has been calculated in chapter 2.2 according to the spectral filtering with a bandwidth of 3nm at a central wavelength of 780nm. In the experiment we found a pulse duration of 176fs, which lies well within the coherence time and guarantees the indistinguishability of multiple SPDC emission pairs. This is also represented by the fact that for a six photon state genuine six partite entanglement has been verified in the previous experiment (see publication 3.1.1 [48]) and makes this UV enhancement cavity a well suited tool for the observation of multi-photon entanglement.

3.2.1 Preprint: Interferometric autocorrelation in the ultra-violet utilizing spontaneous parametric down-conversion

Interferometric autocorrelation in the ultra-violet utilizing spontaneous parametric down-conversion - Version 7

Patrick Michelberger,[1,2,3,*] **Roland Krischek,**[1,2] **Witlef Wieczorek,**[1,2,4] **Akira Ozawa**[1] **and Harald Weinfurter**[1,2]

[1] *Max-Planck-Institut für Quantenoptik, Hans-Kopfermann-Strasse 1, D-85748 Garching, Germany*
[2] *Faultät für Physik, Ludwig-Maximilians-Universität, D-80797 München, Germany*
[3] *Currently with the Clarendon Laboratory, University of Oxford, Parks Road, Oxford OX1 3PU, UK*
[4] *Currently with the Faculty of Physics, University of Vienna, Boltzmanngasse 5, A-1090 Wien, Austria*
[*] *Corresponding author: p.michelberger1@physics.ox.ac.uk*

Autocorrelation is a common method to estimate the duration of ultra-short laser pulses. In the ultra-violet (UV) regime, employing the customary process of second harmonic generation is challenging due to absorption in nonlinear crystals at short wavelengths. Here we show how to utilize spontaneous parametric down-conversion (SPDC) to generate an autocorrelation signal for UV-pulses in the infrared. Our method relies on the nth order emission of the SPDC process, emitting $2n$ photons with a rate approximately proportional to the nth power of the UV intensity for low pumping powers. This allows one to obtain the nth order autocorrelation by simply counting $2n$ down-converted photons. The method is applied to the first direct measurement of approximately 176 fs ultra-short pulses, centered around 390 nm, inside a UV enhancement cavity. © 2010 Optical Society of America

OCIS codes: 000.0000, 999.9999.

Ever since the advent of ultra-short laser pulses, means for determining their duration have been required. If only knowledge about the duration of potentially dispersion-broadened pulses is desired, interferometric autocorrelation is still the method of choice, although more elaborate techniques exist [1, 2]. Despite that this method works fine in most wavelength regions, the ultra-violet (UV) regime is challenging due to absorption and detection limitations associated with the commonly used non-linear process of second-harmonic generation (SHG).

Here we demonstrate a method, which circumvents these problems by employing spontaneous parametric down-conversion (SPDC) for generating an autocorrelation signal in the infrared. It enables us to estimate the duration of ultra-short UV pulses inside an enhancement cavity [3]. However detection of the generated signal demands single photon resolving detectors and results in low count rates compared to SHG based autocorrelation. Thus the method is beneficial if these issues are irrelevant.

In the following, we will prove the applicability of SPDC to create autocorrelation signals by showing its connection to correlation functions of nth order. The method will then be applied to determine the UV pulse duration inside a cavity, which comprises a non-linear crystal for creating SPDC photons. Furthermore we will discuss the particular requisites of the cavity case and ultimately conclude our analysis.

We start by relating SPDC to autocorrelation functions. Thereto collinear type-II SPDC is considered, which produces, in single mode approximation, the state [4]

$$|\Psi\rangle = \sqrt{1 - \tanh^2 |\tau|} \sum_n \frac{\tanh^n |\tau|}{n!} \left(\hat{a}_H^\dagger \hat{a}_V^\dagger \right)^n |0\rangle, \quad (1)$$

with $\hat{a}_H^\dagger$ and $\hat{a}_V^\dagger$ generating a photon from the vacuum $|0\rangle$ with horizontal (H), respectively vertical (V) polarization. The interaction parameter $\tau = g \cdot E_p$ includes the nonlinear crystal parameters in g and two pump pulse electric fields $E_p = \frac{1}{\sqrt{2}} \left(E_p(t) + E_p(t - \tau) \right)$, delayed by a time τ as in SHG-based autocorrelation. Hence the SPDC process generates in its nth order $2n$ photons. For low pumping powers, fulfilled in our case [5] ($|\tau| \in [0.221, 0.293]$), the approximations $\tanh(|\tau|) \approx \tau$, $\sqrt{1 - \tanh^2(|\tau|)} \approx 1$ hold. To retrieve the nth order correlation function, defined as [6]

$$g_n(\tau) = \frac{\int |(E_p(t) + E_p(t - \tau))^n|^2 dt}{\int |E_p(t)^n|^2 dt + \int |E_p(t - \tau)^n|^2 dt}, \quad (2)$$

from the nth order SPDC emission, we denote the count rates for coincidence detection between $n \times$ H and $n \times$ V polarized SPDC photons [7] as

$$\tilde{n}_{(t,t-\tau)} = \langle \hat{a}_{H,n}^\dagger \ldots \hat{a}_{H,1}^\dagger \hat{a}_{V,n}^\dagger \ldots \hat{a}_{V,1}^\dagger$$
$$\hat{a}_{V,n} \ldots \hat{a}_{V,1} \hat{a}_{H,n} \ldots \hat{a}_{H,1} \rangle. \quad (3)$$

The subscripts indicate the pump field to consist of two contributions at times t and $t - \tau$. To yield the total photon count rate obtained from the full duration of both pulses, integration over time is necessary [7]. With appropriate normalisation to the background outside the pulses' interference region, we find

$$g_n(\tau) = \frac{\tilde{n}_{t,t-\tau}}{\tilde{n}_t + \tilde{n}_{t-\tau}}. \quad (4)$$

Thus the nth autocorrelation order is accessible by detecting n SPDC photon pairs.

1

The experimental implementation of this method, illustrated in Fig. 1(a), is based on an ultrafast enhancement cavity for UV pulses, centered around 390 nm, with a nonlinear β-barium-borate (BBO) crystal positioned therein; details are found in [3]. The external pumping pulses, derived from a titanium sapphire laser with subsequent frequency doubling, are split into two copies by a Michelson interferometer prior to cavity coupling. One output of the interferometer is directly observed by a photodiode (PD 1), as is the power level (PD 2) and the UV spectrum inside the cavity, both measured in transmission behind a cavity mirror. The SPDC photon pairs emitted from the BBO crystal are coupled out of the cavity by a dichroic mirror and propagated through a single mode (SM) fiber into a linear optical set-up for photon number counting, described further in [8]. Therein photons get split-up into six distinct spatial modes, each equipped with a polarization analysis unit, enabling coincidence detection between up to six simultaneously generated SPDC photons.
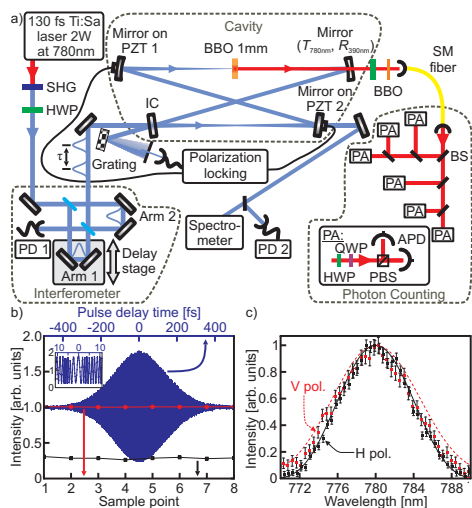

Fig. 1. (a) Experimental set-up described in main text. (b) Interferometric stability prove for the set-up; the black and red data points show the intensity on PD 1 during a measurement run. Red circles correspond to a pulse separation of $\tau = -1850$ fs and black boxes to $\tau = 0$ fs. The blue line represents the $g_1(\tau)$ interference pattern on PD 1 over the entire pulse delay range τ (visibility 0.77) and the inset a cut-out thereof. (c) Calculated and directly measured spectra of the SPDC photons. Black boxes are the measured signal (H pol.) spectrum, red circles the idler spectrum (V pol.). Appropriate colored lines are the expectations for both.

Measuring the $g_n(\tau)$-functions necessitates interferometric stability of the pulse separation τ, phase-matching of the nonlinear process over the spectrum of the UV

pump and the absence of background noise in detection. The latter requirement is satisfied by the low probability of simultaneous dark counts between multiple detectors. Interferometric stability during the measurement time of 8 s per datapoint in the correlation functions is certified by observation of the intensity on PD 1 (Fig. 1(b)). Its fluctuations are contrasted to the total intensity variations in the $g_1(\tau)$ interferogram, which are found to be negligible in comparison. The sufficiency of the BBO's phase-matching bandwidth is assessed by calculating the expected SPDC spectra for our crystal length (1 mm) and pump pulses (sech-shaped with full-width-half-maximum (FWHM) of $\Delta\lambda \approx 1.058$ nm) by the method outlined in [7]. Results are compared to the measured SPDC spectra. We infer from Fig. 1(c) good resemblance for the signal and idler modes and can thus conclude on the absence of spectral cut-off in SPDC as well as in the SM fiber coupling. Particularly for a cavity set-up, the spatial and spectral coupling [9] of external pulses into the cavity must also be preserved to maintain the internal cavity pulses' spectral content. Therefore the internal spectra have been modelled as a function of τ, whose results agree with the directly measured quantities [10].

Experimentally we have observed $g_1(\tau)$ externally on PD 1, inside the cavity on PD 2 and by the two-fold (HV) photon count-rates measured in our linear optical set-up (Fig. 2(a) and (b), respectively). Higher order correlations $g_2(\tau)$ and $g_3(\tau)$ (Fig. 2(c)) were measured by counting four- (HHVV) and six-fold coincidences (HHHVVV). Inside the cavity only values of τ corresponding to interference maxima in the $g_n(\tau)$-functions have been measured, due to the locking procedure [3] for maintaining the spectral coupling, requiring intensity in the cavity. Thus, as interferometric stability has been proven separately, only the upper envelopes in the $g_n(\tau)$-functions have been observed. The interferometer also introduces some residual transverse mode mismatch, resulting in a degraded interference visibility. This leads to lower peak-to-background ratios in the $g_n(\tau)$-functions, without loss of phase information.

For data evaluation, we assume sech-shaped electric fields $E(t) = a \cdot E_0 \cdot \text{sech}\left(\frac{t}{\Delta t}\right)$ and $E(t-\tau) = b \cdot E_0 \cdot \text{sech}\left(\frac{t-\tau}{\Delta t}\right)$ with a and b accounting for incomplete interference between the pulses. Therewith we obtain correlation function envelopes of [10, 11]

$$g_1(\tau) = 1 + \frac{2ab}{a^2 + b^2} \frac{\tau}{\Delta t \sinh\left(\tau/\Delta t\right)} \qquad (5)$$

$$g_2(\tau) = 1 + \frac{18a^2b^2}{a^4 + b^4} \frac{\frac{\tau}{\Delta t}\cosh\frac{\tau}{\Delta t} - \sinh\frac{\tau}{\Delta t}}{\sinh^3\frac{\tau}{\Delta t}}$$
$$+ \frac{3\left(ab^3 + a^3b\right)}{a^4 + b^4} \frac{\sinh\frac{2\tau}{\Delta t} - \frac{2\tau}{\Delta t}}{\sinh^3\frac{\tau}{\Delta t}}. \qquad (6)$$

It shall be noted that cavity coupling has been optimized for $E(t)$, thus a is set to 1 and b consequently accounts for the spatial mode mismatch, which must also
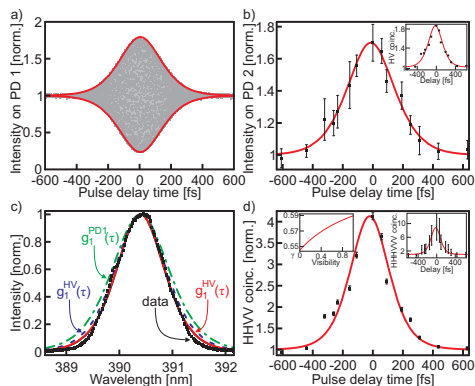
Fig. 2. (a) $g_1^{\mathrm{PD1}}(\tau)$-function. Data measured on PD 1 (gray) and the fit according to eq. (5) to the interference extrema (solid red lines). (b) $g_1^{\mathrm{cav}}(\tau)$ interference maxima of the cavity level (black), fitted by eq. (5) (red line). The inset shows $g_1^{\mathrm{HV}}(\tau)$ for the HV coincidences with error bars from Poissonian counting statistics (equal color coding). (c) Intra-cavity UV pulse spectra (black boxes) and a fit to these (solid black line). Also shown are the spectra obtained by FT of $g_1^{\mathrm{cav}}(\tau)$ (solid red line), $g_1^{\mathrm{HV}}(\tau)$ (dashed blue line) and $g_1^{\mathrm{PD1}}(\tau)$ (dotted-dashed green line). (d) $g_2(\tau)$ interference maxima of the HHVV coincidences fitted by eq. (6). The left inset shows the conversion factor γ, relating the FWHM of $g_2(\tau)$ to the FWHM pulse duration τ_{real}, over the interference visibility for sech-pulses. In the right inset the HHHVVV coincidences with the $g_3(\tau)$ expected from the $g_2(\tau)$ parameters. Error-bars and color coding is as in (b).

be accounted for in the denominators of eqs. (5) and (6) (performing background normalization), due to the reduced cavity coupling of $E(t-\tau)$. Contrary, for $g_1^{\mathrm{PD1}}(\tau)$ measured on PD 1 both pulses contribute fully to the background signal, whereby $\frac{2ab}{a^2+b^2}$ in (5) corresponds to the interference visibility [10]. The measured data for $g_1^{\mathrm{PD1}}(\tau)$ is shown in Fig. 2(a). The intra-cavity UV power level, yielding $g_1^{\mathrm{cav}}(\tau)$, is stated in Fig. 2(b) and $g_1^{\mathrm{HV}}(\tau)$ from the HV coincidences in its inset. Fits according to eq. (5) are displayed by red lines. We achieve comparable interference visibilities [10] of 0.71 inside and 0.77 outside the cavity. The Fourier transform limited pulse durations τ_{FT} are extracted from the FWHM $\Delta\tau_{g_1}$ of the fitted first order correlation functions by the relation [11] $\tau_{\mathrm{FT}} = 0.4048 \cdot \Delta\tau_{g_1}$ for sech-shaped pulses, which is independent of the degree of interference. The UV pulses prior to cavity coupling are consequently found to have a minimal duration of $\tau_{\mathrm{FT}}^{\mathrm{ext}} = 126 \pm 11\,\mathrm{fs}$. However internally $\tau_{\mathrm{FT}}^{\mathrm{cav}} = 150 \pm 16\,\mathrm{fs}$ and $\tau_{\mathrm{FT}}^{\mathrm{HV}} = 140 \pm 17\,\mathrm{fs}$ are obtained, matching within their error boundaries. This intra-cavity pulse broadening stems from the dispersion of the BBO and air inside the resonator, which terminates the overlap of some external frequency comb teeth with cav-

ity resonances during input coupling [9]. The resulting spectral narrowing can also be investigated by examination of the pulse spectrum $S(\lambda)$, derived from $g_1(\tau)$ by Fourier transform [13]. These spectra are depicted in Fig. 2(c) together with the directly measured data, which has been fitted by the expression $S(\lambda) = \mathrm{sech}^2\left(\Delta t\pi^2 c/\lambda\right)$ for a sech-pulse. The former yield FWHM spectral widths of $\Delta\lambda_{\mathrm{ext}} = 1.264 \pm 0.003\,\mathrm{nm}$, $\Delta\lambda_{\mathrm{cav}} = 1.07 \pm 0.04\,\mathrm{nm}$ and $\Delta\lambda_{\mathrm{HV}} = 1.14 \pm 0.05\,\mathrm{nm}$. The FWHM $\Delta\lambda_{\mathrm{meas.}} = 1.058 \pm 0.005\,\mathrm{nm}$ of the latter corresponds to the values of the intra-cavity $g_1(\tau)$-functions, indicating our method to be sensible.

From the $g_2(\tau)$, obtained by the HHVV coincidences, the intra-cavity pulse duration is determined. The recorded data is displayed in Fig. 2(d) together with a fit by eq. (6). Thereof a peak-to-background ratio of 4.18 : 1 is achieved, compared to ideally 8 : 1, due to the incomplete interference between $E(t)$ and $E(t-\tau)$. Importantly the conversion factor γ between the FWHM $\Delta\tau_{g_2}$ of the $g_2(\tau)$-function and the real pulse duration $\tau_{\mathrm{real}} = \gamma \cdot \Delta\tau_{g_2}$ is dependent on the interference visibility, shown in Fig. 2(d). Thus the value of 0.5895 [12] for perfect interference modifies to 0.582 for a visibility of 0.75 extracted from the HHVV coincidence data [10]. Therewith a real pulse duration of $\tau_{\mathrm{real}} = 176 \pm 14\,\mathrm{fs}$ is obtained for the intra-cavity UV pump, comprising an additional dispersive broadening on the order of approximately $30\,\mathrm{fs}$ inside the resonator not revealed by $g_1(\tau)$. Notably six-photon events, providing additional information about the pulse symmetry [13], have also been observed. Since these yield too little statistics, the $g_3(\tau)$-function, as expected for the parameters Δt and b of $g_2(\tau)$, has been calculated instead, showing good resemblance with the data. An improvement could be obtained here by active interferometer stabilization, allowing longer measurement times.

Altogether we have shown a novel method to determine the duration of ultra-short UV pulses by using SPDC. We have applied this method to an optical enhancement cavity, offering the ability to receive multiple correlation orders $g_n(\tau)$ simultaneously. Therewith we estimate pulses to be about $176\,\mathrm{fs}$ long and dispersion broadened by approximately $30\,\mathrm{fs}$. Thus the demonstrated method is a valuable tool for pulse metrology in the UV, which also has the potential for complete pulse reconstruction by extension to frequency resolved optical gating [1].

References

[1] D. J. Kane and R. Trebino, IEEE J. Quantum Electron. **29**, 2 (1993).

[2] C. Iaconis and I. A. Walmsley Opt. Lett. **23**, 10 (1998).

3

[3] R. Krischek, W. Wieczorek, A. Ozawa, N. Kiesel, P. Michelberger, T. Udem and H. Weinfurter, Nature Photonics **4**, 170-173 (2010).

[4] P. G. Kwiat, K. Mattle, H. Weinfurter and A. Zeilinger, Phys. Rev. Lett. **75**, 24 (1995).

[5] This corresponds to $P_{\mathrm{UV}} \in [1.97\,\mathrm{W}, 3.47\,\mathrm{W}]$

[6] K. L. Sala, G. A. Kenney-Wallace and G. E. Hall, IEEE J. Quantum Electron. **16**, 9 (1980).

[7] P. Trojek, *Efficient Generation of Photonic Entanglement and Multiparty Quantum Communication*, PhD dissertation, LMU Munich, 2007.

[8] W. Wieczorek, R. Krischek, N. Kiesel, P. Michelberger, G. Tóth and H. Weinfurter, Phys. Rev. Lett. **103**, 020504 (2009).

[9] R. J. Jones and J. Ye, Opt. Lett. **27**, 20, 1848 (2002).

[10] P. Michelberger, *Femtosecond pulsed enhancement cavity for multi-photon entanglement studies*, Diploma thesis, TU Munich, 2009.

[11] J.-C. M. Diels, J. J. Fontaine, I. C. McMichael and F. Simoni, Appl. Opt. **24**, 9 (1985).

[12] F. Träger *Handbook of Lasers and Optics* (Springer Verlag, 2007)

[13] R. Trebino, *Frequency resolved optical gating: The measurement of ultrashort laser pulses* (Kluwer Academic Publishers, 2000)

4

3.3 Observation of a six photon entangled symmetric Dicke state

In the following we will apply the previously described SPDC source (see section 3.1 [48]) to observe symmetric six photon entangled Dicke states. Dicke states have first been investigated regarding to spontaneous light emission from a cloud of atoms [115]. With respect to quantum information science they have recently become of increasing interest and several proposals have been made to create such states in the laboratory [116, 117, 118]. First experiments concentrated on the observation of a three qubit W state, which are a subgroup of Dicke states, and three qubit W states have been first realized with photons [119, 120, 121, 122]. Additionally, they emerged to have a high robustness against qubit loss in comparison to GHZ states. Further, W states have been created up to 8 qubits realized with ions [32]. Other Dicke states, for example, a symmetric four qubit Dicke state has also been observed [87] and this work revealed another interesting property of Dicke states: by projective measurements depending on the orientation of the projection of the qubit (out of a symmetric four qubit Dicke state), either a three qubit W state or a three qubit GHZ state has been observed [87]. Also other Dicke states can be used for projective measurements [52] and therefore Dicke states have become a general resource generating other entangled states. In the following and in publication 3.3.1 [50], we expand and continue the work which has been done on symmetric Dicke states with four photons [87] to an experiment with six photons.

In general, a symmetric N photon Dicke state with l excitations is given by

$$| D_N^{(l)} \rangle = \binom{N}{l}^{-\frac{1}{2}} \sum_i \mathcal{P}_i \big(| H^{\otimes(N-l)} V^{\otimes l} \rangle \big). \qquad (3.14)$$

with H a horizontally and V a vertically polarized photon and $\sum_i \mathcal{P}_i(...)$ denotes the set over all distinct permutations. In the experimental setup shown in Fig. 3.4 of section 3.1. we are able to observe the symmetric six photon Dicke state with three excitations

$$| D_6^{(3)} \rangle = \frac{1}{\sqrt{20}} \sum_i \mathcal{P}_i \big(| HHHVVV \rangle \big). \qquad (3.15)$$

To this aim, one photon has to be detected in each of the six spatial modes[18] and we have to make sure that the photons are temporally, spatially and spectrally indistinguishable. Due to different group velocities of the H and V polarized photons inside the 1mm thick BBO crystal, the temporal distinguishability has to be compensated with a half wave plate and an additional BBO crystal (see Fig. 3.4), which has half of the length of the pump crystal [70]. The spatial indistinguishability is guaranteed due to coupling of the

---

[18]The theoretical probability to observe the state $| D_6^{(3)} \rangle$ with the linear optics setup shown in Fig. 3.4 is $\frac{6*5*4*3*2*1}{6*6*6*6*6*6} = \frac{5}{324}$
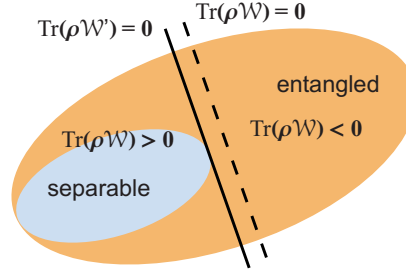
Figure 3.6: **Entanglement witness**. An entanglement witness $\mathcal{W}$ is a hyperplane (dashed line) in the convex space of density matrices and splits the subset of separable states from the entangled states. A witness operator $\mathcal{W}'$ is called optimal (solid line), if it is tangent to the space of separable states.

down conversion photons into a single mode optical fibre [69] (see Fig. 3.4) and spectral indistinguishability with an additional optical interference filter with typical bandwidth of 3nm and a central wavelength of 780nm [19] (see also section 2.2).

To experimentally verify that entanglement of our state is indeed generated and maintained several methods exist. A nice overview for the different techniques to detect a states' entanglement is, for example, given in the review articles [65, 66]. Here, we restrict ourself to entanglement witnesses and Bell inequalities, which have been measured for the state $|D_6^{(3)}\rangle$ and will be shortly explained in the following.

Since entanglement witnesses have been developed [123], they have become a practical tool to detect entanglement in the experiment (see for example [120, 124, 32, 56]). This is due to the fact, that entanglement witnesses allow to detect entanglement with only few measurement settings, in contrast to other criteria, where, for example, the whole density matrix of a state has to be determined (see, for example, the PPT criterion valid for 2 qubits or qutrits [125]). Entanglement witnesses profit from the fact that the space of all density matrices ρ is convex and the subset of all separable states is convex, too. Therefore, an operator $\mathcal{W}$ exists, which defines a hyperplane with $\mathrm{Tr}(\mathcal{W}\rho) = 0$ splitting the space of all density matrices into an entangled and a separable or entangled part. As shown in Fig. 3.6 all states fulfilling $\mathrm{Tr}(\mathcal{W}\rho) < 0$ are entangled and all states with $\mathrm{Tr}(\mathcal{W}\rho) > 0$ are either entangled or separable. The task is now to find the appropriate witness operator. An often used witness is the projector-based witness, which detects entanglement in the vicinity of a pure state $\rho_\xi = |\xi\rangle\langle\xi|$, defined as

$$\mathcal{W}_\xi = \alpha\mathbb{1} - |\xi\rangle\langle\xi| \tag{3.16}$$

with $\alpha = \max_{\phi_{sep}} \left|\langle\phi_{sep}|\xi\rangle\right|^2$ the maximum taken over all separable states $|\phi_{sep}\rangle$. This witness is directly connected to the fidelity of the state $|\xi\rangle$ according to ρ given by $\mathrm{Tr}(\rho|\xi\rangle\langle\xi|) = \langle\xi|\rho|\xi\rangle$. If now the fidelity exceeds a certain value given by α, then the witness is negative and proves entanglement for the state ρ.

---

[19]MaxLine$^{\mathrm{TM}}$ laser line filter from Semrock®

For the Dicke states $|D_N^{(N/2)}\rangle$ and $|D_N^{(1)}\rangle$ the projector based witnesses are given by [32, 126, 120]

$$\mathcal{W}_{D_N^{(N/2)}} = \frac{1}{2}\frac{N}{N-1}\mathbb{1}^{\otimes N} - |D_N^{(N/2)}\rangle\langle D_N^{(N/2)}| \tag{3.17}$$

$$\mathcal{W}_{D_N^{(1)}} = \frac{N-1}{N}\mathbb{1}^{\otimes N} - |D_N^{(1)}\rangle\langle D_N^{(1)}|. \tag{3.18}$$

Further,

$$\text{Tr}(\mathcal{W}_{D_N^{(N/2)}}\rho) = \frac{1}{2}\frac{N}{N-1} - \text{Tr}(|D_N^{(N/2)}\rangle\langle D_N^{(N/2)}|\rho) \tag{3.19}$$

and as the fidelity is given by $F_{D_N^{(N/2)}}(\rho) = \text{Tr}(|D_N^{(N/2)}\rangle\langle D_N^{(N/2)}|\rho)$ we obtain the lower bound for the fidelity of the state $D_N^{(N/2)}$

$$F_{D_N^{(N/2)}}(\rho) > \frac{1}{2}\frac{N}{N-1} \tag{3.20}$$

to proof genuine N partite entanglement. Proceeding the same way for the state $D_N^{(1)}$ we obtain

$$F_{D_N^{(1)}}(\rho) > \frac{N-1}{N} \tag{3.21}$$

For $N = 6$ the bound for $F_{D_6^{(3)}}(\rho)$ is 0.6 and to measure the witness $\mathcal{W}_{D_6^{(3)}}$ we need to determine 183 correlation measurements. Profiting from the permutation invariance of the Dicke states, we reduce this number to 21 measurement settings (see for details publication 3.3.1 [50] and 3.3.2 [57]). In the experiment we measured $F_{D_N^{(N/2)}}(\rho) = 0.654 \pm 0.024$ hence proving genuine six-partite entanglement of the observed state.

Further, it is desirable to prove entanglement with less measurement effort than with a projector-based witness $\mathcal{W}$. To this aim, we are looking for a witness $\tilde{\mathcal{W}}$, which satisfies

$$\mathcal{W} - \alpha'\tilde{\mathcal{W}} \geq 0. \tag{3.22}$$

This means that the expectation value of the above witness for all separable states $|\phi\rangle = |a\rangle|b\rangle$ is still positive

$$\min_{|a\rangle|b\rangle} \langle a, b|(\mathcal{W} - \alpha'\tilde{\mathcal{W}})|a, b\rangle \geq 0 \tag{3.23}$$

and therefore detects entanglement. Using this witness we reduce the measurement settings to detect entanglement of Dicke states to maximally three (see publication 3.3.2 [57]). Witnesses can also be constructed independently from projector-based witnesses. To this end, we are using the ansatz of a simple measurable operator M and design a witness of the form

$$\bar{\mathcal{W}} = \alpha''\mathbb{1}^{\otimes N} - M \tag{3.24}$$

with a constant α'' to ensure that $\langle\bar{\mathcal{W}}\rangle$ is positive on all biseparable states $|\phi\rangle$ and therefore

$$\alpha'' = \max_{|\phi\rangle}\langle\phi|M|\phi\rangle. \tag{3.25}$$

Proceeding in this way, we even obtain a two setting witness to detect entanglement for Dicke states (see publication 3.3.2 [57]).

A different approach to test the entanglement of a probe state is provided by Bell inequalities. They are motived by the famous paper of Einstein, Podolsky and Rosen (EPR) [2], where the completeness of quantum mechanics is questioned. To this end, EPR constructed a gedankenexperiment based on the assumptions of reality and locality also known as local hidden variable model (LHVM), which is apparently in contradiction to quantum mechanics. Based on the EPR gedankenexperiment John Bell derived an inequality referring on the assumptions of a LHVM [3]. If now a Bell inequality is violated in the experiment, then the measurement results can not be described by an LHVM and proves therefore the entanglement of the probe state, because only separable states are in agreement with the LHVM.

For the Dicke state $|D_6^{(3)}\rangle$ a Bell inequality has been found [127]

$$\mathcal{B}_{D_6^{(3)}} = \frac{4}{5}\Big(\frac{\hat{\sigma}_x}{16}\Big(\sum_i \mathcal{P}_i(\hat{\sigma}_z \otimes \hat{\sigma}_z \otimes \hat{\sigma}_z \otimes \hat{\sigma}_z \otimes \hat{\sigma}_x) \tag{3.26}$$

$$-\sum_i \mathcal{P}_i(\hat{\sigma}_z \otimes \hat{\sigma}_z \otimes \hat{\sigma}_x \otimes \hat{\sigma}_x \otimes \hat{\sigma}_x) + \hat{\sigma}_x^5\Big) \tag{3.27}$$

$$+\frac{\hat{\sigma}_y}{16}\Big(\sum_i \mathcal{P}_i(\hat{\sigma}_z \otimes \hat{\sigma}_z \otimes \hat{\sigma}_z \otimes \hat{\sigma}_z \otimes \hat{\sigma}_y) \tag{3.28}$$

$$-\sum_i \mathcal{P}_i(\hat{\sigma}_z \otimes \hat{\sigma}_z \otimes \hat{\sigma}_y \otimes \hat{\sigma}_y \otimes \hat{\sigma}_y) + \hat{\sigma}_y^5\Big)\Big) \tag{3.29}$$

$$\mathcal{B}_{D_6^{(3)}} = \frac{4}{5}(\hat{\sigma}_x \hat{M}_{5,xz} + \hat{\sigma}_y \hat{M}_{5,yz}) \tag{3.30}$$

with $\hat{M}_{N-1,ij}$ being the Mermin operators [128]. This Bell inequality is maximally violated by the state $|D_6^{(3)}\rangle$ and one obtains $\langle\mathcal{B}_{D_6^{(3)}}\rangle = 1$. For the GHZ, for example, the inequality is maximally violated for a smaller value $\langle\mathcal{B}_{GHZ}\rangle = 0.85$ and the general limit for a LHVM is 0.4. In the experiment we determined $\langle\mathcal{B}_{D_6^{(3)}}\rangle_{exp} = 0.43 \pm 0.02$ proving that our state can not be described with a LHVM, but the value is not sufficient to discriminate against a GHZ state.

We have shown that our probe state is entangled approved by witness operators and Bell inequalities. For the next step we would like to show that the state $|D_N^{(N/2)}\rangle$ can serve as a resource to generate other entangled states by either projective measurements or photon loss. To see the result of the projection of one photon we write our input state as

$$|D_N^{(N/2)}\rangle = \frac{1}{\sqrt{2}}\big(|D_{N-1}^{(N/2)}\rangle|H\rangle + |D_{N-1}^{(N/2-1)}\rangle|V\rangle\big) \tag{3.31}$$

and proceeding the same way for a projection of two photons we obtain

$$| D_N^{(N/2)} \rangle = \frac{1}{2} \big(| D_{N-2}^{(N/2)} \rangle | HH \rangle + \sqrt{2} | D_{N-2}^{(N/2-1)} \rangle | HV \rangle + | D_{N-2}^{(N/2-2)} \rangle | VV \rangle \big). \quad (3.32)$$

In the previous example we have chosen horizontally or vertically polarized photons, but also other polarization directions can be projected. In our experiment, we use the state $| D_6^{(3)} \rangle$ and go on by projection on $| H \rangle$ and obtain the state $| D_5^{(3)} \rangle$ or by projection on $| - \rangle$ and obtain the state $\frac{1}{\sqrt{2}} (| D_5^{(2)} \rangle - | D_5^{(3)} \rangle)$. By further projecting on $| HH \rangle$ we are able to obtain the four qubit W state $| D_4^{(1)} \rangle$ or by projection on $| VH \rangle$ we observe the symmetric four photon Dicke state $| D_4^{(2)} \rangle$. Remarkable, even a GHZ state is observed by projection onto $| LR \rangle$ namely $| GHZ_4^- \rangle = \sqrt{1/2} (| D_4^{(1)} \rangle + | D_4^{(3)} \rangle) = \sqrt{1/2} (| + \rangle^{\otimes 4} - | - \rangle^{\otimes 4})$. In publication 3.3.1 [50] we verify the entanglement of the aforementioned states by using witness operators and only for the state $| GHZ_4^- \rangle$ the significance was not high enough to proof entanglement.

Instead of using projections, photon loss serves as well to observe other quantum states. However, in general, mixed states are created. So, if we loose one photon from the state $| D_6^{(3)} \rangle$ we generate the state[20]

$$\rho_5 = \frac{1}{\sqrt{2}} (\rho_{D_5^{(3)}} + \rho_{D_5^{(2)}}). \quad (3.33)$$

After loosing two photons we obtain[21]

$$\rho_4 = \sqrt{\frac{3}{5}} \rho_{D_4^{(2)}} + \frac{1}{\sqrt{5}} (\rho_{D_4^{(1)}} + \rho_{D_4^{(3)}}), \quad (3.34)$$

loosing three photon leads to [22]

$$\rho_3 = \sqrt{\frac{9}{20}} (\rho_{D_3^{(1)}} + \rho_{D_3^{(2)}}) + \sqrt{\frac{1}{20}} (\rho_{D_3^{(0)}} + \rho_{D_3^{(3)}}) \quad (3.35)$$

and finally after loosing four photons one obtains

$$\rho_2 = \sqrt{\frac{3}{5}} \rho_{D_2^{(1)}} + \frac{1}{\sqrt{5}} (\rho_{D_2^{(0)}} + \rho_{D_2^{(2)}}). \quad (3.36)$$

All these states are genuinely entangled. This is a remarkable property of Dicke states in contrast to GHZ states, which loose their entanglement property after loosing one qubit [51].

3.3.1 Publication: Experimental entanglement of a six-photon symmetric Dicke state

---

[20]The probability to loose one H or V photon is $\frac{1}{2}$.

[21]The probability to loose first one H (V) photon and then another H (V) photon is $\frac{3}{6} \frac{2}{5} = \frac{1}{5}$. The probability to loose first one H (V) photon and then a V (H) photon is $\frac{3}{6} \frac{3}{5} = \frac{3}{10}$.

[22]One can proceed like in the previous cases.

Experimental Entanglement of a Six-Photon Symmetric Dicke State

Witlef Wieczorek,[1,2,*] Roland Krischek,[1,2] Nikolai Kiesel,[1,2] Patrick Michelberger,[1,2]
Géza Tóth,[3,4] and Harald Weinfurter[1,2]

[1]*Max-Planck-Institut für Quantenoptik, Hans-Kopfermann-Strasse 1, D-85748 Garching, Germany*
[2]*Department für Physik, Ludwig-Maximilians-Universität, D-80797 München, Germany*
[3]*IKERBASQUE and Department of Theoretical Physics, The University of the Basque Country,
Post Office Box 644, E-48080 Bilbao, Spain*
[4]*Research Institute for Solid State Physics and Optics, Hungarian Academy of Sciences,
Post Office Box 49, H-1525 Budapest, Hungary*
(Received 12 March 2009; published 10 July 2009)

We report on the experimental observation and characterization of a six-photon entangled Dicke state. We obtain a fidelity as high as 0.654 ± 0.024 and prove genuine six-photon entanglement by, amongst others, a two-setting witness yielding -0.422 ± 0.148. This state has remarkable properties; e.g., it allows obtaining inequivalent entangled states of a lower qubit number via projective measurements, and it possesses a high entanglement persistency against qubit loss. We characterize the properties of the six-photon Dicke state experimentally by detecting and analyzing the entanglement of a variety of multipartite entangled states.

Multipartite entangled states have been intensively studied during recent years. Still, the experimental realization of entangled states of more than four particles imposes a considerable challenge, and only a few experiments have yet demonstrated such states [1,2]. So far, many experiments have focused on the observation of graph states [3] like the Greenberger-Horne-Zeilinger (GHZ) states or the cluster states [1], which are, e.g., useful for one-way quantum computation [4]. Dicke states form another important group of states, which were first investigated with respect to light emission from a cloud of atoms [5] and have now come into the focus of both experimental realizations [2,6–8] and theoretical studies [9–12]. W states [13], a subgroup of the Dicke states, first received attention triggered by the seminal work on three-qubit classification based on stochastic local operations and classical communication (SLOCC) by Dür, Vidal, and Cirac [13]. Recently it turned out that other symmetric Dicke states also offer important features. Particularly, by applying projective measurements on a few of their qubits, states of different SLOCC entanglement classes are obtained [8,12]. These Dicke states can act as a rich resource of multipartite entanglement as required for quantum information applications.

In our Letter we experimentally implement and analyze a symmetric six-qubit entangled Dicke state. The entanglement of the Dicke state results from symmetrization and cannot be achieved in a simple way by pairwise interaction, in contrast to, e.g., GHZ states. In order to efficiently characterize the experimentally observed state, we developed optimized methods to determine the fidelity, detect entanglement, and characterize further properties. In particular, we analyze representatives from the variety of multipartite entangled states obtained after projection or loss of qubits.

Generally, Dicke states are simultaneous eigenstates of the total angular momentum, $J_N^2 = J_{N,x}^2 + J_{N,y}^2 + J_{N,z}^2$, and the angular momentum component in the z direction, $J_{N,z}$, where $J_{N,i} = \frac{1}{2}\sum_k \sigma_i^k$ with, e.g., $\sigma_i^3 = \mathbb{1} \otimes \mathbb{1} \otimes \sigma_i \otimes \mathbb{1} \otimes \mathbb{1} \otimes \mathbb{1}$ for $N = 6$ qubits, $i \in \{x, y, z\}$ and σ_i the Pauli spin matrices. A subgroup of the Dicke states is symmetric under permutation of particles and given by

$$|D_N^{(l)}\rangle = \binom{N}{l}^{-1/2} \sum_i \mathcal{P}_i(|H^{\otimes(N-l)}V^{\otimes l}\rangle), \qquad (1)$$

where $\sum_i \mathcal{P}_i(\ldots)$ means the sum over all distinct symmetric permutations and l is the number of excitations in the usual notation of polarization encoded photonic qubits. In our experiment we focus on the symmetric six-qubit Dicke state with three excitations,

$$|D_6^{(3)}\rangle = (1/\sqrt{20})\sum_i \mathcal{P}_i(|HHHVVV\rangle). \qquad (2)$$

To realize the necessary 20 permutations, three horizontally and three vertically polarized photons in a single spatial mode are distributed by polarization-independent beam splitters into six modes, where $|D_6^{(3)}\rangle$ is observed under the condition of detecting a single photon in each of these modes. This scheme can be seen as a continuation of experiments on $D_2^{(1)}$ [6] and $D_4^{(2)}$ [8] and obviously can be extended to higher even photon numbers.

The experimental observation of $|D_6^{(3)}\rangle$ (Fig. 1) is achieved by utilizing a novel source of collinear type II spontaneous parametric down-conversion (SPDC) based on a femtosecond UV-enhancement resonator [14]. The
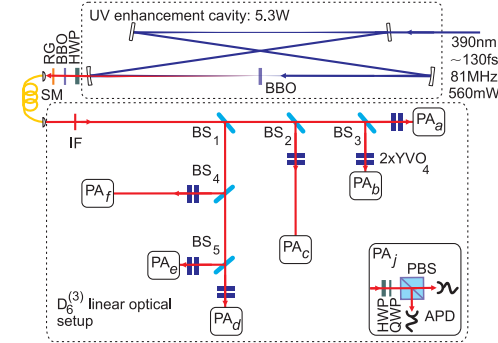
FIG. 1 (color online). Schematic experimental setup for the observation of the Dicke state $|D_6^{(3)}\rangle$. SPDC photons generated in the 1 mm thick β-barium borate (BBO) crystal inside the UV-enhancement cavity pass a half-wave plate (HWP) and a 0.5 mm thick BBO crystal to compensate beam walk-off effects. Their spatial mode is defined by coupling into a single-mode (SM) fiber. Spectral selection is achieved by a band-pass filter (RG) and a 3 nm interference filter (IF) at 780 nm. Birefringence of beam splitters BS_1–BS_5 (BS_1–BS_4 have a splitting ratio of 0.58:0.42 and BS_5 of 0.52:0.48) is compensated for by pairs of birefringent Yttrium-vanadate (YVO$_4$) crystals in the six output modes a, b, c, d, e, f. Polarization analysis (PA$_j$) in each mode is performed via a HWP and a quarter-wave plate (QWP) in front of a polarizing beam splitter (PBS). The photons are detected by single-photon avalanche photodiodes (APDs). The detection signals of the 12 detectors are fed into a FPGA controlled coincidence logic allowing histograming of the 2^{12} possible detection events between the 12 detectors.

resonator allows pumping of the SPDC crystal with femtosecond pulses with an average UV power of 5.3 W at a repetition rate of 81 MHz [14]. The SPDC photons are coupled out of the cavity by a dichroic mirror transparent at 780 nm, are spatially filtered by a single-mode fiber, and are subsequently distributed in free space by polarization-independent beam splitters. Asymmetry in the splitting ratios of the beam splitters reduces the probability of registering $|D_6^{(3)}\rangle$ (0.0126 compared to the optimal value of $5/324 \approx 0.0154$, yielding a six-photon count rate of 3.7

events per minute), but does not influence the state quality. For all data the errors are deduced from Poissonian counting statistics and errors of independently determined relative detector efficiencies.

The first characteristic feature of the state $|D_6^{(3)}\rangle$ is its structure in the z, x, and y bases (Fig. 2); i.e., when analyzing the photons in the six outputs all either along $|H$ or $V\rangle$, $|\pm\rangle = (1/\sqrt{2})(|H\rangle \pm |V\rangle)$ (linear polarization under 45°) and $|L$ or $R\rangle = (1/\sqrt{2})(|H\rangle \pm i|V\rangle)$ (left or right circular polarization), which, in our notation, are the eigenvectors of σ_z, σ_x, and σ_y, respectively. For the z basis [Fig. 2(a)] we find the pronounced 20 terms that are expected for $|D_6^{(3)}\rangle$. However, we also detect coincidences for $HHVVVV$, $HHHHVV$, and permutations thereof. These originate from higher orders of the SPDC process, in particular, from the fourth order emission, where, due to the finite detection efficiency, two of these photons can get lost and the remaining six photons will be registered as a sixfold detector click in the output modes. Thus, $|D_6^{(3)}\rangle$ is mixed with highly colored noise, which exhibits different types of entanglement itself depending on the loss type. Insight into the coherence between the observed coincidences can be obtained from measurements in the x [Fig. 2(b)] and y [Fig. 2(c)] bases. The state $|D_6^{(3)}\rangle$ transforms in these bases to $\sqrt{5/8}|GHZ_6^{\mp}\rangle + \sqrt{3/16}(|D_6^{(4)}\rangle \mp |D_6^{(2)}\rangle)$ with $|GHZ_N^{\mp}\rangle = (1/\sqrt{2}) \times (|0\rangle^{\otimes N} \mp |1\rangle^{\otimes N})$ and $0 = \{+, L\}$, $1 = \{-, R\}$. We observe the GHZ contribution as pronounced coincidence counts for the left- and rightmost projector. The residual counts from other terms [insets of Figs. 2(b) and 2(c)] make the decisive difference to a GHZ state as they are in a superposition with the GHZ terms. Apart from this, noise on top of all counts is also apparent. Most importantly, while the GHZ state shows its two terms only in a single basis, we observe these features now for two bases, which is directly related to the symmetry of $|D_6^{(3)}\rangle$.

A quantitative measure, indicating how well we prepared $|D_6^{(3)}\rangle$ experimentally, is given by the fidelity $F_{D_6^{(3)}}(\rho) = \text{Tr}(|D_6^{(3)}\rangle\langle D_6^{(3)}|\rho)$. Its determination would require 183 correlation measurements in the standard Pauli bases. However, employing the permutational symmetry of
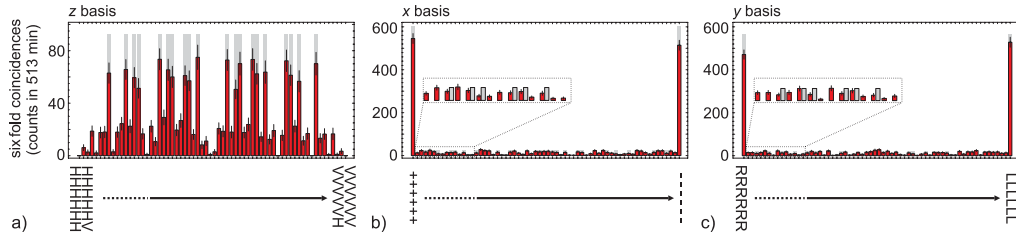
FIG. 2 (color online). Experimentally measured coincidences for the bases (a) z, (b) x, and (c) y with eigenvectors $|H$ or $V\rangle$, $|\pm\rangle$, and $|L$ or $R\rangle$, respectively. Theoretical predictions are shown as pale gray bars normalized to the total number of coincidences. The insets in (b) and (c) are magnified views of a part of all coincidences, where for clarity expected counts are shown next to experimental ones.
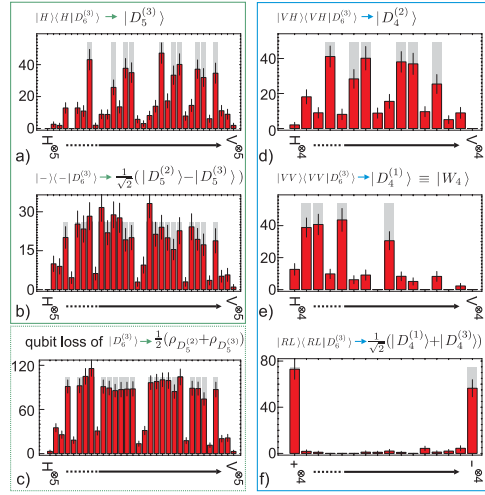
FIG. 3 (color online). Experimentally measured coincidence counts in the z basis [(a)–(e)] and x basis (f) for projections of $|D_6^{(3)}\rangle$ to obtain (a)–(b) five- and (d)–(f) four-qubit entangled states. (c) ρ_5 obtained after a loss of a qubit from $|D_6^{(3)}\rangle$. Each measurement took 279 min. Theoretical predictions are shown as pale gray bars normalized to the total number of coincidences.
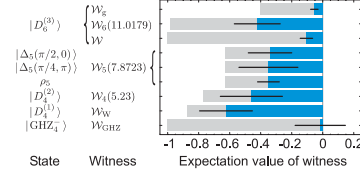

FIG. 4 (color online). Experimental results [dark gray (blue)] and theoretical predictions (pale gray) are shown for the various entanglement witnesses for different states (see text). Negative values prove genuine N-partite entanglement.

the state $|D_6^{(3)}\rangle$ leads to a reduction to only 21 measurement settings [15,16]. We have determined $F_{D_6^{(3)}} = 0.654 \pm 0.024$ with a measurement time of 31.5 h. This allows the application of the generic entanglement witness [10] $\langle \mathcal{W}_g \rangle = 0.6 - F_{D_6^{(3)}} = -0.054 \pm 0.024$ and thus proves genuine six-qubit entanglement of the observed state with a significance of 2 standard deviations (Fig. 4).

Proving entanglement based on witness operators can be much simpler in terms of the number of measurement settings, as due to the symmetry of $|D_6^{(3)}\rangle$ already the two measurements x and y are sufficient [8,10,18]. The generic form of such a witness is given by $\mathcal{W}_N(\alpha) = \alpha \cdot \mathbb{1}^{\otimes N} - (J_{N,x}^2 + J_{N,y}^2)$, where α is obtained by numerical optimization over all biseparable states. For the state $|D_6^{(3)}\rangle$ $\mathcal{W}_6(11.0179)$ [15] has a minimal value of -0.9821. In our experiment we have obtained with the data shown in Figs. 2(b) and 2(c) $\langle \mathcal{W}_6(11.0179) \rangle = -0.422 \pm 0.148$, i.e., after a measurement time of only 17.1 h a higher significance for proving six-qubit entanglement compared to the generic witness (Fig. 4). A different witness, allowing additionally to estimate the fidelity and requiring three measurement settings only, can be obtained by considering higher moments of the $J_{6,i}$ operators and is given as $\mathcal{W} = 1.5 \cdot \mathbb{1}^{\otimes 6} - \sum_{i=x,y,z} \sum_{j=1}^{3} c_{ij} J_{6,i}^{2j}$ [15], with $c_{ij} = (-1/45, 1/36, -1/180; -1/45, 1/36, -1/180; 1007/360, -31/36, 23/360)$. Experimentally, using the three measurements of Fig. 2 we obtain $\langle \mathcal{W} \rangle = -0.105 \pm 0.040$

yielding also a quite accurate bound on the fidelity [15] of $F_{D_6^{(3)}} \geq 0.6 - \langle \mathcal{W} \rangle / 2.5 = 0.642 \pm 0.016$ (Fig. 4).

Another method to reveal entanglement and additionally the nonclassical nature of a quantum state are Bell inequalities. Introduced with the aim to exclude a local-realistic description of measurement results [19,20], they recently became important tools in quantum information processing, e.g., for security analysis [21] or for state discrimination [22,23]. A Bell operator well suited for the latter task is given by $\hat{\mathcal{B}}_{D_6^{(3)}} = \frac{4}{5}(\sigma_x \otimes M_5 + \sigma_y \otimes M_5')$, where M_5 and M_5' are five-qubit Mermin operators [20,23,24]. The associated Bell inequality, $|\langle \hat{\mathcal{B}}_{D_6^{(3)}} \rangle_{\text{avg}}| \leq 0.4$, is maximally violated by the six-photon Dicke state $(\langle \hat{\mathcal{B}}_{D_6^{(3)}} \rangle_{D_6^{(3)}} = 1)$ and much less, e.g., by any six-qubit GHZ state $(\langle \hat{\mathcal{B}}_{D_6^{(3)}} \rangle_{\text{GHZ,max}} = 0.85)$. This again is a consequence of the symmetry of $|D_6^{(3)}\rangle$. While an inequality based on any of the two Mermin terms is maximally violated by a GHZ state, the violation of their sum is only maximal for $|D_6^{(3)}\rangle$ due to its symmetry and equal form in the x and y bases. The experimental value of $\langle \hat{\mathcal{B}}_{D_6^{(3)}} \rangle_{\text{expt}} = 0.43 \pm 0.02$ shows that there is no local-realistic model describing this state, yet due to the higher order SPDC noise, it is not sufficient to discriminate against GHZ states.

The characteristic symmetry and entanglement of $|D_6^{(3)}\rangle$ enables one to observe a wealth of five- and four-qubit entangled states that can be obtained by projective measurements or qubit loss [12]. When we project one of the qubits onto $\cos\theta|V\rangle + \sin\theta e^{-i\phi}|H\rangle$, we first obtain superpositions of five-qubit Dicke states, $|\Delta_5(\theta,\phi)\rangle = \cos\theta|D_5^{(2)}\rangle + \sin\theta e^{i\phi}|D_5^{(3)}\rangle$ with θ, ϕ real. These states belong to two different SLOCC classes, one for the values $\theta = 0$ or $\theta = \pi/2$ and the other one for the remaining value range [12]. Figures 3(a) and 3(b) show measurements in the z basis for a representative state of the two classes, obtained by projecting a qubit either onto $|H\rangle$ $[|\Delta_5(\pi/2,0)\rangle = |D_5^{(3)}\rangle]$ or onto $|-\rangle$ $[|\Delta_5(\pi/4,\pi)\rangle = (1/\sqrt{2})(|D_5^{(2)}\rangle - |D_5^{(3)}\rangle)]$. Figure 4 shows measured expectation values of optimized entanglement witnesses for detecting genuine N-qubit entanglement of these and the following states. When a qubit of $|D_6^{(3)}\rangle$ is lost, one obtains

3.3. OBSERVATION OF A SIX PHOTON ENTANGLED SYMMETRIC DICKE STATE

$\rho_5 = \frac{1}{2}(\rho_{D_5^{(2)}} + \rho_{D_5^{(3)}})$, i.e., an equal mixture of $|D_5^{(2)}\rangle$ and $|D_5^{(3)}\rangle$ [Fig. 3(c)]. Remarkably and in sharp contrast to the case of losing a qubit from a GHZ$_6$ state, this mixed state is also genuine five-qubit entangled (Fig. 4). This fact now clearly provides, after all, a criterion to definitely distinguish these two prominent states and demonstrates the entanglement persistency [25] of $|D_6^{(3)}\rangle$.

By means of a second projective measurement we obtain a variety of SLOCC-inequivalent four-qubit states. In Fig. 3 we exemplarily show coincidences for three of those states. The state $|D_4^{(2)}\rangle$ [8] [Fig. 3(d)] is obtained by projection of one qubit onto $|V\rangle$ and another one onto $|H\rangle$. By projecting two qubits onto the same polarization (here $|V\rangle$) for the first time the four-photon W state [11,26], i.e., $|D_4^{(1)}\rangle$, could be observed in a linear optics experiment [Fig. 3(e)]. Both states are clearly genuine four-partite entangled [8,27] as depicted in Fig. 4. We have determined fidelities of $F_{D_4^{(2)}} = 0.682 \pm 0.022$ and $F_{D_4^{(1)}} = 0.619 \pm 0.043$ using optimized measurement settings [15,17]. Possible applications of $|D_4^{(1)}\rangle$ and $|D_4^{(2)}\rangle$ comprise, for example, quantum telecloning, teleportation, and secret sharing [8,9,28,29]. Most remarkably, one can also obtain a four-qubit GHZ state, which is suitable for, e.g., secret sharing [29]. As mentioned before, there is a strong GHZ component in the state $|D_6^{(3)}\rangle$. Considering the representation in the y basis [Fig. 2(c)], a projection of one photon onto $|R\rangle$ and another one onto $|L\rangle$ filters out just this GHZ component, but the remaining terms coherently superimpose to a four-qubit GHZ state, $|\text{GHZ}_4^-\rangle = (1/\sqrt{2}) \times (|D_4^{(1)}\rangle + |D_4^{(3)}\rangle) = (1/\sqrt{2})(|+\rangle^{\otimes 4} - |-\rangle^{\otimes 4})$. The fourfold coincidence counts shown in Fig. 3(f) reveal the characteristic GHZ structure. However, for this state a two-setting witness measurement [30] resulted in a value of $\langle \mathcal{W}_{\text{GHZ}} \rangle = -0.016 \pm 0.162$, which is not sufficient to prove entanglement with the relevant significance and can be attributed to the low fidelity of $F_{\text{GHZ}} = 0.528 \pm 0.042$ and the asymmetric GHZ structure [Fig. 3(f)].

Altogether, we have experimentally demonstrated in this Letter remarkable entanglement properties of the Dicke state $|D_6^{(3)}\rangle$. It exhibits a high symmetry with characteristic correlations in various bases. As shown, this makes it a perfect resource for observing a wealth of different SLOCC-inequivalent states of a lower qubit number. The novel setup presented here allows experiments with a sufficient count rate and lays the foundations for demonstrations of important applications of $|D_6^{(3)}\rangle$, e.g., for phase-covariant telecloning, multipartite quantum communication, or entanglement enhanced phase measurements.

*witlef.wieczorek@mpq.mpg.de

[1] D. Leibfried *et al.*, Nature (London) **438**, 639 (2005); C.-Y. Lu *et al.*, Nature Phys. **3**, 91 (2007); Phys. Rev. Lett. **102**, 030502 (2009).
[2] H. Häffner *et al.*, Nature (London) **438**, 643 (2005).
[3] M. Hein, J. Eisert, and H. J. Briegel, Phys. Rev. A **69**, 062311 (2004).
[4] R. Raussendorf and H. J. Briegel, Phys. Rev. Lett. **86**, 5188 (2001); P. Walther *et al.*, Nature (London) **434**, 169 (2005).
[5] R. H. Dicke, Phys. Rev. **93**, 99 (1954).
[6] T. E. Kiess *et al.*, Phys. Rev. Lett. **71**, 3893 (1993).
[7] M. Eibl *et al.*, Phys. Rev. Lett. **92**, 077901 (2004); H. Mikami *et al.*, Phys. Rev. Lett. **95**, 150404 (2005).
[8] N. Kiesel *et al.*, Phys. Rev. Lett. **98**, 063604 (2007).
[9] A. Sen(De) *et al.*, Phys. Rev. A **68**, 062306 (2003); P. Agrawal and A. Pati, Phys. Rev. A **74**, 062320 (2006); C. Thiel *et al.*, Phys. Rev. Lett. **99**, 193602 (2007); O. Gühne, F. Bodoky, and M. Blaauboer, Phys. Rev. A **78**, 060301(R) (2008).
[10] G. Tóth, J. Opt. Soc. Am. B **24**, 275 (2007).
[11] T. Tashima *et al.*, Phys. Rev. A **77**, 030302(R) (2008).
[12] W. Wieczorek *et al.*, Phys. Rev. A **79**, 022311 (2009).
[13] W. Dür, G. Vidal, and J. I. Cirac, Phys. Rev. A **62**, 062314 (2000); A. Zeilinger, M. A. Horne, and D. M. Greenberger, NASA Conf. Publ. No. 3135, 1997.
[14] R. Krischek *et al.* (unpublished).
[15] G. Tóth *et al.*, arXiv:0903.3910.
[16] $|D_6^{(3)}\rangle\langle D_6^{(3)}| = \{-0.6[\mathbb{1}] + 0.05([x \pm y \pm \mathbb{1}] - [x \pm z \pm \mathbb{1}] - [y \pm z \pm \mathbb{1}] - [x \pm y \pm z]) + 0.2([x \pm z] + [y \pm z]) + 0.1[x \pm y] + 0.3([x \pm \mathbb{1}] + [y \pm \mathbb{1}]) - 0.6([x] + [y]) + 0.2[z \pm \mathbb{1}] - 0.1[z \pm i\mathbb{1}] - 0.2[z] + 0.6(M_{x,z} + M_{y,z})\}/64$ with $M_{i,j} = \frac{16}{3}\sum_{k=1}^6 [\cos(k\pi/6)\sigma_i + \sin(k\pi/6)\sigma_j]$, $[x + y] = (\sigma_x + \sigma_y)^{\otimes 6}$, and $[x \pm y] = [x + y] + [x - y]$, etc. For decomposition of $M_{i,j}$ see [17].
[17] O. Gühne *et al.*, Phys. Rev. A **76**, 030305(R) (2007).
[18] G. Tóth *et al.*, Phys. Rev. Lett. **99**, 250405 (2007).
[19] J. S. Bell, Physics **1**, 195 (1964).
[20] N. D. Mermin, Phys. Rev. Lett. **65**, 1838 (1990).
[21] P. W. Shor and J. Preskill, Phys. Rev. Lett. **85**, 441 (2000); A. Acin, N. Gisin, and L. Masanes, Phys. Rev. Lett. **97**, 120405 (2006).
[22] C. Schmid *et al.*, Phys. Rev. Lett. **100**, 200407 (2008).
[23] C. Schmid *et al.*, arXiv:0804.3154.
[24] $M_5 = [-\sum_i \mathcal{P}_i(\sigma_z \otimes \sigma_z \otimes \sigma_x \otimes \sigma_x \otimes \sigma_x) + \sum_i \mathcal{P}_i(\sigma_z \otimes \sigma_z \otimes \sigma_z \otimes \sigma_z \otimes \sigma_x) + \sigma_x^{\otimes 5}]/16$; M_5', exchange σ_x with σ_y.
[25] M. Bourennane *et al.*, Phys. Rev. Lett. **96**, 100502 (2006).
[26] X. B. Zou, K. Pahlke, and W. Mathis, Phys. Rev. A **66**, 044302 (2002); Y. Li and T. Kobayashi, Phys. Rev. A **70**, 014301 (2004).
[27] $\mathcal{W}_W = \mathcal{W}_4(5.5934) + 1.47(J_{4,z}^2 - 2J_{4,z})$ [15].
[28] M. Murao *et al.*, Phys. Rev. A **59**, 156 (1999).
[29] M. Hillery, V. Buzek, and A. Berthiaume, Phys. Rev. A **59**, 1829 (1999).
[30] G. Tóth and O. Gühne, Phys. Rev. Lett. **94**, 060501 (2005).

3.3.2 Publication: Practical methods for witnessing genuine multi-qubit entanglement in the vicinity of symmetric states

New Journal of Physics

Practical methods for witnessing genuine multi-qubit entanglement in the vicinity of symmetric states

Géza Tóth[1,2,3,7]**, Witlef Wieczorek**[4,5]**, Roland Krischek**[4,5]**, Nikolai Kiesel**[4,5,6]**, Patrick Michelberger**[4,5] **and Harald Weinfurter**[4,5]

[1] Department of Theoretical Physics, The University of the Basque Country, PO Box 644, E-48080 Bilbao, Spain
[2] Ikerbasque–Basque Foundation for Science, Alameda Urquijo 36, E-48011 Bilbao, Spain
[3] Research Institute for Solid State Physics and Optics, Hungarian Academy of Sciences, PO Box 49, H-1525 Budapest, Hungary
[4] Max-Planck-Institut für Quantenoptik, Hans-Kopfermann-Strasse 1, D-85748 Garching, Germany
[5] Fakultät für Physik, Ludwig-Maximilians-Universität, D-80799 Garching, Germany
[6] Institute for Quantum Optics and Quantum Information (IQOQI), Austrian Academy of Sciences, Boltzmanngasse 3, A-1090 Vienna, Austria
E-mail: toth@alumni.nd.edu

Abstract. We present general numerical methods to construct witness operators for entanglement detection and estimation of the fidelity. Our methods are applied to detecting entanglement in the vicinity of a six-qubit Dicke state with three excitations and also to further entangled symmetric states. All our witnesses are designed to keep the measurement effort small. We also present general results on the efficient local decomposition of permutationally invariant operators, which makes it possible to measure projectors to symmetric states efficiently.

[7] Author to whom any correspondence should be addressed.

Contents

1. Introduction

Entanglement plays a central role in quantum mechanics and in quantum information
processing applications [1]. Moreover, it is also the main goal in today's quantum physics
experiments aiming to create various quantum states [2]. For example, entanglement
has been realized with photonic systems using parametric down-conversion and conditional
detection [3]–[9], with trapped cold ions [10]–[12], in cold atomic ensembles [13], in cold
atoms in optical lattices [14] and in diamond between the electron and nuclear spins [15].
These experiments aimed at creating entangled states. Entanglement makes it possible for some
quantum algorithms (e.g. prime factoring, searching in a database) to outperform their classical
counterparts. Entangled particles are needed for quantum teleportation and other quantum
communication protocols. Moreover, the creation of large entangled states might lead to new
insights about how a classical macroworld emerges from a quantum microworld.

In a multi-qubit experiment, typically the full density matrix is not known, and only few
measurements can be made, yet one would still like to ensure that the prepared state is entangled.
One possibility is applying entanglement witnesses [16, 17]. These are observables that have a
positive expectation value for separable states, while for some entangled states their expectation
value is negative. Since these witness operators are multi-qubit operators, they typically cannot
be measured directly and must be decomposed into the sum of locally measurable operators,
which are just products of single-qubit operators [4, 18, 19].

For many quantum states, like the Greenberger–Horne–Zeilinger (GHZ, [20]) states and
the cluster states [21] such a decomposition of projector-based witness operators seems to be

very difficult: the number of terms in a decomposition to a sum of products of Pauli matrices increases rapidly with the number of qubits. However, practically useful entanglement witnesses with two measurement settings can be constructed for such states [5, 22]. It also turned out that there are decompositions of the projector for GHZ and W states in which the increase with the number of qubits is linear [23].

However, optimal decomposition of an operator is a very difficult, unsolved problem. Moreover, in general, it is still a difficult task to construct efficient entanglement witnesses for a given quantum state. For that, typically we need to obtain the maximum of some operators for product states. In most of the cases, we would like to detect genuine multipartite entanglement. For that, we need to obtain the maximum of these operators for biseparable states, which is again a very hard problem.

In this paper, our goal is to design witnesses that make it possible to detect genuine multipartite entanglement with few measurements, and also to estimate the fidelity of an experimentally prepared state with respect to the target state. Here three strategies are applied to find an experimentally realizable witness. (i) The first strategy is based on measuring the projector-based witness

$$\mathcal{W}^{(P)} = \text{const.} \cdot \mathbb{1} - |\Psi\rangle\langle\Psi| \tag{1}$$

for the detection of genuine multipartite entanglement. $|\Psi\rangle$ is the target state of the experiment. For reducing experimental effort, the aim is to find an efficient decomposition of the projector. (ii) The second strategy is to find a witness that needs fewer measurements than the projector witness, but the price for that might be a lower robustness against noise. The search for such a witness can be simplified if we look for a witness $\mathcal{W}$ such that

$$\mathcal{W} - \alpha\mathcal{W}^{(P)} \geqslant 0 \tag{2}$$

for some $\alpha > 0$. Such a witness is guaranteed to detect genuine multi-qubit entanglement. The advantage of this approach is that the expectation value of $\mathcal{W}$ can be used to find a lower bound on the fidelity. (iii) The third strategy is to find a witness independent from the projector witness. In this case, one has to find an easily measurable operator whose expectation value takes its maximum for the target state. Then, one has to find the maximum of this operator for biseparable states. Any state that has an operator expectation value larger than that is genuine multipartite entangled.

For the optimization of entanglement witnesses for small experimental effort and large robustness to noise, we use semidefinite programming [24]–[29]. Our methods can efficiently be used for multi-qubit systems with up to about 10 qubits. This is important, since there are many situations where semidefinite programming could help theoretically, but in practice the calculations cannot be carried out even for systems of modest size.

We use our methods to design witnesses detecting entanglement in the vicinity of symmetric Dicke states. An N-qubit symmetric Dicke state with m excitations is defined as [30, 31]

$$|D_N^{(m)}\rangle := \binom{N}{m}^{-1/2} \sum_k \mathcal{P}_k(|1_1, 1_2, \ldots, 1_m, 0_{m+1}, \ldots, 0_N\rangle), \tag{3}$$

where $\sum_k \mathcal{P}_k(.)$ denotes summation over all distinct permutations of the spins. $|D_N^{(1)}\rangle$ is the well-known N-qubit W state. The witnesses we will introduce in the following have already been used in the photonic experiment described in [32], aiming to observe a $|D_6^{(3)}\rangle$

4

state [32][8]. We show that genuine multi-qubit entanglement can be detected and the fidelity with respect to the above highly entangled state can efficiently be estimated with two and three measurement settings, respectively. As a byproduct, we will also derive an upper bound for the number of settings needed to measure any permutationally invariant operator. We show that such operators can be efficiently measured even for large systems.

The structure of our paper is as follows. In section 2, we present the basic methods for constructing witnesses. In section 3, we use these methods for constructing witnesses to detect entanglement in the vicinity of a six-qubit symmetric Dicke state with three excitations. In section 4, we present witnesses for states obtained from the above state by measuring some of the qubits. In appendix A, we summarize the tasks that can be solved by semidefinite programming, when looking for suitable entanglement witnesses. In appendix B, we summarize some of the relevant numerical routines of the QUBIT4MATLAB 3.0 program package [34]. In appendix C, we present entanglement conditions for systems with 5–10 qubits that will be relevant in future experiments.

2. Basic definitions and general methods

A multi-qubit quantum state is entangled if it cannot be written as a convex combination of product states. However, in a multi-qubit experiment we would like to detect genuine multi-qubit entanglement [35]: the presence of such entanglement indicates that all the qubits are entangled with each other, not only some of them. We will now need the following definitions:

Definition 1. A pure multi-qubit quantum state is called **biseparable** if it can be written as the tensor product of two, possibly entangled, multi-qubit states

$$|\Psi\rangle = |\Psi_1\rangle \otimes |\Psi_2\rangle. \tag{4}$$

A mixed state is called biseparable, if it can be obtained by mixing pure biseparable states. If a state is not biseparable then it is called **genuine multi-partite entangled**. In this paper, we will consider witness operators that detect genuine multipartite entanglement.

Definition 2. While an entanglement witness is an observable, typically it cannot be measured directly. This is because in most experiments only local measurements are possible. At each qubit k we are able to measure a single-qubit operator M_k, which we can do simultaneously at all the qubits. If we repeat such measurements, then we obtain the expectation values of $2^N - 1$ multi-qubit operators. For example, for $N = 3$ these are $M_1 \otimes \mathbb{1} \otimes \mathbb{1}, \mathbb{1} \otimes M_2 \otimes \mathbb{1}$, $\mathbb{1} \otimes \mathbb{1} \otimes M_3, M_1 \otimes M_2 \otimes \mathbb{1}, M_1 \otimes \mathbb{1} \otimes M_3, \mathbb{1} \otimes M_2 \otimes M_3, M_1 \otimes M_2 \otimes M_3$. The set of single-qubit operators measured is called the **measurement setting** [4] and it can be given as $\{M_1, M_2, M_3, \ldots, M_N\}$. When we consider an entanglement condition, it is important to know how many measurement settings are needed for its evaluation.

Definition 3. Many experiments aim at preparing some, typically pure quantum state ϱ. An entanglement witness is then designed to detect the entanglement of this state. However, in real experiments such a state is never produced perfectly, and the realized state is mixed with noise as given by the following formula:

$$\varrho_{\text{noisy}}(p_{\text{noise}}) = (1 - p_{\text{noise}})\varrho + p_{\text{noise}}\varrho_{\text{noise}}, \tag{5}$$

---

[8] For another experiment aiming to observe a six-qubit Dicke state see Prevedel *et al* [33]. See also the related theoretical work of Campbell *et al* [33].

where p_{noise} is the ratio of noise and ϱ_{noise} is the noise. If we consider white noise then $\varrho_{\text{noise}} = \mathbb{1}/2^N$. The **noise tolerance** of a witness $\mathcal{W}$ is characterized by the largest p_{noise} for which we still have $\text{Tr}(\mathcal{W}\varrho_{\text{noisy}}) < 0$.

In this paper, we will consider three possibilities for detecting genuine multi-qubit entanglement, explained in the following subsections. Later, we will use these ideas to construct various entanglement witnesses.

2.1. Projector witness

A witness detecting genuine multi-qubit entanglement in the vicinity of a pure state $|\Psi\rangle$ can be constructed with the projector as

$$\mathcal{W}_{\Psi}^{(P)} := \lambda_{\Psi}^2 \mathbb{1} - |\Psi\rangle\langle\Psi|, \tag{6}$$

where λ is the maximum of the Schmidt coefficients for $|\Psi\rangle$, when all bipartitions are considered [4]. For the states considered in this paper, projector-based witnesses are given by [4, 12, 37]

$$\mathcal{W}_{\text{D(N,N/2)}}^{(P)} := \frac{1}{2}\frac{N}{N-1}\mathbb{1} - |D_N^{(N/2)}\rangle\langle D_N^{(N/2)}|, \tag{7}$$

$$\mathcal{W}_{\text{D(N,1)}}^{(P)} := \frac{N-1}{N}\mathbb{1} - |D_N^{(1)}\rangle\langle D_N^{(1)}|. \tag{8}$$

These witnesses must be decomposed into the sum of locally measurable terms. For this decomposition, the following observations will turn out to be very important.

Observation 1. A permutationally invariant operator A can always be decomposed as [45]

$$A = \sum_n c_n a_n^{\otimes N}, \tag{9}$$

where a_n are single-qubit operators, and such a decomposition can be straightforwardly obtained.

Proof. Any permutationally invariant multi-qubit operator A can be decomposed as

$$A = \sum_n c_n \sum_k P_k(B_{n,1} \otimes B_{n,2} \otimes B_{n,3} \otimes \cdots \otimes B_{n,N})P_k, \tag{10}$$

where $B_{n,m}$ are single-qubit operators, c_n are constants, and P_k are the full set of operators permuting the qubits. For odd N, we can use the identity

$$\sum_k P_k(B_{n,1} \otimes B_{n,2} \otimes B_{n,3} \otimes \cdots \otimes B_{n,N})P_k$$
$$= 2^{-(N-1)} \sum_{\substack{s_1,s_2,\ldots=\pm 1, \\ s_1 s_2 s_3 \cdots s_N=+1}} (s_1 B_{n,1} + s_2 B_{n,2} + s_3 B_{n,3} + \cdots)^{\otimes N}. \tag{11}$$

Substituting (11) into (10), we obtain a decomposition of the form (9). Equation (11) can be proved by carrying out the summation and expanding the brackets. Due to the $s_1 s_2 s_3 \cdots s_N = +1$ condition, the coefficient of $B_{n,1} \otimes B_{n,2} \otimes B_{n,3} \otimes \cdots \otimes B_{n,N}$ is 1. The coefficient of terms like $B_{n,1} \otimes B_{n,1} \otimes B_{n,3} \otimes \cdots \otimes B_{n,N}$, that is, terms containing one of the variables more than once is zero. For even N, a similar proof can be carried out using[9]

$$\sum_k P_k (B_{n,1} \otimes B_{n,2} \otimes B_{n,3} \otimes \cdots \otimes B_{n,N}) P_k$$
$$= 2^{-(N-1)} \sum_{\substack{s_1, s_2, \ldots = \pm 1, \\ s_1 s_2 s_3 \cdots s_N = +1}} s_1 (B_{n,1} + s_2 B_{n,2} + s_3 B_{n,3} + \cdots)^{\otimes N}. \tag{12}$$

Next, we give two examples for the application of (11) and (12) for the decomposition of simple expressions

$$\sum_k P_k (\sigma_x \otimes \sigma_y) P_k = \frac{1}{2} \left\{ (\sigma_x + \sigma_y)^{\otimes 2} - (\sigma_x - \sigma_y)^{\otimes 2} \right\}, \tag{13}$$

$$\sum_k P_k (\sigma_x \otimes \sigma_y \otimes \sigma_z) P_k = \frac{1}{4} \left\{ (\sigma_x + \sigma_y + \sigma_z)^{\otimes 3} + (\sigma_x - \sigma_y - \sigma_z)^{\otimes 3} + (-\sigma_x - \sigma_y + \sigma_z)^{\otimes 3} \right.$$
$$\left. + (-\sigma_x + \sigma_y - \sigma_z)^{\otimes 3} \right\}, \tag{14}$$

where σ_k are the Pauli spin matrices. While the first example does not reduce the number of settings needed, the second example reduces the number of settings from 6 to 4. $\quad\square$

Next, we present a method to get efficient decompositions for permutationally invariant operators.

Observation 2. Any N-qubit permutationally invariant operator A can be measured with at most

$$\mathcal{L}_N = \tfrac{2}{3} N^3 + N^2 + \tfrac{4}{3} N \tag{15}$$

local measurement settings, using (11) and (12).

Proof. We have to decompose first A into the sum of Pauli group elements as

$$A = \sum_{i,j,m:\, i+j+m \leqslant N} c_{ijm} \sum_k P_k (\sigma_x^{\otimes i} \otimes \sigma_y^{\otimes j} \otimes \sigma_z^{\otimes m} \otimes \mathbb{1}^{\otimes (N-i-j-m)}) P_k, \tag{16}$$

where c_{ijm} are some constants. Then, such a decomposition can be transformed into another one of the form (9), using (11) and (12). All of the settings needed are of the form $\{a, a, a, \ldots, a\}$ where $a = n_x \sigma_x + n_y \sigma_y + n_z \sigma_z$, n_k are integer and $1 \leqslant \sum_k |n_k| \leqslant N$. Simple counting leads to an upper bound $\mathcal{L}_N$ for the number of settings given in (15). Here we considered that (n_x, n_y, n_z) and $(-n_x, -n_y, -n_z)$ describe the same setting. An even better bound can be obtained using that (n_x, n_y, n_z) and (cn_x, cn_y, cn_z) for some $c \neq 0$ represent the same setting. An algorithm based

---

[9] A similar decomposition with continuous number of terms is of the form $\sum_k P_k (B_1 \otimes B_2 \otimes \ldots) P_k \propto \int_{\phi_k \in [0, 2\pi]} [e^{i\phi_1} B_1 + e^{i\phi_2} B_2 + \cdots + e^{i\phi_{N-1}} B_{N-1} + e^{-i(\phi_1 + \phi_2 + \cdots + \phi_{N-1})} B_N]^{\otimes N} d\phi_1 d\phi_2 \cdots d\phi_{N-1}$. Such a construction has been used for the $N = 2$ case in [48].

on this leads to the bounds $\mathcal{L}'_N = 9, 25, 49, 97, 145, 241, 337, 481, 625$ for $N = 2, 3, \ldots, 10$ qubits, respectively.

For the projector $|D_N^{(N/2)}\rangle\langle D_N^{(N/2)}|$, the decomposition to Pauli group elements contain only terms in which each Pauli matrix appears an even number of times. Hence, all of the settings needed are of the form $\{a, a, a, \ldots, a\}$ where $a = 2n_x\sigma_x + 2n_y\sigma_y + 2n_z\sigma_z$, n_k are integer and $1 \leqslant \sum_k |n_k| \leqslant N/2$. For this reason, $\mathcal{L}_{N/2}$ and $\mathcal{L}'_{N/2}$ are upper bounds for the number of settings needed to measure this operator.

Let us discuss the consequences of observations 1 and 2. They essentially state that the number of settings needed to measure a permutationally invariant operator scales only polynomially with the number of qubits. This is important since for operators that are not permutationally invariant, the scaling is known to be exponential [36]. Moreover, even if we can measure only correlation terms of the form $a^{\otimes N}$, we can measure any permutationally invariant operator. □

2.2. Witnesses based on the projector witness

We can construct witnesses that are easier to measure than the projector witness, but they are still based on the projector witness. We use the idea mentioned in the introduction. If $\mathcal{W}^{(P)}$ is the projector witness and (2) is fulfilled for some $\alpha > 0$, then $\mathcal{W}$ is also a witness. This is because $\mathcal{W}$ has a negative expectation value only for states for which $\mathcal{W}^{(P)}$ also has a negative expectation value. The advantage of obtaining witnesses this way is that we can have a lower bound on the fidelity from the expectation value of the witness as

$$\mathrm{Tr}(\varrho|\Psi\rangle\langle\Psi|) \geqslant \lambda_\Psi^2 - \frac{1}{\alpha}\mathrm{Tr}(\mathcal{W}\varrho). \tag{17}$$

We will look for such witnesses numerically, such that the noise tolerance of the witness be the largest possible. This search can be simplified by the following observation.

Observation 3. Since we would like to construct a witness detecting genuine multi-qubit entanglement in the vicinity of a permutationally invariant state, it is enough to consider witness operators that are also permutationally invariant.

Proof. Let us consider a witness operator that detects entanglement in the vicinity of a permutationally invariant state ϱ and its expectation value takes its minimum for ϱ. Then, based on (5), the witness $\mathcal{W}$ detects entanglement if

$$p_{\mathrm{noise}} > \frac{\mathrm{Tr}(W\varrho)}{\mathrm{Tr}(W\varrho) - \mathrm{Tr}(W\varrho_{\mathrm{noise}})}. \tag{18}$$

For a permutationally invariant state ϱ, we have $\varrho = \frac{1}{N_P}\sum_k P_k\varrho P_k$, where N_P is the number of different permutation operators P_k. We assume that the same holds also for ϱ_{noise}. Let us define the permutationally invariant operator $\mathcal{W}' = \frac{1}{N_P}\sum_k P_k\mathcal{W}P_k$. The operator $\mathcal{W}'$ is non-negative on all biseparable states since

$$\inf_{\varrho\in\mathcal{B}} \mathrm{Tr}(W\varrho) = \frac{1}{N_P}\sum_k \inf_{\varrho\in\mathcal{B}} \mathrm{Tr}(\mathcal{W}P_k\varrho P_k) \leqslant \inf_{\varrho\in\mathcal{B}} \mathrm{Tr}(\mathcal{W}'\varrho), \tag{19}$$

where $\mathcal{B}$ is the set of biseparable states. Hence, $\mathcal{W}'$ is a witness detecting genuine multipartite entanglement. Since we have $\mathrm{Tr}(\mathcal{W}\varrho) = \mathrm{Tr}(\mathcal{W}'\varrho)$, and $\mathrm{Tr}(\mathcal{W}\varrho_{\mathrm{noise}}) = \mathrm{Tr}(\mathcal{W}'\varrho_{\mathrm{noise}})$,

8

the robustness to noise of $\mathcal{W}'$ is identical to that of $\mathcal{W}$. Hence, it is sufficient to look for witnesses that are permutationally invariant.

We will first consider measuring the $\{\sigma_x, \sigma_x, \sigma_x, \sigma_x, \sigma_x, \sigma_x\}$ and $\{\sigma_y, \sigma_y, \sigma_y, \sigma_y, \sigma_y, \sigma_y\}$ settings, where σ_l are the Pauli spin matrices. This we call the two-setting case. Then we will consider measuring also the $\{\sigma_z, \sigma_z, \sigma_z, \sigma_z, \sigma_z, \sigma_z\}$ setting, which we call the three-setting case. Due to observation 3, we consider only permutationally invariant witnesses. Such witnesses can be written as

$$\mathcal{W}(\alpha_0, \{\alpha_{ln}\}) := \alpha_0 \cdot \mathbb{1} + \sum_{l=x,y,z} \sum_{n=1}^{N} \alpha_{ln} \sum_k \mathcal{P}_k[\sigma_l^{\otimes n} \otimes \mathbb{1}^{\otimes(N-n)}], \tag{20}$$

where the summation is over all distinct permutations, and α_0 and α_{ln} are some constants. We will consider a simpler but equivalent formulation

$$\mathcal{W}(c_0, \{c_{ln}\}) := c_0 \cdot \mathbb{1} + \sum_{l=x,y,z} \sum_{n=1}^{N} c_{ln} J_l^n, \tag{21}$$

where c_0, c_{ln} are the coefficients of the linear combination defining the witness and J_l are the components of the total angular momentum given as

$$J_l = \frac{1}{2} \sum_{k=1}^{N} \sigma_l^{(k)}. \tag{22}$$

Here $\sigma_l^{(k)}$ denotes a Pauli spin matrix acting on qubit (k).

Finally, if we consider detecting entanglement in the vicinity of $|D_N^{(N/2)}\rangle$ states, then further simplifications can be made. For this state and also for the completely mixed state all odd moments of J_l have a zero expectation value. For any witness of the form (21), the maximum for biseparable states does not change if we flip the sign of c_{ln} for all odd n. Hence, following from an argument similar to the one in observation 3 concerning permutational symmetry, it is enough to consider only even powers of J_l in our witnesses. $\qquad\square$

2.3. Witnesses independent from the projector witness

In general, we can also design witnesses without any relation to the projector witness. We can use an easily measurable operator M to make a witness of the form

$$\mathcal{W} := c\mathbb{1} - M, \tag{23}$$

where c is some constant. To make sure that (23) is a witness for genuine multipartite entanglement, i.e. $\langle \mathcal{W} \rangle$ is positive on all biseparable states, we have to set c to

$$c = \max_{|\Psi\rangle \in \mathcal{B}} \langle M \rangle_{|\Psi\rangle}, \tag{24}$$

where $\mathcal{B}$ is the set of biseparable states. The optimization needed for (24) can be done analytically. For example, for the $|D_4^{(2)}\rangle$ state a witness has been presented that detects genuine four-qubit entanglement by measuring second moments of angular momentum operators [37]. However, analytical calculations become exceedingly difficult as the number of qubits increases.

The optimization can also be done numerically, but one cannot be sure that simple numerical optimization finds the global maximum. (See appendix B for a reference to such a MATLAB program.) Semidefinite programming is known to find the global optimum, but

9

the optimization task (24) cannot be solved directly by semidefinite programming. Instead of looking for the maximum for biseparable states, using semidefinite programming, we can look for the maximum for states that have a positive partial transpose (PPT) [24, 38] (see appendices A and B). This way we can obtain

$$c' := \max_{I} \max_{\varrho \geqslant 0, \varrho^{T_I} \geqslant 0} \langle M \rangle_{\varrho}, \tag{25}$$

for which $c' \geqslant c$. The first maximization is over all bipartitions I. Thus, when putting c' into the place of c in (23), we obtain a witness that detects only genuine multipartite entanglement. In many cases simple numerics show that $c = c'$. In this case, our witnesses are optimal in the sense that some biseparable state gives a zero expectation value for these witnesses.

Finally, let us discuss how to find the operator M in (23) for a two- or a three-setting witness, in particular, for detecting entanglement in the vicinity of $|D_N^{(N/2)}\rangle$. Based on section 2.2, we have to look for an operator that contains only even powers of J_l. Hence, the general form of a two-setting witness with moments up to second order is

$$\mathcal{W}_{\mathrm{D(N,N/2)}}^{(I2)} := c_{DN} - (J_x^2 + J_y^2), \tag{26}$$

where $c_{\mathrm{D}N}$ is a constant[10]. The coefficients of J_x^2 and J_y^2 could still be different, however, this would not lead to witnesses with a better robustness to noise.

For other symmetric Dicke states, based on similar arguments, a general form of a witness containing moments of J_l up to second order such that it takes its minimum for $|D_N^{(m)}\rangle$ is of the form

$$\mathcal{W}_{\mathrm{D(N,m)}}^{(I3)} := c_q - (J_x^2 + J_y^2) + q(J_z - \langle J_z \rangle_{|D_N^{(m)}\rangle})^2, \tag{27}$$

where c_q and q are constants. For the witnesses described in this section, the optimization process is more time-consuming than for the witnesses related to the projector witness. Because of that we presented witnesses of the above type that are constructed only with the first and second moments of the angular momentum operators, and thus contain a few free parameters.

3. Witnesses for a six-qubit Dicke state with three excitations

In this section, we will consider entanglement detection close to a six-qubit symmetric Dicke state with three excitations, denoted as $|D_6^{(3)}\rangle$. There are several proposals for creating Dicke states in various physical systems [40]–[43].

3.1. Witnesses based on the projector witness

3.1.1. Two-setting witness. Let us consider the two-setting case and define first the optimization problem we want to solve. We would like to look for the witness $\mathcal{W}$ with the largest noise tolerance that fulfills the following requirements:

1. $\mathcal{W}$ is a linear combination of certain basis operators B_k, that is, $\mathcal{W} = \sum_k c_k B_k$,
2. $\mathcal{W} - \alpha \mathcal{W}_{\mathrm{D(6,3)}}^{(P)} \geqslant 0$ with some $\alpha > 0$.

[10] Witnesses for the state $|D_6^{(3)}\rangle$ are presented with the structure factor in [39]. In a sense, these witnesses are written with collective quantities, after a site-dependent phase shift is applied.

For the two-setting case we set $\{B_k\} = \{\mathbb{1}, J_x^2, J_y^2, J_x^4, J_y^4, J_x^6, J_y^6\}$. The second condition makes sure that $\mathcal{W}$ is also a witness detecting genuine multipartite entanglement.

Note that *any* optimization algorithm can be used for looking for $\mathcal{W}$. Even if we do not find the global optimum, that is, the witness with the largest possible robustness to white noise, $\mathcal{W}$ is still a witness detecting genuine multipartite entanglement. However, semidefinte programming can be used to find the global optimum (see appendix A). The two-setting witness obtained this way is

$$\mathcal{W}_{\mathrm{D}(6,3)}^{(P2)} := 7.75 \cdot \mathbb{1} - \tfrac{35}{18}(J_x^2 + J_y^2) + \tfrac{55}{72}(J_x^4 + J_y^4) - \tfrac{5}{72}(J_x^6 + J_y^6), \tag{28}$$

which tolerates white noise if $p_{\mathrm{noise}} < 0.1391$. Straightforward calculation shows that $\mathcal{W}_{\mathrm{D}(6,3)}^{(P2)} - 2.5\mathcal{W}^{(P)} \geqslant 0$. Based on (17), $(0.6 - \langle \mathcal{W}_{\mathrm{D}(6,3)}^{(P2)} \rangle / 2.5)$ bounds the fidelity from below.

3.1.2. Three-setting witness. Similarly we can look for the optimal witness for the three-setting case. The result is

$$\mathcal{W}_{\mathrm{D}(6,3)}^{(P3)} := 1.5 \cdot \mathbb{1} - \tfrac{1}{45}(J_x^2 + J_y^2) + \tfrac{1}{36}(J_x^4 + J_y^4) - \tfrac{1}{180}(J_x^6 + J_y^6) + \tfrac{1007}{360}J_z^2 - \tfrac{31}{36}J_z^4 + \tfrac{23}{360}J_z^6. \tag{29}$$

White noise is tolerated if $p_{\mathrm{noise}} < 0.2735$. It is easy to check that $\mathcal{W}$ is a witness as $\mathcal{W}_{\mathrm{D}(6,3)}^{(P3)} - 2.5\mathcal{W}^{(P)} \geqslant 0$.

Based on (17), the expectation value of this witness can be used to bound the fidelity as $F \geqslant 0.6 - \langle \mathcal{W}_{\mathrm{D}(6,3)}^{(P3)} \rangle / 2.5 =: F'$. Here we will demonstrate how well the fidelity estimation works for our witness for noisy states. We consider first white noise, then non-white noise of the form

$$\varrho_{\mathrm{noisy}}^{(\mathrm{NW})} := p_{D63}|D_6^{(3)}\rangle\langle D_6^{(3)}| + \frac{1 - p_{D63}}{2}\left(|D_6^{(2)}\rangle\langle D_6^{(2)}| + |D_6^{(4)}\rangle\langle D_6^{(4)}|\right), \tag{30}$$

with $p_{D63} = 4/7$, which is one of the relevant types of noise for the experiment of [32]. Note that the noise contains the original state $|D_6^{(3)}\rangle\langle D_6^{(3)}|$. The results are shown in figure 1. For the non-white noise (30), the fidelity estimate based on the witness yields a very good estimate.

Note that it is also possible to design a witness for the largest possible tolerance to the noise in (30). Due to the special form of the noise, the fidelity estimate turns out to be equal to the fidelity. This is remarkable: the fidelity can be obtained exactly with only three local measurements.

3.1.3. Measuring the projector-based witness. For measuring the projector-based witness (7) for $N = 6$, one has to decompose the projector in an efficient way. The straightforward decomposition into the weighted sum of products of Pauli spin matrices leads to a scheme that needs 183 settings, since for all local operators all the permutations have to be measured. The number of settings needed can be dramatically decreased if one is looking for a decomposition of the form (9). Observation 1 makes it possible to decompose the projector in this way such that only 25 settings are needed. We could further decrease the number of settings needed and found the following decomposition:

$$\begin{aligned}
64|D_6^{(3)}\rangle\langle D_6^{(3)}| =\ &-0.6[\mathbb{1}] + 0.3[x \pm \mathbb{1}] - 0.6[x] + 0.3[y \pm \mathbb{1}] - 0.6[y] + 0.2[z \pm \mathbb{1}] - 0.2[z] \\
&+ 0.2\mathrm{Mermin}_{0,z} + 0.05[x \pm y \pm \mathbb{1}] - 0.05[x \pm z \pm \mathbb{1}] - 0.05[y \pm z \pm \mathbb{1}] \\
&- 0.05[x \pm y \pm z] + 0.2[x \pm z] + 0.2[y \pm z] + 0.1[x \pm y] \\
&+ 0.6\mathrm{Mermin}_{x,z} + 0.6\mathrm{Mermin}_{y,z}. \tag{31}
\end{aligned}$$

11 **IOP** Institute of Physics Φ DEUTSCHE PHYSIKALISCHE GESELLSCHAFT
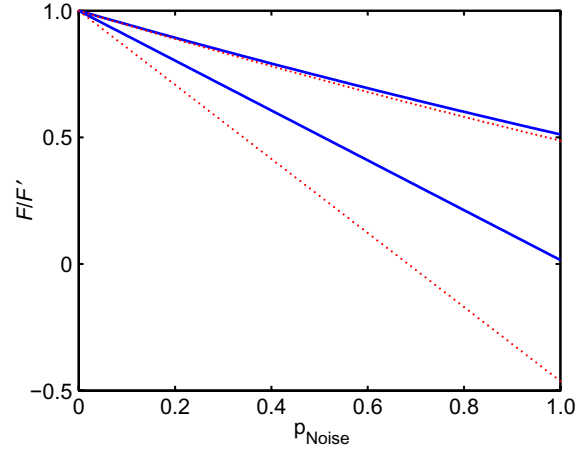
Figure 1. The fidelity F versus noise (solid) and the fidelity estimate F' versus noise (dotted), for the white noise (bottom two curves) and for the non-white noise (30) (top two curves). For the fidelity estimate, the three-setting witness (29) was used.

Here we use the notation $[x + y] = (\sigma_x + \sigma_y)^{\otimes 6}$, $[x + y + \mathbb{1}] = (\sigma_x + \sigma_y + \mathbb{1})^{\otimes 6}$, etc. The $\pm$ sign denotes a summation over the two signs, i.e., $[x \pm y] = [x + y] + [x - y]$. The Mermin operators are defined as

$$\text{Mermin}_{a,b} := \sum_{k \text{ even}} (-1)^{k/2} \sum_{k} \mathcal{P}_k(\otimes_{i=1}^{k} \sigma_a \otimes_{i=k+1}^{N} \sigma_b), \qquad (32)$$

where $\sigma_0 = \mathbb{1}$. That is, it is the sum of terms with even number of σ_a's and σ_b's, with the sign of the terms depending on the number of σ_a's. The expectation value of the operators $\text{Mermin}_{a,b}$ can be measured based on the decomposition [23]

$$\text{Mermin}_{a,b} = \frac{2^{N-1}}{N} \sum_{k=1}^{N} (-1)^k \left[\cos\left(\frac{k\pi}{N}\right) a + \sin\left(\frac{k\pi}{N}\right) b \right]^{\otimes N}. \qquad (33)$$

Hence, $\text{Mermin}_{x,z}$ and $\text{Mermin}_{y,z}$ can be measured with six settings. $\text{Mermin}_{0,z}$, on the other hand, needs only the measurement of the $\{\sigma_z, \sigma_z, \sigma_z, \sigma_z, \sigma_z, \sigma_z\}$ setting. Knowing that $[A]$, $[A + \mathbb{1}]$ and $[A - \mathbb{1}]$ can be measured with a single setting $\{A, A, A, \ldots, A\}$, we find that 21 measurement settings are needed to measure $|D_6^{(3)}\rangle\langle D_6^{(3)}|$: $x, y, z, x \pm y, x \pm z, y \pm z, \sqrt{3}x \pm z, \sqrt{3}z \pm x, \sqrt{3}y \pm z, \sqrt{3}z \pm y$, and $x \pm y \pm z$. The settings are also shown in figure 2(a)[11].

3.2. Witness independent from the projector witness

So far we constructed witnesses that detected fewer states than the projector-based witness, in return, they were easier to measure. When proving that they were witnesses, we used the

---

[11] Note that [33] presents another decomposition that needs also 21 settings.
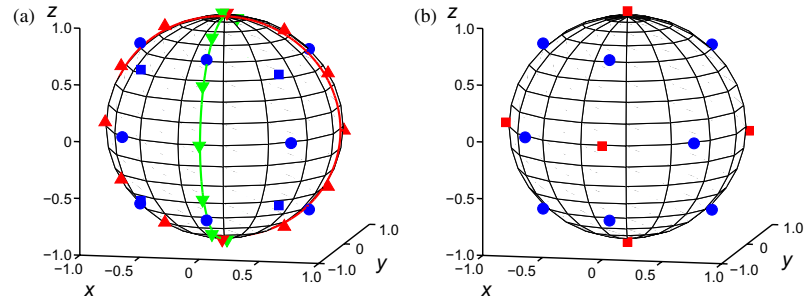
Figure 2. (a) The measurement settings needed to measure the projector to the six-qubit symmetric Dicke state with three excitations based on the decomposition (31). A point at (x, y, z) indicates measuring $x\sigma_x + y\sigma_y + z\sigma_z$ on all qubits. (▲) Settings for Mermin$_{x,z}$, (▼) settings for Mermin$_{y,z}$, (■) $\sigma_x \pm \sigma_y \pm \sigma_z$, and (●) rest of the settings. (b) Settings for the four-qubit Dicke state with two excitations based on (37). (■) $\pm\sigma_x, \pm\sigma_y, \pm\sigma_z$, and (●) $\sigma_x \pm \sigma_y, \sigma_x \pm \sigma_z$, and $\sigma_y \pm \sigma_z$.

Table 1. The list of entanglement witnesses presented in this paper, together with the number of measurement settings needed to measure them and their robustness to white noise. Top four lines: six-qubit witnesses. Bottom five lines: four- and five-qubit witnesses.

Witness	Number of settings	Noise tolerance
$\mathcal{W}_{D(6,3)}^{(P)}$	21	0.4063
$\mathcal{W}_{D(6,3)}^{(P3)}$	3	0.2735
$\mathcal{W}_{D(6,3)}^{(P2)}$	2	0.1391
$\mathcal{W}_{D(6,3)}^{(I2)}$	2	0.1091
$\mathcal{W}_{D(5,2)}^{(I2)}$	2	0.1046
$\mathcal{W}_{D(4,1)}^{(P)}$	7	0.2667
$\mathcal{W}_{D(4,1)}^{(I2)}(q = 1.47)$	3	0.1476
$\mathcal{W}_{D(4,2)}^{(P)}$	9	0.3556
$\mathcal{W}_{D(4,2)}^{(P3)}$	2	0.2759

simple relation (2). Following the example of [37], we now look for a two-setting witness of the form (26) for $N = 6$ that is independent from the projector witness. For determining c_{D6}, we need to compute the maximum of $J_x^2 + J_y^2$ for biseparable states for all the possible bipartitions. As we have discussed in section 2.3, instead of looking for the maximum for states that are

13

separable with respect to a certain bipartition, we can also look for the maximum for PPT states (see appendix A). We obtain

$$c_{D6} := 11.0179. \tag{34}$$

$\mathcal{W}_{\mathrm{D}(6,3)}^{(I2)}$ detects genuine multipartite entanglement if for white noise $p_{\mathrm{noise}} < 0.1091$. Simple numerical optimization leads to the same value for the maximum for biseparable states[12]. Hence we find that our witness is optimal. Finally, the list of witnesses presented in this section are shown in the top part of table 1.

4. Witnesses for states derived from $|D_6^{(3)}\rangle$ via projections

By projective measurements of one or two of the qubits we can obtain several states that are inequivalent under stochastic local operations and classical communication (SLOCC). Surprisingly, these states still possess genuine multipartite entanglement [32, 44]. Next, we discuss how to detect the entanglement of these states.

4.1. Witnesses for the superposition of five-qubit Dicke states

After measuring one of the qubits in some basis and post-selecting for one of the two outcomes, one can obtain states of the form

$$\varrho_{D5} := c_1 |D_5^{(2)}\rangle + c_2 |D_5^{(3)}\rangle, \tag{35}$$

where $|c_1|^2 + |c_2|^2 = 1$. For such states, the expectation value of $J_x^2 + J_y^2$ is maximal, thus a witness of the form (26) for $N = 5$ is used to detect their entanglement. Both semidefinite programing and simple numerical optimization leads to $c_{D5} := 7.8723$. Naturally, $\langle \mathcal{W}_{D5}^{(I2)} \rangle$ is minimal not only for states of the form (35), but for any mixture of such states.

4.2. Witness for the four-qubit W state

Now we will construct witnesses for a four-qubit W state, which is obtained from $|D_6^{(3)}\rangle$ if two qubits are measured in the σ_z basis, and the measurement result is +1 in both cases. We consider a witness of the form (27) for $N = 4$ and $m = 1$. We try several values for q and determine c_q for the witness $\mathcal{W}_{\mathrm{D}(4,1)}(q)$ as a function of q using semidefinite programming. For each witness we also compute the noise tolerance. The results of these computations can be seen in figure 3. It turns out, that the best witness is obtained for $q = 1.47$ and $c_q = 4.1234$. It tolerates white noise if $p_{\mathrm{noise}} < 0.1476$.

4.3. Three-setting witness for the four-qubit Dicke state

A $|D_4^{(2)}\rangle$ state can also be obtained from $|D_6^{(3)}\rangle$, namely if the measurement outcomes are +1 and −1 for two consecutive σ_z measurements. For that case, we look for a three-setting witness, based on the projector witness. For white noise, the result is

$$\mathcal{W}_{\mathrm{D}(4,2)}^{(P3)} := 2 \cdot \mathbb{1} + \tfrac{1}{6}(J_x^2 + J_y^2 - J_x^4 - J_y^4) + \tfrac{31}{12} J_z^2 - \tfrac{7}{12} J_z^4. \tag{36}$$

[12] We used the `maxbisep` routine of the QUBIT4MATLAB V3.0 package [34] with parameters for accuracy [30 000, 100 000, 0.0005]. See also appendix B.
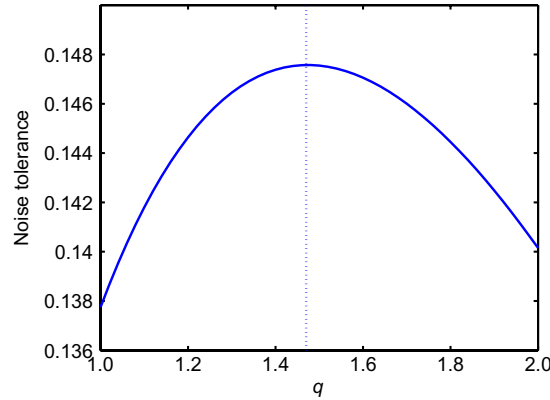
Figure 3. The noise tolerance of the witness $\mathcal{W}_{\mathrm{D}(1,4)}^{(I3)}$ given in (27) as a function of the parameter q. The maximum is in the vicinity of $q = 1.47$.

The witness tolerates white noise if $p_{\mathrm{noise}} < 0.2759$. It is easy to check that $\mathcal{W}$ is a witness: one has to notice that $\mathcal{W}_{\mathrm{D}(4,2)}^{(P3)} - 3\mathcal{W}_{\mathrm{D}(4,2)}^{(P)} \geqslant 0$, were $\mathcal{W}_{\mathrm{D}(4,2)}^{(P)}$ is defined in (7). Thus, the fidelity can be estimated from the measurement of the witness as $F \geqslant 2/9 - \langle \mathcal{W}_{\mathrm{D}(4,2)}^{(P3)} \rangle / 3$.

4.4. Measuring the projector witness for the four-qubit Dicke state

We can also measure the projector witness $\mathcal{W}_{\mathrm{D}(4,2)}^{(P)} = \frac{2}{3}\mathbb{1} - |D_4^{(2)}\rangle\langle D_4^{(2)}|$. The method in observation 1 gives the following decomposition for the projector

$$16|D_4^{(2)}\rangle\langle D_4^{(2)}| = \frac{2}{3}([x] + [x \pm \mathbb{1}] + [y] + [y \pm \mathbb{1}]) + \frac{1}{3}(8[z] - [z \pm \mathbb{1}] - [x \pm z] - [y \pm z])$$
$$+ \frac{1}{6}[x \pm y]. \tag{37}$$

The nine measurement settings are x, y, z, $x \pm y$, $x \pm z$ and $y \pm z$, shown also in figure 2(b). The list of witnesses presented in this section are given in the bottom part of table 1.

5. Conclusions

In summary, we presented general methods for constructing entanglement witnesses for detecting genuine multipartite entanglement in experiments. In particular, we considered projector-based witnesses and found efficient decompositions for them. Then, we constructed two- and three-setting witnesses for symmetric Dicke states that were based on the projector witness, as well as independent of the projector witness. We applied our methods to design witnesses for the recent experiment observing a six-qubit symmetric Dicke state with three excitations [32]. Our methods can be generalized for future experiments. As a first step, in appendix C we list some entanglement witnesses for systems with 5–10 qubits. Moreover, recent results on the symmetric tensor rank problem suggest that decompositions more efficient than the one in observation 1 are possible, however, they involve complex algorithms [45]. Thus, it would be interesting to look for better upper bounds for the number of settings used for symmetric operators.

15 **IOP** Institute of Physics Ⓓ DEUTSCHE PHYSIKALISCHE GESELLSCHAFT

Appendix A. Semidefinite programming used for obtaining witnesses

Here we summarize two optimization problems that are useful for designing entanglement witnesses and can be solved with semidefinite programming. Both tasks are related to designing witnesses that are easy to measure.

1. Semi-definite programming can be used to find the witness $\mathcal{W}$ with the largest noise tolerance as explained in the beginning of section 3.1.1. The corresponding task can be formulated as

$$\begin{aligned} \textbf{minimize} \quad & \sum_k c_k \text{Tr}(B_k \varrho_{\text{noise}}), \\ \textbf{subject to} \quad & \sum_k c_k \text{Tr}(B_k \varrho) = -1, \\ & \sum_k c_k B_k - \alpha \mathcal{W}^{(P)} \geqslant 0, \\ & \alpha > 0. \end{aligned} \tag{A.1}$$

Here ϱ is the state around which we detect entanglement. ϱ_{noise} is the noise, not necessarily white. The optimization is over α and the c_k's.

2. Semi-definite programming can be used to look for the maximum for PPT bipartite states. This gives an upper bound on the maximum for biseparable states. In many cases, the two coincide. The corresponding task can be formulated as a standard semidefinite program as

$$\begin{aligned} \textbf{minimize} \quad & -\text{Tr}(M\varrho), \\ \textbf{subject to} \quad & \varrho \geqslant 0, \\ & \text{Tr}(\varrho) = 1, \\ & \varrho^{T_A} \geqslant 0. \end{aligned} \tag{A.2}$$

Here T_A means partial transpose according to some groups of the qubits.

Appendix B. List of MATLAB subroutines

We summarize some of the MATLAB routines of the QUBIT4MATLAB 3.0 package that can be used for the calculations necessary for designing entanglement witnesses. A full list of the commands is given in [34].

The command `decompose` can be used to obtain a decomposition of a Hermitian operator into the sum of products of Pauli spin matrices. Moreover, `maxsep` and `maxsymsep` can be

used for getting the maximum for separable multi-qudit states and symmetric product states for a Hermitian operator, respectively. The command maxbisep gives the maximum for states that are biseparable with respect to some partitioning of the qubits. The command maxb gives the maximum for all possible bipartitions. All these commands look for the maximum with a simple optimization algorithm that is not guaranteed to find the global maximum, nevertheless, it typically does find it. overlapb gives the maximum overlap of a state $|\Psi\rangle$ and biseparable states. It can be used to construct entanglement witnesses of the type (6).

For semidefinite programming, we used SeDuMi [46] and YALMIP [47]. Two subroutines based on them are now in QUBIT4MATLAB 4.0[13]. The command optwitness looks for the best witness that can be composed linearly from a set of operators, while maxppt determines the maximum of an operator expectation value for states with a PPT for some bipartitioning of the qubits.

Appendix C. Witnesses for systems with 5–10 qubits

A three-setting witness based on the projector witness for the state $|D_8^{(4)}\rangle$ is given by

$$\mathcal{W}_{\mathrm{D}(8,4)}^{(P3)} := 1.3652 \cdot \mathbb{1} + \sum_{l=x,y,z} \sum_{n=1}^{4} c_{ln} J_l^{2n}, \tag{C.1}$$

with

$$\{c_{ln}\} = \begin{pmatrix} 0.0038612 & -0.0052555 & 0.0015016 & -0.00010726 \\ 0.0038612 & -0.0052555 & 0.0015016 & -0.000107266 \\ 3.124 & -1.07699 & 0.11916 & -0.0038992 \end{pmatrix}. \tag{C.2}$$

The noise tolerance for white noise is $p_{\mathrm{noise}} < 0.2578$. For larger N, we can use the ansatz

$$\mathcal{W}_{\mathrm{D}(N,N/2)}^{(P3)} := c_1 \cdot \mathbb{1} + c_{xy}\{(\sigma_x + \mathbb{1})^{\otimes N} + (\sigma_x - \mathbb{1})^{\otimes N} + (\sigma_y + \mathbb{1})^{\otimes N} + (\sigma_y - \mathbb{1})^{\otimes N}\} + \sum_{n=1}^{N/2} c_{zn} J_z^{2n}. \tag{C.3}$$

For $N = 10$, the optimal coefficients are $c_1 = 1.3115$, $c_{xy} = -0.0023069$, and $c_z = \{3.4681, -1.2624, 0.16494, -0.0084574, 0.000146551\}$. White noise is tolerated if $p_{\mathrm{noise}} < 0.2404$. The large noise-tolerance for the $N = 10$ case suggests that a robust three-setting witness for $|D_N^{(N/2)}\rangle$ might be constructed even for large N.

A three-setting witness independent of the projector witness for the N-qubit W state is given by (27) for $m = 1$. For $N = 5$, we have $c_5 = 5.6242$, $q_5 = 2.22$, and the witness tolerates white noise if $p_{\mathrm{noise}} < 0.0744$. For $N = 6$, we have $c_6 = 7.1095$, $q_6 = 3.13$, and noise is tolerated if $p_{\mathrm{noise}} < 0.0401$.

References

[1] For reviews see Horodecki R, Horodecki P, Horodecki M and Horodecki K 2009 *Rev. Mod. Phys.* **81** 865
Plenio M and Virmani S 2007 *Quantum Inf. Comput.* **7** 1
[2] Gühne O and Tóth G 2009 *Phys. Rep.* **474** 1
[3] Pan J W, Bouwmeester D, Daniell M, Weinfurter H and Zeilinger A 2000 *Nature* **403** 515

[13] http://www.mathworks.com/matlabcentral/fileexchange/8433.

[4] Bourennane M, Eibl M, Kurtsiefer C, Gaertner S, Weinfurter H, Gühne O, Hyllus Ph, Bruß D, Lewenstein M and Sanpera A 2004 *Phys. Rev. Lett.* **92** 087902

[5] Kiesel N, Schmid C, Weber U, Tóth G, Gühne O, Ursin R and Weinfurter H 2005 *Phys. Rev. Lett.* **95** 210502

[6] Kiesel N, Schmid C, Tóth G, Solano E and Weinfurter H 2007 *Phys. Rev. Lett.* **98** 063604

[7] Wieczorek W, Schmid C, Kiesel N, Pohlner R, Gühne O and Weinfurter H 2008 *Phys. Rev. Lett.* **101** 010503

[8] Lu C Y, Zhou X Q, Gühne O, Gao W B, Zhang J, Yuan Z S, Goebel A, Yang T and Pan J W 2007 *Nat. Phys.* **3** 91

[9] Gao W B, Lu C Y, Yao X C, Xu P, Gühne O, Goebel A, Chen Y A, Peng C Z, Chen Z B and Pan J W 2008 arXiv:0809.4277

[10] Sackett C A *et al* 2000 *Nature* **404** 256

[11] Leibfried D *et al* 2005 *Nature* **438** 639

[12] Häffner H *et al* 2005 *Nature* **438** 643

[13] Hald J, Sørensen J L, Schori C and Polzik E S 1999 *Phys. Rev. Lett.* **83** 1319

[14] Mandel O, Greiner M, Widera A, Rom T, Hänsch T and Bloch I 2003 *Nature* **425** 937

[15] Neumann P, Mizuochi N, Rempp F, Hemmer P, Watanabe H, Yamasaki S, Jacques V, Gaebel T, Jelezko F and Wrachtrup J 2008 *Science* **320** 1326

[16] Terhal B M 2002 *Theor. Comput. Sci.* **287** 313

[17] Lewenstein M, Kraus B, Cirac J I and Horodecki P 2000 *Phys. Rev.* A **62** 052310

[18] Gühne O, Hyllus P, Bruß D, Ekert A, Lewenstein M, Macchiavello C and Sanpera A 2002 *Phys. Rev.* A **66** 062305

[19] Gühne O, Hyllus P, Bruss D, Ekert A, Lewenstein M, Macchiavello C and Sanpera A 2003 *J. Mod. Opt.* **50** 1079

[20] Greenberger D M, Horne M A, Shimony A and Zeilinger A 1990 *Am. J. Phys.* **58** 1131

[21] Briegel H J and Raussendorf R 2001 *Phys. Rev. Lett.* **86** 910

[22] Tóth G and Gühne O 2005 *Phys. Rev. Lett.* **94** 060501

[23] Gühne O, Lu C Y, Gao W B and Pan J W 2007 *Phys. Rev.* A **76** 030305

[24] Doherty A C, Parrilo P A and Spedalieri F M 2002 *Phys. Rev. Lett.* **88** 187904
Doherty A C, Parrilo P A and Spedalieri F M 2004 *Phys. Rev.* A **69** 022308

[25] Brandão F G S L and Vianna R O 2004 *Phys. Rev. Lett.* **93** 220503

[26] Eisert J, Hyllus P, Gühne O and Curty M 2004 *Phys. Rev.* A **70** 062317

[27] Jafarizadeh M A, Najarbashi G and Habibian H 2007 *Phys. Rev.* A **75** 052326

[28] Hyllus P and Eisert J 2006 *New J. Phys.* **8** 51

[29] Wunderlich H and Plenio M B 2009 arXiv:0902.2093

[30] Dicke R H 1954 *Phys. Rev.* **93** 99

[31] Stockton J K, Geremia J M, Doherty A C and Mabuchi H 2003 *Phys. Rev.* A **67** 022112

[32] Wieczorek W, Krischek R, Kiesel N, Michelberger P, Tóth G and Weinfurter H 2009 *Phys. Rev. Lett.* **103** 020504

[33] Prevedel R, Cronenberg G, Tame M S, Paternostro M, Walther P, Kim M S and Zeilinger A 2009 *Phys. Rev. Lett.* **103** 020503
Campbell S, Tame M S and Paternostro M 2009 *New J. Phys.* **11** 073039

[34] Tóth G 2008 *Comput. Phys. Commun.* **179** 430

[35] Acín A, Bruß D, Lewenstein M and Sanpera A 2001 *Phys. Rev. Lett.* **87** 040401

[36] Gühne O 2004 *PhD Thesis* University of Hannover

[37] Tóth G 2007 *J. Opt. Soc. Am.* B **24** 275

[38] Peres A 1996 *Phys. Rev. Lett.* **77** 1413
Horodecki M, Horodecki P and Horodecki R 1996 *Phys. Lett.* A **223** 1

[39] Krammer P, Kampermann H, Bruss D, Bertlmann R A, Kwek L C and Macchiavello C 2009 arXiv:0904.3860

[40] Unanyan R G and Fleischhauer M 2003 *Phys. Rev. Lett.* **90** 133601

[41] Duan L M and Kimble H J 2003 *Phys. Rev. Lett.* **90** 253601

18

IOP Institute of Physics ⟨Φ⟩ DEUTSCHE PHYSIKALISCHE GESELLSCHAFT

[42] Thiel C, von Zanthier J, Bastin T, Solano E and Agarwal G S 2007 *Phys. Rev. Lett.* **99** 193602
[43] Stockton J K, van Handel R and Mabuchi H 2004 *Phys. Rev.* A **70** 022106
[44] Wieczorek W, Kiesel N, Schmid C and Weinfurter H 2009 *Phys. Rev.* A **79** 022311
[45] P Golub G, Lim L H and Mourrain B 2008 *SIAM J. Matrix Anal. Appl.* **30** 1254
[46] Sturm J *SeDuMi, a MATLAB Toolbox for Optimization Over Symmetric Cones* http://sedumi.mcmaster.ca.
[47] Löfberg J *Yalmip: A Toolbox for Modeling and Optimization in MATLAB* http://control.ee.ethz.ch/~joloef/yalmip.php.
[48] Keilmann T and Garcia-Ripoll J J 2008 *Phys. Rev. Lett.* **100** 110406

3.4 Permutationally invariant quantum state tomography

To obtain the complete information content of a quantum state full quantum state tomography has to be performed [58, 129]. To this aim, an arbitrary quantum state ρ of N qubits can always be decomposed in Pauli spin matrices $\hat{\sigma}_0 = \mathbb{1}, \hat{\sigma}_x, \hat{\sigma}_y$ and $\hat{\sigma}_z$ to

$$\rho = \frac{1}{2^N} \sum_{k_1, k_2 ..., k_N = \{0, x, y, z\}} T_{k_1, k_2, ..., k_N} \, \hat{\sigma}_{k_1} \otimes \hat{\sigma}_{k_2} \otimes ... \otimes \hat{\sigma}_{k_N} \tag{3.37}$$

with 4^N entries of the correlation tensor $T_{k_1, k_2, ..., k_N} \in \mathbb{R}$. To completely reconstruct the quantum state ρ, all entries of the correlation tensors have to be determined. This determines the number of required measurement settings. The correlation tensor can be calculated from the following expectation values

$$T_{k_1, k_2, ..., k_N} = \text{Tr}(\, \rho \, \hat{\sigma}_{k_1} \otimes \hat{\sigma}_{k_2} \otimes ... \otimes \hat{\sigma}_{k_N}). \tag{3.38}$$

Note that in the experiment projectors of the form $P_{x\pm} = \frac{1}{2}(\mathbb{1} \pm \hat{\sigma}_x)$, $P_{y\pm} = \frac{1}{2}(\mathbb{1} \pm \hat{\sigma}_y)$ or $P_{z\pm} = \frac{1}{2}(\mathbb{1} \pm \hat{\sigma}_z)$ are usually measured. How the correlations are deduced from the measured projectors is, for example, explained in Ref. [62]. The total number of the basis settings to be determined can even be reduced down to 3^N, because all correlations containing the identity $\hat{\sigma}_0 = \mathbb{1}$ can be calculated from the measured projectors containing only $\hat{\sigma}_x$, $\hat{\sigma}_y$ and $\hat{\sigma}_z$ operators [62]. However, to perform full quantum tomography 3^N basis settings have to be determined in the experiment and this means that the number of measurement settings scales exponentially with the number of qubits N.

Quantum state tomography has already been performed in several systems for different number of qubits. For example for superconducting qubits up to $N = 3$ [38, 39], for photons up to $N = 4$ [87] and for ions up to $N = 8$ [32]. For higher qubit numbers performing full tomography is experimentally challenging not only because of limited count rates but also because of the exponential scaling of the number of measurement settings, which is for $N = 10$ already 59049, increasing on the one hand the measurement time and on the other hand the computational effort to reconstruct the density matrix. In publication 3.3.2 [59] we propose a method reducing the measurement effort to only quadratically scaling with the number of qubits. To this aim we profit from the fact that the most prominent quantum states are permutationally invariant, like for example, the Greenberger Horne Zeilinger (GHZ) state [130, 53, 85, 131, 28] and all Dicke states [115, 87, 50, 90] which includes also the W state [132, 32]. Therefore we propose to determine the permutationally invariant part of our probe state ρ defined as

$$\rho_{PI} = \frac{1}{N!} \sum_k \Pi_k \rho \Pi_k \tag{3.39}$$

with Π_k are all possible permutations between each qubit with respect to another one[23]. How this reduces the number of settings is first exemplary shown for the case of a 3 qubit W state [132]

$$|W\rangle = \frac{1}{\sqrt{3}}(|100\rangle + |010\rangle + |001\rangle). \qquad (3.40)$$

Because of the permutation invariance of the W state, we do not have to measure all the Pauli spin operators $\hat{\sigma}_x$, $\hat{\sigma}_y$ and $\hat{\sigma}_z$ for each qubit, which would result for $N = 3$ in $3^3 = 27$ combinations, instead we need just to determine the permutationally invariant part of the 27 operators as well, resulting in 10 operators, for example, of the form

1. $$\hat{\sigma}_x \otimes \hat{\sigma}_x \otimes \hat{\sigma}_x$$
2. $$\hat{\sigma}_x \otimes \hat{\sigma}_x \otimes \hat{\sigma}_y = \hat{\sigma}_x \otimes \hat{\sigma}_y \otimes \hat{\sigma}_x = \hat{\sigma}_y \otimes \hat{\sigma}_x \otimes \hat{\sigma}_x$$
3. $$\hat{\sigma}_x \otimes \hat{\sigma}_x \otimes \hat{\sigma}_z = \hat{\sigma}_x \otimes \hat{\sigma}_z \otimes \hat{\sigma}_x = \hat{\sigma}_z \otimes \hat{\sigma}_x \otimes \hat{\sigma}_x$$
4. $$\hat{\sigma}_x \otimes \hat{\sigma}_y \otimes \hat{\sigma}_y = \hat{\sigma}_y \otimes \hat{\sigma}_x \otimes \hat{\sigma}_y = \hat{\sigma}_y \otimes \hat{\sigma}_y \otimes \hat{\sigma}_x$$
5. $$\hat{\sigma}_x \otimes \hat{\sigma}_z \otimes \hat{\sigma}_z = \hat{\sigma}_z \otimes \hat{\sigma}_x \otimes \hat{\sigma}_z = \hat{\sigma}_z \otimes \hat{\sigma}_z \otimes \hat{\sigma}_x$$
6. $$\hat{\sigma}_x \otimes \hat{\sigma}_y \otimes \hat{\sigma}_z = \hat{\sigma}_x \otimes \hat{\sigma}_z \otimes \hat{\sigma}_y = \hat{\sigma}_y \otimes \hat{\sigma}_x \otimes \hat{\sigma}_z = \hat{\sigma}_y \otimes \hat{\sigma}_z \otimes \hat{\sigma}_x = \hat{\sigma}_z \otimes \hat{\sigma}_y \otimes \hat{\sigma}_x = \hat{\sigma}_z \otimes \hat{\sigma}_x \otimes \hat{\sigma}_y$$
7. $$\hat{\sigma}_y \otimes \hat{\sigma}_y \otimes \hat{\sigma}_z = \hat{\sigma}_y \otimes \hat{\sigma}_z \otimes \hat{\sigma}_y = \hat{\sigma}_z \otimes \hat{\sigma}_y \otimes \hat{\sigma}_y$$
8. $$\hat{\sigma}_y \otimes \hat{\sigma}_z \otimes \hat{\sigma}_z = \hat{\sigma}_z \otimes \hat{\sigma}_y \otimes \hat{\sigma}_z = \hat{\sigma}_z \otimes \hat{\sigma}_z \otimes \hat{\sigma}_y$$
9. $$\hat{\sigma}_y \otimes \hat{\sigma}_y \otimes \hat{\sigma}_y$$
10. $$\hat{\sigma}_z \otimes \hat{\sigma}_z \otimes \hat{\sigma}_z.$$

For each line from 1 to 10 only one of the listed correlations has to be measured[24], because the others reveal for a permutationally invariant quantum state theoretically the same result.

To find a general formula how the number of settings for permutationally invariant quantum tomography scales with N qubits is a problem of combinatorial analysis. The question can be formulated as follows: How many ways exist to arrange $\hat{\sigma}_x$, $\hat{\sigma}_y$ and $\hat{\sigma}_z$ on N qubits without being able to distinguish between the Pauli spin operators of the same basis? This problem can be reduced to an arrangement of N operators (represented by dots) and 2 horizontal lines dividing the N operators into 3 groups as

$$\underbrace{\cdots \cdots}_{\hat{\sigma}_x^{\otimes k}} \Big| \underbrace{\cdots \cdots}_{\hat{\sigma}_y^{\otimes l}} \Big| \underbrace{\cdots \cdots}_{\hat{\sigma}_z^{\otimes m}} \qquad (3.41)$$

with $k+l+m = N$. All the operators on the left of the horizontal line correspond to $\hat{\sigma}_x$, in between the two horizontal lines correspond to $\hat{\sigma}_y$ and on the right to $\hat{\sigma}_z$ operators.

---

[23]Note, for a theoretically permutationally invariant quantum state $\rho_{th} = \rho_{PI}$ holds and for a experimental state which is supposed to be permutationally invariant, there exists always a (small) part which is not permutationally invariant $\rho_{exp} = \rho_{PI} + \rho_{notPI}$

[24]Note, that in principle 10 arbitrary directions can be measured, which will be introduced in the following

Now the question is how to arrange the group of N operators on $N + 2$ objects (2 horizontal lines with N dots), which is

$$\mathcal{D}_N = \binom{N+2}{N} = \frac{(N+2)!}{N!(N+2-N)!} = \frac{(N+2)(N+1)}{2} = \frac{1}{2}(N^2 + 3N + 2). \quad (3.42)$$

Now we see that we have reduced the measurement effort to only quadratically scaling with the number of qubits N for permutationally invariant quantum state tomography. In publication 3.4.1 [59] we have shown that it is not possible to reconstruct a permutationally invariant quantum state with fewer than $\mathcal{D}_N$ settings.

In principle, arbitrary directions on the Bloch sphere denoted by $\hat{A}_j^{\otimes N}$ can be measured to reconstruct the density matrix, because any permutationally invariant density operator can be written as a linear combination of the Pauli spin operators $\hat{\sigma}_x$, $\hat{\sigma}_y$, $\hat{\sigma}_z$ and $\mathbb{1}$. This implies that there are real coefficients $c_j^{(k,l,m)}$ with

$$\langle (\hat{\sigma}_x^{\otimes k} \otimes \hat{\sigma}_y^{\otimes l} \otimes \hat{\sigma}_z^{\otimes m} \otimes \mathbb{1}^{\otimes n})_{PI} \rangle = \sum_{j=1}^{\mathcal{D}_N} c_j^{(k,l,m)} \langle (\hat{A}_j^{\otimes (N-n)} \otimes \mathbb{1}^{\otimes n})_{PI} \rangle \quad (3.43)$$

and $(...)_{PI}$ denotes the sum of all permutations between each qubit divided by the number of permutations, like for example, $(\hat{\sigma}_x \otimes \hat{\sigma}_x \otimes \hat{\sigma}_x \otimes \mathbb{1})_{PI} = \frac{1}{4}(\hat{\sigma}_x \otimes \hat{\sigma}_x \otimes \hat{\sigma}_x \otimes \mathbb{1} + \hat{\sigma}_x \otimes \hat{\sigma}_x \otimes \mathbb{1} \otimes \hat{\sigma}_x + \hat{\sigma}_x \otimes \mathbb{1} \otimes \hat{\sigma}_x \otimes \hat{\sigma}_x + \mathbb{1} \otimes \hat{\sigma}_x \otimes \hat{\sigma}_x \otimes \hat{\sigma}_x)$. Finding the optimal coefficients $c_j^{(k,l,m)}$ with respect to ideal directions $\hat{A}_j^{\otimes N}$ is then a problem of numerical optimization. For example, in the previous case of the 3 qubit W state we have found 10 operators to determine the permutationally invariant part of our state, but we still do not know if the directions of these operators are optimal. A quantitative way to perform this optimization is to define a measure of statistical uncertainty in terms of variances (squared errors) of the correlation tensor entries[25] defined as (according to Eq. 3.43)

$$\mathcal{E}^2[(\hat{\sigma}_x^{\otimes k} \otimes \hat{\sigma}_y^{\otimes l} \otimes \hat{\sigma}_z^{\otimes m} \otimes \mathbb{1}^{\otimes n})_{PI}] = \sum_{j=1}^{\mathcal{D}_N} |c_j^{(k,l,m)}| \mathcal{E}^2[(\hat{A}_j^{\otimes (N-n)} \otimes \mathbb{1}^{\otimes n})_{PI}]. \quad (3.44)$$

Minimizing the sum of all variances

$$(\mathcal{E}_{\text{total}})^2 = \sum_{k+l+m+n=N} \mathcal{E}^2[(\hat{\sigma}_x^{\otimes k} \otimes \hat{\sigma}_y^{\otimes l} \otimes \hat{\sigma}_z^{\otimes m} \otimes \mathbb{1}^{\otimes n})_{PI}] \left(\frac{N!}{k!l!m!n!}\right) \quad (3.45)$$

leads iteratively to the coefficients $c_j^{(k,l,m)}$ for the optimal directions $\hat{A}_j$. The term with the factorials in Eq. 3.45 is the number of different permutations between $\hat{\sigma}_x^{\otimes k} \otimes \hat{\sigma}_y^{\otimes l} \otimes \hat{\sigma}_z^{\otimes m} \otimes \mathbb{1}^{\otimes n}$. Note that in practice the variances $\mathcal{E}^2[(\hat{A}_j^{\otimes (N-n)} \otimes \mathbb{1}^{\otimes n})_{PI}]$ depend on the physical implementation and, for example, for photons Poissonian distributed counts are assumed (for details see publication 3.4.1 [59])

---

[25]which have an analogy to Bloch vector elements, because every operator can be written as a linear combination of the Pauli spin matrices, as $\hat{A}_j = a_x \hat{\sigma}_x + a_y \hat{\sigma}_y + a_z \hat{\sigma}_z$ with $a_x^2 + a_y^2 + a_z^2 = 1$ and the point (a_x, a_y, a_z) is an entry of the Bloch unit sphere (see Fig. 2.1)
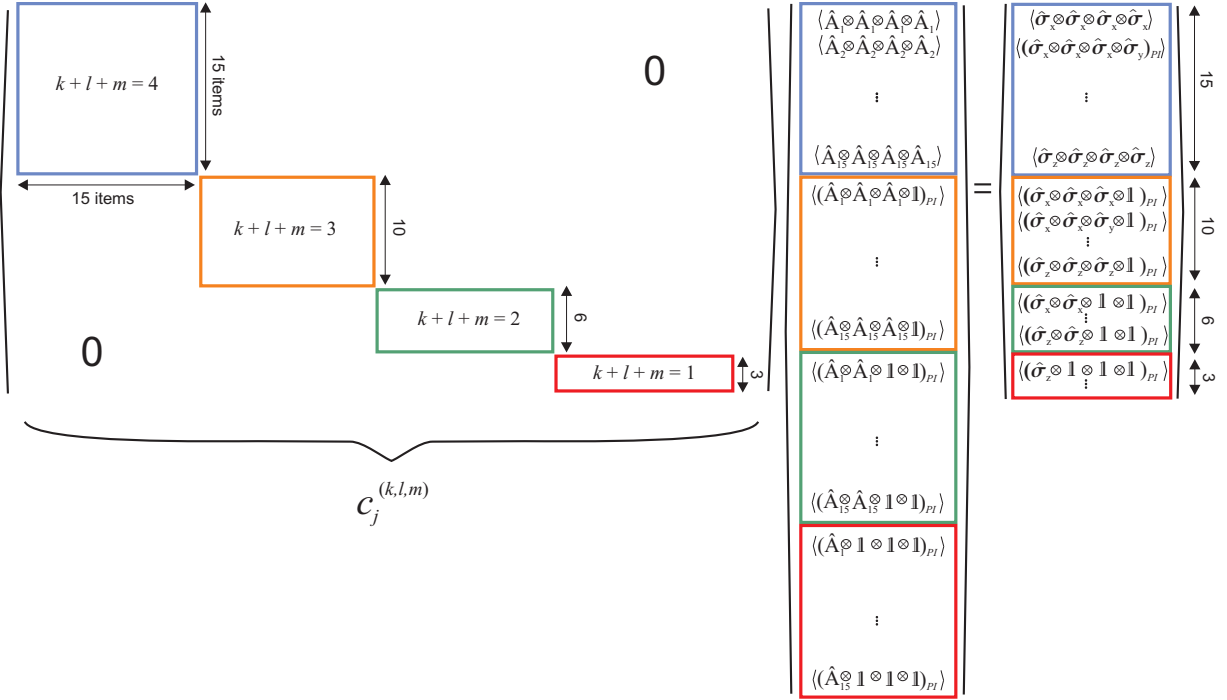
Figure 3.7: **Schematic of how to calculate the permutationally invariant Pauli spin operators decomposition**. Exemplary for $N = 4$ Eq. 3.43 is illustrated with real coefficients $c_j^{(k,l,m)}$ and 15 arbitrary chosen measurement directions $\hat{A}_j$ out of which the entries of the permutationally invariant Pauli spin operators decomposition $\langle(\hat{\sigma}_x^{\otimes k} \otimes \hat{\sigma}_y^{\otimes l} \otimes \hat{\sigma}_z^{\otimes m} \otimes \mathbb{1}^{\otimes n})_{PI}\rangle$ can be calculated.

As an illustration, Fig. 3.7 shows exemplary for the case of $N = 4$ how to reconstruct the entries of the permutationally invariant correlations (in the Pauli spin operators decomposition) out of the experimentally measured correlations $\hat{A}_j^{\otimes N}$ via the coefficients $c_j^{(k,l,m)}$.

Finally, ρ_{PI} calculates to

$$\rho_{PI} = \frac{1}{2^N} \sum_{k_1,k_2...,k_N=\{0,x,y,z\}} T^{PI}_{k_1,k_2,...,k_N} (\hat{\sigma}_{k_1} \otimes \hat{\sigma}_{k_2} \otimes ... \otimes \hat{\sigma}_{k_N})_{PI} \qquad (3.46)$$

with

$$T^{PI}_{k_1,k_2,...,k_N} = \text{Tr}(\rho_{PI} (\hat{\sigma}_{k_1} \otimes \hat{\sigma}_{k_2} \otimes ... \otimes \hat{\sigma}_{k_N})_{PI}). \qquad (3.47)$$

In publication 3.4.1 [59] the method described above is demonstrated in a proof of principle experiment for a four photon symmetric Dicke state with two excitations [87]. To this aim, full quantum tomography and permutationally invariant quantum tomography are performed and compared, achieving an overlap of 94.7%, which shows the

applicabiliy of permutationally invariant quantum state tomography for future characterisations of quantum states.

3.4.1 Publication: Permutationally invariant quantum state tomography

Permutationally Invariant Quantum Tomography

G. Tóth,[1,2,3] W. Wieczorek,[4,5,*] D. Gross,[6] R. Krischek,[4,5] C. Schwemmer,[4,5] and H. Weinfurter[4,5]

[1]*Department of Theoretical Physics, The University of the Basque Country, P.O. Box 644, E-48080 Bilbao, Spain*
[2]*IKERBASQUE, Basque Foundation for Science, E-48011 Bilbao, Spain*
[3]*Research Institute for Solid State Physics and Optics, Hungarian Academy of Sciences, P.O. Box 49, H-1525 Budapest, Hungary*
[4]*Max-Planck-Institut für Quantenoptik, Hans-Kopfermann-Strasse 1, D-85748 Garching, Germany*
[5]*Fakultät für Physik, Ludwig-Maximilians-Universität, D-80797 München, Germany*
[6]*Institute for Theoretical Physics, Leibniz University Hannover, D-30167 Hannover, Germany*
(Received 4 June 2010; revised manuscript received 30 August 2010; published 16 December 2010)

We present a scalable method for the tomography of large multiqubit quantum registers. It acquires information about the permutationally invariant part of the density operator, which is a good approximation to the true state in many relevant cases. Our method gives the best measurement strategy to minimize the experimental effort as well as the uncertainties of the reconstructed density matrix. We apply our method to the experimental tomography of a photonic four-qubit symmetric Dicke state.

Because of the rapid development of quantum experiments, it is now possible to create highly entangled multiqubit states using photons [1–5], trapped ions [6], and cold atoms [7]. So far, the largest implementations that allow for an individual readout of the particles involve on the order of 10 qubits. This number will soon be overcome, for example, by using several degrees of freedom within each particle to store quantum information [8]. Thus, a new regime will be reached in which a complete state tomography is impossible even from the point of view of the storage place needed on a classical computer. At this point the question arises: Can we still extract useful information about the quantum state created?

In this Letter we propose permutationally invariant (PI) tomography in multiqubit quantum experiments [9]. Concretely, instead of the density matrix ϱ, we propose to determine the PI part of the density matrix defined as

$$\varrho_{\mathrm{PI}} = \frac{1}{N!} \sum_k \Pi_k \varrho \Pi_k, \qquad (1)$$

where Π_k are all the permutations of the qubits. Reconstructing ϱ_{PI} has been considered theoretically for spin systems (see, e.g., Ref. [10]). Recently it has been pointed out that photons in a single mode optical fiber will always be in a PI state and that there is only a small set of measurements needed for their characterization [11,12].

Here, we develop a provably optimal scheme, which is feasible for large multiqubit systems: For our method, the measurement effort increases only quadratically with the size of the system. Our approach is further motivated by the fact that almost all multipartite experiments are done with PI quantum states [2–4,6]. Thus, the density matrix obtained from PI tomography is expected to be close to the one of the experimentally achieved state. The expectation values of symmetric operators, such as some entanglement witnesses, and fidelities with respect to symmetric states are the same

for both density matrices and are thus obtained exactly from PI tomography [2–4]. Finally, if ϱ_{PI} is entangled, so is the state ϱ of the system, which makes PI tomography a useful and efficient tool for entanglement detection.

Below, we summarize the four main contributions of this Letter. We restrict our attention to the case of N qubits—higher-dimensional systems can be treated similarly.

(1) In most experiments, the qubits can be individually addressed whereas nonlocal quantities cannot be measured directly. The experimental effort is then characterized by the number of local measurement settings needed, where "setting" refers to the choice of one observable per qubit, and repeated von Neumann measurements in the observables' eigenbases [13]. Here, we compute the minimal number of measurement settings required to recover ϱ_{PI}.

(2) The requirement that the number of settings be minimal does not uniquely specify the tomographic protocol. On the one hand, there are infinitely many possible choices for the local settings that are both minimal and give sufficient information to find ϱ_{PI}. On the other hand, for each given setting, there are many ways of estimating the unknown density operator from the collected data. We present a systematic method to find the optimal scheme through statistical error analysis.

(3) Next, we turn to the important problem of gauging the information loss incurred due to restricting attention to the PI part of the density matrix. We describe an easy test measurement that can be used to judge the applicability of PI tomography before it is implemented.

(4) Finally, we demonstrate that these techniques are viable in practice by applying them to a photonic experiment observing a four-qubit symmetric Dicke state.

Minimizing the number of settings.—We will now present our first main result.

Observation 1.   For a system of N qubits, permutationally invariant tomography can be performed with

3.4. PERMUTATIONALLY INVARIANT QUANTUM STATE TOMOGRAPHY

$$\mathcal{D}_N = \binom{N+2}{N} = \frac{1}{2}(N^2 + 3N + 2) \qquad (2)$$

local settings. It is not possible to perform such a tomography with fewer settings.

Proof.—First, we need to understand the information obtainable from a single measurement setting. We assume that for every given setting, the same basis is measured at every site [14]. Measuring a local basis $\{|\phi_1\rangle, |\phi_2\rangle\}$ is equivalent to estimating the expectation value of the traceless operator $A = |\phi_1\rangle\langle\phi_1| - |\phi_2\rangle\langle\phi_2|$. Merely by measuring $A^{\otimes N}$, it is possible to obtain all the N expectation values

$$\langle (A^{\otimes(N-n)} \otimes \mathbb{1}^{\otimes n})_{\mathrm{PI}}\rangle, \qquad (n = 0, \ldots, N-1), \quad (3)$$

and, conversely, that is all the information obtainable about ϱ_{PI} from a single setting.

Next, we will use the fact that any PI density operator can be written as a linear combination of the pairwise orthogonal operators $(X^{\otimes k} \otimes Y^{\otimes l} \otimes Z^{\otimes m} \otimes \mathbb{1}^{\otimes n})_{\mathrm{PI}}$, where X, Y, and Z are the Pauli matrices. We consider the space spanned by these operators for one specific value of n. Simple counting shows that its dimension is $\mathcal{D}_{(N-n)}$. The same space is spanned by $\mathcal{D}_{(N-n)}$ generic operators of the type $(A^{\otimes(N-n)} \otimes \mathbb{1}^{\otimes n})_{\mathrm{PI}}$. We draw two conclusions: First, any setting gives at most one expectation value for every such space. Hence the number of settings cannot be smaller than the largest dimension, which is $\mathcal{D}_N$. Second, a generic choice of $\mathcal{D}_N$ settings is sufficient to recover the correlations in each of these spaces, and hence completely characterizes ϱ_{PI}. This concludes the proof [15].

The proof implies that there are real coefficients $c_j^{(k,l,m)}$ such that

$$\langle (X^{\otimes k} \otimes Y^{\otimes l} \otimes Z^{\otimes m} \otimes \mathbb{1}^{\otimes n})_{\mathrm{PI}}\rangle$$
$$= \sum_{j=1}^{\mathcal{D}_N} c_j^{(k,l,m)} \langle (A_j^{\otimes(N-n)} \otimes \mathbb{1}^{\otimes n})_{\mathrm{PI}}\rangle. \quad (4)$$

We will refer to the numbers on the left-hand side of Eq. (4) as the elements of the generalized Bloch vector. The expectation values on the right-hand side can be obtained by measuring the settings with A_j for $j = 1, 2, \ldots, \mathcal{D}_N$.

Minimizing uncertainties.—We now have to determine the optimal scheme for PI tomography. To this end, we define our measure of statistical uncertainty as the sum of the variances of all the Bloch vector elements

$$(\mathcal{E}_{\mathrm{total}})^2 = \sum_{k+l+m+n=N} \mathcal{E}^2[(X^{\otimes k} \otimes Y^{\otimes l} \otimes Z^{\otimes m} \otimes \mathbb{1}^{\otimes n})_{\mathrm{PI}}]$$
$$\times \left(\frac{N!}{k!l!m!n!}\right), \quad (5)$$

where the term with the factorials is the number of different permutations of $X^{\otimes k} \otimes Y^{\otimes l} \otimes Z^{\otimes m} \otimes \mathbb{1}^{\otimes n}$. Based on Eq. (4), the variance of a single Bloch vector element is

$$\mathcal{E}^2[(X^{\otimes k} \otimes Y^{\otimes l} \otimes Z^{\otimes m} \otimes \mathbb{1}^{\otimes n})_{\mathrm{PI}}]$$
$$= \sum_{j=1}^{\mathcal{D}_N} |c_j^{(k,l,m)}|^2 \mathcal{E}^2[(A_j^{\otimes(N-n)} \otimes \mathbb{1}^{\otimes n})_{\mathrm{PI}}]. \quad (6)$$

Equation (5) can be minimized by changing the A_j matrices and the $c_j^{(k,l,m)}$ coefficients. We consider the coefficients first. For any Bloch vector element, finding $c_j^{(k,l,m)}$'s that minimize the variance Eq. (6) subject to the constraint that equality holds in Eq. (4) is a least squares problem. It has an analytic solution obtained as follows: Write the operator on the left-hand side of Eq. (6) as a vector $\vec{v}$ (with respect to some basis). Likewise, write the operators on the right-hand side as $\vec{v}_j$ and define a matrix $V = [\vec{v}_1, \vec{v}_2, \ldots, \vec{v}_{\mathcal{D}_N}]$. Then Eq. (4) can be cast into the form $\vec{v} = V\vec{c}$, where $\vec{c}$ is a vector of the $c_j^{(k,l,m)}$ values for given (k, l, m). If E is the diagonal matrix with entries $E_{j,j}^2 = \mathcal{E}^2[(A_j^{\otimes(N-n)} \otimes \mathbb{1}^{\otimes n})_{\mathrm{PI}}]$, then the optimal solution is $\vec{c} = E^{-2}V^T(VE^{-2}V^T)^{-1}\vec{v}$, where the inverse is taken over the range [16].

Equipped with a method for obtaining the optimal $c_j^{(k,l,m)}$'s for every fixed set of observables A_j, it remains to find the best settings to measure. Every qubit observable can be defined by the measurement directions $\vec{a}_j$ using $A_j = a_{j,x}X + a_{j,y}Y + a_{j,z}Z$. Thus, the task is to identify $\mathcal{D}_N$ measurement directions on the Bloch sphere minimizing the variance. In general, finding the globally optimal solution of high-dimensional problems is difficult. In our case, however, $\mathcal{E}_{\mathrm{total}}$ seems to penalize an inhomogeneous distribution of the $\vec{a}_j$ vectors; thus, using evenly distributed vectors as an initial guess, usual minimization procedures can be used to decrease $\mathcal{E}_{\mathrm{total}}$ and obtain satisfactory results [16].

The variance $\mathcal{E}^2[(A_j^{\otimes(N-n)} \otimes \mathbb{1}^{\otimes n})_{\mathrm{PI}}]$ of the observed quantities depends on the physical implementation. In the photonic setup below, we assume Poissonian distributed counts. It follows that (see also Refs. [17,18])

$$\mathcal{E}^2[(A_j^{\otimes(N-n)} \otimes \mathbb{1}^{\otimes n})_{\mathrm{PI}}] = \frac{[\Delta(A_j^{\otimes(N-n)} \otimes \mathbb{1}^{\otimes n})_{\mathrm{PI}}]_{\varrho_0}^2}{\lambda_j - 1}, \quad (7)$$

where $(\Delta A)_\varrho^2 = \langle A^2\rangle_\varrho - \langle A\rangle_\varrho^2$, ϱ_0 is the state of the system, and λ_j is the parameter of the Poissonian distribution, which equals the expected value of the total number of counts for the setting j. The variance depends on the unknown state. If we have preliminary knowledge of the likely form of ϱ_0, we should use that information in the optimization. Otherwise, ϱ_0 can be set to the completely mixed state. For the latter, straightforward calculation shows that $\mathcal{E}^2[(A_j^{\otimes(N-n)} \otimes \mathbb{1}^{\otimes n})_{\mathrm{PI}}] = \binom{N}{n}^{-1}/(\lambda_j - 1)$. For another implementation, such as trapped ions, our scheme for PI tomography can be used after replacing Eq. (7) by a formula giving the variance for that implementation.

Estimating the information loss due to symmetrization.—It is important to know how close the PI quantum state is to the state of the system as PI tomography should

serve as an alternative of full state tomography for experiments aiming at the preparation of PI states.

Observation 2. The fidelity between the original state and the permutationally invariant state, $F(\varrho, \varrho_{PI})$, can be estimated from below as $F(\varrho, \varrho_{PI}) \geq \langle P_s \rangle_\varrho^2$, where $P_s = \sum_{n=0}^{N} |D_N^{(n)}\rangle\langle D_N^{(n)}|$ is the projector to the N-qubit symmetric subspace, and the symmetric Dicke state is defined as $|D_N^{(n)}\rangle = \binom{N}{n}^{-1/2} \sum_k \mathcal{P}_k(|0\rangle^{\otimes(N-n)} \otimes |1\rangle^{\otimes n})$, where the summation is over all the different permutations of the qubits. Observation 2 can be proved based on Ref. [19] and elementary matrix manipulations. Note that Observation 2 makes it possible to estimate $F(\varrho, \varrho_{PI})$ based on knowing only ϱ_{PI}.

Lower bounds on the fidelity to symmetric Dicke states, i.e., $\mathrm{Tr}(|D_N^{(n)}\rangle\langle D_N^{(n)}|\varrho)$ can efficiently be obtained by measuring X, Y, and Z on all qubits, i.e., measuring only three local settings independent of N [20]. With the same measurements, one can also obtain a lower bound on the overlap between the state and the symmetric subspace. For four qubits, this can be done based on $P_s \geq [(J_x^4 + J_y^4 + J_z^4) - (J_x^2 + J_y^2 + J_z^2)]/18$, where $J_x = (1/2)\sum_k X_k$, $J_y = (1/2)\sum_k Y_k$, etc. Operators for estimating $\langle P_s \rangle$ for $N = 6, 8$ are given in Ref. [16]. This allows one to judge how suitable the quantum state is for PI tomography before such a tomography is carried out.

Experimental results.—We demonstrate the method and the benefits of our algorithm for PI tomography for a four-qubit symmetric Dicke state with two excitations $|D_4^{(2)}\rangle$. First, we optimize the $\vec{a}_j$'s and the $c_j^{(k,l,m)}$'s for $\varrho_0 = \mathbb{1}/16$ and only for the uncertainty of full four-qubit correlation terms, which means that when computing $\mathcal{E}_{total}$, we carry out the summation in Eq. (5) only for the terms with $n = 0$. With simple numerical optimization, we were looking for the set of A_j basis matrices that minimize the uncertainty of the full correlation terms. Then, we also looked for the basis matrices that minimize the sum of the squared error of all the Bloch vector elements and considered also density matrices different from white noise, such as a pure Dicke state mixed with noise. We find that the gain in terms of decreasing the uncertainties is negligible in our case and that it is sufficient to optimize for $\varrho_0 = \mathbb{1}/16$ and for the full correlation terms. To demonstrate the benefits of the optimization of the measurement directions, we also compare the results with those obtained with randomly distributed basis matrices.

The Dicke state was observed in a photonic system. Essentially, four photons emitted by the second-order collinear type-II spontaneous parametric down-conversion process were symmetrically distributed into four spatial modes. Upon detection of one photon from each of the outputs, the state $|D_4^{(2)}\rangle$ is observed. Polarization analysis in each mode is used to characterize the experimentally observed state. We collected data for each setting for 5 min, with an average count rate of 410 per minute. The experimental setup has been described in detail in Refs. [2,3].

First, to check the applicability of the PI tomography, we apply our tools described above requiring only the

measurement of the three settings, $X^{\otimes 4}$, $Y^{\otimes 4}$, and $Z^{\otimes 4}$. We determine the expectation value of the projector to the symmetric subspace, yielding $\langle P_s \rangle \geq 0.905 \pm 0.015$. Based on Observation 2, we obtain $F(\varrho, \varrho_{PI}) \geq 0.819 \pm 0.028$. These results show that the state is close to be PI and has a large overlap with the symmetric subspace. Thus, it makes sense to apply PI tomography.

For PI tomography of a four-qubit system, the measurement of 15 settings is needed. We used Eq. (4) to obtain the Bloch vector elements from the experimentally measured quantities. This way, we could obtain all the 34 symmetric correlations of the form $(X^{\otimes k} \otimes Y^{\otimes l} \otimes Z^{\otimes m} \otimes \mathbb{1}^{\otimes n})_{PI}$. In Fig. 1, we give the values of the correlations for optimized and for randomly chosen measurement directions, compared to the results obtained from full tomography, which needed 81 measurement settings. As can be seen in Fig. 1, the uncertainty for the optimized settings is considerably smaller than the one for the randomly chosen settings. Moreover, the results from the optimized settings fit very well the results of the full tomography. In Fig. 2, we compare the density matrices obtained from full tomography [Fig. 2(a)], from PI tomography for optimized [Fig. 2(b)], and for random measurement directions [Fig. 2(c)]. Because of noise, the fidelity of the result of the full tomography with respect to $|D_4^{(2)}\rangle$ is 0.873 ± 0.005, which is similar to the fidelity of the results of the PI tomography with optimized settings, 0.852 ± 0.009 [21]. In contrast, for the method using random measurement directions, the fidelity is 0.814 ± 0.059, for which the
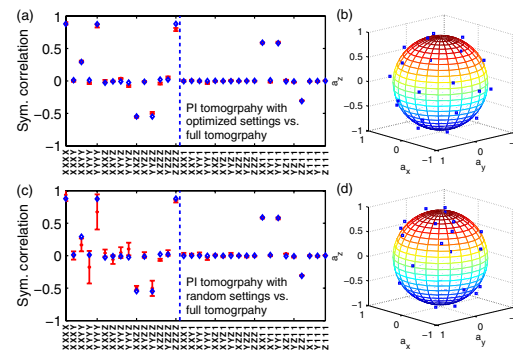
FIG. 1 (color online). (a) Comparison of the 34 symmetrized correlations coming from (crosses with error bars) 15 permutationally invariant measurement settings with optimized A_j matrices for $N = 4$ qubits and (diamonds) from full tomography requiring 81 local settings. The average uncertainty of all symmetrized correlations obtained from full tomography is ± 0.022, and is not shown in the figure. The labels refer to symmetrized correlations of the form given in the left-hand side of Eq. (4). The results corresponding to the 15 full four-qubit correlations are left from the vertical dashed line. (b) Measurement directions. A point at (a_x, a_y, a_z) corresponds to measuring operator $a_x X + a_y Y + a_z Z$. (c) Results for randomly chosen A_j matrices and (d) corresponding measurement directions.
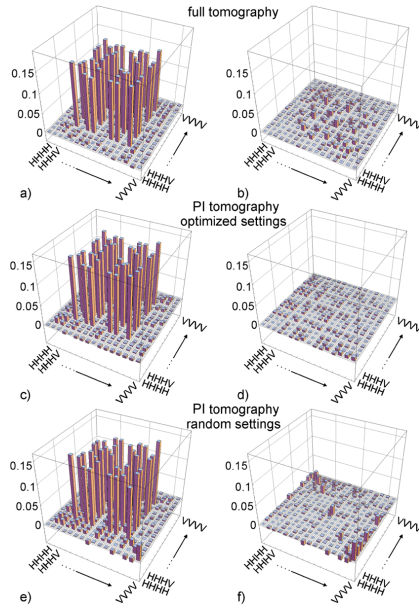
FIG. 2 (color online). (a) The real and (b) imaginary parts of the density matrix coming from full tomography. (c),(d) The same for permutationally invariant tomography with optimized and (e),(f) random measurement directions, respectively.

uncertainty is the largest compared to all previous fidelity values. Finally, we also computed the fidelity of the results with respect to the PI density matrix obtained from full tomography [22]. The results of the PI tomography with optimized settings show a good agreement with full tomography: the fidelity is 0.947, which is quite close to the fidelity between the results of full tomography and its PI part, 0.964. On the other hand, for the PI tomography with random settings the corresponding fidelity is much lower, 0.880. Overall, the PI tomography shows a good agreement with the full tomography for this particular experiment. However, a reasonable choice of measurement directions is needed to obtain uncertainties in the reconstructed Bloch vector elements similar to the ones from full tomography.

Finally, let us comment on how our method can be extended to lager systems. Permutationally invariant operators can be represented efficiently on a digital computer in the basis of $(X^{\otimes k} \otimes Y^{\otimes l} \otimes Z^{\otimes m} \otimes \mathbb{1}^{\otimes n})_{\mathrm{PI}}$ operators. We determined the optimal A_j operators for PI tomography for systems with $N = 6, 8, \ldots, 14$ qubits. To have the same maximum uncertainty of the Bloch vector elements as for the $N = 4$ case, one has to increase the counts per setting by less than 50% [16].

In summary, we presented a scalable method for permutationally invariant tomography, which can be used in place of full state tomography in experiments that aim at preparing permutationally invariant many-qubit states. For our approach, the same operator has to be measured on all qubits,

which is a clear advantage in some experiments. We showed how to choose the measurements such that the uncertainty in the reconstructed density matrix is the smallest possible. This paves the way of characterizing permutationally invariant states of many qubits in various physical systems. Moreover, this work also shows that, given some knowledge or justifiable assumptions, there is a way to obtain scalable state tomography for multiqubit entangled states.

*Present address: Faculty of Physics, University of Vienna, Boltzmanngasse 5, A-1090 Wien, Austria.

[1] J.-W. Pan *et al.*, Nature (London) **403**, 515 (2000); M. Bourennane *et al.*, Phys. Rev. Lett. **92**, 087902 (2004); N. Kiesel *et al.*, *ibid.* **95**, 210502 (2005).

[2] N. Kiesel *et al.*, Phys. Rev. Lett. **98**, 063604 (2007).

[3] W. Wieczorek *et al.*, Phys. Rev. Lett. **103**, 020504 (2009); R. Krischek *et al.*, Nat. Photon. **4**, 170 (2010).

[4] R. Prevedel *et al.*, Phys. Rev. Lett. **103**, 020503 (2009).

[5] W. Wieczorek *et al.*, Phys. Rev. Lett. **101**, 010503 (2008).

[6] C. A. Sackett *et al.*, Nature (London) **404**, 256 (2000); H. Häffner *et al.*, Nature (London) **438**, 643 (2005).

[7] O. Mandel *et al.*, Nature (London) **425**, 937 (2003).

[8] C. Cinelli *et al.*, Phys. Rev. Lett. **95**, 240405 (2005); G. Vallone *et al.*, *ibid.* **98**, 180502 (2007); W.-B. Gao *et al.*, Nature Phys. **6**, 331 (2010).

[9] For other approaches see D. Gross *et al.*, Phys. Rev. Lett. **105**, 150401 (2010); M. Cramer and M. B. Plenio, arXiv:1002.3780; S. T. Flammia *et al.*, arXiv:1002.3839; O. Landon-Cardinal *et al.*, arXiv:1002.4632.

[10] G. M. D'Ariano *et al.*, J. Opt. B **5**, 77 (2003).

[11] R. B. A. Adamson *et al.*, Phys. Rev. Lett. **98**, 043601 (2007).

[12] L. K. Shalm *et al.*, Nature (London) **457**, 67 (2009).

[13] O. Gühne and G. Tóth, Phys. Rep. **474**, 1 (2009).

[14] Otherwise more than $\mathcal{D}_N$ settings are necessary [16].

[15] This is connected to a general idea: It is expected that the determination of an operator within a subspace whose dimension depends polynomially on N needs a number of settings increasing also polynomially with N.

[16] See supplementary material at http://link.aps.org/supplemental/10.1103/PhysRevLett.105.250403 for additional derivations and experimental results.

[17] C. Schmid, Ph.D. thesis, Ludwig-Maximillian-Universität, 2008; D. F. V. James *et al.*, Phys. Rev. A **64**, 052312 (2001).

[18] B. Jungnitsch *et al.*, Phys. Rev. Lett. **104**, 210401 (2010).

[19] J. A. Miszczak *et al.*, Quantum Inf. Comput. **9**, 0103 (2009).

[20] G. Tóth *et al.*, New J. Phys. **11**, 083002 (2009).

[21] Expectation values are obtained directly from the measured data, rather than from ρ_{PI}.

[22] Values without error are deduced from fitted matrices obtained via maximum likelihood estimation [17].

Permutationally Invariant Quantum Tomography - Supplementary Material

Géza Tóth,[1,2,3] Witlef Wieczorek,[4,5,*] David Gross,[6] Roland Krischek,[4,5] Christian Schwemmer,[4,5] and Harald Weinfurter[4,5]

[1]*Department of Theoretical Physics, The University of the Basque Country, P.O. Box 644, E-48080 Bilbao, Spain*
[2]*IKERBASQUE, Basque Foundation for Science, E-48011 Bilbao, Spain*
[3]*Research Institute for Solid State Physics and Optics,
Hungarian Academy of Sciences, P.O. Box 49, H-1525 Budapest, Hungary*
[4]*Max-Planck-Institut für Quantenoptik, Hans-Kopfermann-Strasse 1, D-85748 Garching, Germany*
[5]*Fakultät für Physik, Ludwig-Maximilians-Universität, D-80797 München, Germany*
[6]*Institute for Theoretical Physics, Leibniz University Hannover, D-30167 Hannover, Germany*
(Dated: December 23, 2010)

The supplement contains some derivations to help to understand the details of the proofs of the main text. It
also contains some additional experimental results.

Proof of that we have to measure the same operator on all qubits. From the proof of Observation 1, we know that at least $\mathcal{D}_N$ measurements are needed to get the expectation values of all the $\mathcal{D}_N$ independent symmetric full N-particle correlations. What if we measure $\mathcal{D}_N$ settings, but several of them are not $\{A_j, A_j, ..., A_j\}$-type, but $\{A_j^{(1)}, A_j^{(2)}, ..., A_j^{(N)}\}$-type, i.e., we do not measure the same operator on all qubits? Each setting makes it possible to get a single operator containing full N-qubit correlations. Let us denote this operator by M_k for $k = 1, 2, ..., \mathcal{D}_N$. Then, we know the expectation value of any operator of the space defined by the M_k operators. However, not all M_k's are permutationally invariant. Thus, the size of the PI subspace of the space of the M_k operators is less than $\mathcal{D}_N$. We do not have $\mathcal{D}_N$ linearly independent symmetric operators in this space. Thus, $\mathcal{D}_N$ measurement settings are sufficient to measure ϱ_{PI} only if we have settings of the type $\{A_j, A_j, ..., A_j\}$.

Derivation of Eq. (7). The eigen-decomposition of the correlation term is

$$(A_j^{\otimes(N-n)} \otimes \mathbb{1}^{\otimes n})_{\mathrm{PI}} = \sum_k \Lambda_{j,n,k}|\Phi_{j,k}\rangle\langle\Phi_{j,k}|. \quad (S1)$$

The individual counts $N_C(A_j)_k$ follow a Poissonian distribution $f(n_c, \lambda_{j,k})$, where $\lambda_{j,k}$ are the parameters of the Poissonian distributions and $\sum_k \lambda_{j,k} = \lambda_j$. The conditional variance, knowing that the total count is $N_C(A_j)$, is

$$\mathcal{E}^2[(A_j^{\otimes(N-n)}\otimes\mathbb{1}^{\otimes n})_{\mathrm{PI}}|N_C(A_j)] = \frac{[\Delta(A_j^{\otimes(N-n)} \otimes \mathbb{1}^{\otimes n})_{\mathrm{PI}}]^2}{N_C(A_j)}. \quad (S2)$$

After straightforward algebra, the variance is obtained as

$$\begin{aligned}
&\mathcal{E}^2[(A_j^{\otimes(N-n)} \otimes \mathbb{1}^{\otimes n})_{\mathrm{PI}}] \\
&= \sum_m f(m, \lambda_j)\mathcal{E}^2[(A_j^{\otimes(N-n)} \otimes \mathbb{1}^{\otimes n})_{\mathrm{PI}}|N_C(A_j) = m] \\
&= \frac{[\Delta(A_j^{\otimes(N-n)} \otimes \mathbb{1}^{\otimes n})_{\mathrm{PI}}]^2}{\lambda_j - 1}. \quad (S3)
\end{aligned}$$

Similar results can be obtained through assuming Poissonian measurement statistics and Gaussian error propagation

[S1, S2]. If $\varrho_0 = \mathbb{1}/2^N$, then $\Delta(A_j^{\otimes(N-n)} \otimes \mathbb{1}^{\otimes n})_{\mathrm{PI}}$ is independent from the choice of A_j. By substituting $A_j = Z$, straightforward calculations gives

$$\mathcal{E}^2[(A_j^{\otimes(N-n)} \otimes \mathbb{1}^{\otimes n})_{\mathrm{PI}}] = \frac{\binom{N}{n}^{-1}}{\lambda_j - 1}. \quad (S4)$$

Obtaining the formula for $c_j^{(k,l,m)}$ for the smallest error.
We look for $c_j^{(k,l,m)}$ for which the squared uncertainty given in Eq. (6) is the smallest. In the following, we use the definition given in the main text for $\vec{c}, \vec{v}, V$ and E. Thus, V is matrix mapping a large space $\mathbb{R}^l$ to a small space $\mathbb{R}^s$. Let E be a non-singular diagonal matrix in the small space. We have to solve

$$\min_{\vec{c}} \|E\vec{c}\|^2 \qquad \text{s.t.} \qquad V\vec{c} = \vec{v}, \quad (S5)$$

where $||\vec{a}||$ is the Euclidean norm of $\vec{a}$. Using Lagrangian multipliers, we write down the condition for a minimum fulfilling the constraints $V\vec{c} = \vec{v}$

$$\nabla_{\vec{c}}\Big\{\vec{c}^T E^2\vec{c} + \sum_{i=1}^s \lambda_i\big[(V\vec{c})_i - w_i\big]\Big\} = 0. \quad (S6)$$

Hence, the condition for a local (and, due to convexity, global) minimum is

$$\vec{c} = \frac{1}{2}E^{-2}V^T\vec{\lambda}, \quad (S7)$$

where $\lambda \in \mathbb{R}^s$ is the vector of multipliers. In other words, we have a minimum if and only if $\vec{c} \in \text{range } E^{-2}V^T$. Because the range of V^T is an s-dimensional subspace in $\mathbb{R}^l$, there is a *unique* $\vec{c}$ in that range such that $V\vec{c} = \vec{v}$. A solution in a closed form can be obtained as

$$c = E^{-2}V^T(VE^{-2}V^T)^{-1}\vec{v}. \quad (S8)$$

Simple calculation shows that the $V\vec{c} = \vec{v}$ condition holds

$$Vc = VE^{-2}V^T(VE^{-2}V^T)^{-1}\vec{v} = \vec{v}. \quad (S9)$$

Table S1: Fidelities to the 4-qubit Dicke states.

measurement	$|D_4^{(0)}\rangle$	$|D_4^{(1)}\rangle$	$|D_4^{(2)}\rangle$	$|D_4^{(3)}\rangle$	$|D_4^{(4)}\rangle$	Σ
full tomography	-0.001 ± 0.002	0.023 ± 0.004	0.873 ± 0.005	0.026 ± 0.004	0.002 ± 0.002	0.922
full tomography (max-like)	0.001	0.021	0.869	0.023	0	0.914
PI tomography	-0.001 ± 0.002	0.040 ± 0.007	0.852 ± 0.009	0.036 ± 0.007	-0.002 ± 0.002	0.925
PI tomography (max-like)	0.003	0.038	0.850	0.037	0	0.928
PI tomography (ran)	0.000 ± 0.002	0.055 ± 0.027	0.814 ± 0.059	0.023 ± 0.027	0.001 ± 0.002	0.893
PI tomography (ran,max-like)	0.004	0.050	0.816	0.020	0.007	0.897

Proof of Observation 2. The eigenstates of $\vec{J}^2 = J_x^2 + J_y^2 + J_z^2$ are usually labelled by $|j, m, \alpha\rangle$, where $\vec{J}^2|j, m, \alpha\rangle = j(j+1)|j, m, \alpha\rangle$, $J_z|j, m, \alpha\rangle = m|j, m, \alpha\rangle$, and α is used to label the different eigenstates having the same j and m [S3]. Let $P_{j,\alpha}$ denote the projector to the subspace of a given j and α. The number of subspaces is denoted by $N_{\rm SS}$, and, for a given N, it can be calculated from group theory. Moreover, $P_{\rm s} \equiv P_{N/2,1}$. Using this notation, $\varrho_{\rm PI} = \sum_{j,\alpha} P_{j,\alpha}\varrho P_{j,\alpha} = (P_{\rm s}\varrho P_{\rm s}) + \sum_{j<N/2,\alpha}(P_{j,\alpha}\varrho P_{j,\alpha})$. In the basis of $\vec{J}^2$ eigenstates, $\varrho_{\rm PI}$ can be written as a block diagonal matrix

$$\varrho_{\rm PI} = \bigoplus_{j,\alpha} (\langle P_{j,\alpha}\rangle_\varrho \hat{\varrho}_{j,\alpha}), \qquad (S10)$$

where $\hat{\varrho}_{j,\alpha}$ are density matrices of size $(2j+1) \times (2j+1)$. In another context,

$$\varrho_{\rm PI} = \sum_{j,\alpha} \langle P_{j,\alpha}\rangle_\varrho \varrho_{j,\alpha}, \qquad (S11)$$

where $\varrho_{j,\alpha} = P_{j,\alpha}\varrho P_{j,\alpha}/{\rm Tr}(P_{j,\alpha}\varrho P_{j,\alpha})$. Based on that, we obtain

$$F(\varrho, \varrho_{j,\alpha}) = \langle P_{j,\alpha}\rangle_\varrho. \qquad (S12)$$

Then, due to the separate concavity of the fidelity, i.e., $F(\varrho, p_1\varrho_1 + p_2\varrho_2) \geq p_1 F(\varrho, \varrho_1) + p_2 F(\varrho, \varrho_2)$, we obtain $F(\varrho, \varrho_{\rm PI}) \geq \langle P_{\rm s}\rangle_\varrho F(\varrho, \varrho_{\rm s}) + \sum_{j<N/2,\alpha}\langle P_{j,\alpha}\rangle_\varrho F(\varrho, \varrho_{j,\alpha})$. Substituting Eq. (S12) into this inequality, we obtain $F(\varrho, \varrho_{\rm PI}) \geq \langle P_{\rm s}\rangle_\varrho^2 + \sum_{j<N/2,\alpha}\langle P_{j,\alpha}\rangle_\varrho^2$. Using the fact that $\langle P_{\rm s}\rangle_\varrho + \sum_{j<N/2,\alpha}\langle P_{j,\alpha}\rangle_\varrho = 1$, we obtain

$$F(\varrho, \varrho_{\rm PI}) \geq \langle P_{\rm s}\rangle_\varrho^2 + \frac{(1 - \langle P_{\rm s}\rangle_\varrho)^2}{N_{\rm SS} - 1}. \qquad (S13)$$

In many practical situations, the state ϱ is almost symmetric and N is large. In such cases the second term in Eq. (S13) is negligible. Thus, a somewhat weaker bound presented in Observation 2 can be used.

Numerical optimization used to minimize $\mathcal{E}_{\rm total}$. The measurement directions minimizing $\mathcal{E}_{\rm total}$ can be obtained as follows. Let us represent the measurement directions by three-dimensional vectors $\{\vec{a}_j\}_{j=1}^{\mathcal{D}_N}$. The operators can be obtained as $A_j = a_{j,x}X + a_{j,y}Y + a_{j,z}Z$.

First, we need an initial guess. This can come from a set of randomly chosen vectors representing the measurement directions. One can also use the result of a minimization for
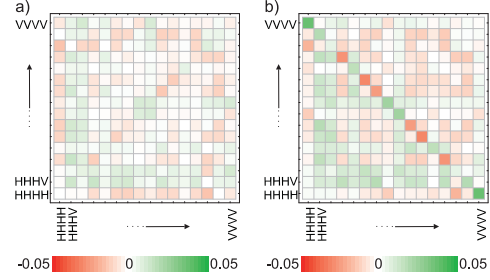
Figure S1: (a) The difference of the real part of the density matrices from optimized settings and the one of full tomography. (b) The difference of the density matrices from random settings and the one of full tomography. For the former, no clear structure is observed, whereas for the latter the largest difference is observed for the antidiagonal elements.

some measure that characterizes how equally the vectors are distributed. Such a measure is defined by

$$\mathcal{F}(\{v_j\}) = \sum_{k,l}(\vec{v}_k \cdot \vec{v}_l)^{2m}, \qquad (S14)$$

where $\vec{v}_k$ represent the measurement directions and $\cdot$ is the scalar product and m is an integer. Such cost functions, called frame potentials, appear in the theory of t-designs essentially for the same purpose.

After we obtain the initial guess from such a procedure, we start an optimization for decreasing $\mathcal{E}_{\rm total}$. At each iteration of the method, we change the measurement directions by rotating them with a small random angle around a randomly chosen axis. If the change decreases $\mathcal{E}_{\rm total}$, then we keep the new measurement directions, while if it does not then we discard it. We repeat this procedure until $\mathcal{E}_{\rm total}$ does not change significantly.

Three-setting witness for estimating the fidelity The three-setting witness for detecting genuine multipartite entanglement in the vicinity of the Dicke state is [S4]

$$\mathcal{W}_{\rm D(4,2)}^{\rm (P3)} = 2\cdot\mathbb{1} + \tfrac{1}{6}(J_x^2 + J_y^2 - J_x^4 - J_y^4) + \tfrac{31}{12}J_z^2 - \tfrac{7}{12}J_z^4. \quad (S15)$$

For this witness we have [S4]

$$\mathcal{W}_{\rm D(4,2)}^{\rm (P3)} - 3\mathcal{W}_{\rm D(4,2)}^{\rm (P)} \geq 0, \qquad (S16)$$
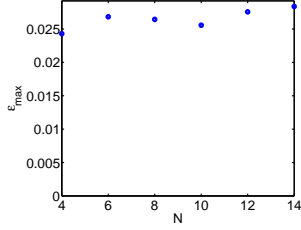
Figure S2: The maximum uncertainty of the Bloch vector elements defined in Eq. (S21) for the optimal measurement settings as a function of the number of qubits, N, for $N = 4, 6, 8, 10, 12$ and 14.

where the projector witness is defined as

$$\mathcal{W}^{(\mathrm{P})}_{\mathrm{D}(4,2)} = \frac{2}{3} \cdot \mathbb{1} - |D_4^{(2)}\rangle\langle D_4^{(2)}|. \quad (S17)$$

Hence, the fidelity with respect to the state $|D_4^{(2)}\rangle$ is bounded from below as [S4]

$$F_{\mathrm{D}(4,2)} \geq \frac{2}{3} - \frac{1}{3}\langle \mathcal{W}^{(\mathrm{P3})}_{\mathrm{D}(4,2)}\rangle. \quad (S18)$$

Fidelities with respect to the four-qubit Dicke states. In Table S1 we summarize the results for full tomography (full) and for permutationally invariant tomography (pi) for random (ran) and optimized (opt) directions. To obtain a physical density matrix with non-negative eigenvalues we perform a maximum-likelihood fit (max-like) of the measured data. In Fig. S1, the differences between the density matrix obtained from full tomography and the ones obtained from permutationally invariant tomography can be seen.

Efficient representation of permutationally invariant operators on a digital computer. Every PI operator O can be decomposed as

$$O = \sum_{k+l+m+n=N} c^{(O)}_{k,l,m,n} (X^{\otimes k} \otimes Y^{\otimes l} \otimes Z^{\otimes m} \otimes \mathbb{1}^{\otimes n})_{\mathrm{PI}}. \quad (S19)$$

Such a decomposition for operators of the form $(A^{\otimes(N-n)} \otimes \mathbb{1}^{\otimes n})_{\mathrm{PI}}$ with $A = a_x X + a_y Y + a_z Z$ is given by

$$\sum_{k,l,m} a_x^k a_y^l a_z^m \frac{(k+l+m)!}{k!l!m!} (X^{\otimes k} \otimes Y^{\otimes l} \otimes Z^{\otimes m} \otimes \mathbb{1}^{\otimes n})_{\mathrm{PI}}, \quad (S20)$$

where the summation is carried out such that $k + l + m + n = N$.

Results for larger systems. We determined the optimal A_j for PI tomography for $N = 4, 6, ..., 14$. In Fig. S2, we plot the maximal uncertainty of the Bloch vector elements

$$\epsilon_{\max} = \max_{k,l,m,n} \mathcal{E}[(X^{\otimes k} \otimes Y^{\otimes l} \otimes Z^{\otimes m} \otimes \mathbb{1}^{\otimes n})_{\mathrm{PI}}] \quad (S21)$$

for the total count realized in the experiment $\lambda_j = \lambda = 2050$ as a function of N, when the state of the system is $\varrho_0 = \mathbb{1}/2^N$. It increases slowly with N. Thus, for large N the number of

counts per measurement setting does not have to increase very much in order to keep the maximal uncertainty of the Bloch vector elements the same as for the $N = 4$ case. In particular, for $N = 14$, a total count of 2797 per setting yields the same maximal uncertainty as we had for the $N = 4$ case.

An upper bound on the uncertainty of PI tomography for ϱ_0 different from the white noise can be obtained by using $[\Delta(A_j^{\otimes(N-n)} \otimes \mathbb{1}^{\otimes n})_{\mathrm{PI}}]^2_{\varrho_0} = 1$ for error calculations. According to numerics, for optimal A_j for $N = 4, 6, ..., 14$, $\epsilon_{\max}$ remains the same as in the case of white noise, since for the full correlation terms with $n = 0$ the upper bound equals the value for white noise, and the full correlations terms contribute to the noise of the Bloch vector elements with the largest uncertainty. Thus, the total count per setting will not increase more with the number of qubits even for states different from the completely mixed state.

The operators that give a bound on $\langle P_{\mathrm{s}}\rangle$ with three settings for $N = 6$ and 8 are the following

$$P_{\mathrm{s}}^{(6)} \geq \frac{2}{225}(Q_2 + J_z^2) - \frac{1}{90}(Q_4 + J_z^4) + \frac{1}{450}(Q_6 + J_z^6),$$

$$P_{\mathrm{s}}^{(8)} \geq -0.001616 Q_2 + 0.002200 Q_4 - 0.0006286 Q_6$$
$$+ \; 0.00004490 Q_8 + 0.003265 J_z^2 - 0.004444 J_z^4$$
$$+ \; 0.001270 J_z^6 - 0.00009070 J_z^8, \quad (S22)$$

where $Q_n = J_x^n + J_y^n$. They were determined using semi-definite programming, with a method similar to one used for obtaining three-setting witnesses in Ref. [S4]. They have an expectation value $+1$ for the Dicke states $|D_6^{(3)}\rangle$ and $|D_8^{(4)}\rangle$, respectively. Moreover, their expectation value give the highest possible lower bound on $\langle P_{\mathrm{s}}\rangle$ for states of the form

$$\varrho_{\mathrm{noisy}}(p) = p\frac{\mathbb{1}}{2^N} + (1-p)|D_N^{(N/2)}\rangle\langle D_N^{(N/2)}| \quad (S23)$$

among the operators that are constructed as a linear combination of the operators J_l^n. The validity of the relations in Eq. (S22) can easily be checked by direct calculation.

Bounding the differences between elements of ϱ and ϱ_{PI} based on the fidelity. For any pure state $|\Psi\rangle$, it is possible to bound the difference between $|\langle\Psi|\varrho_{\mathrm{PI}}|\Psi\rangle|$ and $|\langle\Psi|\varrho|\Psi\rangle|$ as

$$|\langle\Psi|\varrho|\Psi\rangle - \langle\Psi|\varrho_{\mathrm{PI}}|\Psi\rangle| \leq \sqrt{1 - F(\varrho, \varrho_{\mathrm{PI}})}. \quad (S24)$$

Thus, if the fidelity is close to 1, then $\langle\Psi|\varrho|\Psi\rangle \approx \langle\Psi|\varrho_{\mathrm{PI}}|\Psi\rangle$, even if $|\Psi\rangle$ is non-symmetric. If $|\Psi\rangle$ is an element of the product basis, e.g., $|0011\rangle$, then Eq. (S24) is a bound on the difference between the corresponding diagonal elements of ϱ and ϱ_{PI}.

Eq. (S24) can be proved as follows: There is a well-known relation between the trace norm and the fidelity [S5]

$$\frac{1}{2}||\varrho - \varrho_{\mathrm{PI}}||_{\mathrm{tr}} \leq \sqrt{1 - F(\varrho, \varrho_{\mathrm{PI}})}. \quad (S25)$$

Moreover, for a projector P and density matrices ϱ_k we have [S6]

$$|\mathrm{Tr}(P\varrho_1) - \mathrm{Tr}(P\varrho_2)| \leq \frac{1}{2}||\varrho_1 - \varrho_2||_{\mathrm{tr}}. \quad (S26)$$

4

Combining Eq. (S25) and Eq. (S26), leads to Eq. (S24).

---

* Present address: Faculty of Physics, University of Vienna, Boltzmanngasse 5, A-1090 Wien, Austria

[S1] C. Schmid, Ph.D. Thesis, Ludwig-Maximillian-Universität, Munich, Germany, 2008; D.F.V. James *et. al,* Phys. Rev. A **64**, 052312 (2001).

[S2] B. Jungnitsch *et. al*, Phys. Rev. Lett. **104**, 210401 (2010).

[S3] See, for example, J.I. Cirac *et. al*, Phys. Rev. Lett. **82**, 4344 (1999).

[S4] G. Tóth *et al.*, New J. Phys. **11**, 083002 (2009).

[S5] J.A. Miszczak *et al.*, J. Quant. Inf. Comp. **9**, 0103 (2009).

[S6] See Eqs. (9.18) and (9.22) of M.A. Nielsen and I.L. Chuang, *Quantum computation and quantum information* (Cambridge University Press, Cambridge, 2000).

4

Optical quantum enhanced metrology

The aim of quantum enhanced metrology is to improve the precision of measurements with non-classical resources, like for example entangled photons. The parameter of interest, which has to be determined by the measurement, is here the phase of the electromagnetically oscillating light field. In general a phase can only be determined with respect to another phase, a so called phase shift, which is typically measured experimentally in a Mach-Zehnder interferometer [133, 134]. Now, if a phase shift is measured with classical photons the sensitivity can not exceed the so called shot-noise limit [135]. To beat this limit entanglement is a necessary but not a sufficient condition. This means that not all entangled states allow for sub shot noise measurement sensitivities, but if a state achieves sub shot noise sensitivity it is entangled [136, 137]. In this chapter and in the preprint 4.1.3 [60] an extension of the criterion to recognize useful entanglement for sub shot noise sensitivity to a criterion to identify even useful multi-particle entanglement is presented. This allows to quantify the amount of multi-particle entanglement of a probe state contributing for the useful estimation of an unknown phase shift. In the experiment we use a four photon entangled Dicke state to prove the criterion by measuring the Fisher information, which is directly connected to the uncertainty of the phase estimate [138]. Further, to show how to utilize this entanglement a maximum likelihood and a Bayesian phase estimation protocol is implemented once for a 4 photon entangled symmetric Dicke state and once for a separable state for comparison. The results are summarized in preprint 4.1.5 and further described in this chapter. Especially the part of maximum likelihood and Bayesian estimation will be treated in more detail, because it is only shortly described in the preprint 4.1.5.

In the second part of this chapter and in the preprint 4.2.1, an interferometric experiment is implemented for a symmetric six photon Dicke state showing sub shot noise sensitivity. In this case the sensitivity is not calculated by using the Fisher information, but is determined from a measurement observable revealing the uncertainty of the phase estimate by using a simple linearised error model [139]. Further, the benefits of symmetric Dicke states for polarization interferometry are discussed in the context of different measurement directions on the Bloch sphere, where the symmetric Dicke state achieves sub shot noise sensitivity for two orthogonal directions.

4.1 Useful multi-particle entanglement and sub shot noise phase estimation

Entanglement lies at the very heart of quantum mechanics and the technological development to produce such non-classical correlation goes along with theoretical tools proving the created entanglement. There are many methods to prove the entanglement of a quantum state observed in the laboratory, such as the one used in chapter 3.3 or, for example, in Ref. [65, 66]. But all these methods verify entanglement regardless to its usefulness with respect to a specific application like for example quantum lithography [21, 22], quantum positioning [140], quantum imaging [141] or quantum metrology [23]. In this section a criterion for multi-particle entangled states which are useful to overcome classical phase sensitivity in metrology is introduced and experimentally verified by the implementation of a complete sub shot noise phase estimation protocol using maximum likelihood and Bayesian analysis.

First, an introduction to Fisher information and parameter estimation will be given to motivate the idea of the criterion and then the experimental results will be described and discussed.

4.1.1 Fisher information and parameter estimation

Let us assume we do a measurement with the goal to estimate an unknown parameter θ_0 with minimal uncertainty. To this aim, the uncertainty of the estimator is calculated by means of the Fisher information, because this quantity tells us the amount of information we can extract about a parameter θ_0. To motivate this special property of the Fisher information we will give in the following a derivation of the Fisher information according to Ref. [142].

In a general phase estimation scenario (see Fig. 4.1) an initial state ρ is transformed by an unitary transformation with phase shift θ_0 into $\rho(\theta_0)$. Measuring $\rho(\theta_0)$ with outcome μ delivers the probability density $P(\mu|\theta_0)$ from m independent repetitions of the measurement. Out of these probability densities the uncertainty of the estimator $\Delta\theta_{est}$ is then calculated. Assuming no bias b, which means that in the mean the true phase shift θ_0 is equal to the estimator θ_{est} we get

$$b(\theta_0) = \langle \theta_{est}(\mu) - \theta_0 \rangle = \int d\mu(\theta_{est}(\mu) - \theta_0)P(\mu|\theta_0) = 0. \tag{4.1}$$

After differentiating Eq. 4.1 with $\partial/\partial\theta_0$ one obtains

$$\int d\mu(\theta_{est}(\mu) - \theta_0)\frac{\partial P(\mu|\theta_0)}{\partial\theta_0} - \int d\mu P(\mu|\theta_0) = 0. \tag{4.2}$$

Using the identity

$$\frac{\partial P(\mu|\theta_0)}{\partial\theta_0} = P(\mu|\theta_0)\frac{\partial \ln P(\mu|\theta_0)}{\partial\theta_0} \tag{4.3}$$
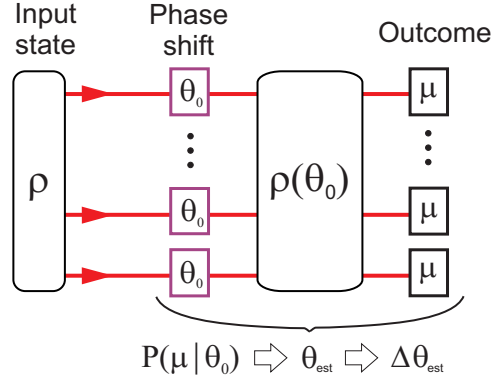
Figure 4.1: **Schematic of a general phase estimation scenario** The input state ρ is transformed by θ_0, the true phase shift, to $\rho(\theta_0)$, which gives the outcome μ. A measurement delivers then the conditional probability density $P(\mu|\theta_0)$, the probability to observe θ_0 for a given outcome μ, out of which the phase estimate θ_{est} and finally the uncertainty of the estimator $\Delta\theta_{est}$ is calculated.

and normalization in $P(\mu|\theta_0)$, i.e. $\int d\mu P(\mu|\theta_0) = 1$, Eq. 4.2 becomes

$$\int d\mu (\theta_{est} - \theta_0)\frac{\partial \ln P(\mu|\theta_0)}{\partial \theta_0}P(\mu|\theta_0) = 1. \tag{4.4}$$

Factorizing the integrand leads to

$$\int d\mu \left[\frac{\partial \ln P(\mu|\theta_0)}{\partial \theta_0}\sqrt{P(\mu|\theta_0)} \right] \left[(\theta_{est}(\mu) - \theta)\sqrt{P(\mu|\theta_0)} \right] = 1. \tag{4.5}$$

By squaring the equation and using the Cauchy-Schwarz inequality we obtain

$$\underbrace{\left[\int d\mu \left(\frac{\partial \ln P(\mu|\theta_0)}{\partial \theta_0} \right)^2 P(\mu|\theta_0) \right]}_{F} \underbrace{\left[\int d\mu (\hat{\theta}_0(\mu) - \theta_0)^2 P(\mu|\theta_0) \right]}_{\Delta\theta^2} \geq 1. \tag{4.6}$$

The integrand on the right is the mean-square error $\Delta\theta^2 = \langle (\theta_{est}(\mu) - \theta_0)^2 \rangle$. So we have found an inequality which gives us a bound on the uncertainty of our estimator. Interestingly, what remains on the left hand side of Eq. 4.6 is the definition of the Fisher Information F. For discrete values of μ, the Fisher information can be written as a sum

$$F[\theta_0] = \sum_\mu \left(\frac{\partial \ln P(\mu|\theta_0)}{\partial \theta_0} \right)^2 P(\mu|\theta_0) = \sum_\mu \frac{1}{P(\mu|\theta_0)} \left(\frac{\partial P(\mu|\theta_0)}{\partial \theta_0} \right)^2. \tag{4.7}$$

In other words, there is a connection between the Fisher Information and the uncertainty of an estimator. This (Eq. 4.6) is also known as Cramér-Rao lower bound [138]

$$\Delta\theta \geq \frac{1}{\sqrt{m}}\frac{1}{\sqrt{F}} \tag{4.8}$$

where we added the factor m, the number of independent repetitions of the measurement.

Accordingly, a quantum mechanical evolution of a system ρ may also depend on a parameter θ_0 leading us to $\rho(\theta_0) = e^{-i\hat{H}\theta_0}\rho_0 e^{i\hat{H}\theta_0}$ with $e^{-i\hat{H}\theta_0}$ a unitary transformation. $\hat{H}$ is hermitian and the generator of the phase shift. The parameter θ_0 is estimated with outcome θ_{est} by the operator $\{\hat{E}(\mu)\}$, with $P(\mu|\theta_0) = \text{Tr}(\hat{E}(\mu)\rho(\theta_0))$. The quantum Fisher information is defined as the maximum of the Fisher information over all possible measurements $\hat{E}(\mu)$ [137, 143],

$$F_Q[\rho(\theta_0)] = \max_{\{\hat{E}(\mu)\}} F[\rho(\theta_0); \{\hat{E}(\mu)\}]. \tag{4.9}$$

To this aim, the quantum Fisher information acts as upper bound for the Fisher information, which is only saturated for an optimal measurement $\hat{E}(\mu)$. With respect to Eq. 4.6 a quantum mechanical counterpart of the Cramér-Rao inequality is derived in the following according to [144] [26]. Let us assume that the bias b is defined as (similar to Eq. 4.1)

$$b(\theta_0) = \langle\theta_{est}(\mu) - \theta_0\rangle = \text{Tr}(\rho\,(\hat{E} - \mathbb{1}\theta_0)) = \text{Tr}(\rho\hat{E}) - \theta_0 \tag{4.10}$$

with $\rho = \rho(\theta_0)$, $\hat{E} = \hat{E}(\mu)$ and $\text{Tr}(\rho) = 1$. Differentiating Eq. 4.10 leads to

$$1 + b'(\theta_0) = \text{Tr}(\hat{E}\frac{\partial\rho}{\partial\theta_0}). \tag{4.11}$$

Now we introduce the operator L as the solution of the operator equation

$$\frac{\partial\rho}{\partial\theta_0} = \frac{1}{2}(\rho L + L\rho). \tag{4.12}$$

with L the symmetrized logarithmic derivative of ρ. At fist sight, the introduction of the operator L in Eq. 4.12 seems to be unmotivated, but this will become clearer in the end of the derivation. If we now subtract $\text{Tr}(\theta_0\partial\rho/\partial\theta_0) = 0$ (is equal to zero because $\text{Tr}(\rho) = 1$) from Eq. 4.11 and insert the expression for L we obtain

$$\begin{aligned}
\left(1 + b'(\theta_0)\right)^2 &= \text{Tr}((\hat{E} - \theta_0)\frac{\partial\rho}{\partial\theta_0})^2 & (4.13)\\
&= \text{Tr}\big((\hat{E} - \theta_0)\frac{1}{2}(L\rho + \rho L)\big)^2 & (4.14)\\
&= \text{Tr}\big((\hat{E} - \theta_0)\frac{1}{2}(L\rho + (L\rho)^\dagger)\big)^2 & (4.15)\\
&= \mathfrak{Re}\big(\text{Tr}(L\rho(\hat{E} - \theta_0))\big)^2 & (4.16)\\
&\leq \left|\text{Tr}(L\rho^{\frac{1}{2}}\rho^{\frac{1}{2}}(\hat{E} - \theta_0))\right|^2 & (4.17)
\end{aligned}$$

---

[26] and with the help of Christian Schwemmer

for the next step we are using the Cauchy-Schwarz inequality for traces, $|\text{Tr}(AB^\dagger)|^2 \leq \text{Tr}(AA^\dagger)\text{Tr}(BB^\dagger)$, and get

$$\left(1 + b'(\theta_0)\right)^2 \leq \text{Tr}(L\rho^{\frac{1}{2}}\rho^{\frac{1}{2}}L)\text{Tr}(\rho^{\frac{1}{2}}(\hat{E} - \theta_0)^2\rho^{\frac{1}{2}}). \tag{4.18}$$

Rearranging Eq. 4.18 we obtain

$$\text{Tr}(\rho(\hat{E} - \theta_0)^2) \geq \frac{\left(1 + b'(\theta_0)\right)^2}{\text{Tr}(\rho L^2)}. \tag{4.19}$$

Assuming no bias, i.e., $b'(\theta_0) = 0$ the quantum mechanical Cramér-Rao inequality results in

$$\langle \theta_{est}(\mu) - \theta_0 \rangle^2 = \text{Tr}\left(\rho\,(\hat{E} - \mathbb{1}\theta_0)^2\right) \geq \frac{1}{\text{Tr}(\rho L^2)}. \tag{4.20}$$

The quantum Fisher information can now be defined according to Eq. 4.20 as $F_Q = \text{Tr}[\rho L^2]$. What we now need to calculate is the expression for L. To do this we use $\rho(\theta_0) = e^{-i\hat{H}\theta_0}\rho_0 e^{i\hat{H}\theta_0}$ and write Eq. 4.12 in a different way

$$\frac{\partial\rho}{\partial\theta_0} = i\hat{H}\rho - i\rho\hat{H} = i[\hat{H}, \rho]. \tag{4.21}$$

Using this notation we can rewrite the expression for the quantum Fisher information

$$F_Q = \text{Tr}(\rho L^2) = \text{Tr}(L\rho L) = \frac{1}{2}(\text{Tr}(\rho L^2) + \text{Tr}(L\rho L)) = \text{Tr}(i[\hat{H}, \rho]L). \tag{4.22}$$

Rewriting the previous formula in the Dirac notation and writing ρ in its eigenbasis $\rho = \sum_k q_k |k\rangle\langle k|$ we obtain

$$F_Q[\rho, \hat{H}] = i\sum_j \langle j|[\hat{H}, \rho]L|j\rangle \tag{4.23}$$

$$= i\sum_{j,k} \langle j|\left(\hat{H}q_k|k\rangle\langle k| - q_k|k\rangle\langle k|\hat{H}\right)L|j\rangle \tag{4.24}$$

$$= i\sum_{j,k} \langle j|\left(\hat{H}q_k|k\rangle\langle k| - q_k|k\rangle\langle k|\hat{H}\right)\sum_l|l\rangle\langle l|L|j\rangle \tag{4.25}$$

$$= i\sum_{j,k,l} \langle j|\left(\hat{H}q_k|k\rangle\langle k| - q_k|k\rangle\langle k|\hat{H}\right)|l\rangle L_{lj} \tag{4.26}$$

$$= i\sum_{j,k,l}(\hat{H}_{jk}q_k\delta_{lk} - q_k\delta_{jk}\hat{H}_{kl})L_{lj} \tag{4.27}$$

$$= i\sum_{j,k}\hat{H}_{jk}q_k L_{kj} - i\sum_{j,k}q_k\hat{H}_{kj}L_{jk} \tag{4.28}$$

$$= i\sum_{j,k}\hat{H}_{jk}q_k L_{kj} - i\sum_{j,k}q_j\hat{H}_{jk}L_{kj} \tag{4.29}$$

$$= i\sum_{j,k}(q_k - q_j)\hat{H}_{jk}L_{kj}. \tag{4.30}$$

To calculate L_{kj} we will use the following identities

$$\rho L + L\rho = \sum_k \left(q_k |k\rangle\langle k| L + L q_k |k\rangle\langle k| \right) \tag{4.31}$$

$$= \sum_{j,k} \left(q_k L_{kj} |k\rangle\langle j| + q_k L_{jk} |j\rangle\langle k| \right) \tag{4.32}$$

$$= \sum_{j,k} (q_k + q_j) L_{kj} |k\rangle\langle j| \tag{4.33}$$

$$\rho L + L\rho \overset{!}{=} 2i[\hat{H}, \rho] \tag{4.34}$$

$$= 2i(\hat{H}\rho - \rho\hat{H}) \tag{4.35}$$

$$= 2i \sum_k \left(\hat{H} q_k |k\rangle\langle k| - q_k |k\rangle\langle k| \hat{H} \right) \tag{4.36}$$

$$= 2i \sum_{j,k} \left(q_k \hat{H}_{jk} |j\rangle\langle k| - q_k \hat{H}_{kj} |k\rangle\langle j| \right) \tag{4.37}$$

$$= -2i \sum_{j,k} (q_k - q_j) \hat{H}_{kj} |k\rangle\langle j| . \tag{4.38}$$

L_{kj} can now be written, by comparing Eq. 4.33 and Eq. 4.38, as follows

$$(q_k + q_j) L_{kj} = -2i(q_k - q_j)\hat{H}_{kj} \tag{4.39}$$

$$L_{kj} = \frac{-2i(q_k - q_j)\hat{H}_{kj}}{(q_k + q_j)}. \tag{4.40}$$

With Eq. 4.30 the quantum Fisher information becomes

$$F_Q[\rho, \hat{H}] = 2 \sum_{j,k} \frac{(q_k - q_j)^2}{q_k + q_j} \hat{H}_{jk}\hat{H}_{jk} \tag{4.41}$$

$$= 2 \sum_{j,k} \frac{(q_k - q_j)^2}{q_k + q_j} |\langle j| \hat{H} |k\rangle|^2 . \tag{4.42}$$

This is the result which has also been obtained in [143] and applies to all mixed states. For pure states the quantum Fisher information can be rearranged as follows[27]:

$$F_Q[\rho, \hat{H}] = 2 \sum_{j,k} \frac{(q_k - q_j)^2}{q_k + q_j} \langle j| \hat{H} |k\rangle\langle k| \hat{H} |j\rangle \tag{4.43}$$

---

[27]private communication by Wieslaw Laskowski

With pure states we can assume that for $k, j = 1$, $q_1 = 1$ with eigenstate $|1\rangle$ and for $k, j > 1$, $q_{k,j} = 0$, which results in

$$F_Q[\rho, \hat{H}] = 2 \sum_{j=1,k>1} \sum_{k=1,j>1} \frac{(q_k - q_j)^2}{q_k + q_j} \langle j | \hat{H} | k \rangle \langle k | \hat{H} | j \rangle \tag{4.44}$$

$$= 2 * 2 \sum_{k>1} \langle 1 | \hat{H} | k \rangle \langle k | \hat{H} | 1 \rangle. \tag{4.45}$$

Now we are using that $\sum_{j>1} | j \rangle \langle j | = \mathbb{1} - | 1 \rangle \langle 1 |$ and obtain

$$F_Q[\rho, \hat{H}] = 4 \langle 1 | \hat{H} \big(\mathbb{1} - | 1 \rangle \langle 1 | \big) \hat{H} | 1 \rangle \tag{4.46}$$

$$= 4 \big(\langle 1 | \hat{H}^2 | 1 \rangle - (\langle 1 | \hat{H} | 1 \rangle)^2 \big) \tag{4.47}$$

$$= 4 \langle \Delta \hat{H}^2 \rangle. \tag{4.48}$$

Finally, we have found an expression for the Fisher information for a quantum situation, which is also called quantum Fisher information. Eq. 4.42 corresponds to to the case of a mixed state and Eq. 4.48 to a pure state. In the experiment mostly mixed states can be observed, making Eq. 4.42 especially useful for experimentalist. But note that to calculate the quantum Fisher information the whole density matrix of a probe state ρ has to be known. In preprint 4.1.5 we will then measure and evaluate the classical and quantum Fisher information for a four photon entangled symmetric Dicke state.

4.1.2 Multi-particle entanglement and Fisher information

General entanglement criteria profit from the separability properties of quantum states and are therefore restricted to a *yes* or *no* answer with respect to the entanglement of a probe state [65, 66]. Recently, it has been shown that an arbitrary probe state ρ consisting of N qubits is entangled and allows at the same time for sub shot noise phase estimation if the condition

$$F_Q[\rho, \hat{H}] > N \tag{4.49}$$

is fulfilled [136]. This is very different from general entanglement measures, because here the entanglement can be directly associated to a technological improvement to estimate a phase shift beyond the shot noise limit $\Delta\theta_{SNL} = 1/\sqrt{N}$ [23]. The ultimate limit of sensitivity which can be achieved is the so called Heisenberg limit $\Delta\theta_{HL} = 1/N$ [23] but this can only be reached if genuine multi-partite entanglement is associated to the probe state [60, 145].

To extend previous work on the connection between phase estimation and entanglement [146, 136, 137], we introduce a criterion to identify the useful k-particle entanglement of a probe state with respect to phase estimation. This is again derived by means of the Fisher information assuming a pure k-particle entangled quantum state which can be written as $| \psi^{k-\text{ent}} \rangle = \bigotimes_{l=1}^{M} | \psi_l \rangle$, with $| \psi_l \rangle$ a state of $N_l \leq k$ particles,

and at least one state $|\psi_l\rangle$ of k particles does not factorize. For the case of $k = 1$ this corresponds to a product state. For a mixed state we assume k-particle entangled if and only if it cannot be written as a sum like $\sum_j p_j \, | \, \psi_j^{k_j-\text{ent}} \rangle \langle \psi_j^{k_j-\text{ent}} \, |$ and $k_j < k$. Finally, for k-particle entangled states the following bounds hold [60, 145]

$$F_Q[\hat{\rho}, \hat{J}] \leq \lfloor \frac{N}{k} \rfloor k^2 + r^2, \tag{4.50}$$

to identify useful k-particle entanglement intrinsic to a probe state ρ, where $\lfloor x \rfloor$ is the largest integer smaller or equal to x and $r = N - \lfloor \frac{N}{k} \rfloor \cdot k$. A detailed derivation of this criteria is given in the preprint 4.1.3 [60] and in [145].

Furthermore, we will use an additional criterion using the average quantum Fisher information with respect to three orthogonal directions on the Bloch sphere (see Fig. 2.1) as $\bar{F}_Q = \frac{1}{3}\big(F_Q[\rho, \hat{J}_x] + F_Q[\rho, \hat{J}_y] + F_Q[\rho, \hat{J}_z]\big)$ and $\hat{J}_j$ is the angular momentum with $\hat{J}_j = \hat{\sigma}_{\vec{n}_j}$ and $\vec{n}_j \in \{x, y, z\}$. This can be understood as if a probe state is prepared for phase estimation but with no control over the axis of rotation and every rotation axis is equally probable. In the following preprint 4.1.3 [60], these two novel criteria are introduced and compared to each other by the theoretical application to different quantum states revealing the states useful entanglement with respect to phase estimation.

Based on the criterion of Eq.4.50, several bounds for the quantum Fisher information can now be calculated to verify the states useful multi-particle entanglement in the experiment. In the next subsection 4.1.5 we have determined the Fisher information experimentally, once for a symmetric four photon entangled Dicke state [87] and once for a separable state. Additionally, we demonstrate their usefulness according to two different phase estimation protocols. Further, we have calculated the corresponding bounds for two- and three particle entanglement.

4.1.3 Preprint: Fisher information, spin squeezing and multi-particle entanglement

Fisher information, spin squeezing, and multiparticle entanglement

Philipp Hyllus[1], Wiesław Laskowski[2,3,4], Roland Krischek[3,4], Christian Schwemmer[3,4],
Witlef Wieczorek[3,4,5], Harald Weinfurter[3,4], Luca Pezzé[6], and Augusto Smerzi[1],
[1]INO-CNR BEC Center and Dipartimento di Fisica, Università di Trento, I-38123 Povo, Italy
[2]Institute of Theoretical Physics and Astrophysics,
University of Gdańsk, PL-80-952 Gdańsk, Poland
[3]Fakultät für Physik, Ludwig-Maximilians Universität München, D-80799 München, Germany
[4]Max-Planck Institut für Quantenoptik, D-85748 Garching, Germany
[5]Faculty of Physics, University of Vienna, A-1090 Vienna, Austria
[6]Laboratoire Charles Fabry, Institut d'Optique, 91127 Palaiseau, France
(Dated: June 24, 2010)

The Fisher information F gives a limit to the ultimate precision that can be obtained in a phase estimation protocol. It has been shown recently that F cannot exceed the number of particles in a linear two-mode interferometer if the input state is separable. This implies that with such input states the shot-noise limit is the ultimate limit of precision. We extend this result by constructing bounds on F for several multiparticle entanglement classes. We further compute similar bounds on the Fisher information averaged over all possible linear interferometers $\bar{F}$. We show that these criteria detect different sets of states and illustrate their strengths by considering several examples. For instance, the criterion based on $\bar{F}$ is able to detect certain bound entangled states. Finally, we comment on the relation to bounds on the spin squeezing parameter for multipartite entangled states obtained previously, pointing out the connection between the Fisher information, spin squeezing, and multipartite entanglement.

I. INTRODUCTION

Entanglement is a distinguishing feature of quantum theory that allows to perform several tasks better than it is possible with classical means [1]. Therefore, it is important to study the connection between the entanglement of quantum states and the usefulness for specific applications. One example of such a task is phase estimation as done in quantum interferometry [2], where the connection between entanglement and phase sensitivity has been investigated recently [3–6]. In general, the structure of the set of entangled bipartite quantum states is understood quite well, while the classification and quantification of multipartite quantum states is less developed [7–9]. In particular, if a mixed quantum state ρ is given, it is typically a difficult question to answer how many particles are entangled in the state [10–16]. Commonly applied criteria to distinguish between different entanglement classes include entanglement witnesses [9] and Bell inequalities [17–20]. Recently, other approaches have led to criteria which can be evaluated directly from elements of the density matrix [21, 22].

In this manuscript, we introduce two sets of novel criteria which can distinguish between different entanglement classes, which are deeply connected to phase estimation. This extends the previous work on the connection between entanglement and phase sensitivity mentioned above. The criteria are based on the Fisher information and linear two-mode interferometers. The first set of criteria is based directly on the quantum Fisher information, which is the optimum of the Fisher information over all output measurements of the phase esti-

mation protocol [23]. We compute the optimal values for different entanglement classes. The second set of criteria is based on the quantum Fisher information averaged over the direction of the interferometer to be defined below. We show that the sets of states that the criteria detect are different and not contained in each other. We consider several examples in order to assess the strength of the criteria. Finally, we comment on the relation of the criteria to the spin squeezing parameter [24] and on bounds thereof for multipartite entanglement classes obtained in [25, 26].

The article is organized as follows. We start by introducing the basic concepts related to general phase estimation protocols, linear two-mode interferometers, and the classification of multiparticle entanglement in Section II. Then we derive the entanglement criteria based on the quantum Fisher information and on the average quantum Fisher information in Section III, where we also make a first comparison of the two. In Section IV, we apply the criteria to several families of entangled states. Finally, we investigate the relation to spin squeezing inequalities in Section V. We conclude in Section VI.

II. BASIC CONCEPTS

In a general phase estimation scenario, an input state ρ is transformed into the state $\rho(\theta)$ depending on a phase shift θ. Then, a general positive operator valued measurement (POVM) with elements $\{\hat{E}_\mu\}_\mu$ is performed. This procedure may be repeated m times, and based on the results collected in the vector $\vec{\mu}$, the phase shift is estimated by an estimator $\theta_{\text{est}}(\vec{\mu})$. If the estimator is

unbiased, *i.e.*, $\langle\theta_{\text{est}}\rangle = \theta$, then its minimal standard deviation is limited by the Cramer-Rao bound [27, 28]

$$\Delta\theta_{\text{est}} \geq \frac{1}{\sqrt{mF}}, \qquad (1)$$

where F is the Fisher information, which is defined as

$$F = \sum_\mu \frac{1}{P(\mu|\theta)}[\partial_\theta P(\mu|\theta)]^2, \qquad (2)$$

where $P(\mu|\theta) = \text{Tr}(\rho(\theta)\hat{E}_\mu)$. A maximum likelihood estimator saturates the Cramer-Rao bound in the central limit, for a sufficiently large m [29]. In this sense, F quantifies the asymptotic usefulness of a quantum state for phase estimation if the phase transformation and the output measurement are fixed. Maximizing F over all possible POVMs leads to the so-called quantum Fisher information F_Q. If the phase shift is generated by an operator $\hat{H}$, and for a mixed input state $\rho = \sum_k \lambda_k|k\rangle\langle k|$, then it is given by [23]

$$F_Q = 2\sum_{k,l} \frac{(\lambda_k - \lambda_l)^2}{\lambda_k + \lambda_l}|\langle l|\hat{H}|k\rangle|^2. \qquad (3)$$

For pure input states this reduces to $F_Q = 4\langle(\Delta\hat{H})^2\rangle$ [23].

In general linear two-mode interferometers and input states of N particles, $\hat{H}$ is given by a collective spin operator $\hat{J}_{\vec{n}} = \vec{n} \cdot \vec{\hat{J}}$, where $\hat{J}_i = \frac{1}{2}\sum_{k=1}^N \sigma_i^{(k)}$ and $\sigma_i^{(k)}$ is the i-th Pauli matrix acting on particle k. The operators $\hat{J}_x$, $\hat{J}_y$, and $\hat{J}_z$ fulfil the commutation relations of spin. We will use the symmetric eigenstates $|j, \mu\rangle$ of $\hat{J}_z$, where $j = \frac{N}{2}$ and $\mu = -\frac{N}{2}, -\frac{N}{2}+1, ..., \frac{N}{2}$, and the eigenstates of σ_z defined by $\sigma_z|l\rangle = (-1)^l|l\rangle$, where $l = 0, 1$, where $|0\rangle$ and $|1\rangle$ are the two states that the interferometer works with. As an example for a linear two-mode interferometer we mention that the Mach-Zehnder interferometer has the generator $\hat{H} = \hat{J}_y$ [30].

For generators $\hat{J}_{\vec{n}}$, there is a direct connection between entanglement and sub shot-noise interferometry. An entangled state of N particles cannot be written as $\rho_{\text{sep}} = \sum_j p_j \bigotimes_{k=1}^N |\psi_j^{(k)}\rangle\langle\psi_j^{(k)}|$, where $\{p_j\}$ forms a probability distribution [31]. It has been shown recently that

$$F_Q[\rho_{\text{sep}}, \hat{J}_{\vec{n}}] \leq N \qquad (4)$$

holds [3, 4]. Therefore, the phase uncertainty is bounded by the shot-noise limit

$$\Delta\theta_{\text{est}} \geq \frac{1}{\sqrt{mN}} \qquad (5)$$

for separable states.

The purpose of this manuscript is to derive similar bounds for multipartite entanglement classes. We consider the following classification of multiparticle entanglement from Ref. [32] (see [11, 33] for alternative classifications): a pure state of N particles is k-partite entangled if there are at most groups of k particles which are fully entangled within the state. We denote such a state as $|\psi_{k-\text{ent}}\rangle$. This is *producible* by interactions between k particles at most. A mixed state is k-partite entangled if it can be written as a mixture of k-partite entangled pure states, *i.e.*, $\rho_{k-\text{ent}} = \sum_k p_k|\psi_{k-\text{ent}}\rangle\langle\psi_{k-\text{ent}}|$. A separable state is 1-partite entangled in this notation. Note that a decomposition of a $k < N$-partite entangled state of N particles may contain states where different sets of particles are entangled. Let us illustrate this by considering $N = 3$. A state $|\psi_{1-\text{ent}}\rangle = |\phi\rangle_1 \otimes |\varphi\rangle_2 \otimes |\chi\rangle_3$ is fully separable, a state $|\psi_{2-\text{ent}}\rangle = |\phi\rangle_{12} \otimes |\chi\rangle_3$ which cannot be written as $|\psi_{1-\text{ent}}\rangle$ is 2-partite entangled, and a state $|\psi_{3-\text{ent}}\rangle$ which cannot be written as a 2-partite entangled state is 3-partite entangled.

III. CRITERIA FOR MULTIPARTITE ENTANGLEMENT FROM THE QUANTUM FISHER INFORMATION

Now we are in a position to derive the desired bounds. We start by deriving bounds on the quantum Fisher information $F_Q[\rho_{k-\text{ent}}; \hat{J}_{\vec{n}}]$ for k-partite entangled states and an arbitrary direction $\vec{n}$. Then, we derive bounds on the quantum Fisher information for a generator $\hat{J}_{\vec{n}}$, averaged over all directions $\vec{n}$. At the end of this section, we show for $k = 1$ and $k = N - 1$ the sets of states that the two criteria detect are different and not contained in each other.

A. Criteria from $\mathbf{F_Q}$

We directly present the result, the derivation follows afterwards.

Observation 1 ($\mathbf{F_Q^{k+1}}$ criterion). *For k-partite entangled states and a linear two-mode interferometer with a generator $\hat{J}_{\vec{n}}$ of an arbitrary direction $\vec{n}$, the quantum Fisher information is bounded by*

$$F_Q[\rho_{k-\text{ent}}; \hat{J}_{\vec{n}}] \leq sk^2 + r^2, \qquad (6)$$

where $s = \lfloor\frac{N}{k}\rfloor$ is the largest integer smaller than or equal to $\frac{N}{k}$ and $r = N - sk$. Hence a violation of the bound (6) proves $(k + 1)$-partite entanglement.

Proof. The basic ingredients of the derivations are the following: (i) The sets of states introduced above are convex. (ii) The Fisher information is convex in the states, *i.e.*, for the generators we consider, $F[p\rho_1 + (1 - p)\rho_2; \hat{J}_{\vec{n}}] \leq pF[\rho_1; \hat{J}_{\vec{n}}] + (1 - p)F[\rho_2; \hat{J}_{\vec{n}}]$ for $p \in [0, 1]$ [34]. Since the quantum Fisher information is equal to the Fisher information for a particular measurement, this holds also for F_Q. It follows that the maximum of F_Q for a fixed $\vec{n}$ and k-partite entangled mixed states is reached on the pure k-partite entangled states. In this case, $F_Q[|\psi\rangle; \hat{J}_{\vec{n}}] = 4\langle(\Delta\hat{J}_{\vec{n}})^2\rangle_{|\psi\rangle}$ as mentioned above. (iii) It is easy to see that for a product state $|\phi_A\rangle \otimes |\chi\rangle_B$, $4\langle(\Delta[\hat{J}_{\vec{n}}]_{AB})^2\rangle_{|\phi\rangle_A \otimes |\chi\rangle_B} =$

$4\langle(\Delta[\hat{J}_{\vec{n}}]_A)^2\rangle_{|\phi\rangle_A} + 4\langle(\Delta[\hat{J}_{\vec{n}}]_B)^2\rangle_{|\chi\rangle_B}$. Here $[\hat{J}_{\vec{n}}]_{AB}$ acts on all the particles while $[\hat{J}_{\vec{n}}]_A$ acts on the particles of $|\psi\rangle_A$ only and in analogy for $[\hat{J}_{\vec{n}}]_B$. (iv) For a state with N particles, $4\langle(\Delta\hat{J}_{\vec{n}})^2\rangle \leq N^2$ holds [3]. The inequality is saturated uniquely by the state $|GHZ\rangle = \frac{1}{\sqrt{2}}(|0\rangle^{\otimes N} + |1\rangle^{\otimes N})$, known as the GHZ [35] or NOON [36] state.

Let us now consider the state $|\psi\rangle = \bigotimes_{j=1}^M |\psi_j\rangle$, where $|\psi_j\rangle$ is a state of N_j particles, and $\sum_j N_j = N$. If we allow for at most k particles to be entangled, then $N_j \leq k$. Since $(N_1+1)^2 + (N_2-1)^2 \geq N_1^2 + N_2^2$ if $N_1 \geq N_2$, the quantum Fisher information is increased by making the N_j as large as possible. Hence the maximum is reached by choosing $N_j = k$ for $s = \lfloor\frac{N}{k}\rfloor$ states, where $\lfloor x \rfloor$ is the largest integer smaller or equal to x, and by collecting the remaining $r = N - sk$ particles in the last state. Therefore, for k-partite entangled states, the quantum Fisher information is bounded by Eq. (6). □

The bound can be saturated by a product of s GHZ states of k particles and another GHZ state of r particles. We point out that for $k = 1$ we recover the bound (4) for separable states, while for $k = N - 1$, the bound is

$$F_Q[\rho_{(N-1)-\text{ent}}; \hat{J}_{\vec{n}}] \leq (N-1)^2 + 1. \tag{7}$$

These results could have been obtained directly by using the Wigner-Yanase information I [37]. The bound (6) has been derived previously for $4I$ in Ref. [10], and directly applies to the quantum Fisher information since I is convex in the states and agrees with the Fisher information on pure states, $F[|\psi\rangle; \hat{J}_{\vec{n}}] = 4I(|\psi\rangle, \hat{J}_{\vec{n}})$. We have presented the derivation here in order to emphasize that the classification relies on GHZ states, and in order to introduce concepts that we will also need in the following.

For a fixed direction $\vec{n}$, the criterion (6) has a clear operational meaning, because if the bound is surpassed, then the state contains $(k+1)$-partite entanglement, and it will enable a better precision when used in the interferometer defined by $\hat{J}_{\vec{n}}$ than all k-partite entangled states. If used as a criterion for multiparticle entanglement, it is therefore advantageous to optimize the direction $\vec{n}$, which can be done analytically as follows: the quantum Fisher information can be written as [6]

$$F[\rho; \hat{J}_{\vec{n}}] = 4\vec{n}^T \Gamma_C \vec{n}. \tag{8}$$

The matrix Γ_C is real and symmetric and has the entries

$$[\Gamma_C]_{ij} = \frac{1}{2}\sum_{l,m} \frac{(\lambda_l - \lambda_m)^2}{\lambda_l + \lambda_m}\langle l|\hat{J}_i|m\rangle\langle m|\hat{J}_j|l\rangle, \tag{9}$$

where the states $|k\rangle$ and the variables λ_k are defined by the eigenvalue decomposition of the input state, $\rho = \sum_k \lambda_k |k\rangle\langle k|$. It follows that $F_Q^{\max}[\rho] \equiv \max_{\vec{n}} F_Q[\rho; \hat{J}_{\vec{n}}] = 4\lambda_{\max}(\Gamma_C)$, where $\lambda_{\max}(\Gamma_C)$ is the maximal eigenvalue of Γ_C [6]. We will always use $F_Q^{\max}[\rho]$

in the following and refer to the bound (6) as F_Q^{k+1} criterion since it allows for the detection of $(k+1)$-entanglement *via* its violation.

B. Criteria from $\bar{F}_Q$

We will now derive similar bounds for the average quantum Fisher information, which we define as

$$\bar{F}_Q[\rho] = \frac{1}{4\pi}\int_{|\vec{n}|^2=1} d^3\vec{n}\ F_Q[\rho; \hat{J}_{\vec{n}}]. \tag{10}$$

The prefactor ensures normalization in the sense that if $F[\rho; \hat{J}_{\vec{n}}] = F[\rho; \hat{J}_x]$ is independent of the direction $\vec{n}$, then $\bar{F}_Q = F[\rho; \hat{J}_x]$. The quantity $\bar{F}_Q$ has the following meaning: suppose that an experiment implements an interferometer with a fixed phase shift θ, but with no control over the axis $\vec{n}$ of rotation, such that in each run of the experiment, the interferometer operation is given by $\exp[-i\hat{J}_{\vec{n}}\theta]$, with a random direction $\vec{n}$. If all directions appear with equal probability, and for $m \gg 1$ independent repetitions of the experiment, the corresponding quantum Fisher information would be given $m\ \bar{F}_Q$.

The average can be written as $\bar{F}_Q = \frac{1}{\pi}\sum_{i,j}[\Gamma_C]_{i,j}\int_{|\vec{n}|^2=1} d^3\vec{n}\ n_i n_j$. Evaluating the integrals leads to

$$\bar{F}_Q = \frac{4}{3}\text{Tr}[\Gamma_C] = \frac{1}{3}\Big(F_Q[\rho; \hat{J}_x] + F_Q[\rho; \hat{J}_y] + F_Q[\rho; \hat{J}_z]\Big). \tag{11}$$

We would like to determine bounds on $\bar{F}_Q$ for k-partite entangled states in analogy to the bounds that we found for F_Q. Again, we directly state the results and derive them afterwards.

Observation 2 ($\bar{F}_Q^{k+1}$ criteria). *For k-partite entangled states and a linear two-mode interferometer with a generator $\hat{J}_{\vec{n}}$ with an arbitrary direction $\vec{n}$, the average quantum Fisher information is bounded by*

$$\bar{F}_Q[\rho_{k-\text{ent}}] \leq \frac{1}{3}[s(k^2 + 2k - \delta_{k,1}) + r^2 + 2r - \delta_{r,1}], \tag{12}$$

where $s = \lfloor\frac{N}{k}\rfloor$ and $r = N - sk$. Hence a violation of the bound (12) proves $(k+1)$-partite entanglement. For separable states, corresponding to $k = 1$, the bound becomes

$$\bar{F}_Q[\rho_{\text{sep}}] \leq \frac{2}{3}N. \tag{13}$$

The maximal value for any quantum state is given by

$$\bar{F}_Q \leq \frac{1}{3}[N^2 + 2N]. \tag{14}$$

Proof. Let us first prove Eq. (14). Since $\bar{F}_Q$ can be written as the sum of three quantum Fisher informations, it is also convex in the states. Therefore, the maximum is again reached for pure states. Hence

4

$\bar{F} \leq \frac{4}{3} \max_{|\psi\rangle} [\langle \vec{\hat{J}}^2 \rangle_{|\psi\rangle} - \langle \vec{\hat{J}} \rangle_{|\psi\rangle}^2] \leq \frac{4}{3} j(j+1)$. This leads to Eq. (14) since $j = \frac{N}{2}$. The last inequality follows because $\langle \vec{\hat{J}} \rangle_{|\psi\rangle}^2 \geq 0$ and

$$\langle \vec{\hat{J}}^2 \rangle_{|\psi\rangle} \leq j(j+1) \tag{15}$$

holds in general, while equality is reached by the symmetric states of N particles.

For the state $|\psi\rangle = \bigotimes_{j=1}^{M} |\psi_j\rangle$ introduced in the proof of Observation 1, the average quantum Fisher information is given by $\bar{F}_Q = \frac{4}{3} \sum_{j=1}^{M} [\langle \vec{\hat{J}}_j^2 \rangle_{|\psi_j\rangle} - \langle \vec{\hat{J}}_j \rangle_{|\psi_j\rangle}^2] \leq \frac{1}{3} \sum_{j=1}^{M} [N_j^2 + 2N_j - 4\langle \vec{\hat{J}}_j \rangle_{|\psi_j\rangle}^2]$, where $\vec{\hat{J}}_j$ is the vector of collective spin operators acting on the particles contained in state $|\psi_j\rangle$. The inequality is due to Eq. (15). In the same way as it was for F_Q, it is advantageous to increase the N_j as much as possible. This is true even though if $N_j = 1$ then $\bar{F}_Q$ is reduced by $\frac{1}{3}$ since $\langle \vec{\hat{J}} \rangle_{|\psi_j\rangle}^2 = \frac{1}{4}$ in this case. For $k \in [1, N]$, we obtain the bound (12), where $s = \lfloor \frac{N}{k} \rfloor$ and $r = N - sk$ as above, and we obtain Eq. (13) for $k = 1$. $\qquad \square$

If a state violates the bound (12), then it is $(k+1)$-entangled. Therefore, we refer to this bound as $\bar{F}_Q^{k+1}$ criterion. Let us note that the bound for $k = N-1$ is

$$\bar{F}_Q[\rho_{(N-1)-\text{ent}}] \leq \frac{1}{3}[N^2 + 1]. \tag{16}$$

C. F_Q criteria vs. $\bar{F}_Q$ criteria

Since both the F_Q^{k+1} criteria and the $\bar{F}_Q^{k+1}$ criteria seem to be very much related, it is natural to ask whether or not one set of criteria is stronger than the other. We examine this question for $k = 1$ and $k = N-1$ only, since the other possible values of k depend on N. The result is as follows.

Observation 3. *For $k = 1$ and $k = N-1$, the F_Q^{k+1} criteria and the $\bar{F}_Q^{k+1}$ criteria detect different sets of states which are not contained in each other.*

In order to prove this, we consider states of the form

$$\rho(p) = p|\psi\rangle\langle\psi| + (1-p)\frac{\mathbb{1}}{2^N}, \tag{17}$$

mixtures of a pure state and the totally mixed state. It can be shown directly from Eq. (9) that

$$\Gamma_C[\rho(p)] = \gamma_{p,N} \Gamma_C[|\psi\rangle], \quad \gamma_{p,N} = \frac{p^2 2^{N-1}}{p(2^{N-1}-1)+1} \tag{18}$$

holds. Let us first consider the case $k = N-1$. The criteria (7) and (16) can be rewritten as $\gamma_{p,N} \leq \alpha_N^{(1,2)}$, where $\alpha_N^{(1)} = [(N-1)^2 + 1]/F_Q^{\max}[|\psi\rangle]$ and $\alpha_N^{(2)} = [N^2 + 1]/4\text{Tr}(\Gamma_C[|\psi\rangle])$, respectively. In order to violate

the criteria,

$$p > \alpha_N^{(1,2)} \frac{1 - 2^{1-N}}{2} \left[1 + \sqrt{1 + \frac{1}{\alpha_N^{(1,2)}} \frac{2^{3-N}}{(1-2^{1-N})^2}} \right]. \tag{19}$$

This function is strictly monotonically increasing with $\alpha_N^{(1,2)}$. If, for instance, $\alpha_N^{(1)} < \alpha_N^{(2)}$, then the F_Q^N criterion detects the states as multipartite entangled already for a smaller value of p than the $\bar{F}_Q^N$ criterion. Therefore, we can prove the claim by comparing the α coefficients for different states $|\psi\rangle$.

We employ the GHZ state introduced above and the twin-Fock state $|\text{TF}_N\rangle = |\frac{N}{2}, 0\rangle$ with an equal number of particles in both states [38], which is well known to provide sub shot-noise phase sensitivity [38–40]. For the GHZ states, the eigenvalues of $4\Gamma_C$ are N^2, N, and N, while for the twin-Fock states, the eigenvalue are $\frac{N^2}{2} + N$ appears twice, and the third eigenvalue vanishes [6]. While the GHZ state achieves the highest value of the Fisher information possible for $\vec{n} = \hat{z}$, where $\hat{z}$ is the unit vector pointing in the z-direction, it is shot-noise limited for any direction in the $x - y$ plane [6]. In contrast, the twin-Fock state surpasses the shot-noise limit for any direction in the $x - y$-plane, and does not provide any information on the phase when the z-direction is used [6, 41, 42]. We obtain $F_Q^{\max} = N^2$ and $\bar{F}_Q = N^2 + 2N$ for the GHZ state and $F_Q^{\max} = \frac{N^2}{2} + N$, and $\bar{F}_Q = N^2 + 2N$ for the twin-Fock state. Inserting these values into $\alpha_N^{(1,2)}$, we directly see that $\alpha_N^{(1)}(\text{GHZ}) < \alpha_N^{(2)}(\text{GHZ})$ while $\alpha_N^{(1)}(\text{TF}) > \alpha_N^{(2)}(\text{TF})$. This proves the claim for $k = N-1$.

We can apply the same reasoning to the case $k = 1$, where we have to adapt $\alpha_N^{(1)} \rightarrow \beta^{(1)} = N/F_Q^{\max}[|\psi\rangle]$ and $\alpha_N^{(2)} \rightarrow \beta^{(2)} = N/2\text{Tr}(\Gamma_C[|\psi\rangle])$. For the GHZ state, we obtain as before that $\beta^{(1)}(\text{GHZ}) < \beta^{(2)}(\text{GHZ})$ while for the twin-Fock state $\beta^{(1)}(\text{TF}) = \beta^{(2)}(\text{TF})$ holds. However, we can construct an example where the $\bar{F}_Q^2$ criterion is stronger. We observe that $\beta^{(1)} > \beta^{(2)} \Leftrightarrow 2\text{Tr}(\Gamma_C[|\psi\rangle]) > F_Q^{\max}[|\psi\rangle]$. An interesting class of states which fulfills this condition is defined by $4\Gamma_C = c_N \mathbb{1}$. These states have the same value $F_Q = c_N = \bar{F}_Q$ for *any* direction $\vec{n}$. One way of constructing such states is by considering a symmetric state $|\psi\rangle = \sum_k \alpha_k |j, m_k\rangle$, and by choosing the α_k and m_k such that $\langle \vec{\hat{J}} \rangle = 0$ and $\langle \hat{J}_x^2 \rangle = \langle \hat{J}_y^2 \rangle = \langle \hat{J}_z^2 \rangle$. The condition $|m_k - m_k'| > 2$ for all k and k' can be used to ensure $\langle \hat{J}_x \rangle = \langle \hat{J}_y \rangle = 0$. We just mention the example $\sqrt{\frac{1}{3}}|2, 2\rangle + \sqrt{\frac{2}{3}}|2, -1\rangle$ for $N = 4$, with $\Gamma_C = 2\mathbb{1}$, and hence $F_Q^{\max} = \bar{F}_Q = 8$. This concludes the proof of our claim.

The last example is interesting because it shows that there are states that cannot beat the shot-noise limit for a fixed direction $\vec{n}$, but that perform better than a separable state on average. We consider various interesting states in the following section.

Criterion	detected 2-ent. [%]	detected 3-ent. [%]
F_Q^2	94.32	-
$\bar{F}_Q^2$	98.38	-
$\mathcal{W}$	-	18.99
DME	-	80.63
DME'	-	82.61
F_Q^3	-	22.93
$\bar{F}_Q^3$	-	27.99

TABLE I: Percentage of detected 2-partite and 3-partite entangled pure three-qubit states. See text for details. DME' the whole family of DME conditions, which is obtained by permuting the qubits of the state.

Criterion	detected DME [%]	detected DME' [%]
$\mathcal{W}$	50.56	12.27
F_Q^3	19.45	4.77
$\bar{F}_Q^3$	13.14	3.25

TABLE II: Percentage of 3-partite entangled states which are detected by the entanglement witness, the criterion F_Q^3 and the crition $\bar{F}_Q^3$. In the middle column, only states violating the DME condition (20) have been generated, while in the last column, also states violating any of the other DME conditions obtained by permutations of the particles have been generated.

IV. EXAMPLES

A. Pure states of 3 particles

In order to get an impression of the strength of the criteria, we randomly choose a three-qubit state $|\psi\rangle$ and analyze it using various criteria. First, we evaluate the criteria F_Q^2 and $\bar{F}_Q^2$ which detect entanglement. Further, we compare several criteria detecting multiparticle entanglement: (i) the entanglement witness $\mathcal{W} = \frac{1}{2}\mathbb{1} - |\text{GHZ}\rangle\langle\text{GHZ}|$, which has a positive expectation value for all 2-partite entangled states [43], (ii) the density matrix element condition (DME) which states that

$$|\rho_{18}| \leq \sqrt{\rho_{22}\rho_{77}} + \sqrt{\rho_{33}\rho_{66}} + \sqrt{\rho_{44}\rho_{55}} \qquad (20)$$

for all 2-entangled states (ρ_{ij} denote coefficients of a given density matrix $\rho = |\psi\rangle\langle\psi|$) [44], and (iii) the multipartite criteria F_Q^3 and $\bar{F}_Q^3$.

To generate a random pure state [45], we take a vector of a random unitary matrix distributed according to the Haar measure on U(8):

$$|\psi\rangle = (\cos\alpha_7, \cos\alpha_6\sin\alpha_7 e^{i\phi_7}, \cos\alpha_5\sin\alpha_6\sin\alpha_7 e^{i\phi_6}, \\ \dots, \sin\alpha_1\cdots\sin\alpha_7 e^{i\phi_1}), \qquad (21)$$

where $\alpha_i \in [0, \pi/2]$ and $\phi_k = [0, 2\pi]$. The parameters are drawn with the probability densities: $P(\alpha_i) = i\sin(2\alpha_i)(\sin\alpha_i)^{2i-2}$ and $P(\phi_i) = 1/2\pi$. The calculations were performed for a set of 10^6 states. The results are presented in Tab. I. The averaged criteria seem to detect more states in general. It is surprising that the witness condition detects nearly as many states as the criteria F_Q^3 and $\bar{F}_Q^3$.

B. GHZ-diagonal states

The DME criterion (20) and the criteria obtained thereof by permutations of the qubits completely characterize the GHZ-diagonal states of three qubits [21], which can be written as

$$\frac{1}{\mathcal{N}}\begin{pmatrix} \lambda_1 & 0 & 0 & 0 & 0 & 0 & 0 & \mu_1 \\ 0 & \lambda_2 & 0 & 0 & 0 & 0 & \mu_2 & 0 \\ 0 & 0 & \lambda_3 & 0 & 0 & \mu_3 & 0 & 0 \\ 0 & 0 & 0 & \lambda_4 & \mu_4 & 0 & 0 & 0 \\ 0 & 0 & 0 & \mu_4 & \lambda_5 & 0 & 0 & 0 \\ 0 & 0 & \mu_3 & 0 & 0 & \lambda_6 & 0 & 0 \\ 0 & \mu_2 & 0 & 0 & 0 & 0 & \lambda_7 & 0 \\ \mu_1 & 0 & 0 & 0 & 0 & 0 & 0 & \lambda_8 \end{pmatrix} \qquad (22)$$

with real coefficients λ_i and μ_i, where $\mathcal{N}$ is a normalization factor. If $\lambda_i = \lambda_{9-i}$ for $i = 5, 6, 7, 8$, then these states are diagonal in the GHZ-basis $|\psi_{kl}^{\pm}\rangle = \frac{1}{\sqrt{2}}(|0kl\rangle \pm |1\bar{k}\bar{l}\rangle)$, where k and l are equal to 0 or 1, and $\bar{1} = 0$ and $\bar{0} = 1$. We generated 10^6 random states of this form violating Eq. (20) directly, which states $|\mu_1| \leq \lambda_2 + \lambda_3 + \lambda_4$ in this case. The results are shown in Tab. II in the middle column. Then, we generated again 10^6 states violating Eq. (20) or its other forms obtained by permuting the qubits. The results are shown in the right column of Tab. II. The witness criterion detects significantly more states than the criteria based on the Fisher information. Contrary to the case of pure states, the F_Q^3 criterion detects more states than $\bar{F}_Q^3$ in this case. Note that the percentage of detected states reduces significantly for all criteria in the DME' case. The reason is that all criteria work best for the *symmetric* GHZ state, which has the highest weight in the state if only condition (20) is used [21].

The family of states (22) also comprises bound entangled states if $\lambda_1 = \lambda_8 = \mu_1 = 1$ and $\lambda_7 = 1/\lambda_2$, $\lambda_6 = 1/\lambda_3$, $\lambda_5 = 1/\lambda_4$, and $\mu_2 = \mu_3 = \mu_4 = 0$, as long as $\lambda_2\lambda_3 \neq \lambda_4$. Then the states have a positive partial transpose (PPT) [46] for any bipartition of the three particles while still being entangled [33]. It follows that the state cannot be distilled to a GHZ state [11, 47]. We generated again 10^6 random states of these class and applied F_Q^2 and $\bar{F}_Q^2$, but neither criterion detected any of these states. However, we will see presently that $\bar{F}_Q$ is in fact able to detect bound entanglement.

C. Detecting bound entangled states

We consider two families of states where the state has a PPT with respect to some bipartitions, but not with respect to others. Due to the PPT bipartitions it is not possible to distill these states to a GHZ state nontheless [11].

1. Dür state

Interestingly, the $\bar{F}_Q^2$ criterion (13) can reveal entanglement of a bound entangled state introduced by Dür [48]:

$$\rho_N = \frac{1}{N+1}\left(|\phi\rangle\langle\phi| + \frac{1}{2}\sum_{k=1}^{N}(P_k + \bar{P}_k)\right), \quad (23)$$

with $|\phi\rangle = \frac{1}{\sqrt{2}}\left[|0\rangle_1...|0\rangle_N + e^{i\varphi_N}|1\rangle_1...|1\rangle_N\right]$ (φ_N is an arbitrary phase), and P_k being a projector on the state $|0\rangle_1...|1\rangle_k...|0\rangle_N$ with "1" on the kth position ($\bar{P}_k$ is obtained from P_k after replacing "0" by "1" and vice versa). As an example, let us consider cases for $N = 4, 6$ and 8. The corresponding values of $\overline{F}_Q$ are equal to $136/45 \approx 3.02, 104/21 \approx 4.95$ and $560/81 \approx 6.91$, whereas the bounds for entanglement are equal to $8/3 \approx 2.67$, 4 and $16/3 \approx 5.33$, respectively. In the three cases we prove entanglement of the state ρ_N. However, note that in all cases the F_Q^2 criterion does not detect the entanglement. Hence the state is not useful for sub shot-noise interferometry for any direction $\vec{n}$, even though it is more useful than separable states on average over all directions.

2. Generalized Smolin state

As a second example, consider the generalized Smolin state [49]:

$$\rho_N = \frac{1}{2^N}\left(\mathbb{1}^{\otimes N} + (-1)^{N/2}\sum_{i=1}^{3}\sigma_i^{\otimes N}\right). \quad (24)$$

Similarly as above, take the cases of four, six and eight qubits. For these states, the average quantum Fisher information $\overline{F}_Q$ is equal to 4,6 and 8, respectively. The corresponding bounds for entanglement are $8/3 \approx 2.67$, 4 and $16/3 \approx 5.33$ are violated. Again, F_Q^2 does not detect the entanglement of the states.

V. RELATION TO SPIN SQUEEZING INEQUALITIES

A. Spin squeezing parameter and multiparticle entanglement

Let us now compare the criteria based on F_Q and $\bar{F}_Q$ to spin squeezing criteria. Introducing two orthogonal unit vectors $\vec{n}_1$ and $\vec{n}_2$, then the so-called spin-squeezing parameter ξ can be defined as [24]

$$\xi^2 = \frac{N|\langle\hat{J}\rangle_{\vec{n}_1}|^2}{\langle(\Delta\hat{J}_{\vec{n}_2})^2\rangle}. \quad (25)$$

If $\xi < 1$, the corresponding state is useful for sub shot-noise interferometry [24] and entangled, since $\xi^2 \geq 1$ holds for all separable states [25]. This also follows directly from the following inequality

$$F_Q[\rho; \hat{J}_{\vec{n}_3}] \geq \frac{N}{\xi^2}, \quad (26)$$

where $\vec{n}_3$ is a unit vector orthogonal to $\vec{n}_1$ and $\vec{n}_2$ (the vectors may form a right- or left-handed coordinate system) [50].

¿From Eq. (26) it also follows that the F_Q^2 criterion detects all states that the spin-squeezing criterion detects. In fact, it detects more states. For instance, all states with $\langle\vec{\hat{J}}\rangle = 0$, such as the twin Fock state, are not spin squeezed. Nevertheless, the twin Fock state is entangled and useful for sub shot-noise interferometry.

Similarly, bounds on multiparticle entanglement for ξ have been derived as follows [26]. First, the authors regard a single spin-j particle, and compute

$$f_j(\langle\hat{J}_z\rangle) = \min_\rho\langle(\Delta\hat{J}_x)^2\rangle\Big|_{\langle\hat{J}_z\rangle_\rho=\langle\hat{J}_z\rangle}, \quad (27)$$

where the minimization is performed over all states ρ of the spin-j particle which fulfil $\langle\hat{J}_z\rangle_\rho = \langle\hat{J}_z\rangle$. It is then shown that for separable states of s spin-j particles, $\rho_{\text{sep}} = \sum_k p_k \otimes_{l=1}^{s} |\psi_k^{(l)}\rangle\langle\psi_k^{(l)}|$, where $|\psi_k^{(l)}\rangle$ is a state of a spin-j particle, the inequality

$$\langle(\Delta\hat{J}_x)^2\rangle \geq s f_j\left(\frac{\langle\hat{J}_z\rangle}{s}\right) \quad (28)$$

holds. If the spin-j particles are composed of k spin-$\frac{1}{2}$ particles, then this condition is fulfilled by all k-particle entangled states, and a violation proves the presence of $(k+1)$-particle entanglement. Note that this criterion assumes that in the decomposition of the separable states each state is separable with respect to *the same* partition and that $N = sk$ holds. Both assumptions can be relaxed [51].

Due to Eq. (26), we obtain that for fixed $\langle\hat{J}_z\rangle$, and for $\vec{n}_1 = \hat{z}$, $\vec{n}_2 = \hat{x}$, and $\vec{n}_3 = \hat{y}$, the bounds

$$\frac{N}{\xi^2} \leq \frac{|\langle\hat{J}_z\rangle|^2}{\langle(\Delta\hat{J}_x)^2_{\rho^*_{k-\text{ent}}}\rangle} \leq F_Q[\rho^*_{k-\text{ent}}; \hat{J}_y]$$

$$\leq \max_\rho F_Q[\rho; \hat{J}_y]_{\langle\hat{J}_z\rangle_\rho=\langle\hat{J}_z\rangle} \leq nk^2 + r^2, \quad (29)$$

where $\rho^*_{k-\text{ent}}$ is a k-partite entangled state that minimizes $\langle(\Delta\hat{J}_x)^2\rangle$ for a given $\langle\hat{J}_z\rangle$. The third inequality might be strict due to the limitations of the spin squeezing inequalities, which do not recognize the usefulness of states with

$\langle \vec{\hat{J}} \rangle = 0$, as mentioned above. The last inequality is due to Eq. (6), which bounds the maximal quantum Fisher for *any* k-partite entangled state, not restricted to the subspace with fixed $\langle \hat{J}_z \rangle$.

Note that the condition (28) may recognize a state as $(k+1)$-partite entangled that is not detected by the F_Q^{k+1} criterion (6). This kind of $(k+1)$-entanglement is then not more useful for interferometry than k-partite entanglement. This happens precisely when some of the inequalities are strict.

B. Relation of $\bar{\mathbf{F}}_\mathbf{Q}$ and a generalized spin squeezing criterion

Finally, let us point out a connection to a different criterion which detects entanglement, but is not directly related to interferometry. The so-called *generalized* spin squeezing criteria are entanglement criteria based only on first and second moments of collective operators $\hat{J}_{\vec{n}}$ [52, 53]. In particular, for all general mixed separable states the following inequality holds [54]

$$4[(\Delta \hat{J}_x)^2 + (\Delta \hat{J}_y)^2 + (\Delta \hat{J}_z)^2] \geq 2N. \qquad (30)$$

For pure states, the left hand side equals $3\bar{F}$, and therefore, this bound is complementary to the bound (13). However, for pure states, equality holds in both Eq. (30) and Eq. (13), and no contradiction arises.

VI. CONCLUSIONS AND OUTLOOK

We have introduced criteria based on the quantum Fisher information for the detection of entangled states of different multipartite entanglement classes. Additionally, we showed that the quantum Fisher information averaged over all directions on the Bloch sphere is a suitable alternative to detect multipartite entanglement. We considered several examples, showing in particular that the average quantum Fisher information can be used to detect bound entangled states. It remains an interesting open question whether or not there exist bound entangled states which are detected by the quantum Fisher information, since this would imply that such states could be used for sub shot-noise interferometry. We also pointed out the relation of the bounds we derived for the quantum Fisher information to bounds on the spin squeezing parameter for multipartite entanglement classes derived by Sørensen and Mølmer [26].

Note added: Independently from our work, a paper on the relationship between multipartite entanglement and Fisher information is under preparation [55].

[1] M. A. Nielsen and I. L. Chuang, *Quantum Computation and Quantum Information* (Cambridge University Press, 2000).
[2] V. Giovannetti, S. Lloyd, and L. Maccone, Science **306**, 1330 (2004).
[3] V. Giovannetti, S. Lloyd, and L. Maccone, Phys. Rev. Lett. **96**, 010401 (2006).
[4] L. Pezzé and A. Smerzi, Phys. Rev. Lett. **102**, 100401 (2009).
[5] The connection between shot-noise limit and separability for a non-fixed number of particles has been discussed in P. Hyllus, L. Pezzé, and A. Smerzi, arXiv:1003.0649.
[6] P. Hyllus, O. Gühne, and A. Smerzi, arXiv:0912.4349.
[7] R. Horodecki, P. Horodecki, M. Horodecki, and K. Horodecki, Rev. Mod. Phys. **81**, 865 (2009).
[8] M.B. Plenio and S. Virmani, Quant. Inf. Comp. **7**, 1 (2007).
[9] O. Gühne and G. Tóth, Physics Reports **474**, 1 (2009).
[10] Z. Chen, Phys. Rev. A **71**, 052302 (2005).
[11] W. Dür, J.I. Cirac, and R. Tarrach, Phys. Rev. Lett. **83**, 3562 (1999); W. Dür and J.I. Cirac, Phys. Rev. A **61**, 042314 (2000).
[12] M. Horodecki, P. Horodecki, and R. Horodecki, Phys. Lett. A **283**, 1 (2001).
[13] P. Wocjan and M. Horodecki, Open Syst. Inf. Dyn. **12**, 331 (2005).
[14] C.S. Yu and H.S. Song, Phys. Rev. A **72**, 022333 (2005).
[15] A.S.M. Hassan and P.S. Joag, QIC **8**, 773 (2008).
[16] M. Hillery, H.T. Dung, and H. Zheng, Phys. Rev. A **81**, 062322 (2010).
[17] D. Collins, N. Gisin, S. Popescu, D. Roberts, and V. Scarani, Phys. Rev. Lett. **88**, 170405 (2002).
[18] M. Seevinck and J. Uffink, Phys. Rev. A **65**, 012107 (2002).
[19] C. Schmid, N. Kiesel, W. Laskowski, W. Wieczorek, and M. Żukowski, and H. Weinfurter, Phys. Rev. Lett. **100**, 200407 (2008).
[20] J.-D. Bancal, C. Branciard, N. Gisin, and S. Pironio, Phys. Rev. Lett. **103**, 090503 (2009).
[21] O. Gühne and M. Seevinck, New Jour. Phys. **12**, 053002 (2010).
[22] M. Huber, F. Minter, A. Gabriel, and B.C. Hiesmayr,

Phys. Rev. Lett. **104**, 210501 (2010).

[23] S. L. Braunstein and C. M. Caves, Phys. Rev. Lett. **72**, 3439 (1994).

[24] D.J. Wineland, J.J. Bollinger, W.M. Itano, and D.J. Heinzen, Phys. Rev. A **50**, 67 (1994).

[25] A. Sørensen, L.-M. Duan, J. I. Cirac, and P. Zoller, Nature **409**, 63 (2001).

[26] A. Sørensen and K. Mølmer, Phys. Rev. Lett. **86**, 4431 (2001).

[27] C. W. Helstrom, *Quantum Detection and Estimation Theory* (Academic Press, New York, 1976).

[28] A. S. Holevo, *Probabilistic and Statistical Aspects of Quantum Theory* (North-Holland, Amsterdam, 1982).

[29] H. Cramer, Mathematical methods of Statistics (Princeton University Press, Princeton, NJ, 1946), esp. pp. 500-504.

[30] B. Yurke, S. L. McCall, and J. R. Klauder, Phys. Rev. A **33**, 4033 (1986).

[31] R. F. Werner, Phys. Rev. A **40**, 4277 (1989).

[32] O. Gühne, G. Tóth, and H. J. Briegel, New J. Phys. **7**, 229 (2005); O. Gühne and G. Tóth, Phys. Rev. A 73, 052319 (2006).

[33] A. Acín, D. Bruß, M. Lewenstein, and A. Sanpera, Phys. Rev. Lett. **87**, 040401 (2001).

[34] M. L. Cohen, IEEE Transactions on Information Theory **14**, 591 (1968).

[35] D. M. Greenberger, M. Horne, and A. Zeilinger, Am. J. Phys. **58**, 1131 (1990).

[36] H. Lee, P. Kok, and J. P. Dowling, J. Mod. Opt. **49**, 2325 (2002).

[37] E.P. Wigner and M.M. Yanase, Proc. Natl. Acad. Sci. U.S.A. **49**, 910 (1963).

[38] M. J. Holland and K. Burnett, Phys. Rev. Lett. **71**, 1355 (1993).

[39] R. A. Campos, C. C. Gerry, and A. Benmoussa, Phys. Rev. A **68**, 023810 (2003).

[40] L. Pezzé and A. Smerzi, Phys. Rev. A **73**, 011801(R) (2006).

[41] W. Wieczorek, R. Krischek, W. Laskowski and H. Weinfurter, in preparation.

[42] W. Wieczorek, PhD thesis, LMU Munich (2009).

[43] M. Bourennane, M. Eibl, Ch. Kurtsiefer, S. Gaertner, H. Weinfurter, O. Gühne, P. Hyllus, D. Bruss, M. Lewenstein, A. Sanpera, Phys. Rev. Lett. **92**, 087902 (2004).

[44] O. Gühne, M. Seevinck, New J. Phys. **12**, 053002 (2010).

[45] K. Życzkowski, H. Sommers, J. Phys. A: Math. Gen. **34** 7111 (2001).

[46] A. Peres, Phys. Rev. Lett. **77**, 1413 (1996); M. Horodecki, P. Horodecki, and R. Horodecki, Phys. Lett. A **223**, 1 (1996).

[47] M. Horodecki, P. Horodecki, and R. Horodecki, Phys. Rev. Lett. **80**, 5239 (1998).

[48] W. Dür, Phys. Rev. Lett. **87**, 230402 (2001).

[49] J. A. Smolin, Phys. Rev. A **63**, 032306 (2001); R. Augusiak, P. Horodecki, Phys. Rev. A **73**, 012318 (2006).

[50] This inequality was derived in Ref. [5]. Note that for pure states it follows simply from the commutation relations of the collective spin operators $[\hat{J}_{\vec{n}_1}, \hat{J}_{\vec{n}_2}] = \pm i\hat{J}_{\vec{n}_3}$, where the sign depends on the coordinate system used. Heisenberg's uncertainty relation $\langle(\Delta\hat{J}_{\vec{n}_2})^2\rangle\langle(\Delta\hat{J}_{\vec{n}_3})^2\rangle \geq \frac{|\langle\hat{J}_{\vec{n}_1}\rangle|^2}{4}$ leads to Eq. (26) since $F_Q[\rho; \hat{J}_{\vec{n}_3}] = 4\langle(\Delta\hat{J}_{\vec{n}_3})^2\rangle$ for pure states.

[51] P. Hyllus, W. Laskowski, R. Krischek, C. Schwemmer, W. Wieczorek, H. Weinfurter, L. Pezzé, and A. Smerzi, in preparation.

[52] G. Tóth, C. Knapp, O. Gühne, and H. J. Briegel, Phys. Rev. Lett. **99**, 250405 (2007).

[53] G. Tóth, C. Knapp, O. Gühne, and H. J. Briegel, Phys. Rev. A **79**, 042334 (2009).

[54] G. Tóth, Phys. Rev. A **69**, 052327 (2004).

[55] G. Tóth, in preparation (2010).

4.1.4 Maximum likelihood and Bayesian phase estimation

Bayesian and maximum likelihood phase estimation are common protocols to estimate an unknown phase shift. Both have already been implemented experimentally [147, 148, 149] but not for sub shot noise sensitivity of more than two particles. Here we implement these protocols with a separable and an entangled state of four photons to highlight the enhanced sensitivity of the entangled with respect to the separable state. The photons are generated by the same down-conversion source as described in Ref. [48]. The linear optics setup shown in Fig. 4.2 allows us to observe both states, the symmetric four photon entangled Dicke state [87]
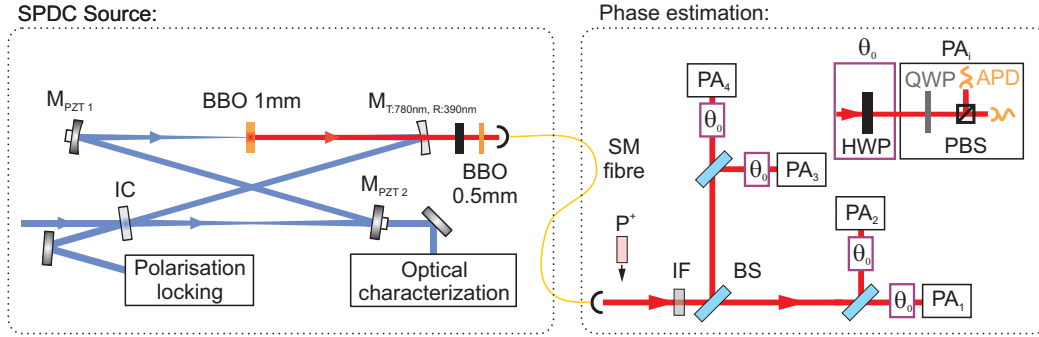
Figure 4.2: **Experimental phase estimation setup**. The spontaneous parametric down-conversion (SPDC) source consists of a 4 mirror (M) bow-tie cavity with a β-Barium Borate (BBO) crystal of 1mm length inside [48]. The cavity is pumped with a pulsed laser of 130fs at 390nm and 0.6W input power. To observe the state ρ_D the power inside the cavity is enhanced to 1.38W. For the state ρ_{sep} to 2.95W. The down converted photons, generated in the BBO crystal, pass a mirror reflective (R) at 390nm and transmissive (T) at 780nm and are then guided via a single mode (SM) fiber to the phase estimation setup. Each qubit can be addressed individually. The setup allows to observe the symmetric four photon Dicke state in Eq. 4.51 at the four output arms. By inserting a $|+\rangle$ polarizer (P$^+$) in front of the first beam splitter (BS) we are also able to observe the separable four photon $|+\rangle$ state in Eq. 4.52. The four photon count rates for both states are $\sim 420\text{min}^{-1}$. Although the enhancement inside the cavity for ρ_{sep} is higher the count rate is not increased with respect to ρ_D, because the polariser acts as a filter and absorbs all photons which are not $|+\rangle$ polarised. For the phase estimation we rotate each qubit by $\exp[-i\hat{\sigma}_y\theta_0/2]$. PZT, piezo electric transducer; IC, input coupler; IF, interference filter; PA, polarization analysis; PBS, polarizing beam-splitter; APD, avalanche photo-diode; QWP, quarterwave-plate; HWP, half wave-plate.

$$| D_4^{(2)} \rangle \;=\; \frac{1}{\sqrt{6}} \Big(| HHVV \rangle + | HVHV \rangle + | HVVH \rangle$$
$$+ | VHHV \rangle + | VHVH \rangle + | VVHH \rangle \Big). \tag{4.51}$$

and by inserting a $|+\rangle$-polarizer in front of the fist beam splitter in Fig. 4.2, we observe the separable state

$$| \Psi_{sep} \rangle \;=\; | + + + + \rangle. \tag{4.52}$$

With these two input states, $\rho_D = | D_4^{(2)} \rangle\langle D_4^{(2)} |$ and $\rho_{sep} = | \Psi_{sep} \rangle\langle \Psi_{sep} |$, we now implement our phase estimation analysis. A phase shift θ_0 is described by the following transformation

$$\hat{R}(\theta_0) = e^{-\frac{i}{2} \sum_{k=1}^{3} \hat{\sigma}_{\vec{n}_j}^{(k)} \theta_0}, \tag{4.53}$$

where $\hat{\sigma}_{\vec{n}_j}$ are the Pauli spin matrices with respect to the rotation direction x, y and z. For the symmetric Dicke state ρ_D every rotation axis lying on the x-y plane reveals the highest phase sensitivity (see ref. [137] and the preprint 4.1.3 [60] for a more detailed discussion). Here we choose $\vec{n}_j = y$. Experimentally, the phase shift is applied by rotating a half-wave plate as depicted in Fig. 4.2, which corresponds to the following rotations [150]

$$\begin{pmatrix} \cos\frac{\theta}{2} & \sin\frac{\theta}{2} \\ \sin\frac{\theta}{2} & -\cos\frac{\theta}{2} \end{pmatrix} \;=\; \sin\frac{\theta}{2}\hat{\sigma}_x + \cos\frac{\theta}{2}\hat{\sigma}_z \tag{4.54}$$

$$= \; i\Big(-i\sin\frac{\theta}{2}\hat{\sigma}_x - i\cos\frac{\theta}{2}\hat{\sigma}_z\Big) \tag{4.55}$$

$$= \; i\Big(-\sin\frac{\theta}{2}\hat{\sigma}_y\hat{\sigma}_z - i\cos\frac{\theta}{2}\hat{\sigma}_z\Big) \tag{4.56}$$

$$= \; i\Big(i\sin\frac{\theta}{2}\hat{\sigma}_y + \cos\frac{\theta}{2}\mathbb{1}\Big)(-i\hat{\sigma}_z) \tag{4.57}$$

$$= \; e^{i\frac{\pi}{2}} e^{i\theta\hat{J}_y} e^{-i\pi\hat{J}_z} \tag{4.58}$$

where we have used the identity $e^{i\theta\hat{J}_j} = i\sin\frac{\theta}{2}\hat{\sigma}_{\vec{n}_j} + \cos\frac{\theta}{2}\mathbb{1}$ with $\hat{J}_j = \frac{1}{2}\hat{\sigma}_{\vec{n}_j}$. From right to the left, the first factor in Eq. 4.58 is a fixed rotation around $\hat{J}_z$. For the input state ρ_D, which lies parallel to $\hat{J}_z$, this rotation has no influence. For the input state ρ_{sep}, which lies parallel to $\hat{J}_x$, this has an influence and therefore we have to redefine the angle for the effective phase shift in the experiment to $\theta_0 = \theta + \pi$ (for ρ_D $\theta_0 = \theta$). The middle term in Eq. 4.58 is the desired rotation around $\hat{J}_y$ and the last term is a global phase. Estimating a phase shift θ_0 by rotating a half-wave plate (see Eq. 4.54) is thus state dependent and under the aforementioned considerations formally equivalent to a Mach-Zehnder interferometer [150].
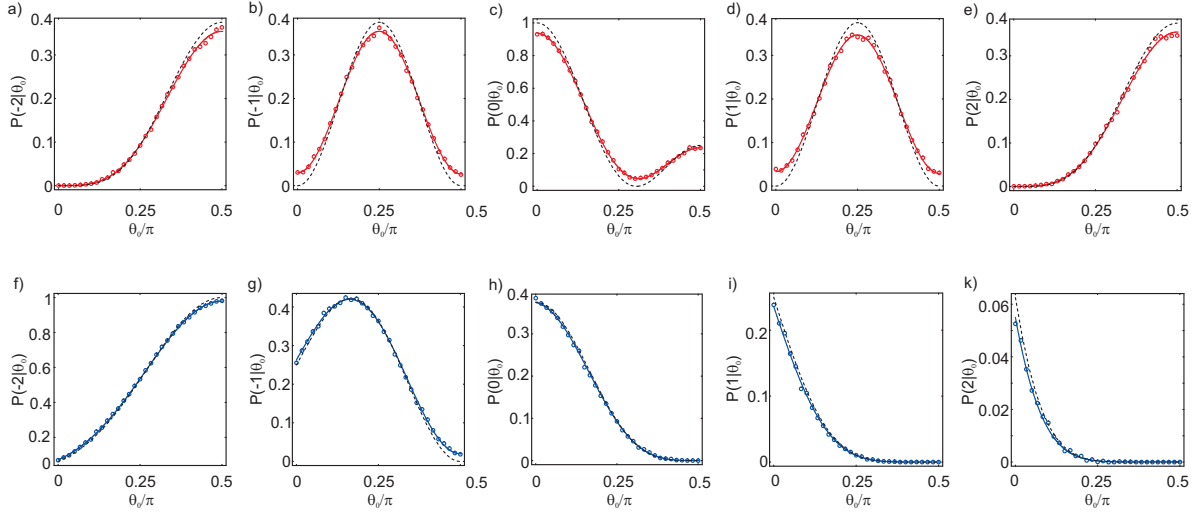
Figure 4.3: **Calibration curves**. The conditional probabilities $P_{exp}(\mu|\theta)$ are shown for the state ρ_D in a) - e) and ρ_{sep} in f) - k). For both states 31 points are measured in the interval $[0, \frac{\pi}{2}]$ indicated with red (ρ_D) or blue (ρ_{sep}) circles. The black dotted lines correspond to the ideal theoretical curves. The continuous red and blue lines are fits to to the measured data points.

In the following we will now apply different phase shifts to our two probe states. The connection between the applied phase shift θ_0 and the observed four photon count rates is given by the conditional probabilities $P(\mu|\theta_0)$ with

$$\mu = \frac{N_H - N_V}{2} \tag{4.59}$$

and $N_H - N_H$ the difference of the number of H and V polarized photons. The conditional probability $P(\mu|\theta_0)$ is the probability for a given μ to observe θ_0. For four photons the possible values for μ are $-2, -1, 0, 1, 2$. In the experiment, the conditional probabilities are measured for 31 different phase shifts θ_0 evenly distributed in the interval $[0, \frac{\pi}{2}]$ and counting the number of μ-events in the detectors. Fig. 4.3 shows the results of the conditional probabilities for both input states and compares the results with the theoretical curves. For the state ρ_D the ideal probabilities are given by

$$P_{id}(\pm 2|\theta_0) = \frac{3}{8}\sin^4(\theta_0) \tag{4.60}$$

$$P_{id}(\pm 1|\theta_0) = \frac{3}{8}\sin^2(2\theta_0) \tag{4.61}$$

$$P_{id}(0|\theta_0) = \frac{1}{16}(1 + 3\cos(2\theta_0))^2 \tag{4.62}$$

and for the state ρ_{sep} as

$$P_{id}(\mu|\theta_0) = \frac{4!}{(2-\mu)!(2+\mu)!}\big(\sin(\frac{\theta_0}{2}-\frac{\pi}{4})\big)^{4+2\mu}\big(\cos(\frac{\theta_0}{2}-\frac{\pi}{4})\big)^{4-2\mu} \qquad (4.63)$$

Each point is measured ~ 6700 times for ρ_D and ~ 9500 times for ρ_{sep}. The different count rates result out of different measurement times. However, the error bars are for both states smaller than the size of the plotted points and are not shown. A fit to these points provides the conditional probabilities $P_{exp}(\mu|\theta)$. The fits for the calibration curves are provides with the ansatz

$$P_{exp}(\mu|\theta_0) = \sum_{\mu=-2}^{2} P(\mu|\mu')P_{id}(\mu'|\theta_0). \qquad (4.64)$$

A least square fit is then performed to the measurement results for both input states for all μ values. To ensure proper normalisation $\sum_{\mu} P_{exp}(\mu|\theta_0) = 1$ for all θ_0 values the additional condition $\sum_{\mu} P(\mu|\mu') = 1$ has to hold for all μ'.

The fitted conditional probabilities $P_{exp}(\mu|\theta_0)$ can now be used to directly calculate the Fisher information in Eq. 4.7 to verify the bounds identifying useful k-particle entanglement introduced in the previous subsection in Eq. 4.50. Several bounds have been determined and are shown in Fig. 4.4 to verify the usefulness of our two probe states. The limit for the Fisher information for separable states with four particles is four and as expected the state ρ_{sep}^{exp} lies for all θ_0 values below this value. This is different for the state ρ_D^{exp}, which is beyond the limit for separable states for several θ_0 values and useful 3-particle entanglement could be identified. Note that the state ρ_D^{exp} can even be identified for useful 4-particle entanglement assuming optimizations over the local directions, further described in the preprint 4.1.5 or in [137].

For the next step, we would like to directly demonstrate the usefulness of our input state ρ_D^{exp} for quantum enhanced metrology in comparison to the separable state ρ_{sep}^{exp}. To this aim, we experimentally implement two different phase estimation protocols. The true phase shift θ_0 is then estimated from the measurement outcomes $\mu_1, \mu_2, ..., \mu_m$ of m independent repetitions of the interferometric protocol to which we will refer as one m-experiment.

First, we will treat maximum likelihood phase estimation, where the true phase shift is estimated with the value θ_{est} by weighting the measurement results μ_i with the prior information of the conditional probabilities and maximizing the likelihood function [138]

$$\mathcal{L}(\theta) = \prod_{i=1}^{m} P_{exp}(\mu_i|\theta) \qquad (4.65)$$

with

$$\theta_{est} = \big\{\theta \,|\, \mathcal{L}(\theta) = \max_{\theta'} \mathcal{L}(\theta')\big\}. \qquad (4.66)$$

For each m-experiment the likelihood function gives an estimator θ_{est} which fluctuates for different m-experiments with standard deviation $\Delta\theta_{est}$. The rescaled uncertainties
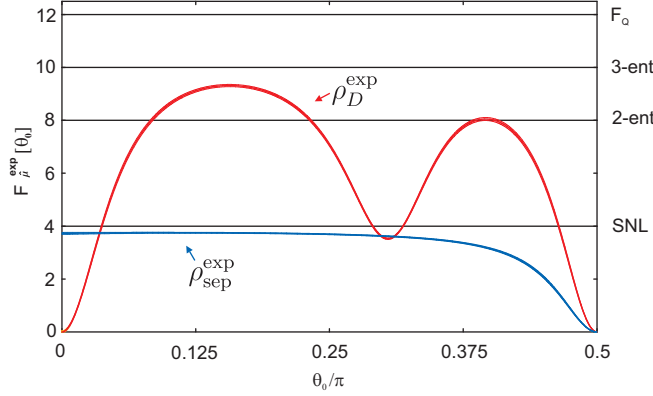
Figure 4.4: **Experimental Fisher information**. The Fisher information is obtained from the conditional probabilities $P_{exp}(\mu|\theta)$ shown in Fig. 4.3 with the formula in Eq. 4.7. The thickness of the red (ρ_D) and blue (ρ_{sep}) lines corresponds to $F[\theta_0] \pm \Delta F[\theta_0]$. The errors $\Delta F[\theta_0]$ are calculated with a monte carlo simulation assuming Poissonian distributed count rates obtained in the calibration measurement of the conditional probabilities. The shot noise limit (SNL) for the Fisher information of four particles is 4 (see Eq. 4.49). With $N = 4$ qubits, 2-particle entangled states have $F_Q \leq 8$ and 3-particle entangled states $F_Q \leq 10$. For the ideal Dicke state $|D_4^{(2)}\rangle$, the quantum Fisher information reaches its maximum value at $F_Q[|D_N^{(N/2)}\rangle, \hat{J}] = N(N+2)/2 = 12$. The maximal value for any 4 qubit quantum state is given by $F_Q \leq N^2 = 16$ which is saturated by the so-called Greenberger-Horne-Zeilinger (GHZ) state [130, 146, 136].

of the estimator (for maximum likelihood estimation: $\Delta_{res} = \sqrt{m}\Delta\theta_{est}$) saturates for a large number of m-experiments the Cramér-Rao lower bound [138], which will be verified in the following experiment. Experimentally we test the estimation protocol for 9 evenly distributed phase shifts θ_0 in the interval $(0, \frac{\pi}{2})$ and for each phase shift we collected ~ 12000 μ_i values for both states. These μ_i values can now be grouped in arrays of length m. In Fig. 4.5 a) - d) the histograms are shown for arrays of length $m = 1, 3, 10$ and 100. The total number of m-experiments is therefore $\sim 12000, \sim 4000, \sim 1200$ and ~ 120. The true phase shift is here 0.2π and the distribution of the estimators are shown in a histogram of 51 bins between $[0, \frac{\pi}{2}]$ after normalization. For small values of m the estimator scatters strongly around the true value θ_0, whereas for big m the spreading gets smaller. This is illustrated in Fig. 4.6 with stars, where the standard deviation of the estimator $\Delta\theta_{est}$ is plotted for 9 phase shifts, once for $m = 10$ and once for $m = 100$. The solid red and blue curve are the inverse Fisher information of ρ_D^{exp} and ρ_{sep}^{exp} from Fig. 4.4. The agreement of the stars to the inverse Fisher information illustrates the overlap with the Cramér-Rao lower bound. For $m = 10$ the agreement is small but for $m = 100$ the inverse Fisher information can be reproduced as expected and sub shot noise sensitivity for several estimators can be proven. The relation between the accordance of the Cramér-Rao lower bound and the number of m's can also be
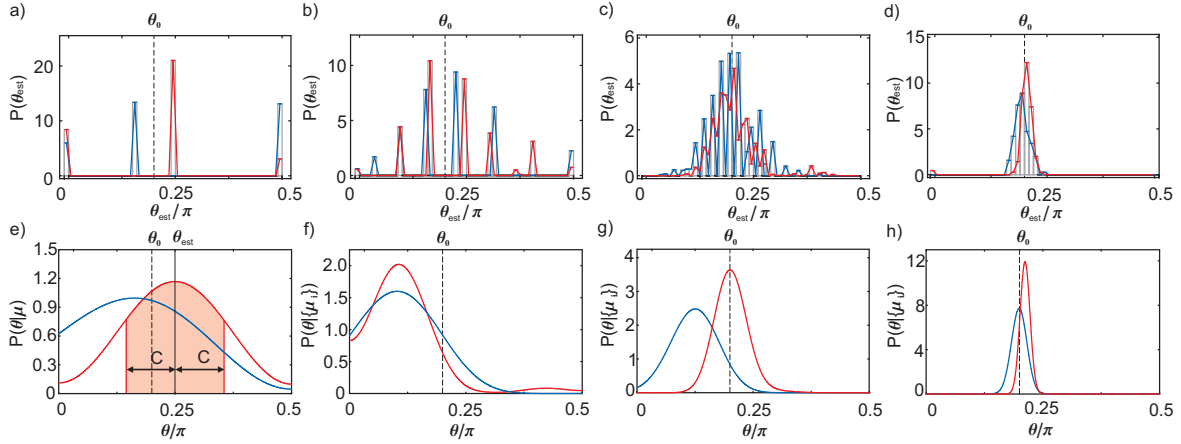
Figure 4.5: **Comparison of maximum likelihood and Bayesian phase estimation**. In the upper row the histograms show the spread of the estimators θ_{est} for a large number of m-experiments for a) $m = 1$, b) $m = 3$, c) $m = 10$ and d) $m = 100$. Blue lines correspond to ρ_{sep} and red lines to ρ_D. For $m = 1$ there are just 3 possible values for θ_{est}, because they correspond to the maxima of the calibration curves in Fig. 4.3. For bigger m the possible values for θ_{est} increase and tend more precisely towards the true value of the phase shift θ_0, indicated with a black dotted line. The lower row shows the Bayesian distribution $P(\theta|\{\mu_i\}_{i=1}^{m})$ exemplary for one single m-experiment for the cases e) $m = 1$, f) $m = 3$, g) $m = 10$ and h) $m = 100$. The maximal value of the probability distribution is chosen as the estimator θ_{est}. The confidence C of the estimator, as illustrated in e), is chosen as the interval containing 68% of the probability and is indicated with the light-colored area (see text for details).
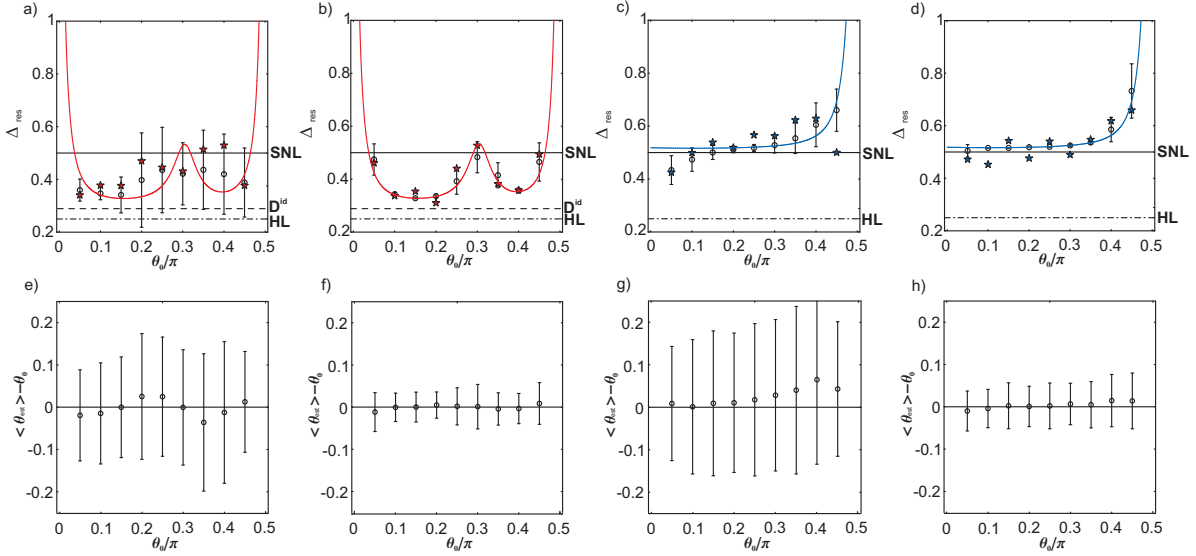
Figure 4.6: **Results of the phase estimation protocols**. In the upper row, the rescaled phase uncertainties are shown for ML phase estimation as rescaled standard deviation of the estimator $\Delta_{res} = \sqrt{m}\Delta\theta_{est}$ (red and blue stars) and for Bayesian phase estimation as rescaled average confidences $\Delta_{res} = \sqrt{m}\langle C\rangle$ (black circles) with its standard deviation as error bars for ρ_D^{exp} in a) and b) and for ρ_{sep}^{exp} in c) and d). a) and c) correspond to the case $m = 10$ and b) and d) to the case $m = 100$. The solid red and blue curves are the inverse Fisher information (out of Fig. 4.4) for ρ_D^{exp} and ρ_{sep}^{exp}, respectively. The dash-dotted horizontal line is the Heisenberg limit (HL) $\Delta_{res} = 1/4$, the dotted line the ideal value for ρ_D (D^{id}) $\Delta_{res} = 1/\sqrt{F_Q[|D_4^{(2)}\rangle]}$ and the solid line is the shot noise limit $\Delta_{res} = 1/\sqrt{F_Q[|\psi_{sep}\rangle]} = 1/2$. The lower row, e)-h), shows the influence of the bias $b = \langle\theta_{est}\rangle - \theta_0$, for the figures a)-d), with the standard deviation $\Delta\theta_{est}$ as error bars. The bias is reduced for $m = 100$ with respect to $m = 10$, which explains also the bigger overlap with the Cramér-Rao lower bound for $m = 100$ with respect to $m = 10$.

observed in Fig. 4.6 e) - h) where the bias $b = \langle\theta_{est}\rangle - \theta_0$ with its standard deviation (error bars) is plotted for both states for $m = 10$ and $m = 100$. For $m = 10$ the bias is bigger with respect to $m = 100$ and therefore the Cramér Rao lower bound is just vaguely reproduced, because we assumed no bias for the derivation of the Cramér-Rao lower bound (see Eq. 4.1, 4.19, 4.20).

An other phase estimation strategy is provided by Bayesian analysis. As the name suggests, we will estimate the true value of the phase shift with the help of Bayes' theorem. In general, Bayes' theorem connects the conditional and the prior probabilities

of the events A and B with [151]

$$P(A|B) = \frac{P(B|A)P(A)}{P(B)} \qquad (4.67)$$

assuming that $P(B) \neq 0$. $P(A)$ is the prior probability in the sense that it does not include any information about B. $P(B)$ is the prior probability of B and acts as a normalization constant. $P(A|B)$ is the conditional probability of A given B and $P(B|A)$ vice versa. In this form Bayes' theorem provides a mathematical formula of how the conditional probability of an event A given B is related to the converse conditional probability of B given A. In the language of phase estimation we would like to link the probabilities of our measurement outcomes μ_i with the probabilities of estimating the true phase shift θ_0. What we usually measure is the conditional probability $P(\mu|\theta_0)$, the probability of obtaining the click μ in our detector if we have applied the phase shift θ_0. But to estimate a phase shift, we are much more interested in the conditional probability of measuring the phase shift θ, if we have observed the detector events $\mu_1, \mu_2, ..., \mu_m$. Using Bayes' theorem in Eq. 4.67 we obtain

$$P(\theta|\{\mu_i\}_{i=1}^m) = \frac{P_{\exp}(\{\mu_i\}_{i=1}^m|\theta)P(\theta)}{P(\{\mu_i\}_{i=1}^m)}. \qquad (4.68)$$

Assuming that every phase shift θ is a priori equally probable, thats means that $P(\theta)$ is constant in the interval $[0, \frac{\pi}{2}]$, then $P(\theta)$ can be set to $P(\theta) = \frac{2}{\pi}$. The term $P(\{\mu_i\}_{i=1}^m)$ acts as normalization constant as $\int_0^{\frac{\pi}{2}} P(\theta|\{\mu_i\}_{i=1}^m)d\mu = 1$. Here, the phase shift is also estimated as the maximum of the probability density, because the Bayesian probability distribution is proportional to the likelihood function in Eq. 4.65 $P(\theta|\{\mu_i\}_{i=1}^m) \propto \prod_{i=1}^m P_{\exp}(\mu_i|\theta) = \mathcal{L}(\theta)$. The Bayesian probability distributions are shown in Fig. 4.5 e) - h) for the case $m = 1, 3, 10$ and 100.

As an example, we take the state ρ_{sep} (blue curve) in Fig. 4.5 f) for the case $m = 3$. Here, the Bayesian probability density is calculated form the first 3 μ events entering the detector, which are $\{-1, -1, 0\}$. The Bayesian probability density can now be calculated, without taking constant factors into account, as $P(\theta|\{-1, -1, 0\}) \propto P_{exp}(-1|\theta_0)P_{exp}(-1|\theta_0)P_{exp}(0|\theta_0)$. The $P_{exp}(\mu|\theta_0))$ are the calibration curves from Fig. 4.3. In Fig. 4.7 the evolution of the Bayesian density distributions is exemplary plotted starting from $m = 1$ up to 20 for the first 20 μ events entering the detector (out of ~ 12000). It nicely illustrates how the probability densities of the Bayesian distributions converge to the true vale of the phase shift, in this case $\theta_0 = 0.4\pi$, for increasing m.

In Fig. 4.5 e) - h) one observes that the red curves of ρ_D are all narrower than the blue curves of ρ_{sep}. This is the expected behaviour of the entangled Dicke state in comparison to the separable state. The width of these curves is then quantified as a confidence interval C around the estimator θ_{est}. This is illustrated in Fig. 4.5 e). In contrast to the maximum likelihood phase estimation the confidence interval C defines a meaningful error of the estimator (even for a single μ event), as for maximum likelihood phase estimation only the standard deviation of the scattered estimators can
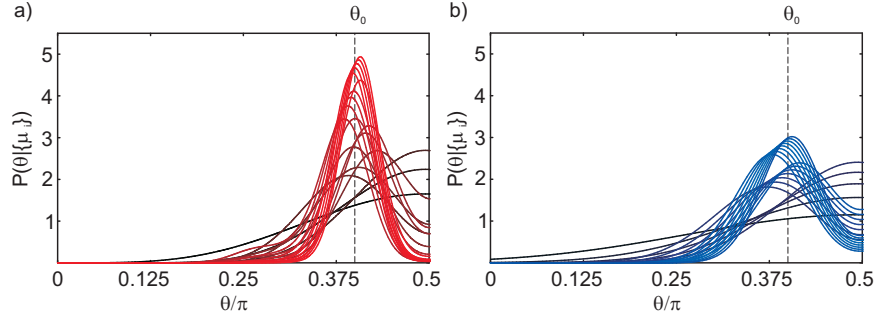
Figure 4.7: **Evolution of the Bayesian probability distributions**. The evolution of the Bayesian probability distributions is exemplary shown for the true phase shift $\theta_0 = 0.4\pi$ (dashed line) starting at $m = 1$ up to 20 for the fist 20 μ events entering the detector (out of ~ 12000). The probability densities $P(\theta|\{\mu_1\})$ up to $P(\theta|\{\mu_1, \mu_2, ..., \mu_{20}\})$ are plotted in a) for ρ_D and the μ values $\{-2, -2, -2, -1, -2, 0, 1, 0, 2, 1, 1, 2, -2, 2, 0, -1, 2, 2, -2, -2\}$ and in b) for ρ_{sep} and the μ values $\{-2, -2, -2, -2, -2, -1, -2, -2, -2, -2, -2, -2, -1, -2, -2, -2, -2, -2, -2, -2\}$. For $m = 1$ the curves are plotted in black and for increasing m they become red (ρ_D) or blue (ρ_{sep}), respectively.

be indicated (which is not possible for a single μ event). The confidence interval C is calculated as[28]

$$\int_{\theta_{est}-C}^{\theta_{est}+C} P(\phi|\{\mu_i\}_{i=1}^m)d\phi = 0.68 \tag{4.69}$$

assuming that the area under the curve of the probability densities is normalized to one. At the border of the interval $[0, \frac{\pi}{2}]$, the integration might result in a value below 0.68 and therefore the integration limits have to be defined as $\int_0^{\theta_{est}+C} P(\phi|\{\mu_i\}_{i=1}^m)d\phi = 0.68$ or $\int_{\theta_{est}-C}^{\frac{\pi}{2}} P(\phi|\{\mu_i\}_{i=1}^m)d\phi = 0.68$, respectively, in order not to underestimate the error. The average confidences $\langle C \rangle$ for the states ρ_D and ρ_{sep} for $m = 10$ and $m = 100$ are shown in Fig. 4.6 as circles with the standard deviation ΔC as error bars. For $m = 10$ the mean value of the confidences disagree with the Cramér-Rao lower bound. For $m = 100$ the agreement is much better and follows the Cramér-Rao lower bound. Sub shot noise sensitivity can also be proven and additionally to maximum likelihood estimation, the standard deviation of the rescaled uncertainty can be specified.

Furthermore, the overlap with the inverse Fisher information is even better than for the stars of the maximum likelihood estimation. This is exemplary shown for an increasing number of m-experiments for the point 0.2π in Fig. 4.8. For the Bayesian estimation almost all points lie, within the error bars, on the inverse Fisher information (horizontal line), whereas for the maximum likelihood, even for bigger values of m, the

---

[28]For large m the confidence interval C corresponds to the standard deviation of the estimator, because the phase distribution becomes Gaussian
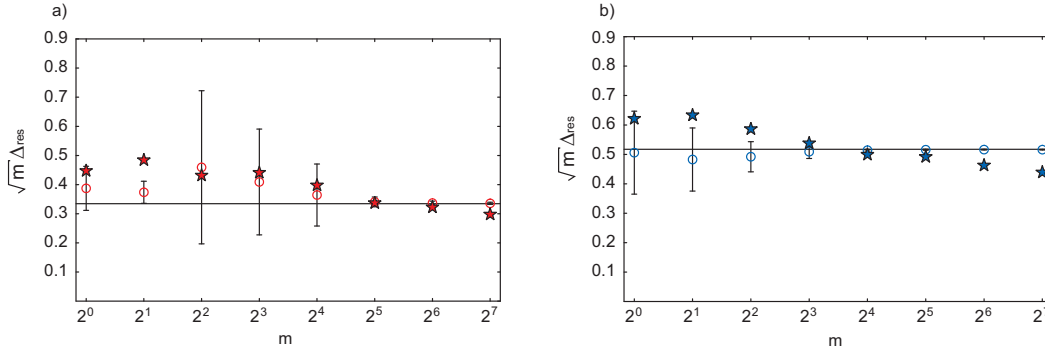
Figure 4.8: **Scaling of rescaled uncertainty**. The rescaled uncertainty is compared between the maximum likelihood (stars with $\Delta_{res} = \sqrt{m}\Delta\theta_{est}$) and the Bayesian (circles $\Delta_{res} = \sqrt{m}\langle C\rangle$ with $\sqrt{m}\Delta C$ as error bars) phase estimation for increasing number of m-experiments. In a) the scaling is shown for the state ρ_D^{exp} and in b) for the state ρ_{sep}^{exp}. Both plots are exemplary shown for the point 0.2π, because the other points do not show a principally different behavior. The horizontal lines correspond to the value of $1/\sqrt{F_{\hat{\mu}}[0.2\pi, \rho^{exp}]}$ for ρ_D^{exp} in a) and ρ_{sep}^{exp} in b).

inverse Fisher information is not exactly reproduced.

Finally, we have shown how to identify useful multi-particle entanglement of quantum states by means of Fisher information. In the experiment this has been successfully verified with a maximum likelihood and Bayesian phase estimation. For both protocols, sub-shot-noise sensitivity has been proved for a symmetric for photon Dicke state. The protocols are also compared to each other and Bayesian phase estimation has turned out to be especially useful, because even for one single event a meaningful error in terms of a confidence interval to the estimator can be indicated. In addition, the standard deviation of the rescaled uncertainties for Bayesian phase estimation helps to interpret the significance of the measured uncertainties.

4.1.5 Preprint: Useful multiparticle entanglement and sub shot noise estimation

Useful multiparticle entanglement and sub shot-noise phase estimation

Roland Krischek,[1,2] Christian Schwemmer,[1,2] Witlef Wieczorek,[1,2,3]
Harald Weinfurter,[1,2] Philipp Hyllus,[4] Luca Pezzé,[5] and Augusto Smerzi[4]

[1]*Fakultät für Physik, Ludwig-Maximilians Universität München, D-80799 München, Germany*
[2]*Max-Planck Institut für Quantenoptik, Hans-Kopfermann Str. 1, D-85748 Garching, Germany*
[3]*Present address: Faculty of Physics, University of Vienna, Boltzmanngasse 5, A-1090 Vienna, Austria*
[4]*INO-CNR BEC Center and Dipartimento di Fisica, Università di Trento, I-38123 Povo, Italy*
[5]*Laboratoire Charles Fabry de l'Institut d'Optique,*
CNRS and Univ. Paris-Sud, F-91127 Palaiseau cedex, France

We experimentally demonstrate a general criterion to identify states for entanglement enhanced metrology useful for the estimation of an unknown phase shift with a sensitivity higher than the shot-noise limit. Additionally, we show how to exploit this entanglement on the examples of a maximum likelihood and of a Bayesian phase estimation protocol. Using an entangled four-photon state we achieve a phase sensitivity clearly beyond the shot-noise limit. Our detailed comparison of methods and quantum states for entanglement enhanced metrology reveals the connection between multipartite entanglement and sub shot-noise sensitivity, both in a frequentist and in a Bayesian phase estimation setting.

The field of quantum enhanced metrology is attracting increasing interest and impressive experimental progress has been achieved with photons [1–3], cold/thermal atoms [4], ions [5] and Bose-Einstein condensates [6, 7]. Several experiments have demonstrated phase super resolution [2, 5], which, if observed with a high visibility of the interference fringes, allows to utilize the state for quantum enhanced metrology [8, 9]. So far, only few experiments have implemented a complete interferometric measurement beating the shot-noise limit $\Delta\hat\theta = 1/\sqrt{N}$, where N is the number of particles, with $N > 2$ [4–6]. In this context it is generally assumed that the experimental observation of sub shot-noise sensitivity is a consequence of quantum correlations in the input probe state used for the phase estimation protocol. However, it has been recently emphasized that not all entangled states allow for quantum enhanced metrology [10, 11]: entanglement is not a sufficient condition to overcome the classical limit. In this letter, we experimentally demonstrate the relation between entanglement and sub shot-noise sensitivity. For the first time, we show how to identify useful entanglement and compare the suitability of different quantum states as well as of different phase estimation protocols for entanglement enhanced metrology.

The usefulness of a state created experimentally can be quantified by the quantum Fisher information (QFI) $F_Q[\rho, \hat{J}]$ [16] (see supplementary material). A probe state ρ of N qubits is entangled *and* allows for sub shot-noise phase estimation if the condition

$$F_Q[\rho, \hat{J}] > N \qquad (1)$$

is fulfilled [10]. Here $\hat{J} = \frac{1}{2}\sum_{i=1}^{N} \hat\sigma_{\vec{n}_i}^{(i)}$ is the linear generator of the phase shift, and $\hat\sigma_{\vec{n}_i}^{(i)} = \vec{n}_i \cdot \hat\sigma$ is a Pauli matrix rotating the qubit i along the arbitrary direction $\vec{n}_i$. The maximal F_Q further depends on the hierarchical entanglement structure of the probe state and genuine

multiparticle entanglement is needed to reach the Heisenberg limit [12], the ultimate sensitivity allowed by quantum mechanics. With $N = 4$ qubits, 2-particle entangled states have $F_Q \leq 8$, while for 3-particle entangled states $F_Q \leq 10$ [12]. The maximal value is $F_Q \leq N^2 = 16$ which is saturated by the so-called Greenberger-Horne-Zeilinger (GHZ) state [10, 13, 14].

There is a strict relation between the condition to recognize useful entanglement provided by equation (1) and the possibility to achieve sub shot noise phase sensitivity. According to the Cramer-Rao theorem [15, 16], the standard deviation of unbiased phase estimation is bounded by

$$\Delta\theta \geq \frac{1}{\sqrt{mF_{\hat\mu}[\theta_0, \rho, \hat{J}]}} \geq \frac{1}{\sqrt{mF_Q[\rho, \hat{J}]}}. \qquad (2)$$

The first inequality defines the Cramer-Rao lower bound (CRLB). Here θ_0 is the true value of the phase shift, m is the number of independent repetitions of the experiment, and

$$F_{\hat\mu}[\theta_0, \rho, \hat{J}] = \sum_\mu \frac{1}{P(\mu|\theta_0)}\Big(\frac{\mathrm{d}P(\mu|\theta)}{\mathrm{d}\theta}\Big|_{\theta_0}\Big)^2 \leq F_Q[\rho, \hat{J}]. \qquad (3)$$

The Fisher information $F_{\hat\mu}[\theta_0, \rho, \hat{J}]$ depends on the conditional probabilities $P(\mu|\theta_0)$ to obtain the result μ in the measurement when the true phase shift is equal to θ_0. It is bounded by the quantum Fisher information [[10] and see supplementary material], the equality being saturated for an optimal measurement $\hat\mu_{\mathrm{opt}}$. From equations (1,2) and the bounds for multi-partite entanglement we can thus infer that if the experimentally obtained F_Q exceeds the value for k-partite entanglement [see supplementary material], one can achieve a phase sensitivity better than that achievable with any $(k-1)$-particle entangled state.

For the experimental demonstration, we use the symmetric four-photon entangled Dicke state [17] $|D_4^{(2)}\rangle =$
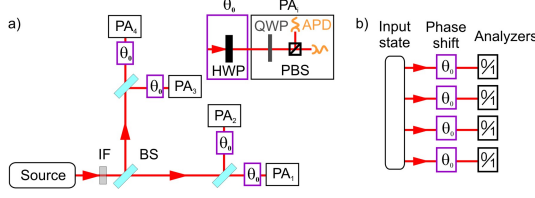
FIG. 1: Phase estimation setup. a) Experimental setup (the source uses pulsed parametric down conversion with a type II cut β-Barium-Borate crystal ($\lambda_{pump} = 390$nm); for details see supplementary material): IF, interference filter; BS, beam splitter; PA, polarization analysis; HWP, halfwave-plate; QWP, quarterwave-plate; PBS, polarizing beam-splitter; APD, avalanche photo-diode. Each qubit can be addressed individually. The Dicke state $|D_4^{(2)}\rangle$ is observed if one photon is detected at each of the four output arms [19]. The separable state $|\psi_{\mathrm{sep}}\rangle$ is created by inserting a $|+\rangle$ polarizer before the first BS. In our experiment we rotate each qubit by $\exp[-i\hat{\sigma}_y\theta/2]$ (violet box). b) Schematic of our interferometric setup.

$\frac{1}{\sqrt{6}}\Big(|HHVV\rangle + |HVHV\rangle + |HVVH\rangle + |VHHV\rangle + |VHVH\rangle + |VVHH\rangle\Big)$ and the separable state $|\psi_{\mathrm{sep}}\rangle = |+ + + +\rangle$ as observed from multiphoton parametric down conversion [19]. Here $|HHVV\rangle = |H\rangle_1 \otimes |H\rangle_2 \otimes |V\rangle_3 \otimes |V\rangle_4$, $|H\rangle_i$ ($|V\rangle_i$) refer to the horizontal (vertical) polarization of a photon in the spatial mode i and $|\pm\rangle = \frac{1}{\sqrt{2}}(|H\rangle \pm |V\rangle)$. From the measured density matrices (see supplementary material) we deduce a fidelity of 0.8872 ± 0.0055 for $|D_4^{(2)}\rangle$ and 0.9859 ± 0.0062 for $|\psi_{\mathrm{sep}}\rangle$. From these tomographic data we also evaluate the QFI to determine the suitability of the of the experimentally observed states. For the ideal Dicke state $|D_4^{(2)}\rangle$, the QFI reaches its maximum value, $F_Q[|D_N^{(N/2)}\rangle, \hat{J}] = N(N+2)/2 = 12$, when $\hat{\sigma}_{\vec{n}_i} = \hat{\sigma}_y$ for all i ($\hat{J} \equiv \hat{J}_y$) [11]. In the experiment, this choice leads to $F_Q[\rho_D^{\mathrm{exp}}, \hat{J}_y] = 9.999 \pm 0.095$, a value which proves useful 3-particle entanglement. An optimization over the local directions $\vec{n}_i$, as described in Ref. [11], leads to the optimal value $F_Q^{\mathrm{opt}}[\rho_D^{\mathrm{exp}}, \hat{J}^{\mathrm{opt}}] = 10.326 \pm 0.093$. Hence the experimentally created state overcomes the limit for useful 4-particle entanglement by 3.5 standard deviations. Note, that this state can be clearly proven to be genuine 4-particle entangled using witness operators [17]. Yet, witness operators merely recognize the entanglement, whereas the new tool directly indicates the state's applicability for a quantum task. Ideally, the seperable state $|\psi_{\mathrm{sep}}\rangle$ allows for sensitivity at the shot-noise limit, $F_Q[|\psi_{\mathrm{sep}}\rangle, \hat{J}_y] = N = 4$. The reconstructed density matrix leads to $F_Q[\rho_{\mathrm{sep}}^{\mathrm{exp}}, \hat{J}_y] = 3.894 \pm 0.023$, a value close, as expected, to the separable limit. An optimization over the local directions as above indeed leads to the optimal

value $F_Q^{\mathrm{opt}}[\rho_D^{\mathrm{exp}}, \hat{J}^{\mathrm{opt}}] = 4.014 \pm 0.025$.

In order to demonstrate the connection between the Fisher information, multiparticle entanglement and sub shot noise sensitivity, we experimentally implement a phase estimation analysis with the input states $|D_4^{(2)}\rangle$ and $|\psi_{\mathrm{sep}}\rangle$. Our interferometric protocol transforms the probe state by $U(\theta_0) = \exp[-i\sum_{k=1}^{4}\hat{\sigma}_{\vec{n}_i}^{(k)}\theta_0/2]$ using the halfwave-plate depicted in Fig. 1 a). The unknown value of the phase shift θ_0 is inferred from the difference in the number of particles, $2\mu = N_H - N_V$ ($\mu = -2, -1, 0, 1, 2$), in the states V and H. For the ideal states and the rotation directions $\vec{n}_i = y$, this measurement is optimal, and hence $F_{\hat{\mu}} = F_Q$. Experimentally, the optimized direction and measurement can be different because of noise and misalignment. However, for the observed states the expected improvement would be rather small.

The relation between the phase shift and the possible results of a measurement is provided by the conditional probabilities $P(\mu|\theta_0)$. These can be measured experimentally and compared with the theoretical ones for both the separable and the entangled state. The results of these calibration measurements are plotted in Fig. 2 a)-k). A fit to the measured conditional probabilities provides $P_{\mathrm{exp}}(\mu|\theta)$, which is used to calculate the Fisher information shown in Fig. 2 l). As expected, our experimental apparatus can surpass the shot noise limit for a broad range of phase values (where $F_{\hat{\mu}}^{\mathrm{exp}} > 4$), and even exploit useful three particle entanglement (where $F_{\hat{\mu}}^{\mathrm{exp}} > 8$).

The phase shift θ_0 is inferred from the results, $\mu_1, \mu_2, ..., \mu_m$, of m independent repetitions of the interferometric protocol. We will refer to such a collection of measurements as a single m-experiment. In the following we will implement a maximum likelihood (ML) and a Bayesian phase estimation protocol. While both have been recently used in literature for phase estimation [3, 20], here they are compared in detail and applied for the first time to demonstrate sub shot noise sensitivity with more than two particles.

In the ML protocol the estimator $\hat{\theta}$ of the unknown phase shift is determined as the value maximizing the likelihood function $\mathcal{L}(\theta) = \prod_{i=1}^{m} P_{\mathrm{exp}}(\mu_i|\theta)$ [15]. For different m-experiments it fluctuates with standard deviation $\Delta\hat{\theta}$, which has to be calculated from a large number of repetitions of single m-experiments. In the limit of large m, $\Delta\hat{\theta}$ is known to saturate the CRLB equation (2) [15].

We set the phase shift to 9 known values θ_0. For each θ_0, 12000 results μ_i are independently measured and grouped into vectors of length m to perform the ML analysis for different values of m ($= 1, 10, 100$). Fig. 3 shows the distributions of the estimator $\hat{\theta}$ for the phase shift $\theta_0 = 0.2\pi$ and different values of m. With increasing m the standard deviation $\Delta\hat{\theta}$ of the distributions P decreases and the histograms approach a Gaussian shape.
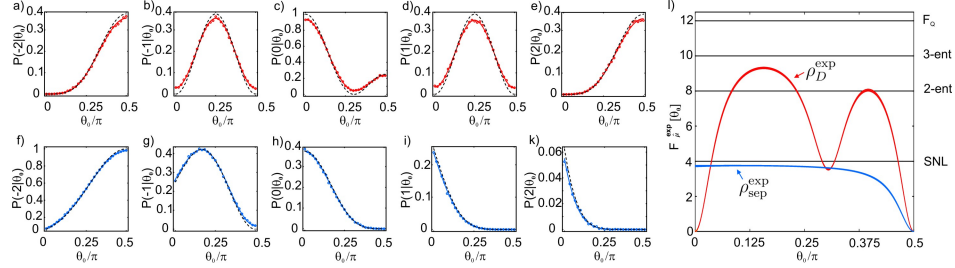
FIG. 2: Calibration curves and derived Fisher information. The small panels show conditional probabilities $P_{\exp}(\mu|\theta_0)$ for the state $\rho_D^{\exp}$ [a)-e)] and for $\rho_{\text{sep}}^{\exp}$ [f)-k)]. Dashed black lines are the ideal probabilities $P(\mu|\theta)$, dots experimental results. The red (blue) curves $P_{\exp}(\mu|\theta_0)$ for the state $\rho_D^{\exp}$ ($\rho_{\text{sep}}^{\exp}$) are fits obtained by assuming that the main source of errors are misalignments in the polarization optics (see supplementary material). The measurements are performed for 31 values of θ_0 by collecting roughly 7000 events for each phase value. In l), the Fisher information [equation (3)] obtained from the fits $P_{\exp}(\mu|\theta_0)$ is plotted. The line widths correspond to the error intervals $F_{\hat{\mu}}^{\exp}[\theta_0] \pm \Delta F_{\hat{\mu}}^{\exp}[\theta_0]$ with $\Delta F_\mu[\rho_D^{\exp}] \leq 0.08$ and $\Delta F_{\hat{\mu}}[\rho_{\text{sep}}^{\exp}] \leq 0.04$. Horizontal lines indicate multiparticle entanglement limits (see text). Theoretically, we expect $F_{\hat{\mu}}^{\text{id}} = F_Q^{\text{id}}$ for the ideal input states, phase operations and output measurements. Experimentally, we observe $F_{\hat{\mu}}^{\exp} < F_Q^{\exp}$ as the performed measurements are not optimal for the state which is actually produced. Moreover, the Fisher information $F_{\hat{\mu}}^{\exp}[\theta_0]$ strongly depends on the phase shift. In particular, it is strongly reduced for values of the phase shift where the conditional probabilities of the figures a)-k) tend to the extremal values 0 or 1, where the reduced visibility of the input state has the biggest impact.

As expected, the width of the histograms is smaller for the Dicke state (red lines) as for the separable state (blue lines). For better comparison we use the phase sensitivity $\mathcal{S}$ [9], which for ML estimation is $\mathcal{S} = \sqrt{m}\Delta\hat{\theta}$ shown in Fig. 4.

For $m = 10$ the standard deviation is below the CRLB (2) for several θ_0 values. This is possible because the estimation is biased, i.e., for $b \equiv \langle\hat{\theta}\rangle - \theta_0$ we have $b \neq 0$ and $\partial_{\theta_0}b \neq 0$ (see supplementary material and [15]). Bias can be taken into account by replacing the numerator in the CRLB equation (2) by $|1 - \partial_{\theta_0}b|$. For even smaller m, only few different likelihood functions $\mathcal{L}(\theta)$ can occur, see Figs 3 a)-c). Then, $\hat{\theta}$ scatters significantly and hardly allows for an unbiased phase estimate. When $m = 100$, b is strongly reduced and the agreement of $\Delta\hat{\theta}$ with the unbiased CRLB is improved significantly. While the bias is still large enough to cause apparent sensitivities below the shot-noise limit for the separable state, for the Dicke state the CRLB as determined from equation (2) using the experimentally obtained Fisher information from Fig. 2 l) is saturated for a large phase interval. This clearly proves that the multiparticle entangled Dicke state created experimentally indeed achieves the sub shot noise sensitivity.

A conceptually different phase estimation protocol is given by the Bayesian approach assuming that the phase shift is a random variable. The probability density for the true value of the phase shift being equal to θ, conditioned on the measured results $\mu_1, \mu_2, ..., \mu_m$, is provided by Bayes' theorem, $P(\theta|\{\mu_i\}_{i=1}^m) = P_{\exp}(\{\mu_i\}_{i=1}^m|\theta)P(\theta)/P(\{\mu_i\}_{i=1}^m)$. To de-

fine the a priori probability density $P(\theta)$ we adopt the maximum ignorance principle and take $P(\theta)$ to be constant in the phase interval considered. The Bayesian probability density then is given by $P(\theta|\{\mu_i\}_{i=1}^m) \propto \prod_{i=1}^m P_{\exp}(\mu_i|\theta) = \mathcal{L}(\theta)$. Given $P(\theta|\{\mu_i\}_{i=1}^m)$, the phase shift can be estimated as the maximum of the probability density as before. However, in contrast to the ML method, the Bayesian analysis allows to assign a meaningful uncertainty to this estimate even for a single m-experiment and biased estimators. This can be taken, for instance, as a confidence interval C around the estimate, where the area of $P(\theta|\{\mu_i\}_{i=1}^m)$ is equal to 68% [see Fig. 3 d)]. Thus, even from a single m-experiment, we can deduce the corresponding phase uncertainty $\Delta\theta\hat{=}C$. For comparison we use again the phase sensitivity, now given by $\mathcal{S} = \sqrt{m}C$.

Fig. 3 illustrates how the Bayesian probability densities evaluated for single m-experiments [Figs 3 d)-f)] are close to become Gaussians with a width $\propto 1/\sqrt{mF_{\hat{\mu}}}$, already for small values of m. Consequently, the phase sensitivities exhibits stronger scatter for the ML- when compared to the Bayesian protocol (see Fig. 4). The quantum enhancement drastically reduces for phases where one or more $P(\mu_i|\theta)$ ideally go to 0 (for $\theta_0 = 0, 0.3\pi, 0.5\pi$), but do not due to the limited visibility of the calibration (see Fig. 2). For other values of θ_0, however, we obtain the expected sub shot-noise phase sensitivity close to the CRLB.

In conclusion, we have investigated experimentally, the relation between sub shot noise phase estimation and the entanglement properties of a probe state. We have iden-
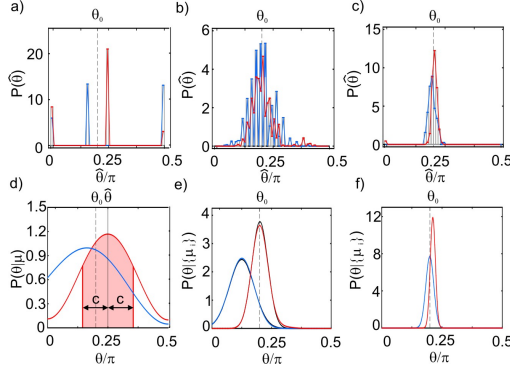
FIG. 3: **Comparison of the maximum likelihood method to the Bayesian approach**. In the upper row, the distributions of the ML estimators $\hat{\theta}$ obtained from large number of repetitions of m-experiments are shown as histograms for a) $m = 1$, b) $m = 10$ and c) $m = 100$. The true value of the phase shift is $\theta_0 = 0.2\pi$ (dashed black line). Red solid lines show the results of the state $\rho_D^{\exp}$ and blue solid lines show the results of the state $\rho_{\text{sep}}^{\exp}$. The histograms are normalized to one. The lower row shows exemplary Bayesian probability densities $P(\theta|\{\mu_i\}_{i=1}^m)$ of *single* m-experiments for d) m=1, e) m=10 and f) m=100 for the state $\rho_D^{\exp}$ (solid red lines) and $\rho_{\text{sep}}^{\exp}$ (solid blue lines). The solid black lines in e) correspond to a Gaussian with widths $\propto 1/\sqrt{10\, F_{\hat{\mu}}}$. For m=1, the μ-value observed for the Dicke state is $\{1\}$, while for the separable state it was $\{-1\}$. For the Bayesian method the estimator is chosen as the maximum of the distribution (vertical solid black line), whereas the confidence interval $[\hat{\theta} - C, \hat{\theta} + C]$ contains 68% of $P(\theta|\{\mu_i\}_{i=1}^m)$ and is delimited by red vertical lines [see supplementary material for details].

tified useful multiparticle entanglement by determining the quantum Fisher information from the tomographical data of a Dicke state of four photons. The benefit of such entanglement has been directly proved by implementing two different phase estimation analyses, both of which saturate the Cramer Rao bound and clearly surpass the shot noise limit. The approach is completely general: it applies for any probe state, is scalable in the number of particles and does not require state selection. Our study thus provides a guideline for the future technological exploitation of multiparticle entanglement to outperform current metrological limits.

[1] J.G. Rarity *et al.*, Phys. Rev. Lett. **65**, 1348 (1990); T. Nagata, *et al.*, Science **316**, 726 (2007).

[2] M. W. Mitchell, J.S. Lundeen & A.M. Steinberg, Nature **429**, 161 (2004); P. Walther *et al.*, Nature **429**, 158 (2004).
[3] M. Kacprowicz *et al.*, Nature Phot. **4** 357 (2010).
[4] J. Appel *et al.*, PNAS **106**, 10960 (2009); M. H. Schleier-Smith *et al.*, Phys. Rev. Lett. **104** 073604 (2010).
[5] D. Leibfried *et al.*, Science **304**, 1476 (2004).
[6] C. Gross *et al.*, Nature **464**, 1165 (2010).
[7] M. F. Riedel *et al.*, Nature **464**, 1170 (2010).
[8] K.J. Resch *et al.*, Phys. Rev. Lett. **98**, 223601 (2007).
[9] R. Okamoto *et al.*, N. Jour. Phys. **10**, 073033 (2008).
[10] L. Pezzé & A. Smerzi, Phys. Rev. Lett. **102**, 100401 (2009).
[11] P. Hyllus, O. Gühne & A. Smerzi, Phys. Rev. A **82**, 012337 (2010).
[12] P. Hyllus *et al.*, http://arxiv.org/abs/1006.4366 (2010); G. Tóth, http://arxiv.org/abs/1006.4368 (2010).
[13] D.M. Greenberger, M.A. Horne, A. Zeilinger, Going beyond Bell's theorem, Kluwer Academics (1989).
[14] V. Giovannetti, S. Lloyd & L. Maccone, Phys. Rev. Lett. **96**, 010401 (2006).
[15] H. Cramér, Mathematical Methods of Statistics, Princeton Univ. Press (1946).
[16] C.W. Helstrom, Phys. Lett. **25A**, 101 (1967); S.L. Braunstein & C.M. Caves, Phys. Rev. Lett. **72** 3439 (1994).
[17] N. Kiesel *et al.*, Phys. Rev. Lett. **98**, 063604 (2007).
[18] M.J. Holland & K. Burnett, Phys. Rev. Lett. **71** 1355 (1993).
[19] W. Wieczorek *et al.*, Phys. Rev. Lett. **103**, 020504 (2009).
[20] L. Pezzé *et al.*, Phys. Rev. Lett. **99**, 223602 (2007); Z. Hradil *et al.*, Phys. Rev. Lett. **76**, 4295 (1996).
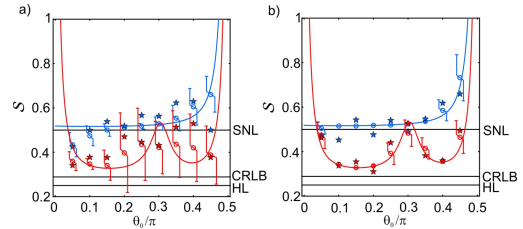
FIG. 4: Phase sensitivities $\mathcal{S}$ obtained with the probe state $\rho_D^{\exp}$ (red) and $\rho_{\text{sep}}^{\exp}$ (blue), with a) $m = 10$ and b) $m = 100$. The solid red (blue) line is the expected sensitivity given by the CRLB [equation (2)] with the experimental $F_{\hat{\mu}}$ [see Fig. 2 l)] for the state $\rho_D^{\exp}$ ($\rho_{\text{sep}}^{\exp}$). Stars are the results of the ML analysis (standard deviation of the ML estimator $\hat{\theta}$) with $\mathcal{S} = \sqrt{m}\Delta\hat{\theta}$, circles with error bars are the results of the Bayesian analysis with $\mathcal{S} = \sqrt{m}\langle C \rangle$. Horizontal lines are the Heisenberg limit (HL) $\sqrt{m}\Delta\theta_{\text{HL}} = 1/4$, the CRLB for the ideal Dicke state $1/\sqrt{F_Q} = 1/\sqrt{12}$ and the shot noise limit (SNL) $\sqrt{m}\Delta\theta_{\text{SNL}} = 1/2$.

Supplementary material: Useful multiparticle entanglement and sub shot-noise phase estimation

Roland Krischek,[1,2] Christian Schwemmer,[1,2] Witlef Wieczorek,[1,2,3]
Harald Weinfurter,[1,2] Philipp Hyllus,[4] Luca Pezzé,[5] and Augusto Smerzi[4]

[1]*Fakultät für Physik, Ludwig-Maximilians Universität München, D-80799 München, Germany*
[2]*Max-Planck Institut für Quantenoptik, Hans-Kopfermann Str. 1, D-85748 Garching, Germany*
[3]*Present address: Faculty of Physics, University of Vienna, Boltzmanngasse 5, A-1090 Vienna, Austria*
[4]*INO-CNR BEC Center and Dipartimento di Fisica, Università di Trento, I-38123 Povo, Italy*
[5]*Lab. Charles Fabry de l'Institut d'Optique, CNRS and Univ. Paris-Sud, F-91127 Palaiseau cedex, France*

Experimental setup. The photons used to prepare our two input states (see Fig. 1) are generated by spontaneous parametric down conversion (SPDC). To this aim, laser pulses with a duration of 130 fs produced inside a Titanium-sapphire oscillator at a wavelength of 780 nm are frequency doubled to 390 nm by a lithium triborate crystal and then guided into an enhancement resonator for femtosecond pulses [1]. Inside the resonator, a 1 mm thick β-barium borate crystal is pumped for type-II collinear SPDC generating the state $|n, n\rangle_{H,V}$ with $n\,H$ and $n\,V$ polarised photons. With the enhancement resonator we are able to set the UV pump power of the SPDC process to values between 0.6W and 7.2W [1]. The appropriate UV pump power is chosen such that a considerably high 4-photon count rate as well as a high fidelity of the probe states can be achieved. A large data set is required for the accumulation of sufficient statistical data in the phase measurement. This is guaranteed by a high count rate (~ 420 min^{-1} for each four-photon state) and stability in our experimental setup allowing the utilization of 4 photons for quantum enhanced metrology. The generated SPDC photons are coupled to single mode fibre and guided to a linear optics setup shown in Fig. 1 of the main text [1, 2]. To achieve spectral selection, a narrowband interference filter ($\Delta\lambda = 3$ nm) is placed at the output of the fibre. The photons are symmetrically distributed onto 4 spatial modes using 3 nonpolarising beam-splitters. The birefringence of these beam-splitters is compensated by pairs of perpendicularly orientated 200 μm thick birefringent yttrium-vanadate crystals (YVO$_4$). In each arm we apply a phase-shift with half- and quarterwaveplates and detect the photons in the outputs of a polarising beam-splitter using single-photon avalanche photodiodes. The detection signals are analysed by a FPGA-controlled coincidence logic allowing the simultaneous registration of any possible coincidence.

Fits and errors. For the fits to the calibration curves we used the ansatz $P_{\exp}(\mu|\theta) = \sum_{\mu'} P(\mu|\mu') P_{\mathrm{id}}(\mu'|\theta)$, where $P_{\mathrm{id}}(\mu|\theta)$ are the ideal distributions. This is a classical model for misalignments in the polarization analyzers, leading to the result μ when the true result was μ'. We performed a least squares fit to the
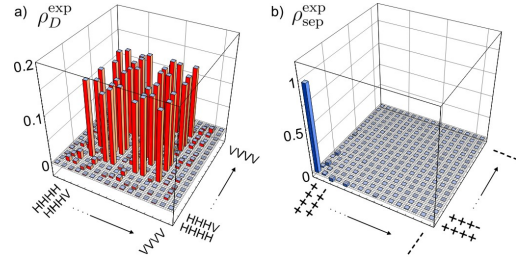
FIG. 1: Density matrices of the real part of our two input states ρ_D^{exp} [a]] and ρ_{sep}^{exp} [b]] obtained by full tomography [3] are shown. The input states are observed with a fidelity of 0.8872 ± 0.0055 [a] and 0.9859 ± 0.0062 [b]

curves for all μ values simultaneously with the condition $\sum_\mu P(\mu|\mu') = 1$ for all μ', which ensures the proper normalization $\sum_\mu P_{\exp}(\mu|\theta) = 1$ for all θ. The errors of the Fisher information and the quantum Fisher information were computed by a Monte Carlo method assuming poissonian errors in the measurement counts obtained in the calibration and in the tomography, respectively. Except for full tomography (see Fig. 1) all measurements are not corrected for relative detector efficiencies.

Quantum Fisher Information and Multiparticle Entanglement. The quantum Fisher information is given by [4]

$$F_Q\left[\rho, \hat{J}\right] = 2 \sum_{j,k} \frac{(q_j - q_k)^2}{q_j + q_k} |\langle j|\hat{J}|k\rangle|^2, \qquad (1)$$

where $\rho = \sum_k q_k |k\rangle\langle k|$ ($q_k > 0$, $\sum_k q_k = 1$). For pure states, $\rho = |\psi\rangle\langle\psi|$, the quantum Fisher information simplifies to $F_Q\left[|\psi\rangle, \hat{J}\right] = 4(\Delta\hat{J})^2$.

A pure k-particle entangled state can be written as $|\psi^{k-\mathrm{ent}}\rangle = \bigotimes_{l=1}^M |\psi_l\rangle$, where $|\psi_l\rangle$ is a state of $N_l \leq k$ particles, and at least one $|\psi_l\rangle$ is a state of k particles which does not factorize. For $k = 1$, this corresponds to a product state. A mixed state is k-partite entangled iff it cannot be written as $\sum_j p_j |\psi_j^{k_j-\mathrm{ent}}\rangle\langle\psi_j^{k_j-\mathrm{ent}}|$ with
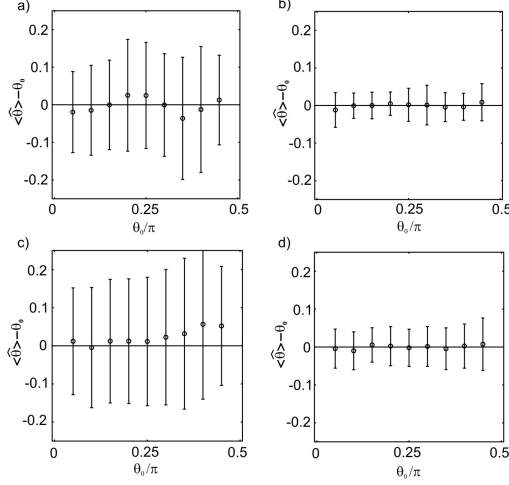
FIG. 2: Bias. Mean of the ML estimator $\hat{\theta}$ with error bars $\Delta\hat{\theta}$, showing that the absolute value of the bias $b = \langle\hat{\theta}\rangle - \theta_0$ is reduced when going from $m = 10$ [a)&c)] to $m = 100$ [b)&d)]. Figures a) & b) correspond to ρ_D^{exp} and c) & d) to ρ_{sep}^{exp} Note, in particular, that $\partial_{\theta_0} b \neq 0$ in many cases, which explains the apparent violation of the CRLB in Fig. 4 of the main text. [8].

$k_j < k$. For k-particle entangled states we have

$$F_Q[\hat{\rho}, \hat{J}] \leq \lfloor \frac{N}{k} \rfloor k^2 + r^2, \qquad (2)$$

where $\lfloor x \rfloor$ is the largest integer smaller or equal to x and $r = N - \lfloor \frac{N}{k} \rfloor \cdot k$ [5, 6].

Phase estimation. The confidence interval is calculated as $\int_{\hat{\theta}-C}^{\hat{\theta}+C} P(\phi|\{\mu_i\}_{i=1}^m)\mathrm{d}\phi = 0.68$. Note that this corresponds to the standard deviation if the phase distribution is a Gaussian function. If $\hat{\theta}$ is close to the borders of the interval $[0, \frac{\pi}{2}]$, the integral might give a value below 68% even when C takes the maximal value possible. If this happens for $\hat{\theta} \gtrsim 0$ then we define the confidence by $\int_0^{\hat{\theta}+C} P(\phi|\{\mu_i\}_{i=1}^m)\mathrm{d}\phi = 68\%$ in order not to underestimate the error. We proceed in analogy when $\hat{\theta} \lesssim \frac{\pi}{2}$.

In the ideal case, the probabilities $P(\mu|\theta)$ for the Dicke state $|D_4^{(2)}\rangle$ are given by: $P(\pm 2|\theta) = (3/8)\sin^4\theta$,

$P(\pm 1|\theta) = (3/8)\sin^2 2\theta$, and $P(0|\theta) = (1+3\cos 2\theta)^2/16$. The ideal conditional probabilities for the separable state $|\psi_{\mathrm{sep}}\rangle$ are given by $P(\mu|\theta) = [4!/(2-\mu)!(2+\mu)!]\big[\sin(\theta/2-\pi/4)\big]^{4+2\mu}\big[\cos(\theta/2-\pi/4)\big]^{4-2\mu}$.

Further results used in the manuscript are: (i) Concerning Fig. 1 d)-f) in the main text, it can be shown that, in the central limit, the most likely distribution $P(\theta|\{\mu_i\}_{i=1}^m)$ is a Gaussian centered at the true value of the phase shift with a width $\sigma = 1/\sqrt{mF}$ if the prior distribution $P(\theta)$ is flat [7]. (ii) The condition $\Delta\hat{\theta} \gg |\langle\hat{\theta}\rangle - \theta_0|$ ensures that $\Delta\hat{\theta} \approx \sqrt{\langle(\hat{\theta}-\theta_0)^2\rangle}$, hence $\Delta\hat{\theta}$ is approximately equal to the standard deviation with respect to the true value of the phase shift θ_0. (iii) In the presence of bias, when $b = \langle\hat{\theta}\rangle - \theta_0 \neq 0$, the Cramér-Rao lower bound takes the form $\Delta\theta \geq |1 - \partial_{\theta_0} b|/\sqrt{mF_{\hat{\mu}}[\theta_0, \rho, \hat{J}]}$ [8].

[1] Krischek, R., Wieczorek, W., Ozawa, A., Kiesel, N., Michelberger, P., Udem, T. & Weinfurter, H. Ultraviolet enhancement cavity for ultrafast nonlinear optics and high-rate multiphoton entanglement experiments. *Nature Phot.* **4**, 170-173 (2010).

[2] Wieczorek, W., Krischek, R., Kiesel, N., Michelberger, P., Tóth, G. & Weinfurter, H. Experimental Entanglement of a Six-Photon Symmetric Dicke State. *Phys. Rev. Lett.* **103**, 020504-020507 (2009).

[3] Kiesel, N., Schmid, C., Tóth, G., Solano, E. & Weinfurter, H. Experimental Observation of Four-Photon Entangled Dicke State with High Fidelity. *Phys. Rev. Lett.* **98**, 063604-063607 (2007).

[4] Braunstein, S. L. & Caves, C. M. Statistical distance and the geometry of quantum states. *Phys. Rev. Lett.* **72** 3439-3442 (1994).

[5] Hyllus, P., Laskowski, W., Krischek, R., Schwemmer, C., Wieczorek, W., Weinfurter, H., Pezzé, L. & Smerzi, A. Fisher information, spin squeezing, and multiparticle entanglement. Preprint at http://arxiv.org/abs/1006.4366 (2010).

[6] Tóth, G. Multipartite entanglement and high precision metrology. Preprint at http://arxiv.org/abs/1006.4368 (2010).

[7] Cramér, H. Mathematical Methods of Statistics. *Princeton Univ. Press, Princeton, NJ* (1946).

[8] Helstrom, C. W. Minimum mean-square error of estimates in quantum statistics. *Phys. Lett.* **25A**, 101-102 (1967).

4.2 Sub shot noise phase estimation using six photon symmetric Dicke states

The first experiments with photons in the field of quantum enhanced metrology have demonstrated two photon interference in a Mach-Zehnder type interferometer [152, 153]. There have been several experiments showing a reduced de Broglie wavelength with four [154, 155] or even six photons [156], but so far, sub shot noise phase sensitivity has been reported for only up to four photons [157]. Another experiment proved sub shot noise sensitivity of even eight qubits, which corresponds to also 4 photons by exploiting the polarization and momentum degrees of freedom [158]. In the preprint 4.2.1 we show, that we achieve sub shot noise sensitivity with symmetric Dicke states using up to 6 photons.

In the previous section we have used the Fisher information to quantify the sensitivity of phase estimation beyond the shot noise limit. To motivate a different derivation of the phase sensitivity (by simple error propagation, which will also be used in the preprint 4.2.1), we look at a phase shift in a more intuitive way resulting from the measurement of intensities at the output ports of a phase sensitive device, like for example an interferometer (see Fig. 4.9). Assuming the light intensity at input port A of Fig. 4.9 a) is I_A, then the output intensities can be written as [159]

$$I_C = I_A \sin^2 \frac{\theta}{2} \tag{4.70}$$

$$I_D = I_A \cos^2 \frac{\theta}{2} \tag{4.71}$$
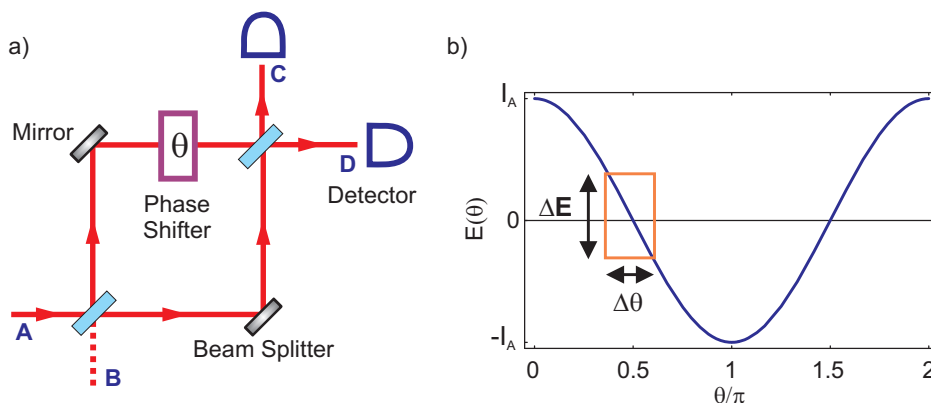
Figure 4.9: **Mach-Zehnder interferometry.** In a) a typical setup for a Mach-Zehnder interferometer with input A, B and output C, D is shown. We assume in our case that the light enters the interferometer at port A with I_A. The phase shift θ is applied in one arm of the interferometer. In b) the difference of the intensities D and C is shown, i.e. $E(\theta) = I_D - I_C = I_A \cos \theta$ (the figures are adapted from [159]).

Finally we are measuring the intensity difference of output port C and D, this can be written as follows,

$$E(\theta) = I_D - I_C = I_A \cos\theta. \tag{4.72}$$

What we are now interested in, is to estimate the precision of the interferometric device. Varying θ (x-axis of Fig. 4.9 b)) by $\Delta\theta$ is related to the change of E (y-Axis) by ΔE. If the changes are small, we can approximate the following relation with differentials,

$$\frac{\Delta E}{\Delta\theta} = \frac{\partial E}{\partial\theta} \tag{4.73}$$

which can be rewritten as

$$\Delta\theta = \frac{\Delta E}{\frac{\partial E}{\partial\theta}}. \tag{4.74}$$

Here we arrive at an expression of the phase sensitivity $\Delta\theta$, which consists of the standard deviation of the measurement ΔE and the derivative of E. In the above example we obtain for the sensitivity $\Delta\theta = \Delta E/(I_A \sin\theta)$. We see now that with Eq. 4.74 and Fig. 4.9 the phase sensitivity $\Delta\theta$ is smallest, when the slope of the curve $\partial E/\partial\theta$ is largest [29].

We obtain a similar result, if we consider a measurement operator $\hat{A}$ which estimates an unknown parameter. The estimated value has usually an uncertainty, which fluctuates with the variance given by $(\Delta A)^2 = \langle\hat{A}^2\rangle - \langle\hat{A}\rangle^2$. The root mean square error $\Delta\theta$ of the inferred phase θ is then determined by error propagation [161, 150]

$$\Delta\theta = \frac{\Delta A}{\left|\frac{\partial\langle\hat{A}\rangle}{\partial\theta}\right|}. \tag{4.75}$$

In the preprint 4.2.1 $\Delta\theta$ will be determined experimentally for symmetric N particle Dicke states with $N/2$ excitations

$$|D_N^{(N/2)}\rangle = \binom{N}{\frac{N}{2}}^{-\frac{1}{2}} \sum_i \mathcal{P}_i \, |H^{\otimes\frac{N}{2}}V^{\otimes\frac{N}{2}}\rangle. \tag{4.76}$$

The sensitivity is then calculated by measuring the correlation function (corresponds here to the operator $\hat{A}$ in Eq. 4.75) along well defined directions on the Bloch sphere. The correlation functions are defined as (see also in [64]),

$$\hat{C}_{jk}(\theta) = \left((\cos\theta)\hat{\sigma}_j + (\sin\theta)\hat{\sigma}_k\right)^{\otimes N} \tag{4.77}$$

with j, k taking all distinct permutations of x, y and z. Measuring, for example, $\hat{C}_{zx}(\theta)$ corresponds to a measurement on the plane perpendicular to the y-axis of the Bloch

---

[29]Note that this is not in general the case, if reduced detection efficiency and interference fringe visibility are assumed [160]

sphere. The sensitivity of the phase shift $\Delta\theta$ calculates then, according to Eq. 4.75, to [64]

$$\Delta\theta = \frac{\sqrt{1 - \langle \hat{C}_{jk}(\theta)^{\otimes N}\rangle^2}}{\left|\frac{\partial\langle\hat{C}_{jk}(\theta)^{\otimes N}\rangle}{\partial\theta}\right|}. \tag{4.78}$$

To motivate the performance of symmetric N particle Dicke states with $N/2$ excitations, we will compare them with the Greenberger-Horne-Zeilinger (GHZ) state [130], a state which achieves a measurement sensitivity up to the Heisenberg limit. This will be shortly demonstrated in the next few lines. Let us assume we have a N-particle GHZ state in polarization

$$|GHZ_{in}\rangle = \frac{1}{\sqrt{2}}(\underbrace{|H...H\rangle}_{N-\text{times}} + \underbrace{|V...V\rangle}_{N-\text{times}}). \tag{4.79}$$

If we now apply a phase shift $U(\theta)$ between H and V, like for example in a Mach-Zehnder interferometer, which corresponds to the following transformation

$$U(\theta) = \begin{pmatrix} 1 & 0 \\ 0 & e^{i\theta} \end{pmatrix}^{\otimes N} \tag{4.80}$$

we obtain,

$$|GHZ_{out}\rangle = U(\theta)|GHZ_{in}\rangle = \frac{1}{\sqrt{2}}(|H...H\rangle + e^{iN\theta}|V...V\rangle) \tag{4.81}$$

and we see that the phase between horizontally and vertically polarized photons scales proportional to the number of particles N. Applying the phase shift in Eq. 4.80 corresponds to the measurement operator $(e^{i\theta\hat{J}_z})^{\otimes N} = (i\sin(\theta/2)\hat{\sigma}_z + \cos(\theta/2)\mathbb{1})^{\otimes N}$ (refers here to the operator $\hat{A}$ in Eq. 4.75). The sensitivity in Eq. 4.75 can then be calculated for the GHZ to $\Delta\theta = 1/N$ [23], which corresponds to the Heisenberg limit, the best allowed by quantum mechanics.

If we do the same for the symmetric N particle Dicke state with $N/2$ excitations and apply the phase operator of Eq. 4.80 also in the $\hat{\sigma}_z$ basis as the GHZ above, we observe that all *ket*-terms in Eq. 4.76 have the same amount of H and V and add therefore just the global phase $e^{i\theta\frac{N}{2}}$ to the state $|D_N^{(N/2)}\rangle$

$$|D_{out}\rangle = U(\theta)|D_N^{(N/2)}\rangle = \binom{N}{\frac{N}{2}}^{-\frac{1}{2}}(e^{i\theta\frac{N}{2}}|\underbrace{H...H}_{\frac{N}{2}-\text{times}}\underbrace{V...V}_{\frac{N}{2}-\text{times}}\rangle + ... + e^{i\theta\frac{N}{2}}|\underbrace{V...V}_{\frac{N}{2}-\text{times}}\underbrace{H...H}_{\frac{N}{2}-\text{times}}\rangle) \tag{4.82}$$

$$= e^{i\theta\frac{N}{2}}|D_N^{(N/2)}\rangle. \tag{4.83}$$

Hence, we are not able to measure any phase difference between horizontally and vertically polarized photons and have to look for another basis where the phase resolution

Figure 4.10: **Theoretical comparison of probability amplitudes of GHZ and symmetric Dicke state with two excitations for four qubits.** In a) - c) the GHZ state is shown in the basis $\hat{\sigma}_z$, $\hat{\sigma}_x$ and $\hat{\sigma}_y$. In d) - f) the symmetric Dicke state is shown with the same basis settings for comparison.

of the state is better. This can also be illustrated in a bar chart with the probability amplitudes of the GHZ and the symmetric N particle Dicke states with $N/2$ excitations in the $\hat{\sigma}_z$, $\hat{\sigma}_x$ and $\hat{\sigma}_y$ basis (shown in Fig. 4.10), for the case of, for example, four qubits. We see that Fig. 4.10 a) and Fig. 4.10 e), f) have quite a similar structure: the contribution of the bars at the very left and right is highest. This can also be verified by transforming the symmetric Dicke state $|D_N^{(N/2)}\rangle$ analytically to the $\hat{\sigma}_x$ and $\hat{\sigma}_y$ basis, resulting in $\sqrt{5/8}\,|GHZ_N^{\mp}\rangle + \sqrt{3/16}(|D_N^{(N/2+1)}\rangle \mp |D_N^{(N/2-1)}\rangle)$ with $|GHZ_N^{\mp}\rangle = \sqrt{1/2}(|0\rangle^{\otimes N} \mp |1\rangle^{\otimes N})$ and $0 = \{+, L\}$, $1 = \{-, R\}$ [50]. We obviously see the high contribution of the GHZ terms. Fig. 4.10 a) is plotted in the basis $(\hat{\sigma}_z)$ where the GHZ state reaches Heisenberg sensitivity, and one could guess, that the symmetric N particle Dicke states with $N/2$ excitations achieves a similar sensitivity for the basis $\hat{\sigma}_x$ and $\hat{\sigma}_y$ [30].

This is indeed the case and can also be calculated via the quantum Fisher information (see Eq. 4.48). For the N particle GHZ state $F_Q[\rho_{GHZ}, \hat{J}_z] = N^2$ reaches the Heisenberg limit and for the directions $\hat{J}_{x,y}$ the shot noise limit $F_Q[\rho_{GHZ}, \hat{J}_{x,y}] = N$. For the symmetric N particle Dicke state with $N/2$ excitations the quantum Fisher information in $\hat{J}_z$ is $F_Q[\rho_D, \hat{J}_z] = 0$, which indicates that we do not have any phase sensitivity in this case, while for the directions $\hat{J}_{x,y}$ we obtain $F_Q[\rho_D, \hat{J}_{x,y}] = \frac{N^2}{2} + N$. So, the symmetric Dicke state achieves for large N a scaling of $\frac{N^2}{2}$ which is up to a factor of $\frac{1}{2}$ proportional to N^2 the Heisenberg limit. This means the Dicke state achieves

---

[30]Note, that it has already been shown theoretically that the symmetric N particle Dicke state reaches his maximal phase sensitivity in the $\hat{\sigma}_x$ and $\hat{\sigma}_y$ basis [137].

Heisenberg like scaling for the directions $\hat{J}_x$ and $\hat{J}_y$, which is remarkable and explains the similarities in the bar charts of Fig. 4.10. In addition, if we calculate the sum of the quantum Fisher information (divided by three) along three orthogonal directions on the Bloch sphere (we call it average quantum Fisher information $\bar{F}_Q$) we obtain for the directions x, y and z for the GHZ and Dicke state, $\bar{F}_Q[\rho_{D,GHZ}] = \frac{1}{3}(N^2 + 2N)$, which is also the maximum achievable for any quantum state and is to my knowledge only saturated by the GHZ and symmetric N particle Dicke state with $N/2$ excitations (see preprint 4.2.1).

In the experiment (see preprint 4.2.1) we have observed a six photon symmetric Dicke state and measured the phase sensitivity according to Eq. 4.75 with the operators $\hat{C}_{zy}$ and $\hat{C}_{zx}$ (see Eq. 4.77), which corresponds to the measurement directions in the plane perpendicular to the x-axis of the Bloch sphere and y-axis, respectively. For both directions, we could clearly prove sub-shot noise sensitivity, which is the first time observed with a six photon entangled state and demonstrates the performance of symmetric Dicke states, according to two orthogonal measurement directions on the Bloch sphere.

4.2.1 Preprint: Experimental quantum metrology with Dicke and Twin-Fock states for determining two complementary phases beyond the shot noise limit

Experimental quantum metrology with Dicke and Twin-Fock states for determining two complementary phases beyond the shot noise limit

Witlef Wieczorek,[1,2,3] Roland Krischek,[1,2] Wiesław Laskowski,[1,2,4] and Harald Weinfurter[1,2]

[1] *Max-Planck-Institut für Quantenoptik, Hans-Kopfermann-Strasse 1, D-85748 Garching, Germany*
[2] *Fakultät für Physik, Ludwig-Maximilians-Universität, D-80797 München, Germany*
[3] *Present address: Faculty of Physics, University of Vienna, A-1090 Wien, Austria*
[4] *Institute of Theoretical Physics and Astrophysics,
University of Gdansk, PL-80-952 Gdansk, Poland*

Non-classical resources can speed up classical information processing but can also improve on the precision of measurements [1]. The goal of quantum metrology [2] is to develop methods for the latter, for example to determine a parameter like a phase shift from a measurement observable with an uncertainty beyond the classical shot noise limit. Well-known non-classical resources as the Greenberger-Horne-Zeilinger [3–5] or N00N states [6, 7] have been identified to be suitable for this purpose and have also been implemented experimentally, see for example [8–12]. In our work, we consider symmetric Dicke [13, 14] and two-mode Fock states [15–17] for measurements better than the classical limit. These states approach the ultimate Heisenberg limit by a small constant factor [15–17]. In our work, we show using the description of a two-state system, that multi-partite entangled Dicke states allow to achieve this uncertainty for two complementary directions on the Bloch sphere. For a quantification thereof, we introduce a novel criterion, which allows to identify such suitable states. We experimentally demonstrate the benefits of these states for, in our case, polarization interferometry. To this end, we use up to six photons [18–20] and are able to beat the classical shot noise limit. Our work reveals another aspect of phase determination in quantum metrology. (version:)

Nowadays, the shot noise limit (SNL) is reached in more and more interferometric applications, foremost in atomic clocks or gravitational wave detectors. This limit determines the lowest uncertainty obtainable in a measurement on independent particles or photons, respectively. Here, we consider the measurement of a phase θ that can be determined from an observable $\hat{O}$ with an uncertainty

$$\Delta\theta = \Delta\hat{O} / \left| \frac{\partial \langle \hat{O} \rangle}{\partial \theta} \right|, \qquad (1)$$

using a simple linearized error model and the variance $(\Delta\hat{O})^2 = \langle \hat{O}^2 \rangle - \langle \hat{O} \rangle^2$. Thus, a measurement on N independent particles yields the SNL of $\Delta\theta_{\mathrm{SNL}} = 1/\sqrt{N}$. This result can also be obtained by considering the distinguishability of quantum states using general methods as the quantum Cramér-Rao bound (QCR) or the quantum Fisher information [21, 22].

The major goal of quantum metrology is now to improve precision measurements beyond the SNL by utilizing non-classical resources like entangled or squeezed states. Thereby, the uncertainty can be reduced down to $\Delta\theta_{\mathrm{HL}} = 1/N$, the Heisenberg limit (HL). N00N-states [6, 7] ($|N00N\rangle = (|N,0\rangle_{l,u} + |0,N\rangle_{l,u})/\sqrt{2}$) of N indistinguishable particles being in a superposition of all traversing the upper (u) or the lower (l) arm of an interferometer can be used to determine a collective phase shift θ at the HL [fig. 1(a)]. Alternatively, when using N individually addressable particles for interferometry [fig. 1(b)], θ can be determined at the HL by using multi-partite entangled GHZ-states [3, 4, 10]
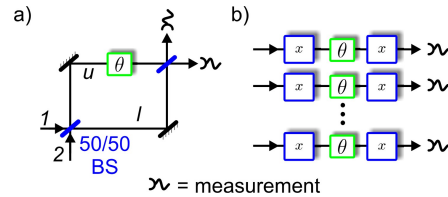

FIG. 1: Typical interferometric arrangements. (a) Schematic of Mach-Zehnder interferometry [23], where an incoming beam is divided by a 50/50 beam splitter (BS), followed by a relative phase shift θ and the recombination at a second BS. The phase shift is applied collectively to all photons traversing the upper (u) arm. (b) In Ramsey interferometry, one usually considers a sequence of rotations on the Bloch sphere of a qubit [4] [cf. fig. 2(a)]: a $\pi/2$ rotation around, say, the x direction, a further rotation by θ around the z direction, and, finally, a second rotation by $\pi/2$ around the x direction. In this case, the phase θ is applied to each particle individually. The overall state transformation of Mach-Zehnder and Ramsey interferometry is essentially equivalent.

($|\mathrm{GHZ}_N\rangle = (|00\ldots0\rangle + |11\ldots1\rangle)/\sqrt{2}$), with N particles being in a superposition of states $|00\ldots0\rangle$ and $|11\ldots1\rangle$. Effectively, both approaches, i.e. collective or individual phase shifts, are equivalent as it is only essential that the same phase shift is applied to all N particles.

Based on developments in quantum information theory, research in multi-partite entanglement is at a stage to apply particular features of other multi-partite entangled states for quantum metrology applicable for both cases. In this letter, we aim at this and reveal new as-

4.2. SUB SHOT NOISE PHASE ESTIMATION USING SIX PHOTON SYMMETRIC DICKE STATES

pects for interferometry by studying and demonstrating the properties of the two-mode Fock states $|\text{TMF}\rangle$ suitable for the determination of a collective phase shift [15–17] (cf. eq. 3) and of their analogy for individually addressable particles, multi-partite entangled Dicke states $|D_N^{(e)}\rangle$ [13, 14] (cf. eq. 4). To this end, let us consider the properties of quantum states in terms of correlation functions, which are given as the product of measurement results on individual particles. For qubits, i.e., particles having two possible states like $|0\rangle$ and $|1\rangle$, a single particle observable is given by

$$\hat{O}(\gamma, \phi) = (\sin\gamma\cos\phi)\,\hat{\sigma}_x + (\sin\gamma\sin\phi)\,\hat{\sigma}_y + (\cos\gamma)\,\hat{\sigma}_z, \quad (2)$$

where $\hat{\sigma}_i$ denote the Pauli matrices ($i \in \{x, y, z\}$), and γ and ϕ are spherical coordinates [fig. 2(a)]. The measurement of $\hat{O}(\gamma, \phi)$ can be used to deduce the latter and, in the case of N particles, $\hat{O}(\gamma, \phi)$ has to be measured for each particle in order to infer γ and ϕ with the smallest uncertainty. This results in the determination of the N-particle correlation $\langle \hat{O}(\gamma, \phi)^{\otimes N}\rangle$. Comparing the latter to conventional interferometry, like Mach-Zehnder interferometry (MZI)[23] as used for gravitational wave detection or Ramsey interferometry [4] as used in atomic clocks (see fig. 1), it can be shown that the overall state transformation in conventional interferometry is analogous to $\hat{O}(\gamma/2, 0)$ (Methods). Obviously, this does not utilize the full dependence of $\hat{O}(\gamma, \phi)$ on both angles γ and ϕ. In the following, we therefore generalize conventional interferometry and show the benefits of particular multi-partite entangled states in this context. To quantify the improvement relative to the SNL let us use $\mathcal{S}_{\vec{n}} = \Delta\theta_{\text{SNL}}/\Delta\theta$ [24]. Here, $\vec{n}$ indicates the orientation of the interferometer, which is restricted to the y direction for conventional interferometry (Methods). As explained in Methods, $S_{\vec{n}}$ is closely related to the Fisher information or squeezing. We now have the freedom to choose any interferometer orientation and also to analyze the variation of an initial state caused by the phases γ and ϕ. To take this extension into account, we introduce the improvement over the SNL along the three interferometer directions x, y and z as $(S_{\text{tot}})^2 = (S_x)^2 + (S_y)^2 + (S_z)^2$.

In order to demonstrate the power of generalized interferometry, let us now turn to particular multi-partite entangled states. Symmetric Dicke states or their MZI analogue, the two-mode Fock states have been discussed in the context of interferometry, noticing that their performance falls slightly behind GHZ or N00N states[15–17]. In the following we show that for generalized interferometry these states turn out to be superior. Two-mode Fock states are given as N_1 (N_2) photons in input mode 1 (2) of a MZI (cf. fig. 1),

$$|\text{TMF}\rangle = |N_1, N_2\rangle_{1,2}. \quad (3)$$

Analogous to these states are the symmetric Dicke states (Methods), which are given as superpositions of all distinct symmetric permutations $\mathcal{P}_i(|0^{\otimes(N-e)}1^{\otimes e}\rangle)$ of $(N-e)$ qubits in state 0 and e in state 1:

$$|D_N^{(e)}\rangle = (C_N^e)^{-1/2} \sum_i \mathcal{P}_i(|0^{\otimes(N-e)}1^{\otimes e}\rangle), \quad (4)$$

with $C_N^e = \binom{N}{e}$ and N is an even integer throughout this work. Prominent examples are symmetric Dicke states with an equal number of qubits in the excited and ground state ($e = N/2$), as originally discussed in the context of superradiance [13], or the recently introduced W-state with only one excitation ($e = 1$), discussed in the context of quantum information [25]. The improvement over the SNL for $|D_N^{(e)}\rangle$ is given by $\mathcal{S}_y = \sqrt{1 + 2(N - e)\frac{e}{N}}$. Hence, already the W-state improves on the SNL. However, for increasing N, it approaches a constant value of $\sqrt{3}$, barely better than the SNL. This is in stark contrast to the state $|D_N^{(N/2)}\rangle$ with $\mathcal{S}_y = \sqrt{N/2 + 1}$ [16, 17], which for large N approaches $\sqrt{N}/\sqrt{2}$, i.e., a HL-like scaling equal to the GHZ state up to a factor of $\sqrt{2}$.

To identify the full dependence on γ and ϕ, let us come back to correlation functions. Fig. 2(b) and (c) compare $\langle \hat{O}(\gamma, \phi)^{\otimes N}\rangle$ for the six-qubit Dicke state $|D_6^{(3)}\rangle$ and the GHZ state $|\text{GHZ}_6\rangle$. For the latter (fig. 2(c)) one recognizes the 6-fold oscillation period for a rotation around the z direction, yielding the HL. Yet, for rotations around x or y one obtains a lower oscillation period, which yields in both cases the SNL. Contrary to this, the significantly different symmetry of the Dicke state results in no sensitivity to rotations around z, whereas steep gradients close to the poles yield HL-like scaling for *both x and y* rotations. This can be quantified by S_{tot}, which, remarkably, is equal for both states and reaches the maximal value of $(\mathcal{S}_{\text{tot}})^2 = N + 2$ (Methods). While the GHZ state reaches the HL for z rotations ($(\mathcal{S}_z)^2 = N$), only the SNL is available for the other cases ($(\mathcal{S}_x)^2 = (\mathcal{S}_y)^2 = 1$), see fig. 2(d). For the Dicke state, the HL is almost reached for x *and* y ($(\mathcal{S}_x)^2 = (\mathcal{S}_y)^2 = 1 + N/2$, see fig. 2(d)), while no resolution at all is achieved for the third direction ($(\mathcal{S}_z)^2 = 0$). This also gives a general viewpoint to squeezing (Methods), where now particularly for $|D_N^{(N/2)}\rangle$ two complementary orientations are below the SNL (fig. 2(d)), while the third one has an increased uncertainty. The commonly considered squeezing ellipsoids [23, 26] turn into structured bodies, shown in fig. 2(e) and (f) for the $|\text{GHZ}_6\rangle$ and Dicke states, respectively.

Let us now demonstrate these features in an experimental implementation with photons (fig. 3). An ideal photon source for this purpose is the process of collinear type II spontaneous parametric down conversion (SPDC), as it delivers in its $(N/2)$-th order emission already the two-mode Fock state $|N/2, N/2\rangle_{H,V}$ (called Twin-Fock state) in horizontal (H) and vertical (V) polarization modes. Hence, we consider the case of polarization interferometry, whereby the goal is to determine an optical phase shift between H and V polarization.
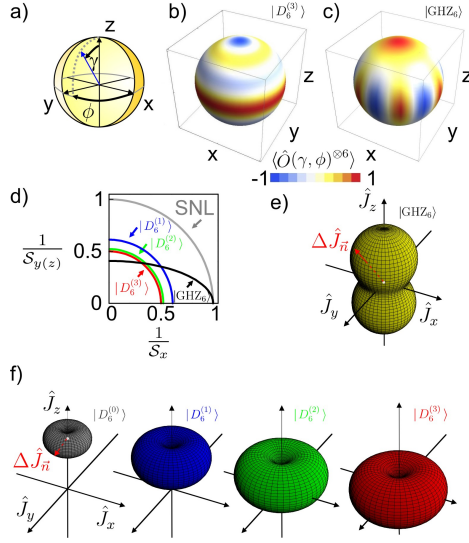
FIG. 2: Comparing Dicke and GHZ states. (a) Bloch sphere of a qubit: The polar angle of a pure state vector is γ and its azimuthal angle is ϕ. For comparing the states (b) $|D_6^{(3)}\rangle$ and (c) $|GHZ_6\rangle$ the expectation value of the observable $\langle\hat{O}(\gamma,\phi)^{\otimes 6}\rangle$ is drawn on a sphere. Thereby, $\langle\hat{O}(\gamma,\phi)^{\otimes 6}\rangle$ is rotationally invariant around the z axis for $|D_6^{(3)}\rangle$, but not for $|GHZ_6\rangle$. (d) Reduced phase uncertainty (i.e. $1/S_{\vec{n}}$) for the states $|D_6^{(e)}\rangle$ ($e \in \{1, 2, 3\}$) for rotations around an axis lying in the x-y plane and for the state $|GHZ_6\rangle$ in the x-z plane. A relation of interferometry to squeezing can be illustrated by considering the expectation values of the angular momenta $\hat{J}_i$ and their variance $\Delta\hat{J}_i$, where usually ellipsoids are used as illustrations [23, 26] (Methods). The variance $\Delta\hat{J}_x, \Delta\hat{J}_y, \Delta\hat{J}_z$ is shown centered around $\langle\hat{J}_x\rangle, \langle\hat{J}_y\rangle, \langle\hat{J}_z\rangle$ for the states (e) $|GHZ_6\rangle$ and (f) $|D_6^{(e)}\rangle$ ($e \in \{0, 1, 2, 3\}$). The larger $\Delta\hat{J}_i$, the smaller the phase uncertainty.
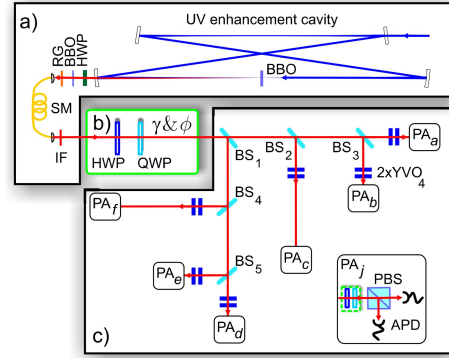

FIG. 3: Experimental phase measurement setup. The experimental setup consists of (a) the spontaneous parametric down conversion (SPDC) photon source given by a ultraviolet (UV) enhancement cavity [30] pumping a β-barium-borate (BBO) crystal, (b) the application of the phases γ and ϕ for determining $\hat{O}(\gamma,\phi)$ by setting appropriate angles of a half-wave plate (HWP) and quarter-wave plate (QWP) and (c) a linear-optical setup for distributing the photons into maximally six spatial modes PA_j with $j \in \{a, b, c, d, e, f\}$ and subsequent photon polarization analysis (PA) and detection. SM, single mode fibre; RG, bandpass filter; BS, polarization-independent beam splitter; IR, interference filter; YVO$_4$, yttrium-vanadate crystal; PBS, polarizing beam splitter; APD, avalanche photo diode.

Starting with the state $|N/2, N/2\rangle_{H,V}$ we are also able to observe the polarization-entangled symmetric Dicke states $|D_N^{(N/2)}\rangle$ after subsequent distribution of the photons into N spatial modes and conditional detection of a single photon in each of the modes [18–20, 27] (fig. 3). In our work, we implemented the phase measurement with up to six photons (see Supplementary Information for state fidelities and count rates). We could choose whether to measure $\hat{O}(\gamma,\phi)$ for each photon individually [i.e. in modes $a, b, c, \ldots$, marked in fig. 3 (c) with a dashed green line], or collectively [fig. 3 (b)], data shown here are for the latter case, for the other case see Supplementary Information.

Fig. 4(a) shows the measurement results for the correlation function $\hat{O}(\gamma, 0)$, i.e. a rotation around the y direction, between six photons observed in spatial modes

a, b, c, d, e, f. To analyze S_y we fit the data with two different models: a Fourier decomposition (shown here) and a SPDC noise model taking into account noise due to higher order SPDC emissions[20, 28, 29] (see Supplementary Information). From the fitted curve we deduce the improvement S_y over the SNL (fig. 4(c)). The results show that we not only observe the respective high oscillation rate of the correlation function, but that also the state's quality is high enough to clearly surpass the SNL and to reach an improvement of $S_y = 1.27 \pm 0.06$. Note, due to the presence of noise the minimal uncertainty is not achieved at angles around $\gamma \approx n \cdot \pi/2$ ($n \in \{0, 1, \ldots\}$), but at $\gamma \approx 1.15 \cdot (\pi/2)$. To illustrate the advantage of the input state for generalized interferometry, we perform the same procedure for a rotation around the x axis [$\hat{O}(\gamma, \pi/2)$, see fig. 4(b)]. The achieved uncertainty along that direction [fig. 4(c)] is even lower than the previous one reaching an improvement as high as $S_x = 1.35 \pm 0.07$ compared to the SNL (now for $\gamma \approx 1.18 \cdot (\pi/2)$).

The determination of the phase relies on previous knowledge of the expected phase interval. For the six-photon case this interval has to be known within $\approx \pi/8$. In our experiment we can make direct use of other SPDC emission orders, where, for example, the 2nd and 1st order emissions deliver four and two photons, respectively.
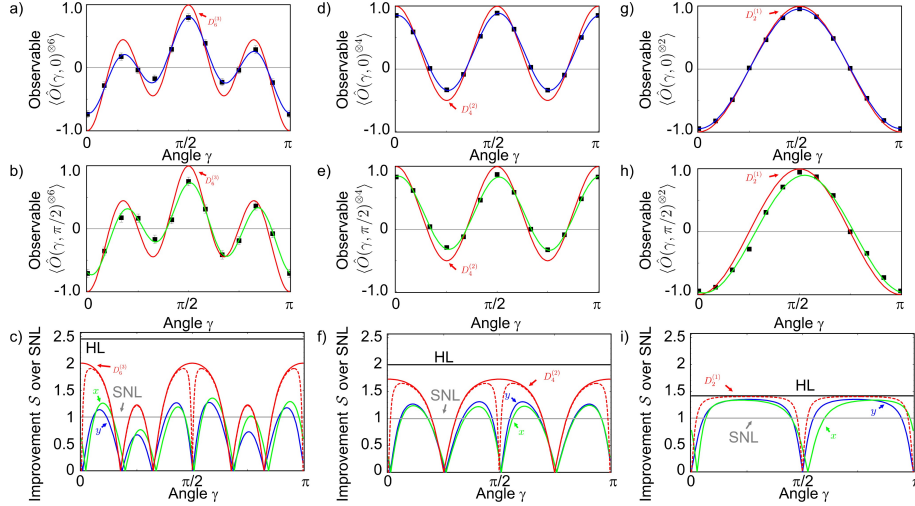
4

FIG. 4: Experimental data for phase determination. The measurement results for $\langle \hat{O}(\gamma,\phi)^{\otimes 6}\rangle$ for (a) y [$\hat{O}(\gamma,0)$] and (b) x [$\hat{O}(\gamma,\pi/2)$] rotations on the Bloch sphere are depicted along with a fit corresponding to a Fourier decomposition (blue curve in (a) and green curve in (b)). The red curve shows the expectation for the ideal state $|D_6^{(3)}\rangle$. (c) The improvement $\mathcal{S}$ over the shot noise limit (SNL) for the fitted data. The SNL is surpassed maximally for angles $\gamma \approx 1.15\cdot(\pi/2)$ for y and $\gamma \approx 1.18\cdot(\pi/2)$ for x rotations. Admixture of white noise to $|D_6^{(3)}\rangle$ would also lead to a reduction and shift (dashed red curve). In (d,e,f) the corresponding results for the 4-qubit observable $\langle \hat{O}(\gamma,\phi)^{\otimes 4}\rangle$ and in (g,h,i) for the 2-qubit observable $\langle \hat{O}(\gamma,\phi)^{\otimes 2}\rangle$ are shown, upon detection of 4 or 2 photons, respectively. In both cases, the SNL is surpassed: for four photons 1.31 ± 0.01 (1.25 ± 0.02) times SNL for y (x) rotations and for two photons 1.348 ± 0.006 (1.334 ± 0.041) times SNL.

Thereby, we can determine successively the phase shift better than the respective SNL also within the intervals $\approx \pi/4$ [fig. 4(d,e,f)] and $\approx \pi/2$ [fig. 4(g,h,i)] (see also Supplementary Information).

We want to emphasize that the generalized approach to interferometry together with the utilization of multipartite entangled states reveals novel and powerful features such as HL-like scaling for two complementary directions, which can be ideal for example for tracking magnetic field fluctuations. This enables significant advances for entanglement-enhanced metrology. In particular, multi-partite entangled Dicke and Twin-Fock states turn out to be ideal input states for this purpose as evidenced by a novel criterion, which will foster the search for further suitable states. In our experiment, we demonstrated sub-shot noise uncertainty for phase measurements using up to six photons. Practical usage of our particular experimental implementation would be greatly enhanced by reducing photon losses. For example, the utilization of highly efficient, photon-number resolving detectors would enable higher state qualities [20, 28, 29] and, thus, an overall stronger improvement as well as a direct usage of all SPDC emission orders and, thus, an increased throughput. We are grateful to fruitful discussions with Philipp Hyllus, Augusto Smerzi, Luca

METHODS

Dicke states, two-mode Fock states and interferometry.

The symmetric Dicke states $|D_N^{(e)}\rangle$ are eigenstates of the total angular momentum squared $\hat{J}^2$ and the angular momentum in the z direction $\hat{J}_z$ [13, 14], whereby the $\hat{J}$-operators are angular momentum operators $\hat{J}_i = \frac{1}{2}\sum_k \hat{\sigma}_i^k$ ($i \in \{x,y,z\}$) with $\hat{\sigma}_i^k$ acts on the k-th qubit ($\hat{J}^2|D_N^{(e)}\rangle = N/2(N/2+1)|D_N^{(e)}\rangle$ and $\hat{J}_z|D_N^{(e)}\rangle = (N/2-e)|D_N^{(e)}\rangle$). For the states $|D_N^{(N/2)}\rangle$, we have $\Delta\hat{J}_x = \Delta\hat{J}_y = \sqrt{N(N+2)/8}$ and $\Delta\hat{J}_z = 0$. The states $|D_N^{(e)}\rangle$ are isomorphic to the two-mode Fock states $|N_H, N_V\rangle_{H,V}$, in particular $|D_N^{(N/2)}\rangle$ to the Twin-Fock state $|N/2, N/2\rangle_{H,V}$ (see Supplementary Information).

5

The observable $\hat{O}(\gamma, \phi)$ can also be regarded as a unitary transformation for rotations around the y and z directions of the Bloch sphere [fig. 2(a)], $\hat{O}(\gamma, \phi) = e^{i\pi/2} e^{-i\phi\hat{J}_z} e^{-i2\gamma\hat{J}_y} e^{-i(\pi-\phi)\hat{J}_z}$. For $\hat{O}(\gamma/2, 0) = e^{i\pi/2} e^{-i\gamma\hat{J}_y} e^{-i\pi\hat{J}_z}$ the transformation of MZI or Ramsey interferometry is obtained [4, 23], up to the reflection $e^{-i\pi\hat{J}_z}$ and the global phase $e^{i\pi/2}$. For the symmetric Dicke states $|D_N^{(e)}\rangle$ one obtains $\langle \hat{O}(\gamma, \phi)^{\otimes N}\rangle_{D_N^{(e)}} = \sum_{k=0}^{e}(-1)^{k+e} C_{N-e}^k C_e^k (\cos\gamma)^{N-2k}(\sin\gamma)^{2k}$.

Fisher information, improvement over the shot noise limit and squeezing.

The improvement over the SNL $\mathcal{S}_{\vec{n}}$ is connected with the Fisher information $F_Q(\rho_{\text{in}})$ [21, 22] as $\mathcal{S}_{\vec{n}} = \sqrt{F_Q(\rho_{\text{in}}, \hat{J}_{\vec{n}})}/\sqrt{N}$. The Fisher information essentially measures the information content of the observable $\hat{J}_{\vec{n}}$ for the amount of rotation around the axis $\vec{n}$ when using ρ_{in}. It can be calculated for pure states [21, 22] $\rho_{\text{in}} = |\psi\rangle_{\text{in}}\langle\psi|_{\text{in}}$ as $F_Q(\rho_{\text{in}}, \hat{J}_{\vec{n}}) = 4\langle\Delta\hat{J}_{\vec{n}}^2\rangle$ with $\hat{J}_{\vec{n}} = (\cos\alpha\sin\beta)\hat{J}_x + (\sin\alpha\sin\beta)\hat{J}_y + (\cos\beta)\hat{J}_z$. For the states $|D_N^{(e)}\rangle$ one obtains $F_Q(\rho_{\text{in}}, \hat{J}_{\vec{n}}) = (N + 2e(N-e))\sin^2\beta$, and for the states $|\text{GHZ}_N\rangle$, $F_Q(\rho_{\text{in}}, \hat{J}_{\vec{n}}) = N(\sin^2\beta + N\cos^2\beta)$. For the total improvement over the SNL S_{tot} we obtain the following general bound

$$
\begin{aligned}
(S_{\text{tot}})^2 &= (S_x)^2 + (S_y)^2 + (S_z)^2 \\
&= (F_Q(\rho_{\text{in}}, \hat{J}_x) + F_Q(\rho_{\text{in}}, \hat{J}_y) + F_Q(\rho_{\text{in}}, \hat{J}_z))/N \\
&\leq 4\langle\Delta\hat{J}_x^2 + \Delta\hat{J}_y^2 + \Delta\hat{J}_z^2\rangle/N \\
&\leq 4\langle\hat{J}_x^2 + \hat{J}_y^2 + \hat{J}_z^2\rangle/N = 4\langle\hat{J}^2\rangle/N \\
&= 4N(N+2)/(4N) = N + 2,
\end{aligned}
$$

which is saturated by the states $|D_N^{(N/2)}\rangle$ and $|\text{GHZ}_N\rangle$.

To obtain a comparison with the notion of squeezing, we consider the product of the reduced phase uncertainty (i.e. $1/\mathcal{S}_{\vec{n}}$) for two different rotations: $\frac{1}{\mathcal{S}_{\vec{n}_1}} \cdot \frac{1}{\mathcal{S}_{\vec{n}_2}}$, see also fig. 2(d). Then, the SNL ($\mathcal{S}^{\text{SNL}} = 1$) yields the bound $\frac{1}{\mathcal{S}_{\vec{n}_1}^{\text{SNL}}} \cdot \frac{1}{\mathcal{S}_{\vec{n}_2}^{\text{SNL}}} \geq 1$. For the states $|D_N^{(N/2)}\rangle$ and rotations along x and y a smaller value than the SNL is obtained ($\frac{1}{1+N/2}$), which is even lower than the one for the $|\text{GHZ}_N\rangle$ state for rotations along x and z ($\frac{1}{\sqrt{N}}$).

———

[1] Nielsen, M. A. & Chuang, I. L. *Quantum Computation and Quantum Information* (Cambridge University Press, 2000).

[2] Giovannetti, V., Lloyd, S. & Maccone, L. Quantum-enhanced measurements: Beating the standard quantum limit. *Science* **306**, 1330–1336 (2004). URL http://www.sciencemag. org/cgi/content/abstract/306/5700/1330. http://www.sciencemag.org/cgi/reprint/306/5700/1330.pdf.

[3] Greenberger, D. M., Horne, M. A. & Zeilinger, A. Going beyond bell's theorem. In *Bell's Theorem, Quantum theory and Conceptions of the Universe*, 69–72 (Kluwer Academic Publishers, 1989).

[4] Wineland, D. J., Bollinger, J. J., Itano, W. M., Moore, F. L. & Heinzen, D. J. Spin squeezing and reduced quantum noise in spectroscopy. *Phys. Rev. A* **46**, R6797–R6800 (1992).

[5] Bollinger, J. J. ., Itano, W. M., Wineland, D. J. & Heinzen, D. J. Optimal frequency measurements with maximally correlated states. *Phys. Rev. A* **54**, R4649–R4652 (1996). URL http://link.aps.org/abstract/ PRA/v54/pR4649.

[6] Boto, A. N. *et al.* Quantum interferometric optical lithography: Exploiting entanglement to beat the diffraction limit. *Phys. Rev. Lett.* **85**, 2733–2736 (2000).

[7] Dowling, J. P. Quantum optical metrology -the lowdown on high-n00n states. *Cont. Phys.* **49**, 125–143 (2008). URL http://www.informaworld.com/10.1080/ 00107510802091298.

[8] Meyer, V. *et al.* Experimental demonstration of entanglement-enhanced rotation angle estimation using trapped ions. *Phys. Rev. Lett.* **86**, 5870–5873 (2001).

[9] Edamatsu, K., Shimizu, R. & Itoh, T. Measurement of the photonic de broglie wavelength of entangled photon pairs generated by spontaneous parametric downconversion. *Phys. Rev. Lett.* **89**, 213601 (2002).

[10] Leibfried, D. *et al.* Toward heisenberg-limited spectroscopy with multiparticle entangled states. *Science* **304**, 1476–1478 (2004). URL http://www.sciencemag. org/cgi/content/abstract/304/5676/1476. http://www.sciencemag.org/cgi/reprint/304/5676/1476.pdf.

[11] Nagata, T., Okamoto, R., O'Brien, J. L., Sasaki, K. & Takeuchi, S. Beating the Standard Quantum Limit with Four-Entangled Photons. *Science* **316**, 726–729 (2007). URL http://www.sciencemag. org/cgi/content/abstract/316/5825/726. http://www.sciencemag.org/cgi/reprint/316/5825/726.pdf.

[12] Jones, J. A. *et al.* Magnetic Field Sensing Beyond the Standard Quantum Limit Using 10-Spin NOON States. *Science* **324**, 1166–1168 (2009). URL http://www.sciencemag. org/cgi/content/abstract/324/5931/1166. http://www.sciencemag.org/cgi/reprint/324/5931/1166.pdf.

[13] Dicke, R. H. Coherence in spontaneous radiation processes. *Phys. Rev.* **93**, 99–110 (1954). URL http: //link.aip.org/link/?PR/93/99/1.

[14] Stockton, J. K., Geremia, J. M., Doherty, A. C. & Mabuchi, H. Characterizing the entanglement of symmetric many-particle spin-(1/2) systems. *Phys. Rev. A* **67**, 022112 (2003). URL http://link.aps.org/ abstract/PRA/v67/e022112.

[15] Holland, M. J. & Burnett, K. Interferometric detection of optical phase shifts at the heisenberg limit. *Phys. Rev. Lett.* **71**, 1355–1358 (1993).

[16] Campos, R. A., Gerry, C. C. & Benmoussa, A. Optical interferometry at the heisenberg limit with twin fock states and parity measurements. *Phys. Rev. A* **68**, 023810 (2003).

[17] Hradil, Z. & Rehcek, J. Quantum interference and fisher information. *Phys. Lett. A* **334**, 267 – 272 (2005). URL http://www.sciencedirect.

com/science/article/B6TVM-4DWVPFW-2/2/
2eb270cfdaa70b866e11fdabe9b04987.

[18] Kiesel, N., Schmid, C., Tóth, G., Solano, E. & Weinfurter, H. Experimental observation of four-photon entangled dicke state with high fidelity. *Phys. Rev. Lett.* **98**, 063604 (2007). URL http://link.aps.org/abstract/PRL/v98/e063604.

[19] Wieczorek, W. *et al.* Experimental entanglement of a six-photon symmetric dicke state. *Phys. Rev. Lett.* **103**, 020504 (2009). URL http://link.aps.org/abstract/PRL/v103/e020504. ArXiv: 0903.2213 [quant-ph].

[20] Prevedel, R. *et al.* Experimental realization of dicke states of up to six qubits for multiparty quantum networking. *Phys. Rev. Lett.* **103**, 020503 (2009). URL http://link.aps.org/abstract/PRL/v103/e020503. ArXiv: 0903.2212 [quant-ph].

[21] Braunstein, S. L. & Caves, C. M. Statistical distance and the geometry of quantum states. *Phys. Rev. Lett.* **72**, 3439–3443 (1994).

[22] Pezze, L. & Smerzi, A. Entanglement, nonlinear dynamics, and the heisenberg limit. *Phys. Rev. Lett.* **102**, 100401 (2009). URL http://link.aps.org/abstract/PRL/v102/e100401.

[23] Yurke, B., McCall, S. L. & Klauder, J. R. Su(2) and su(1,1) interferometers. *Phys. Rev. A* **33**, 4033–4054 (1986).

[24] Okamoto, R. *et al.* Beating the standard quantum limit: phase super-sensitivity of n-photon interferometers. *New J. Phys.* **10**, 073033 (9pp) (2008). URL http://stacks.iop.org/1367-2630/10/073033.

[25] Dür, W., Vidal, G. & Cirac, J. I. Three qubits can be entangled in two inequivalent ways. *Phys. Rev. A* **62**, 062314 (2000).

[26] Wineland, D. J., Bollinger, J. J., Itano, W. M. & Heinzen, D. J. Squeezed atomic states and projection noise in spectroscopy. *Phys. Rev. A* **50**, 67–88 (1994).

[27] Kiesel, N. *et al.* Operational multipartite entanglement classes for symmetric photonic qubit states. *Phys. Rev. A* **81**, 032316 (2010). ArXiv:0911.5112v1 [quant-ph].

[28] Laskowski, W., Wiesniak, M., Żukowski, M., Bourennane, M. & Weinfurter, H. Interference contrast in multi-source few-photon optics. *J. Phys. B* **42**, 114004 (12pp) (2009). URL http://stacks.iop.org/0953-4075/42/114004.

[29] Wieczorek, W., Kiesel, N., Schmid, C. & Weinfurter, H. Multiqubit entanglement engineering via projective measurements. *Phys. Rev. A* **79**, 022311 (2009). URL http://link.aps.org/abstract/PRA/v79/e022311. ArXiv:0901.4091 [quant-ph].

[30] Krischek, R. *et al.* Ultraviolet enhancement cavity for ultrafast nonlinear optics and high-rate multiphoton entanglement experiments. *Nat. Photon.* **4**, 170–173 (2010). URL http://dx.doi.org/10.1038/nphoton.2009.286.

5
Conclusions and outlook

In this thesis, we have contributed with respect to several aspects to the development and exploration of photonic entanglement. A key point is the development of a novel source for the generation of multi-qubit quantum registers based on the spontaneous parametric down conversion (SPDC) process (see publication 3.1.1 [48]). All experiments in this thesis have been performed with this source and it is therefore considered as the heart of the work presented here. Furthermore, we have characterized different multi-photon entangled states and have found a particular state, which can also be considered as a resource to create other quantum states (see publication 3.3.1 [50]). In addition, we have found an effective method to tomographically characterise a desired quantum state using the symmetry of the probe state (see publication 3.4.1 [59]). Finally, we have also demonstrated an explicit application of entangled photons in terms of phase estimation and have shown that entangled photons can perform this task better than possible with classical photons (see preprints 4.1.3 [60], 4.1.5 and 4.2.1).

In the last years, the exploration of entangled photons has always been related to the technological developments of appropriate photon sources. This is also the case here and the development of this novel SPDC source led to a series of other experiments presented in this work. The novelty of this photon source comes from the fact that to pump the process of SPDC, which is widely used for the generation of multiple entangled photons, an enhancement cavity for ultrashort ultraviolet laser pulses has been developed. This is the first experimental realization of an enhancement cavity at this wavelength for femtosecond laser pulses. With this cavity we have been able to increase the yield of the observation of genuine six partite entangled states on two orders of magnitude, compared to SPDC sources pumped with todays commercially available laser systems. Pumping a non-linear crystal with intense UV laser pulses for SPDC is still the workhorse to generate mulit-photon entangled states. In the future, the SPDC source presented here can even without substantial improvements lead to the observation of an eight photon entangled state [162]. The main concern to observe entangled photons of even higher numbers is, on the one hand, due to the highly probabilistic nature of the SPDC process itself and, on the other hand, due to noise originating from higher order SPDC emission disturbing the proper observation of a desired state, especially for increasing pump powers [163]. A possibility to decrease the noise of SPDC emission is to increase the overall detection efficiency. An effective way to perform this task is to

improve the efficiency of single photon detectors for the infrared wavelength region. In the future, considerable progress is expected from the development of superconducting detectors (see for example [94, 95] and references therein). An alternative to the probabilistic SPDC process is the development of triggered single photon sources, which also allow in principle to generate multi-photon entangled states in the future (for a review see, for example, [96]).

Besides the development of a new SPDC source, we have observed different multi-photon entangled states by processing the photons in linear optical networks. A specially designed linear optics setup allowed us to observe the symmetric six photon entangled Dicke state. In the experiment we have been able to observe the symmetric six photon Dicke state with a fidelity of 0.654 ± 0.024 and verified the entanglement of the probe state with Bell inequalities and entanglement witnesses. This state has especially attracted our interest, because it can also be used as a resource to generate other multi-partite entangled states of lower qubit number by projective measurements. This allowed us to observe out of a symmetric six photon Dicke state other five or four photon states, like for example, the four photon W state or the four photon Greenberger Horne Zeilinger (GHZ) state. The four photon W state has the first time been observed here. Furthermore, the six-photon symmetric Dicke state can also be used for open destination teleportation, telecloning and quantum secret sharing [90, 64], which makes this state even more important for the field of quantum information.

Characterizing the entanglement of a probe state is usually performed with only few settings compared to full quantum state tomography. But if the entire information content of a quantum state is desired, full quantum state tomography is still the method of choice. The disadvantage of full quantum state tomography is that the number of measurement settings is scaling exponentially with the number of qubits. In this work, we present an alternative using the fact that a lot of quantum states, like for example the GHZ and all Dicke states, are permutationally invariant, which means that under exchange of two qubits, the state stays the same. Using this symmetry we can reduce the measurement effort from exponential scaling to only quadratic scaling with the number of qubits. For photons, quantum state tomography has already performed with four qubits [87]. For six photons, performing full quantum state tomography assuming 3.7 six fold counts per minute [50] for 729 basis settings with a measurement statistics of 300 counts per basis results in a measurement time of approximately 41 days! By using permutationally invariant quantum state tomography we are able to reduce the number of settings to 28, which results with the same assumptions from above in only 1.5 days, which makes it reasonable to perform permutationally invariant tomography for a six-photon entangled state in the future. Because permutation invariant tomography is a general method and applies to all kind of qubits, it could in principle also be used to perform tomography of more than, for example, eight ions [32], because not only the measurement time can be reduced, but also the computational effort to reconstruct the density matrix, which is another difficulty for an increasing number of qubits [164].

Finally, we have experimentally demonstrated a direct application of entangled pho-

tons to highlight their improved performance with respect to classical photons. This has been realized for the estimation of an unknown phase shift, which is also known as quantum enhanced metrology. Because not every entangled state is equally useful for phase estimation, we first identify useful entanglement with the help of a criterion and then experimentally prove its usefulness by implementing two different phase estimation protocols. In the experiment we use a symmetric four photon Dicke state and compare its benefit with respect to a separable state. For the entangled state we clearly prove a phase sensitivity beyond the shot-noise-limit, which is not achievable with a separable state. In another experiment we could even prove sub shot noise sensitivity for a symmetric six photon Dicke state, which has not yet been observed for this photon number. Altogether, our study of entangled states useful for phase estimation, identified by a novel criterion, establishes a guideline to perfectly exploit entanglement for quantum enhanced metrology.

All experiments presented in this work have been performed with photons. But there exist many other systems, which have also successfully realized different tasks in the field of quantum information. Some might be more advantageous than others and some less. Combining different quantum systems in the future will definitively be of interest and because quantum states can in the end easily be transmitted by optical glass fibres over large distances it would be surprising if photons will not be involved in one possible combination in the future.

Bibliography

[1] A. Einstein. ber einen die erzeugung und verwandlung des lichtes betreffenden heuristischen gesichtspunkt. *Annalen der Physik*, 322:132 –148, 1905.

[2] A. Einstein, B. Podolsky, and N. Rosen. Can quantum-mechanical description of physical reality be considered complete? *Phys. Rev.*, 47:777–780, 1935.

[3] J.S. Bell. On the einstein-podolsky-rosen paradox. *Physics*, 1:195, 1964.

[4] J. F. Clauser, M. A. Horne, A. Shimony, and R. A. Holt. Proposed experiment to test local hidden-variable theories. *Phys. Rev. Lett.*, 23:880–884, 1969.

[5] John F. Clauser and Michael A. Horne. Experimental consequences of objective local theories. *Phys. Rev. D*, 10:526–535, 1974.

[6] S. J. Freedman and J. F. Clauser. Experimental test of local hidden-variable theories. *Phys. Rev. Lett.*, 28:938–941, 1972.

[7] A. Aspect, P. Grangier, and G. Roger. Experimental tests of realistic local theories via bell's theorem. *Phys. Rev. Lett.*, 47:460–463, 1981.

[8] A. Aspect, J. Dalibard, and G. Roger. Experimental test of bell's inequalities using time- varying analyzers. *Phys. Rev. Lett.*, 49:1804–1807, 1982.

[9] G. Weihs, T. Jennewein, C. Simon, H. Weinfurter, and A. Zeilinger. Violation of bell's inequality under strict einstein locality conditions. *Phys. Rev. Lett.*, 81:5039–5043, 1998.

[10] M. A. Rowe, D. Kielpinski, V. Meyer, C. A. Sackett, W. M. Itano, C. Monroe, and D. J. Wineland. Experimental violation of a bell's inequality with efficient detection. *Nature*, 409:791 – 794, 2001.

[11] P. H. Eberhard. Background level and counter efficiencies required for a loophole-free einstein-podolsky-rosen experiment. *Phys. Rev. A*, 47:R747–R750, 1993.

[12] A. J. Leggett. Nonlocal hidden-variable theories and quantum mechanics: An incompatibility theorem. *Found. Phys.*, 33:1469 – 1493, 2003.

[13] S. Groblacher, T. Paterek, R. Kaltenbaek, C. Brukner, , M. Zukowksi, M. Aspelmeyer, and A. Zeilinger. An experimental test of non-local realism. *Nature*, 446:871, 2007.

[14] Cyril Branciard, Alexander Ling, Nicolas Gisin, Christian Kurtsiefer, Antia Lamas-Linares, and Valerio Scarani. Experimental falsification of leggett's non-local variable model. *Phys. Rev. Lett.*, 99:210407, 2007.

[15] T. Paterek, A. Fedrizzi, S. Gröblacher, T. Jennewein, M. Żukowski, M. Aspelmeyer, and A. Zeilinger. Experimental test of nonlocal realistic theories without the rotational symmetry assumption. *Phys. Rev. Lett.*, 99:210406, 2007.

[16] M.A. Nielsen and I.L. Chuang. Quantum information and quantum computation. *Cambridge University Press*, 2000.

[17] D. Deutsch. Quantum theory, the church-turing principle and the universal quantum computer. *,” Proc. Roy. Soc. Lond. A*, 400,:97, 1985.

[18] L. K. Grover. Quantum mechanics helps in searching for a needle in a heystack. *Phys. Rev. Lett.*, 79:325, 1997.

[19] P. W. Shor. Algorithms for quantum computation: Discrete logarithms and factoring. *In: Proceedings of the 35th Annual Symposium on Foundations of Computer Science*, pages 124 – 134, IEEE Computer Society Press, Los Alamitos, 1994.

[20] N. Gisin, G. Ribordy, W. Tittel, and H. Zbinden. Quantum cryptography. *Rev. Mod. Phys.*, 74:145–195, 2002.

[21] A. N. Boto, P. Kok, D. S. Abrams, S. L. Braunstein, C. P. Williams, and J. P. Dowling. Quantum interferometric optical lithography: Exploiting entanglement to beat the diffraction limit. *Phys. Rev. Lett.*, 85:2733–2736, 2000.

[22] M. D'Angelo, M. V. Chekhova, and Y. Shih. Two-photon diffraction and quantum lithography. *Phys. Rev. Lett.*, 87:013602, 2001.

[23] V. Giovannetti, S. Lloyd, and L. Maccone. Quantum-enhanced measurements: Beating the standard quantum limit. *Science*, 306:1330, 2004.

[24] D. P. DiVincenzo. The physical implementation of quantum computation. *Fortschritte der Physik*, 48:771 – 784, 2000.

[25] E. Knill, R. Laflamme, and G. J. Milburn. A scheme for efficient quantum computation with linear optics. *Nature*, 409:46 – 52, 2001.

[26] P. Kok, W. J. Munro, K. Nemoto, T. C. Ralph, J. P. Dowling, and G. J. Milburn. Linear optical quantum computing with photonic qubits. *Rev. Mod. Phys.*, 79:135–174, 2007.

[27] J. O'Brien. Optical quantum computing. *Science*, 318:1567 – 1570, 2007.

[28] D. Leibfried, E. Knill, S. Seidelin, J. Britton, R. B. Blakestad, J. Chiaverini, D. B. Hume, W. M. Itano, J. D. Jost, C. Langer, R. Ozeri, R. Reichle, and D. J. Wineland. Creation of a six-atom schrdinger cat state. *Nature*, 438:639 – 642, 2005.

[29] S. D. Barrett, P. P. Rohde, and T. M. Stace. Scalable quantum computing with atomic ensembles. *New J. Phys.*, 12:093032, 2010.

[30] I. Bloch. Quantum coherence and entanglement with ultracold atoms in optical lattices,. *Nature*, 453:1016, 2008.

[31] J. I. Cirac and P. Zoller. Quantum computations with cold trapped ions. *Phys. Rev. Lett.*, 74:4091–4094, 1995.

[32] H. Häffner, W. Hänsel, C. F. Roos, J. Benhelm, D. Chek-al kar, M. Chwalla, T. Körber, U. D. Rapol, M. Riebe, P. O. Schmidt, C. Becher, O. Gühne, W. Dür, and R. Blatt. Scalable multiparticle entanglement of trapped ions. *Nature*, 438:643 – 646, 2005.

[33] R. Blatt and D. J. Wineland. Entangled states of trapped atomic ions. *Nature*, 453:1008, 2008.

[34] L. M. K. Vandersypen and I. L. Chuang. Nmr techniques for quantum control and computation. *Rev. Mod. Phys.*, 76:1037–1069, 2005.

[35] C. Negrevergne, T. S. Mahesh, C. A. Ryan, M. Ditty, F. Cyr-Racine, W. Power, N. Boulant, T. Havel, D. G. Cory, and R. Laflamme. Benchmarking quantum control methods on a 12-qubit system. *Phys. Rev. Lett.*, 96:170501, 2006.

[36] D. Loss and D. P. DiVincenzo. Quantum computation with quantum dots. *Phys. Rev. A*, 57:120–126, 1998.

[37] P. Borri, S. Schneider, W. Langbein, and D. Bimberg. Ultrafast carrier dynamics in ingaas quantum dot materials and devices. *Journal of Optics A: Pure and Applied Optics*, 8:S33, 2005.

[38] M. Neeley, R. C. Bialczak, M. Lenander, E. Lucero, Matteo Mariantoni, A. D. O'Connell, D. Sank, H. Wang, M. Weides, J. Wenner, Y. Yin, T. Yamamoto, A. N. Cleland, and J. M. Martinis. Generation of three-qubit entangled states using superconducting phase qubits. *Nature*, 467:570 – 573, 2010.

[39] L. DiCarlo, M. D. Reed, L. Sun, B. R. Johnson, J. M. Chow, J. M. Gambetta, L. Frunzio, S. M. Girvin, M. H. Devoret, and R. J. Schoelkopf. Preparation and measurement of three-qubit entanglement in a superconducting circuit. *Nature*, 467:574 – 578, 2010.

[40] L. Childress, M. V. G. Dutt, J. M. Taylor, A. S. Zibrov, F. Jelezko, J. Wrachtrup, P. R. Hemmer, and M. D. Lukin. Coherent dynamics of coupled electron and nuclear spin qubits in diamond. *Science*, 314:281 – 285, 2006.

[41] M.V.G. Dutt, L. Childress, L. Jiang, E. M. J. Togan, F. Jelezko, A. S. Zibrov, P. R. Hemmer, and M. D. Lukin. Quantum register based on individual electronic and nuclear spin qubits in diamond. *Science*, 316:1312 – 1316, 2007.

[42] Thomas Monz, Philipp Schindler, Julio T. Barreiro, Michael Chwalla, Daniel Nigg, William A. Coish, Maximilian Harlander, Wolfgang Hänsel, Markus Hennrich, and Rainer Blatt. 14-qubit entanglement: Creation and coherence. *Phys. Rev. Lett.*, 106:130506, 2011.

[43] P. Walther, K. J. Resch, T. Rudolph, E. Schenck, H. Weinfurter, V. Vedral, M. Aspelmeyer, and A. Zeilinger. Experimental one-way quantum computing. *Nature*, 434:169 –176, 2005.

[44] T. Jennewein M. Aspelmeyer A. Zeilinger, G. Weihs. Happy centenary, photon. *Nature*, 433:230 – 238, 2005.

[45] R. Jason Jones, Kevin D. Moll, Michael J. Thorpe, and Jun Ye. Phase-coherent frequency combs in the vacuum ultraviolet via high-harmonic generation inside a femtosecond enhancement cavity. *Phys. Rev. Lett.*, 94:193201, 2005.

[46] C. Gohle, T. Udem, M. Herrmann, J. Rauschenberger, R. Holzwarth, H. A. Schüessler, F. Krausz, and T. W. Hansch. A frequency comb in the extreme ultraviolet. *Nature*, 436:234 – 237, 2005.

[47] A. Ozawa, J. Rauschenberger, Ch. Gohle, M. Herrmann, D. R. Walker, V. Pervak, A. Fernandez, R. Graf, A. Apolonski, R. Holzwarth, F. Krausz, T. W. Hänsch, and Th. Udem. High harmonic frequency combs for high resolution spectroscopy. *Phys. Rev. Lett.*, 100:253901, 2008.

[48] R. Krischek, W. Wieczorek, A. Ozawa, N. Kiesel, P. Michelberger, T. Udem, and H. Weinfurter. Ultraviolet enhancement cavity for ultrafast nonlinear optics and high-rate multiphoton entanglement experiments. *Nature Photonics*, 4:170–173, 2010.

[49] R. J. Jones. Quantum optics: Enhanced quantum light generation. *Nature Photonics*, 4:138 – 140, 2010.

[50] W. Wieczorek, R. Krischek, N. Kiesel, P. Michelberger, G. Tóth, and H. Weinfurter. Experimental entanglement of a six-photon symmetric dicke state. *Phys. Rev. Lett.*, 103:020504, 2009.

[51] John K. Stockton, J. M. Geremia, Andrew C. Doherty, and Hideo Mabuchi. Characterizing the entanglement of symmetric many-particle spin-$\frac{1}{2}$ systems. *Phys. Rev. A*, 67:022112, 2003.

[52] Witlef Wieczorek, Nikolai Kiesel, Christian Schmid, and Harald Weinfurter. Multiqubit entanglement engineering via projective measurements. *Phys. Rev. A*, 79:022311, 2009.

[53] D. Bouwmeester, J.-W. Pan, M. Daniell, H. Weinfurter, and A. Zeilinger. Observation of three-photon greenberger-horne-zeilinger entanglement. *Phys. Rev. Lett.*, 82:1345–1349, 1999.

[54] J.-W. Pan, M. Daniell, S. Gasparoni, G. Weihs, and A. Zeilinger. Experimental demonstration of four-photon entanglement and high-fidelity teleportation. *Phys. Rev. Lett.*, 86:4435–4438, 2001.

[55] Zhi Zhao, Tao Yang, Yu-Ao Chen, An-Ning Zhang, Marek Żukowski, and Jian-Wei Pan. Experimental violation of local realism by four-photon greenberger-horne-zeilinger entanglement. *Phys. Rev. Lett.*, 91:180401, 2003.

[56] C.-Y. Lu, X.-Q. Zhou, O. Ghne, W.-B. Gao, J. Zhang, Z.-S. Yuan, A. Goebel, , T. Yang, and J.-W. Pan. Experimental entanglement of six photons in graph states. *Nature Physics*, 3:91 – 95, 2007.

[57] G. Tóth, W. Wieczorek, R. Krischek, N. Kiesel, P. Michelberger, and H. Weinfurterh. Practical methods for witnessing genuine multi-qubit entanglement in the vicinity of symmetric states. *New Journal of Physics*, 11:083002, 2009.

[58] Daniel F. V. James, Paul G. Kwiat, William J. Munro, and Andrew G. White. Measurement of qubits. *Phys. Rev. A*, 64:052312, 2001.

[59] G. Tóth, W. Wieczorek, D. Gross, R. Krischek, C. Schwemmer, and H. Weinfurter. Permutationally invariant quantum tomography. *Phys. Rev. Lett.*, 105:250403, 2010.

[60] P. Hyllus, W. Laskowski, R. Krischek, C. Schwemmer, W. Wieczorek, H. Weinfurter, L. Pezzé, and A. Smerzi. Fisher information, spin squeezing, and multiparticle entanglement. *arXiv*, 1006.4366v1, 2010.

[61] R. F. Werner. Quantum states with einstein-podolsky-rosen correlations admitting a hidden-variable model. *Phys. Rev. A*, 40:4277–4281, 1989.

[62] N. Kiesel. Experiments on multiphoton entanglement. *Ph.D. Thesis, Ludwig-Maximilians-Universität München*, 2007.

[63] C. Schmid. Multi-photon entanglement and applications in quantum information. *Ph.D. Thesis, Ludwig-Maximilians-Universität München*, 2008.

[64] W. Wieczorek. Multi-photon entanglement. *Ph.D. Thesis, Ludwig-Maximilians-Universität München*, 2009.

[65] O. Gühne and G. Tóth. Entanglement detection. *Physics Reports*, 474:1–75, 2009.

[66] R. Horodecki, P. Horodecki, M. Horodecki, and K. Horodecki. Quantum entanglement. *Rev. Mod. Phys.*, 81:865–942, 2009.

[67] J.D Jackson. Classical electrodynamics. *John Wiley & Sons*, 1998.

[68] V. G. Dmitriev, G. G. Gurzadyan, and D. N. Nicogosyan. Handbook of nonlinear optical crystals. *Springer Verlag, Berlin*, 1999.

[69] C. Kurtsiefer, M. Oberparleiter, and H. Weinfurter. High-efficiency entangled photon pair collection in type-ii parametric fluorescence. *Phys. Rev. A*, 64:023802, 2001.

[70] P. G. Kwiat, K. Mattle, H. Weinfurter, A. Zeilinger, A. V. Sergienko, and Y. Shih. New high-intensity source of polarization-entangled photon pairs. *Phys. Rev. Lett.*, 75:4337–4341, 1995.

[71] P. Kok and S. L. Braunstein. Postselected versus nonpostselected quantum teleportation using parametric down-conversion. *Phys. Rev. A*, 61:042304, 2000.

[72] L. Mandel and E. Wolf. Optical coherence and quantum optics. *Cambridge University Press*, 1995.

[73] G. Di Giuseppe, L. Haiberger, F. De Martini, and A. V. Sergienko. Quantum interference and indistinguishability with femtosecond pulses. *Phys. Rev. A*, 56:R21–R24, 1997.

[74] W. P. Grice, R. Erdmann, I. A. Walmsley, and D. Branning. Spectral distinguishability in ultrafast parametric down-conversion. *Phys. Rev. A*, 57:R2289–R2292, 1997.

[75] Timothy E. Keller and Morton H. Rubin. Theory of two-photon entanglement for spontaneous parametric down-conversion driven by a narrow pump pulse. *Phys. Rev. A*, 56:1534–1541, 1997.

[76] P. Michelberger. Femtosecond pulsed enhancement cavity for mutli-photon entanglement studies. *Diploma Thesis,Technische Universitt Mnchen*, 2010.

[77] S. Barz, G. Cronenberg, A. Zeilinger, and P. Walther. Heralded generation of entangled photon pairs. *Nature Photonics*, 4:553 – 556, 2010.

[78] C. Wagenknecht, C.-M. Li, A. Reingruber, X.-H. Bao, A. Goebel, Y.-A. Chen, Q. Zhang, K. Chen, and J.-W. Pan. Experimental demonstration of a heralded entanglement source. *Nature Photonics*, 4:549 – 552, 2010.

[79] R. Ghosh and L. Mandel. Observation of nonclassical effects in the interference of two photons. *Phys. Rev. Lett.*, 59:1903–1905, 1987.

[80] C. K. Hong, Z. Y. Ou, and L. Mandel. Measurement of subpicosecond time intervals between two photons by interference. *Phys. Rev. Lett.*, 59:2044–2046, 1987.

[81] Y. H. Shih and C. O. Alley. New type of einstein-podolsky-rosen-bohm experiment using pairs of light quanta produced by optical parametric down conversion. *Phys. Rev. Lett.*, 61:2921–2924, 1988.

[82] Z. Y. Ou and L. Mandel. Violation of bell's inequality and classical probability in a two-photon correlation experiment. *Phys. Rev. Lett.*, 61:50–53, 1988.

[83] T. E. Kiess, Y. H. Shih, A. V. Sergienko, and C. O. Alley. Einstein-podolsky-rosen-bohm experiment using pairs of light quanta produced by type-ii parametric down-conversion. *Phys. Rev. Lett.*, 71:3893–3897, 1993.

[84] Y. H. Shih, A. V. Sergienko, Morton H. Rubin, T. E. Kiess, and C. O. Alley. Two-photon entanglement in type-ii parametric down-conversion. *Phys. Rev. A*, 50:23–28, 1994.

[85] J.-W. Pan, D. Bouwmeester, M. Daniell, H. Weinfurter, and A. Zeilinger. Experimental test of quantum nonlocality in three-photon greenbergerhornezeilinger entanglement. *Nature*, 403:515 – 519, 2000.

[86] M. Eibl, S. Gaertner, M. Bourennane, C. Kurtsiefer, M. Żukowski, and H. Weinfurter. Experimental observation of four-photon entanglement from parametric down-conversion. *Phys. Rev. Lett.*, 90:200403, 2003.

[87] N. Kiesel, C. Schmid, G. Tóth, E. Solano, and H. Weinfurter. Experimental observation of four-photon entangled dicke state with high fidelity. *Phys. Rev. Lett.*, 98:063604, 2007.

[88] W. Wieczorek, C. Schmid, N. Kiesel, R. Pohlner, O. Gühne, and H. Weinfurter. Experimental observation of an entire family of four-photon entangled states. *Phys. Rev. Lett.*, 101:010503, 2008.

[89] Z. Zhao, Y.-A. Chen, T. Zhang, A.-N.and Yang, H. J. Briegel, and J.-W. Pan. Experimental demonstration of five-photon entanglement and open-destination teleportation. *Nature*, 430:54 – 58, 2004.

[90] R. Prevedel, G. Cronenberg, M. S. Tame, M. Paternostro, P. Walther, M. S. Kim, and A. Zeilinger. Experimental realization of dicke states of up to six qubits for multiparty quantum networking. *Phys. Rev. Lett.*, 103:020503, 2009.

[91] M. Rådmark, M. Wieśniak, M. Żukowski, and M. Bourennane. Experimental filtering of two-, four-, and six-photon singlets from a single parametric down-conversion source. *Phys. Rev. A*, 80:040302, 2009.

[92] M. Rådmark, M. Żukowski, and M. Bourennane. Experimental test of fidelity limits in six-photon interferometry and of rotational invariance properties of the photonic six-qubit entanglement singlet state. *Phys. Rev. Lett.*, 103:150501, 2009.

[93] H. S. Eisenberg, G. Khoury, G. A. Durkin, C. Simon, and D. Bouwmeester. Quantum entanglement of a large number of photons. *Phys. Rev. Lett.*, 93:193901, 2004.

[94] Eds., A. Migdal, and J. Dowling. Special issue: Single-photon: detectors, applications, and measurement methods. *Journal of Modern Optics*, 51, 2004.

[95] A. P. Worsley, H. B. Coldenstrodt-Ronge, J. S. Lundeen, P. J. Mosley, B. J. Smith, G. Puentes, N. Thomas-Peter, and I. A. Walmsley. Absolute efficiency estimation of photon-number-resolving detectors using twin beams. *Opt. Express*, 17:4397–4411, 2009.

[96] B. Lounis and M. Orrit. Single-photon sources. *Rep. Prog. Phys.*, 68:1129, 2005.

[97] P. Fendel. Präzisionsspektroskopie an wasserstoff und deuterium. *Ph.D. thesis, Ludwig-Maximilians-Universität München*, 2005.

[98] J. Reichert, R. Holzwarth, T. Udem, and T. W. Hnsch. Measuring the frequency of light with mode-locked lasers. *Opt. Commun.*, 172:59 – 68, 1999.

[99] R. Szipöcs, K. Ferencz, C. Spielmann, and F. Krausz. Chirped multilayer coatings for broadband dispersion control in femtosecond lasers. *Opt. Lett.*, 19:201, 1994.

[100] T. W. Hänsch and B. Couillaud. Laser frequency stabilization by polarization spectroscopy of a reflecting reference cavity. *Opt. Commun.*, 35:441 – 444, 1980.

[101] R. W. P. Drever, J. L. Hall, F. V. Kowalski, J. Hough, G. M. Ford, A. J. Munley, and H. Ward. Laser phase and frequency stabilization using an optical resonator. *Appl. Phys. B*, 31:97 – 105, 1983.

[102] T. Udem, R. Holzwarth, and T.W. Hänsch. Optical frequency metrology. *Nature*, 416:233 – 237, 2002.

[103] C. Gohle. A coherent frequency comb in the extreme ultraviolet. *Ph.D. Thesis, Ludwig-Maximilians-Universität München*, 2006.

[104] R. Trebino and D. J. Kane. Using phase retrieval to measure the intensity and phase of ultrashort pulses: frequency-resolved optical gating. *J. Opt. Soc. Am. A*, 10:1101–1111, 1993.

[105] C. Iaconis and I. A. Walmsley. Spectral phase interferometry for direct electric-field reconstruction of ultrashort optical pulses. *Opt. Lett.*, 23:792–794, 1998.

[106] F. (Ed.) Träger. Handbook of lasers and optics. *Springer Scienece + Buisiness Media, LLC New York*, 2007.

[107] J. I. Dadap, G. B. Focht, D. H. Reitze, and M. C. Downer. Two-photon absorption in diamond and its application to ultraviolet femtosecond pulse-width measurement. *Opt. Lett.*, 16:499 – 501, 1991.

[108] N. F. Kleimeier, T. Haarlammert, H. Witte, U. Schhle, J.-F. Hochedez, A. Ben-Moussa, and H. Zacharias. Autocorrelation and phase retrieval in the uv using two-photon absorption in diamond pin photodiodes. *Opt. Express*, 18:6945 – 6956, 2010.

[109] M. Morita and T. Yajima. A nonlinear correlation method using multiphoton ionization for the measurement of uv ultrashort pulses. *Appl. Phys. B*, 18:25, 1982.

[110] M. H. R. Hutchinson, I. A. McIntyre, G. N. Gibson, and C. K. Rhodes. Measurement of 248-nm, subpicosecond pulse durations by two-photon fluorescence of xenon excimers. *Opt. Lett.*, 12:102, 1987.

[111] S. P. Le Blanc, G. Szabo, and R. Sauerbrey. Femtosecond single-shot phase-sensitive autocorrelator for the ultraviolet. *Opt. Lett.*, 16:1508, 1991.

[112] H. Schulz, H. Schiller, T. Engers, and D. von der Linde. Measurement of intense ultraviolet subpicosecond pulses using degenerate four-wave mixing. *IEEE Journal of Quantum Electronics*, 25,:2580, 1989.

[113] H.-St. Albrecht, P. Heist, J. Kleinschmidt, D. van Lap, and T. Schrder. Measurement of ultraviolet femtosecond pulses using the optical kerr effect. *Appl. Phys. B*, 55:362 – 364, 1992.

[114] K. L. Sala, G. A. Kenny-Wallace, and G.E. Hall. Cw autocorrelation measurements of poicosecond laser pulses. *IEEE*, QE-16:990 – 996, 1980.

[115] R. H. Dicke. Coherence in spontaneous radiation processes. *Phys. Rev.*, 93:99, 1954.

[116] L.-M. Duan and H. J. Kimble. Efficient engineering of multiatom entanglement through single-photon detections. *Phys. Rev. Lett.*, 90:253601, 2003.

[117] XuBo Zou, K. Pahlke, and W. Mathis. Generation of arbitrary superpositions of the dicke states of excitons in optically driven quantum dots. *Phys. Rev. A*, 68:034306, 2003.

[118] J. K. Stockton, R. van Handel, and H. Mabuchi. Deterministic dicke-state preparation with continuous measurement and control. *Phys. Rev. A*, 70:022106, 2004.

[119] N Kiesel, M. Bourennane, C. Kurtsiefer, H. Weinfurter, D. Kaszlikowskia, W. Laskowski, and M. Zukowski. Three-photon w-state. *Journal of Modern Optics*, 50:1131 – 1138, 2003.

[120] Mohamed Bourennane, Manfred Eibl, Christian Kurtsiefer, Sascha Gaertner, Harald Weinfurter, Otfried Gühne, Philipp Hyllus, Dagmar Bruß, Maciej Lewenstein, and Anna Sanpera. Experimental detection of multipartite entanglement using witness operators. *Phys. Rev. Lett.*, 92:087902, 2004.

[121] M. Eibl, N. Kiesel, M. Bourennane, C. Kurtsiefer, and H. Weinfurter. Experimental realization of a three-qubit entangled *w* state. *Phys. Rev. Lett.*, 92:077901, 2004.

[122] Hideharu Mikami, Yongmin Li, Kyosuke Fukuoka, and Takayoshi Kobayashi. New high-efficiency source of a three-photon *w* state and its full characterization using quantum state tomography. *Phys. Rev. Lett.*, 95:150404, 2005.

[123] M. Horodecki, P. Horodecki, and R. Horodecki. Separability of mixed states: necessary and sufficient conditions. *Physics Letters A*, 223:1 – 8, 1996.

[124] N. Kiesel, C. Schmid, U. Weber, G. Tóth, O. Gühne, R. Ursin, and H. Weinfurter. Experimental analysis of a four-qubit photon cluster state. *Phys. Rev. Lett.*, 95:210502, 2005.

[125] A. Peres. Separability criterion for density matrices. *Phys. Rev. Lett.*, 77:1413–1415, 1996.

[126] G. Tóth. Detection of multipartite entanglement in the vicinity of symmetric dickestates. *J. Opt. Soc. Am. B*, 24:275, 2007.

[127] C. Schmid, N. Kiesel, W. Laskowski, W. Wieczorek, M. Żukowski, and H. Weinfurter. Discriminating multipartite entangled states. *arXiv*, 0804.3154, 2008.

[128] N. D. Mermin. Extreme quantum entanglement in a superposition of macroscopically distinct states. *Phys. Rev. Lett.*, 65:1838–1840, 1990.

[129] M. edited by Paris and J. Rehacek. *Quantum State Estimation*. Springer, Berlin Heidelberg, 2004.

[130] D. M. Greenberger, M. A. Horne, A. Shimony, and A Zeilinger. Bell's theorem without inequalities. *Am. J. Phys.*, 58:1131 – 1143, 1990.

[131] C. A. Sackett, D. Kielpinski, B. E. King, C. Langer, V. Meyer, C. J. Myatt, M. Rowe, Q. A. Turchette, W. M. Itano, D. J. Wineland, and C. Monroe. Experimental entanglement of four particles. *Nature*, 404:256 – 259, 2000.

[132] W. Dür, G. Vidal, and J. I. Cirac. Three qubits can be entangled in two inequivalent ways. *Phys. Rev. A*, 62:062314, 2000.

[133] L. Zehnder. *Z. Instrum.kd.*, 11:275, 1891.

[134] L. Mach. *Z. Instrum.kd*, 12:89, 1892.

[135] L. Pezzé, A. Smerzi, G. Khoury, J. F. Hodelin, and D. Bouwmeester. Phase detection at the quantum limit with multiphoton mach-zehnder interferometry. *Phys. Rev. Lett.*, 99:223602, 2007.

[136] L. Pezzé and A. Smerzi. Entanglement, nonlinear dynamics, and the heisenberg limit. *Phys. Rev. Lett.*, 102:100401, 2009.

[137] P. Hyllus, O. Gühne, and A. Smerzi. Not all pure entangled states are useful for sub-shot-noise interferometry. *Phys. Rev. A*, 82:012337, 2010.

[138] H. Cramér. *Mathematical Methods of Statistics*. Princeton University Press, 1946.

[139] Z. Hradil and J. Rehacek. Quantum interference and fisher information. *Phys. Lett. A*, 334:267 – 272, 2005.

[140] V. Giovannetti, S. Lloyd, and L. Maccone. Quantum-enhanced positioning and clock synchronization. *Nature*, 412:417, 2001.

[141] N. Treps, U. Andersen, B. Buchler, P. K. Lam, A. Maître, H.-A. Bachor, and C. Fabre. Surpassing the standard quantum limit for optical imaging using non-classical multimode light. *Phys. Rev. Lett.*, 88:203601, 2002.

[142] B. R. Frieden. *Science from Fisher Information: A Unification*. Cambridge University Press, 2004.

[143] S. L. Braunstein and C. M. Caves. Statistical distance and the geometry of quantum states. *Phys. Rev. Lett.*, 72:3439–3443, 1994.

[144] C. W. Helstrom. Minimum mean-square error of estimates in quantum statistics. *Phys. Lett. A*, 25:101–102, 1967.

[145] G. Tóth. Multipartite entanglement and high precision metrology. *arXiv*, 1006.4368v1, 2010.

[146] Vittorio Giovannetti, Seth Lloyd, and Lorenzo Maccone. Quantum metrology. *Phys. Rev. Lett.*, 96:010401, 2006.

[147] Z. Hradil, R. Myška, J. Peřina, M. Zawisky, Y. Hasegawa, and H. Rauch. Quantum phase in interferometry. *Phys. Rev. Lett.*, 76:4295–4298, 1996.

[148] L. Pezzé, A. Smerzi, G. Khoury, J. F. Hodelin, and D. Bouwmeester. Phase detection at the quantum limit with multiphoton mach-zehnder interferometry. *Phys. Rev. Lett.*, 99:223602, 2007.

[149] R. Kacprowicz, M.and Demkowicz-Dobrzański, W. Wasilewski, K. Banaszek, and I. A. Walmsley. Experimental quantum-enhanced estimation of a lossy phase shift. *Nature Photonics*, 4:357–360, 2010.

[150] B. Yurke, S. L. McCall, and J. R. Klauder. Su(2) and su(1,1) interferometers. *Phys. Rev. A*, 33:4033–4054, 1986.

[151] E. T. Jaynes. Probability theory: the logic of science. *Cambridge University Press*, 2003.

[152] J. G. Rarity, P. R. Tapster, E. Jakeman, T. Larchuk, R. A. Campos, M. C. Teich, and B. E. A. Saleh. Two-photon interference in a mach-zehnder interferometer. *Phys. Rev. Lett.*, 65:1348–1351, 1990.

[153] Z. Y. Ou, X. Y. Zou, L. J. Wang, and L. Mandel. Experiment on nonclassical fourth-order interference. *Phys. Rev. A*, 42:2957–2965, 1990.

[154] P. Walther, J.-W. Pan, M. Aspelmeyer, R. Ursin, S. Gasparoni, and A. Zeilinger. De broglie wavelength of a non-local four-photon state. *Nature*, 429:158 – 161, 2004.

[155] M. W. Mitchell, J. S. Lundeen, and A. M. Steinberg. Super-resolving phase measurements with a multiphoton entangled state. *Nature*, 429:161 – 164, 2004.

[156] K. J. Resch, K. L. Pregnell, R. Prevedel, A. Gilchrist, G. J. Pryde, J. L. O'Brien, and A. G. White. Time-reversal and super-resolving phase measurements. *Phys. Rev. Lett.*, 98:223601, 2007.

[157] T. Nagata, R. Okamoto, J.L. O'Brien, K. Sasaki, and S. Takeuchi. Beating the standard quantum limit with four-entangled photons. *Science*, 316:726, 2007.

[158] W.-B. Gao, C.-Y. Lu, X-C. Yao, P. Xu, O. Ghne, A. Goebel, Y.-A. Chen, C.-Z. Peng, Z.-B. Chen, and J.-W. Pan. Experimental demonstration of a hyper-entangled ten-qubit schrdinger cat state. *Nature Physics*, 6:331 – 335, 2010.

[159] J. P. Dowling. Quantum optical metrology - the lowdown on high-n00n states. *Contemporary Physics*, 49:125 – 143, 2008.

[160] R. Okamoto, H. F. Hofmann, T. Nagata, J. L. O'Brien, K. Sasaki, and S. Takeuchi. Beating the standard quantum limit: phase super-sensitivity of n -photon interferometers. *New Journal of Physics*, 10:073033, 2008.

[161] B. Yurke. Input states for enhancement of fermion interferometer sensitivity. *Phys. Rev. Lett.*, 56:1515–1517, 1986.

[162] W. Wieczorek, R. Krischek, A. Ozawa, G. Tóth, N. Kiesel, P. Michelberger, T. Udem, and H. Weinfurter. Six-photon entangled dicke state enabled by a uv enhancement cavity as novel spdc photon source. *Quantum Optics Proceedings of SPIE*, 7727:77270L, 2010.

[163] W. Laskowski, M. Wiesniak, M. Zukowski, M. Bourennane, and H. Weinfurter. Interference contrast in multisource few-photon optics. *Journal of Physics B*, 42:114004, 2009.

[164] M. S. Kaznady and D. F. V. James. Numerical strategies for quantum tomography: Alternatives to full optimization. *Phys. Rev. A*, 79:022109, 2009.

Danksagung / Acknowledgements

Ein besonderer Dank möchte ich an Esther Vogt aussprechen. Sie stand mir stets wegweisend zur Seite, besonders in Situation, wenn man vor lauter Bäumen den Wald nicht mehr sieht, hat Sie meinen Blick immer wieder auf das Wesentliche gerichtet und damit diese Arbeit - und viel mehr - erst ermöglicht. Dafür und überhaupt möchte ich Ihr, sowie Fabienne, Nadine und Toni von ganzem Herzen danken.

Auch meiner Mutter möchte ich an dieser Stelle besonders danken. Sie hat mich bei allem was ich tat immer tatkräftig unterstützt und mich auf meinem ganzen Werdegang begleitet. Nicht nur dafür sondern für alles möchte ich Ihr herzlichst danken. Dieser Dank gilt auch Bruno Marti, der mich schon seit klein auf kennt und immer wie ein Vater für mich war.

Prof. Dr. Harald Weinfurter möchte ich danken, dass er mich als Doktorand in seine Arbeitsgruppe aufnahm und mir somit die Forschung auf dem Gebiet der verschränkten Photonen ermöglichte. Dadurch bekam ich Einblicke in aktuelle und grundlegende Forschungsthemen der Quantenphysik und bin deshalb sehr dankbar für diese interessante Zeit.

All meinen Arbeitskollegen möchte ich danken für die vielen anregenden Gespräche und Diskussionen über Quantenphysik im Allgemeinen oder über die Experimente, die wir zusammen druchgeführt haben. Ich habe nicht nur fachlich, sonder auch persönlich viel von Euch gelernt. Ganz besonders natürlich der ganzen "Garchinger-Crew" (Witlef Wieczorek, Christian Schwemmer, Daniel Richart, Alexander Niggebaum, Yvo Fischer, Patrick Michelberger, Christian Schmid, Pavel Trojek und Nikolai Kiesel), die sich immer und überall - sei das nun am Mittagstisch, Büro, Labor oder sonst irgendwo - die Zeit nahmen, mir Fragen zu beantworten oder zusammen über irgend welche Themen zu diskutieren. Dann natürlich allen anderen Gruppenmitgliedern aus der Stadt (Daniel Schlenk, Markus Weber, Wenjamin Rosenfeld, Florian Henkel, Sebastian Nauerth, Martin Fürst, Julian Hofmann, Michael Krug, Juliane Hermelbracht, Hennig Weier, Markus Rau, Norbert Ortegel, ...) für die angenehmen Gespräche und konstruktiven Ratschläge bei oder nach der Gruppensitzung.

Während meiner Doktorarbeit habe ich auch mit anderen Arbeitsgruppen zusammengearbeitet und möchte allen für diese Kooperation danken. So auch Philipp Hyllus für die meist langen, konstruktiven und immer unterhaltsamen Gespräche über Skype, wie auch Augusto Smerzi und Luca Pezzé für die gemeinsame Zusammenarbeit zum Thema "Fisher Information". Dann natürlich auch Géza Tóth und Wieslaw Laskowski für die zahlreichen Diskussionen und verschiedenen Arbeiten die wir zusammen durchgeführt haben.

Und schliesslich allen Freunden und Bekannten die durch meine Erzählungen grosse Teile dieser Zeit miterlebt haben und mir so viele wertvolle Impulse und Anregungen weitergaben.

Publication List and Contribution

W. Wieczorek, **R. Krischek**, N. Kiesel, P. Michelberger, G. Tóth and H. Weinfurter
Experimental Entanglement of a Six-Photon Symmetric Dicke State
Physical Review Letters, 103:020504, 2009
Contribution: conceived the experiment together with W.W. and H.W.; performed the experiment together with W.W. and P.M.; analysed the data together with W.W., N.K., P.M., G.T. and H.W. and wrote parts of the manuscript

G. Tóth, W. Wieczorek, **R. Krischek**, N. Kiesel P. Michelberger and H. Weinfurter
Practical methods for witnessing genuine multi-qubit entanglement in the vicinity of symmetric states
New Journal of Physics, 11:083002, 2009
Contribution: discussed the paper in an experimental context and edited the manuscript

R. Krischek, W. Wieczorek, A. Ozawa, N. Kiesel, P. Michelberger, T. Udem and H. Weinfurter
Ultraviolet enhancement cavity for ultrafast nonlinear optics and high-rate multiphoton entanglement experiments
Nature Photonics, 4:170-173, 2010
Contribution: conceived the experiment together with W.W., A.O., T.U. and H.W.; performed the experiment together with W.W. and P.M.; analysed the data together with W.W., A.O., N.K., P.M., T.U. and H.W. and wrote parts of the manuscript

G. Tóth, W. Wieczorek, D. Gross, **R. Krischek**, C. Schwemmer and H. Weinfurter
Permutationally invariant quantum tomography
Physical Review Letters, 105:250403, 2010
Contribution: performed the experiment together with W.W. and C.S; analysed the data together with G.T., W.W., D.G., C.S. and H.W. and edited the manuscript

P. Hyllus, W. Laskowski, **R. Krischek**, C. Schwemmer, W. Wieczorek, H. Weinfurter, L. Pezzé, A. Smerzi
Fisher information, spin squeezing, and multiparticle entanglement
arXiv, 1006.4366v1, 2010
Contribution: discussed the paper in an experimental context and edited the manuscript

P. Michelberger, **R. Krischek**, W. Wieczorek, A. Ozawa and H. Weinfurter
Interferometric autocorrelation in the ultra-violet utilizing spontaneous parametric down-conversion
in preparation
Contribution: conceived the experiment together with P.M., W.W., A.O. and H.W.; performed the experiment together with P.M. and W.W. and edited the manuscript

R. Krischek, C. Schwemmer, W. Wieczorek, H. Weinfurter, P. Hyllus, L. Pezzé and A. Smerzi
Useful multiparticle entanglement and sub shot-noise phase estimation
accepted for publication in Physical Review Letters
<u>Contribution:</u> conceived the experiment together with C.S., W.W., H.W., P.H., L.P. and A.S.; performed the experiment together with C.S. and W.W.; analysed the data together with C.S., W.W., H.W., P.H., L.P. and A.S. and wrote parts of the manuscript

W. Wieczorek, **R. Krischek**, W. Laskowski and H. Weinfurter
Experimental quantum metrology with Dicke and Twin-Fock states for determining two complementary phases beyond the shot noise limit
in preparation
<u>Contribution:</u> conceived the experiment together with W.W., W.L. and H.W.; performed the experiment together with W.W.; analysed the data together with W.W., W.L. and H.W. and edited the manuscript

Curriculum vitae

Personal data

Name:	Roland Patrik Krischek
Date of birth:	25th of August, 1982
Place of birth:	Sarnen (Switzerland)
Nationality:	Swiss

Education

2007 - 2011	PhD thesis in the Experimental Quantum Physics group of Prof. Dr. Harald Weinfurter at the Max-Planck-Institute of Quantum Optics in Garching near Munich
2001 - 2007	Diploma in physics from the Swiss Federal Institute of Technology (ETH) in Zurich
2004/05	Exchange program (ERASMUS) in Paris for one year at the "Université Pierre et Marie Curie" (Paris VI)
1995 - 2001	High school in Sarnen (Switzerland) with "Matura" (university-entrance diploma)
1989 - 1995	Elementary school in Alpnach Dorf (Switzerland)